Online ISSN: 1920-3853

Print ISSN : 1715-9997

Vol. 4, No. 3, October 2010

Canadian Journal of pure & applied sciences

an International Journal

SENRA

Academic Publishers

Burnaby, British Columbia

Print ISSN 1715-9997
Online ISSN 1920-3853

Volume 4, Number 3
October 2010

CANADIAN JOURNAL OF PURE AND APPLIED SCIENCES

EDITOR
MZ Khan, SENRA Academic Publishers
Burnaby, British Columbia, Canada

ASSOCIATE EDITORS
Errol Hassan, University of Queensland
Gatton, Australia

Paul CH Li, Simon Fraser University
Burnaby, British Columbia, Canada

EDITORIAL STAFF
Jasen Nelson
Walter Leung
Sara Ali
Hao-Feng (howie) Lai
Ben Shieh

MANAGING DIRECTOR
Mak, SENRA Academic Publishers
Burnaby, British Columbia, Canada

The Canadian Journal of Pure and Applied Sciences (CJPAS-ISSN 1715-9997) is a peer reviewed multi-disciplinary specialist journal aimed at promoting research worldwide in Agricultural Sciences, Biological Sciences, Chemical Sciences, Computer and Mathematical Sciences, Engineering, Environmental Sciences, Medicine and Physics (all subjects).

Every effort is made by the editors, board of editorial advisors and publishers to see that no inaccurate or misleading data, opinions, or statements appear in this journal, they wish to make clear that data and opinions appearing in the articles are the sole responsibility of the contributor concerned. The CJPAS accept no responsibility for the misleading data, opinion or statements.

CJPAS is indexed by:
Ulrich's Periodicals Directory,
Index Copernicus, Directory of Open Access Journals, Google Scholar,
Yahoo, Bing, Ask, CABI,
Chemical Abstracts, Zoological Records,
Biblioteca Central, Collection of Computer Science Bibliography.
CJPAS has received Index Copernicus Journals Evaluation for 2009 = 4.98

Editorial Office
E-mail: editor@cjpas.ca
: editor@cjpas.net

SENRA Academic Publishers
7845 15th Street Burnaby
British Columbia V3N 3A3 Canada
www.cjpas.net
E-mail: senra@cjpas.ca

Board of Editorial Advisors

Richard Callaghan
University of Calgary, AB, Canada
David T Cramb
University of Calgary, AB, Canada
Matthew Cooper
Grand Valley State University, AWRI, Muskegon, MI, USA
Anatoly S Borisov
Kazan State University, Tatarstan, Russia
Ron Coley
Coley Water Resource & Environment Consultants, MB, Canada
Chia-Chu Chiang
University of Arkansas at Little Rock, Arkansas, USA
Michael J Dreslik
Illinois Natural History, Champaign, IL, USA
David Feder
University of Calgary, AB, Canada
David M Gardiner
University of California, Irvine, CA, USA
Geoffrey J Hay
University of Calgary, AB, Canada
Chen Haoan
Guangdong Institute for drug control, Guangzhou, China
Hiroyoshi Ariga
Hokkaido University, Japan
Gongzhu Hu
Central Michigan University, Mount Pleasant, MI, USA
Moshe Inbar
University of Haifa at Qranim, Tivon, Israel
SA Isiorho
Indiana University - Purdue University, (IPFW), IN, USA
Bor-Luh Lin
University of Iowa, IA, USA
Jinfei Li
Guangdong Coastal Institute for Drug Control, Guangzhou, China
Collen Kelly
Victoria University of Wellington, New Zealand
Hamid M.K.AL-Naimiy
University of Sharjah, UAE
Eric L Peters
Chicago State University, Chicago, IL, USA
Roustam Latypov
Kazan State University, Kazan, Russia
Frances CP Law
Simon Fraser University, Burnaby, BC, Canada
Guangchun Lei
Ramsar Convention Secretariat, Switzerland
Atif M Memon
University of Maryland, MD, USA
SR Nasyrov
Kazan State University,Kazan, Russia
Russell A Nicholson
Simon Fraser University, Burnaby, BC, Canada
Borislava Gutarts
California State University, CA, USA
Sally Power
Imperial College London, UK
Gordon McGregor Reid
North of England Zoological Society, UK
Pratim K Chattaraj
Indian Institute of Technology, Kharagpur, India
Andrew Alek Tuen
Institute of Biodiversity, Universiti Malaysia Sarawak, Malaysia
Dale Wrubleski
Institute for Wetland and Waterfowl Research, Stonewall, MB, Canada
Dietrich Schmidt-Vogt
Asian Institute of Technology, Thailand
Diganta Goswami
Indian Institute of Technology Guwahati, Assam, India
M Iqbal Choudhary
HEJ Research Institute of Chemistry, Karachi, Pakistan
Daniel Z Sui
Texas A&M University, TX, USA
SS Alam
Indian Institute of Technology Kharagpur, India
Biagio Ricceri
University of Catania, Italy
Zhang Heming
Chemistry & Environment College, Normal University, China
C Visvanathan
Asian Institute of Technology, Thailand
Indraneil Das
Universiti Malaysia, Sarawak, Malaysia
Gopal Das
Indian Institute of Technology , Guwahati, India
Melanie LJ Stiassny
American Museum of Natural History, New York, NY, USA
Kumlesh K Dev
Bio-Sciences Research Institute, University College Cork, Ireland.
Shakeel A Khan
University of Karachi, Karachi, Pakistan
Xiaobin Shen
University of Melbourne, Australia
Maria V Kalevitch
Robert Morris University, PA, USA
Xing Jin
Hong Kong University of Science & Tech.
Leszek Czuchajowski
University of Idaho, ID, USA
Basem S Attili
UAE University, UAE
David K Chiu
University of Guelph, Ontario, Canada
Gustavo Davico
University of Idaho, ID, USA
Andrew V Sills
Georgia Southern University Statesboro, GA, USA
Charles S. Wong
University of Alberta, Canada
Greg Gaston
University of North Alabama, USA

Canadian Journal of
pure&applied
sciences

Volume 4, Number 3
October 2010

CONTENTS

LIFE SCIENCES

PHYSICAL SCIENCES

SENRA Academic Publishers, Burnaby, British Columbia
Vol. 4, No. 3, pp. 1233-1242, October 2010
Online ISSN: 1920-3853; Print ISSN: 1715-9997

Canadian Journal of pure&applied sciences

HISTOPATHOLOGICAL AND BIOCHEMICAL EFFECTS OF COLCHICINE AND TRIMETHYLCOLCHICINIC ACID ON LIVER FIBROSIS INDUCED BY BILE DUCT LIGATION IN ALBINO RATS

*Saber A Sakr[1], Hoda A Mahran[1], Nahed S Bassily[2] and Mona E Saif[2]
[1]Department of Zoology, Faculty of Science, Menoufia University, Egypt
[2]General Branch of Basic Medical Science, National Organization for Drug Control and Research Cairo, Egypt

ABSTRACT

The present study investigated the effect of colchicine and trimethylcolchicinic acid on liver fibrosis induced by common bile duct ligation in albino rats. Bile duct ligated rats showed cirrhosis where liver architecture completely distorted with diffused fibrosis and generation of abnormal nodules. Hepatocytes with nuclear changes and highly proliferated bile ductules were also detected. Alpha smooth muscle actin positive cells increased markedly. Biochemical results also showed elevation in serum transaminases (AST, ALT) and alkaline phosphatase activities as well as total bilirubin concentration. Most of these effects were gradually reversed with colchicine and trimethylcolchicinic acid treatment. Both colchicine and trimethylcolchicinic acid were nearly similar in there therapeutic effect when used at the same dose and under similar conditions. Moreover, higher doses of trimethylcolchicinic acid were more efficient and safer than colchicine in treating liver fibrosis in the experimental animals.

Keywords: Colchicine, trimethylcolchicinic acid, bile duct ligation, liver, cirrhosis.

INTRODUCTION

Liver fibrosis is the excessive accumulation of extracellular matrix proteins (ECM) in the liver (Bataller and Brenner, 2005). Patients with liver fibrosis can be asymptomatic for 15-20 years with morbidity and mortality only occurring after progression to cirrhosis (Friedman, 2003; Bataller and Brenner, 2005). Cirrhosis is a diffuse process characterized by fibrosis and the conversion of normal liver architecture into structurally abnormal nodules (Anthony *et al*., 1978).

Hepatic fibrosis was historically thought to be a passive and irreversible process due to the collapse of the hepatic parenchyma and its substitution with a collagen-rich tissue (Schaffner and Klion, 1968; Popper and Uenfriend, 1970). Currently, it is considered a model of wound-healing response to chronic liver injury (Albanis and Friedman, 2001). During the last 40 years, research focused on the cellular origin of enhanced hepatic matrix synthesis within the damaged liver tissue (Ramadori and Saile, 2004). In 1980s, hepatic stellate cells (HSCs) were identified as the main collagen-producing cells in the liver (Friedman *et al*., 1985).

During liver injury, HSCs get activated and their number drastically increases (van de Bovenkamp, 2006), migrate and accumulate at the sites of tissue repair, expressing myogenic markers as alpha-smooth muscle actin (α-SMA), secreting large amounts of ECM and regulate ECM degradation (Bataller and Brenner, 2005). Thus, HSCs participate pathophysiologically in both fibrogenesis and fibrolysis “tissue remodeling” (Gressner and Weiskirchen, 2006).

It has been reported that colchicine, alkaloid obtained from various species of *Colchicum*, usually *Colchicum autumnale* (Robbers *et al*., 1996), protects the liver of experimental animals against CCl_4, galactosamine and acetaminophen intoxication (Mourelle *et al*., 1988; Mourelle and Meza, 1989; Muriel *et al*., 1993 respectively). In addition, Kershenobich *et al*. (1988) and Muntoni *et al*. (2010) have shown some beneficial effects of colchicine in the treatment of cirrhotic patients. However, diarrhea, nausea and vomiting are the common side effects of colchicine even at therapeutic doses (Sweetman, 2007). Therefore, colchicine should be given at very low doses because of its toxicity that attributed to its ability to bind with microtubule protein (tubulin). Trimethylcolchicinic acid (TMCA) is a colchicine derivative, which does not bind with tubulin (Zweig and Chignell, 1973). Therefore, higher doses of TMCA may be more effective and harmless than colchicine in treating liver cirrhosis. The effect of TMCA on liver fibrosis was studied by few investigators (Cedillo *et al*.1996 and Muriel *et al*., 2005). The aim of this work is to compare the histopathological, immunohistochemical, and biochemical effects of colchicine and trimethylcolchicinic acid on liver fibrosis induced by common bile duct ligation in albino rats.

MATERIALS AND METHODS

Chemicals used

Colchicine was obtained from El-Nasr Pharmaceutical Chemical Company (ADWIC), Egypt, as white tablets

---

*Corresponding author email: sabsak@yahoo.com

each contain 500µg of colchicine. Trimethylcolchicinic acid was obtained from Sigma Chemical Company, USA, in the form of yellow powder. Colchicine and TMCA were dissolved in distilled water and were orally given to the experimental animals. Colchicine was administered at a dose level of 50µg/kg body weight/day (Poo *et al.*, 1993) while TMCA was administered at two dose levels; low dose (50µg/kg/day) and high dose (150µg/kg body weight /day).

Experimental design

Adult female albino rats (*Rattus norvegicus),* of an average body weight 200±10g were used. They were obtained from the animal house of The National Organization for Drug Control and Research (NODCAR). Animals were kept in the laboratory under almost constant condition of temperature (24±2°C) for 2 weeks before and throughout the experimental work. They were fed on standard rodent diet manufactured specially for laboratory purposes, as well as some vegetables. Water was given *ad libitum*. Biliary cirrhosis was induced surgically through double ligation and division of the common bile duct under light ether anesthesia.

Animals were divided into two main groups bile duct ligated group (BDL) and sham operated group. After 4 weeks from surgery 6 animals were dissected from each group and the remaining animals were divided as following. 1- BDL group divided into: non-treated subgroup, 50µg/kg body weight/day colchicine treated subgroup, 50µg/kg body weight/day TMCA treated subgroup and 150µg/kg body weight/day TMCA treated subgroup. 2- Sham operated group divided into: non-treated subgroup, 50µg/kg body weight/day colchicine treated subgroup and 150µg TMCA treated subgroup. All these subgroups were treated for 4 weeks.

Histological and immunohistochemical studies

Six animals from each subgroup were sacrificed 6 and 8 weeks after surgery. Small liver slices were rapidly removed, fixed in Bouin's fluid and stained with hematoxylin and eosin for histological examination under light microscopy. Other liver slices were fixed in Zenker's solution and stained with Mallory trichrome technique (Weesner, 1968) for demonstration of collagen fibers. Fibrous tissue area was measured by computerized image analysis system "*Image Proplus version 5*" in each subgroub. For analysis, six power fields per each liver section were taken at X 40 (4 objective X 10 ocular). The percent of fibrotic tissue area per examined liver sections were calculated in each group (Froh *et al.*, 2007). Alpha-smooth muscle actin positive cells were visualized immunohistochemically using liver slices fixed in 10% formalin.

Biochemical study

Blood was collected according to the retro-orbital plexus method (Schermer, 1967). Serum activities of aspartate aminotransferase (AST), alanine aminotransferase (ALT) were determined according to Reitman and Frankel (1957), while serum alkaline phosphatase (ALP) activity was measured according to Belfield and Goldberg (1971). Total bilirubin concentration was determined according to Jendrassik and Gróf (1938). For statistical analysis, one-way ANOVA was used in order to compare the group's means. Differences were considered significant for *P*<0.05.

RESULTS

Histopathological observations

In sham operated groups, no histological alterations were detected (Fig.1). On the other hand, all examined liver sections taken from BDL animals after 4 and 6 weeks showed cirrhosis. The hepatic architecture was completely distorted, liver lobules nearly disappeared and were replaced with macro and micro nodules separated by wide fibrous tissue area admixed with highly proliferated and dilated bile ductules (Fig. 2). Hepatic cells appeared with variable changes in their nuclei including hypertrophy, marginal chromatin, pyknosis, clumped, crescent shape, and irregular nuclear envelope. Mild to moderate inflammation and prominent enlarged Kupffer cells were seen in the fibrous tissue stroma.

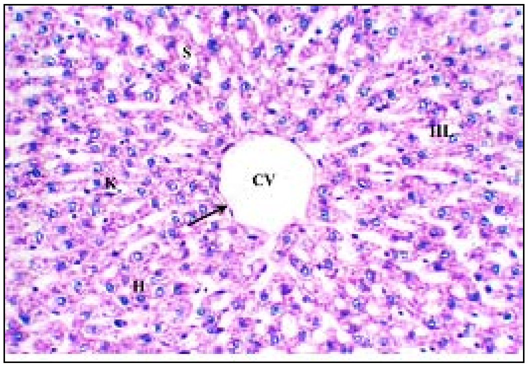

Fig. 1. Liver section of sham operated rat showing hepatic lobule (HL), central vein (CV) with it's endothelial cell lining (arrow), polygonal hepatic cells (H), sinusoids (S) and Kupffer cells (K), (H&E, X 200).

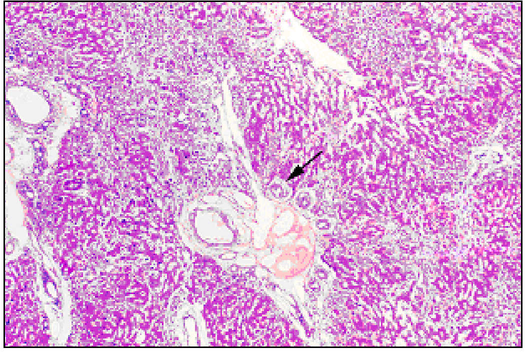

Fig. 2. Liver section of common bile duct ligated rat for 4 weeks duration showing complete distortion of hepatic architecture and hyper proliferated bile ductules (arrow), (H&E, X 40).

In BDL groups treated daily with either 50µg colchicine/kg or 50µg TMCA/kg for 2 weeks**,** 50% of examined liver sections still showing evidence of marked loss of hepatic lobular architecture. However, in the remaining 50% of examined cases, lobular architecture started to be distinguished (Figs. 3, 4). Treating BDL rats daily with 50µg colchicine/kg for 4 weeks, more progress in retaining well organized hepatic lobular architecture was seen in 50% of examined liver sections with appearance of thin fibrous band partitions invaded with inflammatory cells and marked reduction in number of the proliferated bile ductules. In addition, treating BDL animals daily with 50µg TMCA/kg for 4 weeks, showed also diffused well formed hepatic lobules in two thirds of the treated animals.

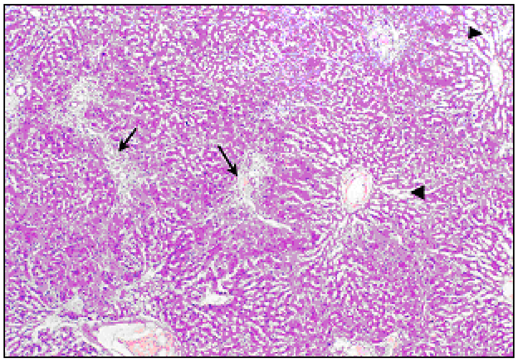

Fig. 3. Section of liver of BDL rat treated with 50µg colchicine/kg for 2 weeks. Distinguished hepatic lobules separated by moderately widened fibrotic portal areas (arrow) and widely dilated sinusoidal spaces (arrow head) are prominently seen, (H&E, X 40).

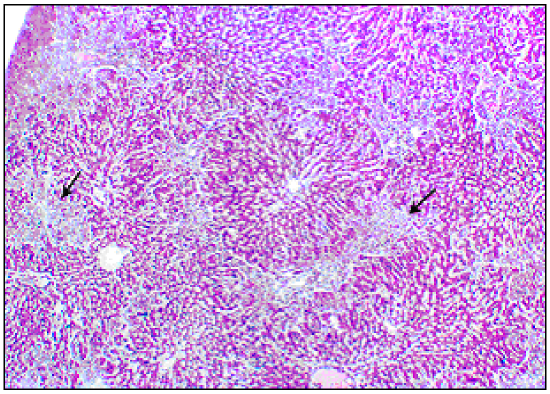

Fig. 4. Section of liver of BDL rat treated with 50µg TMCA/kg for 2 weeks showing well recognized hepatic lobular architecture in most areas. Mild fibrotic portal areas with bile ductular proliferation are seen (arrow), (H&E, X 40).

Examination of BDL rats treated with 150µg TMCA/kg/day for 2 weeks revealed moderate improvement in the hepatic lobular architecture in 84% of animals. In the remaining 16% of cases, hepatocellular lobulation was much well formed, with localized portal areas and more or less normal appearing nuclei .When BDL rats were treated with 150µg TMCA/kg/day for 4 weeks, well formed hepatocellular lobulation with slightly dilated sinusoids was seen in all examined cases. The hepatic lobules were separated with only thin bands of fibrous tissue, infiltrated with moderately dense inflammatory cells. Few bile ductules were occasionally seen in portal areas (Fig. 5) and most of the hepatocytes appeared with normal nuclei.

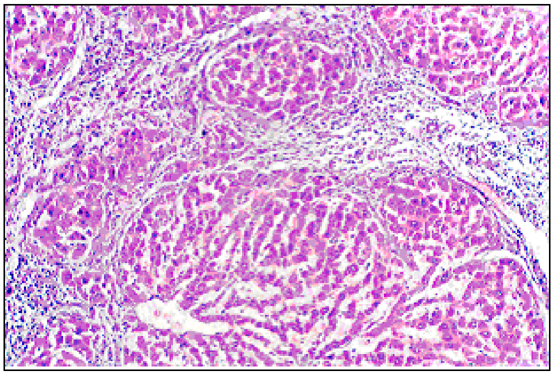

Fig. 5. Section of liver of BDL rat treated with 150µg TMCA/kg for 4 weeks showing well formed hepatic lobules separated by thin fibrous bands invaded with moderately dense inflammatory cells, (H&E, X 100).

Image analysis data of liver sections stained with Mallory trichrome technique showed that area of fibrosis decreased significantly ($P<0.05$) in BLD animals treated with 150µg TMCA/kg/day (Fig. 6).

Immunohistochemical observations

The activated stellate cells in liver sections were determined by immune-staining of α-SMA, a definitive marker of activated HSC (myofibroblasts). In liver sections of sham operated rats, α-SMA was normally expressed only in the intermediary layer of portal tract vessels and in some cells around the terminal liver venules. α-SMA positive cells increased markedly and stained as clusters lay within or in the vicinity of accumulated fibers in BDL animals for 6 weeks (Fig.7).

In BDL rats treated with 50µg colchicine/kg for 4 weeks, α-SMA positive cells were decreased as compared with BDL group (Fig. 8). On the other hand, liver sections of BDL rats treated with 50µg TMCA/kg for 4 weeks occasionally showed tiny areas of mild to moderate brownish deposit. α-SMA positive cells were markedly reduced as compared to either BDL group or 50µg colchicine treated BDL group (Fig. 9). Finally, liver sections of BDL rats treated with 150µg TMCA/kg for 4 weeks showed wide expanding areas of hepatic tissue completely negative of α-SMA positive cells.

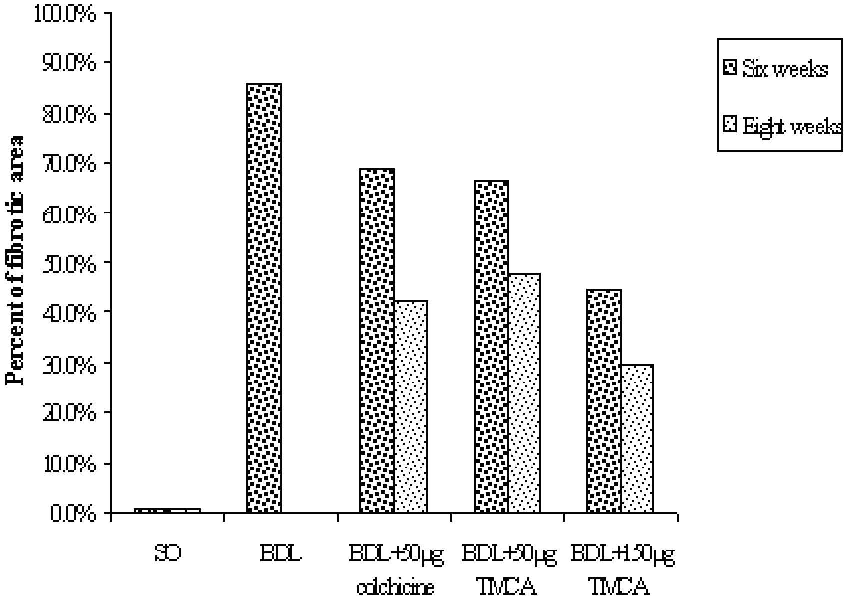

Fig. 6. Histogram showing percent of fibrotic tissue area per examined liver sections in different experimental groups at different time intervals.

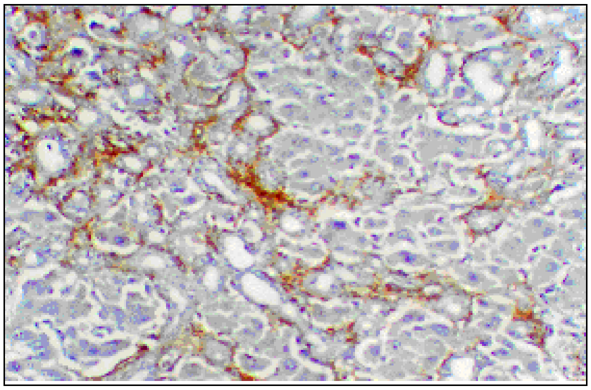

Fig. 7. Liver section of BDL rat for 6 weeks. Clusters of α-SMA positive cells lie within accumulated fibers, and encircling the proliferated bile ductules, (X 200).

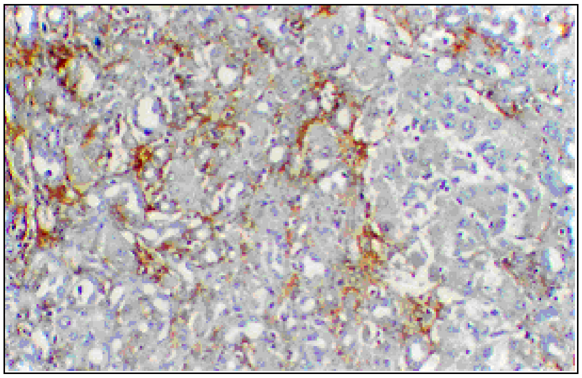

Fig. 8. Liver section of BDL rat treated with 50µg colchicine/kg for 4 weeks showing moderate α-SMA positive cells, (X 200).

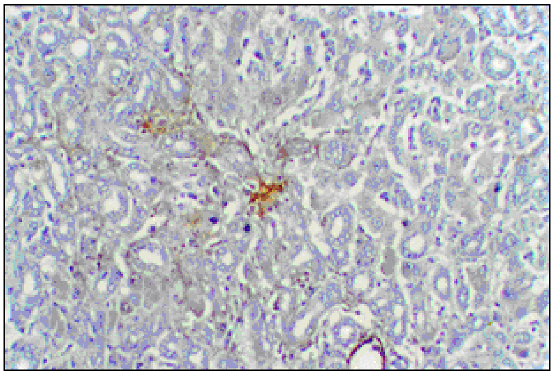

Fig. 9. Liver section of BDL rat treated with 50µg TMCA/kg for 4 weeks showing tiny brown deposit, (X 200).

Biochemical results

Data in figures 10 and 11 showed the change in activity of AST and ALT in different experimental groups. There was no significant changes in AST and ALT activities between sham operated none treated rats and those received 50µg colchicine or 150µg TMCA/kg. Bile duct ligated animals for either 4 or 6 weeks showed significant increase in serum AST and ALT activities when compared with sham operated group at the same duration. Colchicine or TMCA-treated BDL rats significantly decreased the elevated serum AST and ALT activities when compared with BDL rats. Before the end of 8 weeks of BDL, all of the BDL rats failed to survive, while BDL groups treated with colchicine or TMCA succeeded to survive till the end of the experiment. They not only

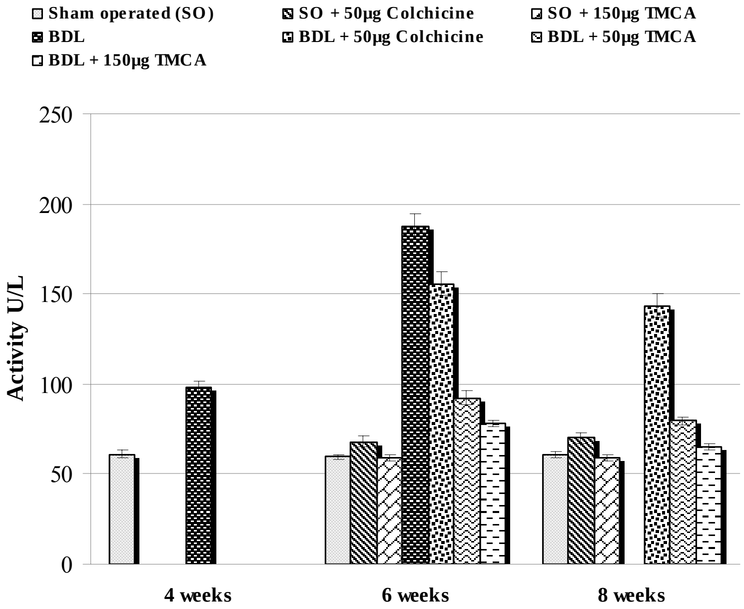

Fig. 10. Serum AST activity in different experimental groups.

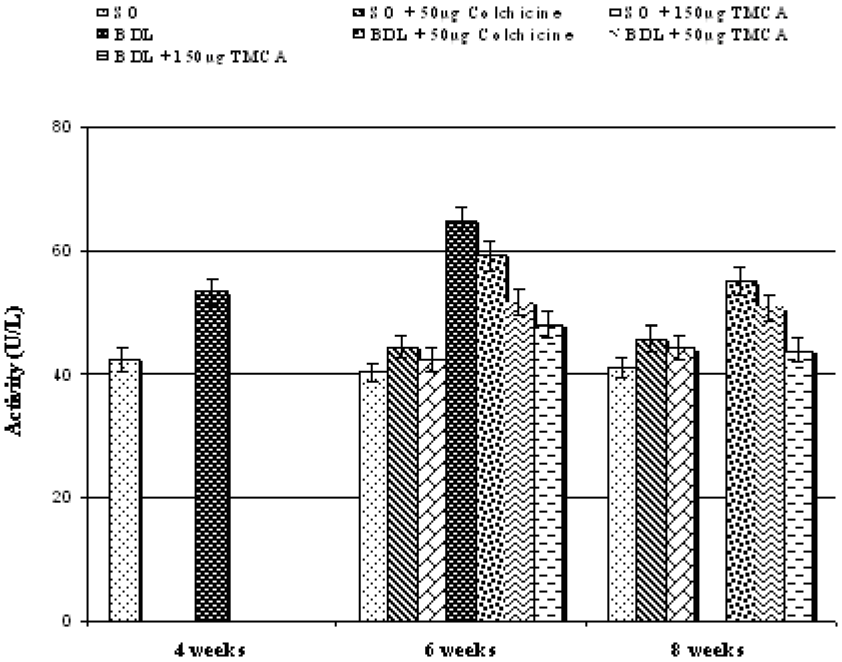

Fig. 11. Serum ALT activity in different experimental groups.

succeeded to survive but also showed marked reduction in transaminases activities.

Concerning the change in alkaline phosphatase activity, bile duct ligation for 4 or 6 weeks significantly increased serum ALP activity when compared with sham operated group at the same durations. Treatment of BDL animals with 50µg colchicine or 50µg TMCA/kg failed to reduce elevated serum ALP activity when compared with BDL rats. On the other hand, treatment of BDL rats with 150µg TMCA/kg significantly reduced elevated ALP activity when compared with BDL animals for 4 and 6 weeks respectively (Fig. 12).

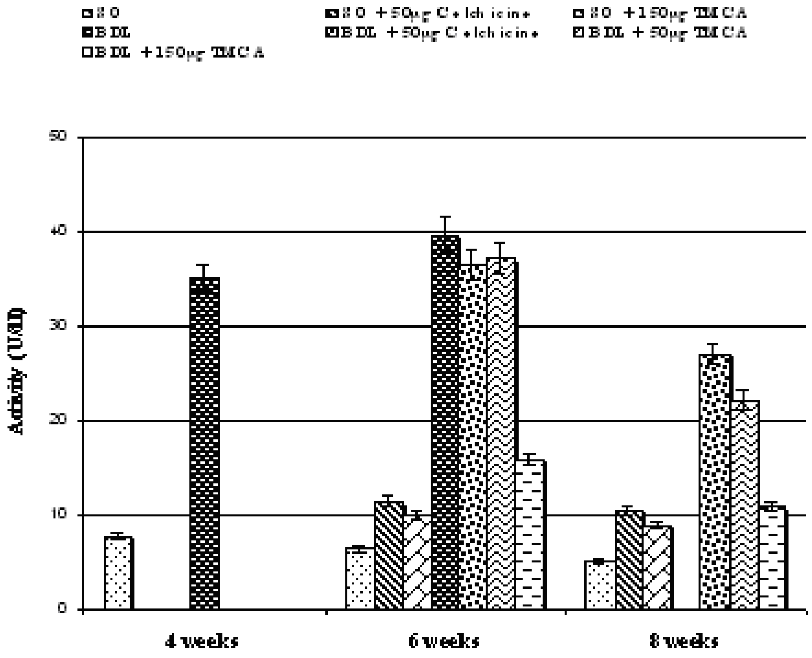

Fig. 12. Change in serum ALP activity in different experimental groups.

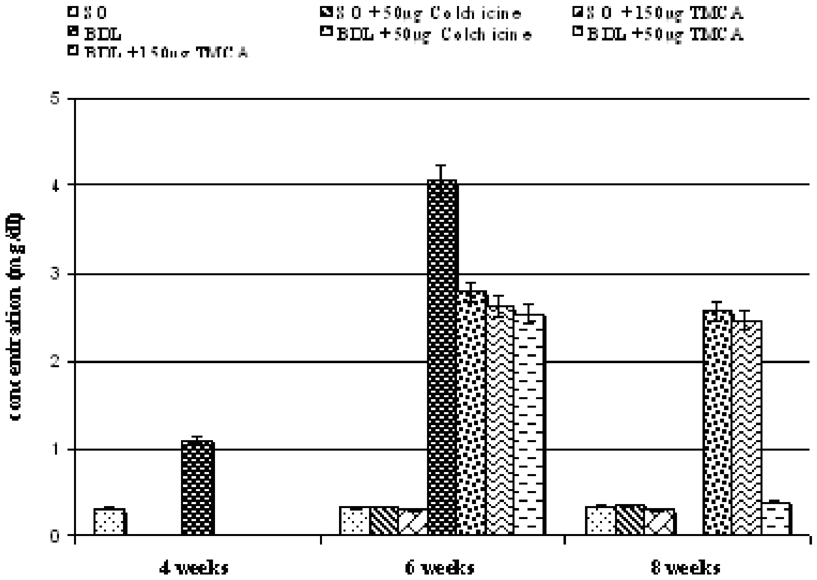

Fig. 13. Serum total Bilirubin concentration in different experimental groups.

Data in figure 13 showed that there was no significant difference in serum total bilirubin concentration between sham operated (non-treated) group and sham operated groups treated with either 50µg colchicine or 150µg TMCA/kg at the same period. Biliary obstruction increased serum total bilirubin concentration over sham operated group in the different periods. Treatment of BDL rats with 50µg colchicine or 50µg TMCA showed significant decrease in the elevated bilirubin concentration and 150µg TMCA was more efficient than 50µg colchicine and 50µg TMCA in reducing elevated total bilirubin concentration.

DISCUSSION

The animal model of common bile duct ligation has attracted considerable attention, because it simulates many histopathological features of human chronic biliary fibrosis and cirrhosis (Guyot *et al.*, 2006). Results obtained in the present work revealed that biliary obstruction in rats induced liver cirrhosis. Kountouras *et al.* (1984) reported that biliary obstruction for 4 weeks, developed cirrhosis in the majority of the animals. Histopathological changes displayed by livers of BDL rats in the present work included distortion of the hepatic lobular architecture, marked dilatation and proliferation of bile ductules with accentuated collagen deposits, degeneration, frequent areas of necrosis, enlarged Kupffer cells and dilated blood vessels. Extracellular matrix deposition increased with time and after 6 weeks of BDL fibrous tissue area expanded to occupy 85.7% of the examined liver sections. Most of these histopathological features were also previously detected by Muriel and Deheza (2003) and Prado *et al.* (2003).

Crawford (1999) reported that extrahepatic biliary obstruction results in cholestasis. The morphological features of cholestasis in human frequently include bile pigment accumulation within the hepatic parenchyma that can take on a wispy appearance (feathery or foamy degeneration) and in dilated bile canaliculi. Rupture of canaliculi, leads to bile extravasation which is phagocytosed by Kupffer cells. The author added that obstruction of the biliary tree induces distention of upstream bile ducts. The bile stasis and back pressure induce proliferation and reduplication of ducts. The labyrinthine ducts further slow the bile flow and favor the formation of concrements, which obstruct the ductal lumens.

Unrelieved obstruction leads to portal tract fibrosis which extends into and subdivides the parenchyma and develop to cirrhosis (biliary cirrhosis). In this respect, Prado *et al.* (2003) observed enlarged Kupffer cells filled with bile in long-term cholestatic rats.

In the present work, mild to moderate inflammation was seen which was also noticed by Abdel-Aziz *et al.* (1990) and Soylu *et al*. (2006). The authors observed extensive bile duct proliferation and formation of periportal fibrosis, with only slight inflammation and necrosis in their experimental model of extrahepatic cholestasis in rats.

Treatment of BDL rats with 50µg colchicine/kg for 2 weeks showed reappearance of only few scattered hepatic lobules in 50% of the cases. In bile duct ligated rats treated daily with the same dose of colchicine for 4 weeks, progress in retaining well organized hepatic lobular architecture was clearly seen. The fibrous tissue area decreased to form around 42% of the examined liver sections and appeared invaded with inflammatory cells. Similar results were obtained by Poo *et al*. (1993) who reported that early treatment of BDL rats with colchicine (50µg/kg/day, p.o.) for 4 weeks significantly increased hepatocyte and sinusoidal volume fractions than in BDL rats that received placebo. In addition, bile duct volume fractions, connective tissue fractions and portal pressure were significantly lowered than those in BDL rats received placebo. Jiang *et al.* (1996) observed that when mice infected with *Shistosoma japonicum* were treated with colchicine (0.25µg/g body weight), thick layer of inflammatory cells was found in granuloma in the liver. They suggested that colchicine can stimulate monocytes which phagocytized collagen and leads to disruption and inhibition of collagen accumulation. Colchicine is an agent that disrupts microtubules formation and inhibits collagen transport and synthesis (Rojkind and Kershenobich, 1975; Dumont *et al.*, 1994). Moreover, Warnes (1991) added that in experimental animals and *in vitro,* colchicine inhibited collagen synthesis and also increased collagen degradation by activating collagenase.

Treating BDL rats with 50µg TMCA/kg, daily for 2 weeks showed reappearance of hepatic lobules in 50% of cases. Fibrous tissue area slightly decreased to form 66% of the examined liver sections, but it was not significantly reduced as compared with colchicine treatment (68%) at the same duration. By treating BDL rats with 50µg TMCA for further 2 weeks, more improvement in liver architecture was noticed. Fibrous tissue area decreased but it is still greater than that in 50µg colchicine treated group at the same time. Colchicine and TMCA were nearly similar in their effect at the same dose level and under similar condition.

When TMCA was administered at a dose level of 150µg/kg/day for 4 weeks to sham operated rats, no side effects was noticed on the contrary with colchicine treatment (50µg/kg) under the same conditions. This indicated that higher dose of TMCA (150µg/kg) is more safe than colchicine (50µg/kg). When BDL rats treated with 150µg TMCA/kg, for 2 weeks, well formed hepatocellular lobulation and mild bile ductular proliferation was noticed in 84% of examined cases. On the other hand, after 4 weeks of treating BDL rats with 150µg TMCA/kg, all examined cases showed improvement in hepatic lobular architecture. The hepatic lobules separated with only a thin fibrous tissue bands densely infiltrated with inflammatory cells. Few bile ductules were occasionally seen and fibrous tissue area reduced more to occupy only 29.7% of the examined liver section. These results indicated that administration of TMCA at higher doses is more efficient than colchicine in treating liver cirrhosis.

Immunohistochemical data denoted that an intermediate filament protein, α-smooth muscle actin, is expressed by activated HSCs. This marker was used to identify activated HSCs. After BDL for 6 weeks, α-SMA positive cells dramatically increased in number and diffused throughout the liver tissue. They formed layers around proliferated bile ductules. This was in agreement with Kinnman *et al.* (2000) who reported that the main cell population involved in extracellular matrix deposition following ligation of the common bile duct is activated hepatic stellate cells, reaching the periductular region by chemotaxis and migration. In the same respect, Gibelli *et al.* (2008) added that the expression of α-SMA by the stellate cells began to appear on the 5th day post BDL, and the expression increased, reaching maximum level on the 28th day.

Bile duct segments isolated from cholestatic rats exert a potent chemotactic action on HSCs (Kinnman *et al.*, 2000). Cholangiocytes are known to express platelet derived growth factor in BDL model (Grappone *et al.*, 1999). Platelet derived growth factor expression may explain local accumulation of matrix-producing cells in proximity to newly formed bile ducts, as a result of chemotaxis and proliferation (Pinzani *et al.*, 1989; Kinnman *et al.,* 2001).

Colchicine treated BDL rats for 4 weeks showed decrease in α-SMA positive cells as compared with BDL group. This was in agreement with Lee *et al.* (2004) who found that treatment of cirrhotic rats with colchicine significantly decreased the number of α-SMA positive cells. They also added that colchicine at the concentration of 30-100 nM *in vitro,* notably inhibited the induction of α-SMA protein and transforming growth factor β1, indicating that colchicine directly inhibited activated stellate cells. Treating BDL rats with 50µg TMCA/kg, for 4 weeks markedly reduced the number of α-SMA positive cells. They appeared as tiny areas of mild brownish deposits. This reduction was more than the reduction observed with colchicine treatment at the same duration. BDL rats treated with 150µg TMCA/kg showed completely negative wide expanding areas of hepatic tissue. Mild linear brownish deposits were infrequently seen encircling hepatic nodules close to the hepatic capsule. These results may be explained by inactivation of hepatic stellate cells with TMCA. Iredale *et al.* (1998) added that they could not exclude the possibility of some HSCs to undergo reversion from an activated to a quiescent phenotype. However, their data suggested that the majority of loss of α-SMA positive cells is mediated via apoptosis.

Biochemical results showed significant elevation in serum alanine aminotransferase, aspartate aminotransferase, alkaline phosphatase activities and total bilirubin concentration in BDL animals for 4 and 6 weeks when compared with the values in sham operated group at the same durations. These elevations reflect the severity of hepatic injury and cholestasis that observed in the histopathological examination in the present study.

Total bilirubin was highly increased after 4 and 6 weeks of BDL rats because obstruction of the common bile duct impaired bile flow into the intestine producing cholestasis in the liver and regurgitation into the blood stream. Crawford (1999) reported that elevated serum alkaline phosphatase is one of the characteristic findings in cholestasis, as this enzyme present in bile duct epithelium and in the canalicular membrane of the hepatocytes. Several studies recorded marked increase in serum aspartate aminotransferase, alanine aminotransferase, alkaline phosphatase activities and bilirubin concentration in rats following BDL for 4 weeks (Marra *et al.*, 2005; Fernandez-Martinez *et al.*, 2006; Soylu *et al.*, 2006; Reyes-Gordillo *et al.,* 2008).

The biochemical findings indicated that TMCA is better than colchicine in reducing elevated serum enzymes activities and bilirubin concentration, when used at the same dose for the same duration. Moreover, Cedillo *et al.* (1996) found that both colchicine and TMCA administered orally at a dose level of 10µg/rat/day were able to significantly reverse serum γ-GTP and alkaline phosphatase activities elevated by CCl_4- induced cirrhosis. Treating BDL animals with 150µg TMCA/kg showed marked reduction in the elevated AST, ALT, ALP activities and total bilirubin concentration when compared with BDL rats.

Thus, it is concluded from the results obtained in the present work that, trimethylcolchicinic acid at higher doses seems to be a better option than 50µg colchicine in the treatment of liver cirrhosis.

REFERENCES

Abdel-Aziz, G., Le, beau, G., Rescan, PY., Clément, B., Rissel, M., Deugnier, Y., Campion, JP. and Guillouzo, A. 1990. Reversibility of hepatic fibrosis in experimentally induced cholestasis in rat. Am. J. Pathol. 137(6):1333-1342.

Albanis, E. and Friedman, SL. 2001. Hepatic fibrosis. Pathogenesis and principles of therapy. Clin. Liver Dis. 5(2):315-334.

Anthony, PP., Ishak, KG., Nayak, NC., Poulsen, HE., Scheuer, PJ. and Sobin, LH. 1978. The morphology of cirrhosis. Recommendations on definition, nomenclature and classification by a working group sponsored by the World Health Organization. J. Clin. Pathol. 31:395-414.

Bataller, R. and Brenner, DA. 2005. Liver Fibrosis. J. Clin. Invest. 115(2):209-218.

Belfield, A. and Goldberg, DM. 1971. Revised assay for serum alkaline phosphatase activity using 4-amino-antipyrine. Enzyme. 12(5):561-573.

Cedillo, A., Mourelle, M. and Muriel, P. 1996. Effect of colchicine and trimethylcolchicinic acid on CCl_4-induced cirrhosis in the rat. Pharmacol. Toxicol. 79(5):241-246.

Crawford, JM. 1999. The liver and the biliary tract. In: Robins Pathologic Basis of Disease. Eds. Cotran RS., Kumar, V. and Collins T. (6th ed.). Saunders Company, USA.

Dumont, M., D'Hont, C., Lamri, Y., Durand-Schneider, AM., Jacquemin, E., Feldmann, G. and Erlinger, S. 1994. Effects of phalloidin and colchicine on diethylmaleate-induced choleresis and ultrastructural appearance of rat hepatocytes. Liver.14(6):308-313.

Fernández-Martínez, E., Pérez-Alvarez, V., Tsutsumi, V., Shibayama, M. and Muriel, P. 2006. Chronic bile duct obstruction induces changes in plasma and hepatic levels of cytokines and nitric oxide in the rat. Exp. Toxicol. Pathol. 58(1):49-58.

Friedman, SL. 2003. Liver fibrosis-from bench to bedside. J. Hepatol. 38(1):S38-S53.

Friedman, SL., Roll, FJ., Boyles, J. and Bissell, DM. 1985. Hepatic lipocytes: the principal collagen-producing cells of normal rat liver. Proc. Natl. Acad. Sci. USA. 82(24):8681-8685.

Froh, M., Conzelmann, L., Walbrun, P., Netter, S., Wiest, R., Wheeler, M.D., Lehnert, M., Uesugi, T., Scholmerich, J. and Thurman, RG. 2007. Heme oxygenase-1 overexpression increases liver injury after bile duct ligation in rats. World J. Gastroenterol. 13(25):3478-3486.

Gibelli, NE., Tannuri, U. and Mello, ES. 2008. Immunohistochemical studies of stellate cells in experimental cholestasis in newborn and adult rats. Clinics. 63(5):689-694.

Grappone, C., Pinzani, M., Parola, M., Pellegrini, G., Caligiuri, A., DeFranco, R., Marra, F., Herbst, H., Alpini, G. and Milani, S. 1999. Expression of platelet-derived growth factor in newly formed cholangiocytes during experimental biliary fibrosis in rats. J. Hepatol. 31(1):100-109.

Gressner, AM. and Weiskirchen, R. 2006. Modern pathogenetic concepts of liver fibrosis suggest stellate cells and TGF-β as major players and therapeutic targets. J. Cell Mol. Med. 10(1):76-99.

Guyot, C., Lepreux, S., Combe, C., Doudnikoff, E., Bioulac-Sage, P., Balabaud, C. and Desmoulière, A. 2006. Hepatic fibrosis and cirrhosis: the (myo) fibroblastic cell subpopulations involved. Int. J. Biochem. Cell Biol. 38(2):135-151.

Iredale, JP., Benyon, RC., Pickering, J., McCullen, M., Northrop, M., Pawley, S., Hovell, C. and Arthur, MJ. 1998. Mechanisms of spontaneous resolution of rat liver fibrosis. Hepatic stellate cell apoptosis and reduced hepatic expression of metalloproteinase inhibitors. J. Clin. Invest. 102(3):538-549.

Jendrassik, L. and Gróf, P. 1938. Vereinfachte photometrische methoden zur bestimmung des blutbilirubins. Biochem. Zeitschrift. 297:82-89.

Jiang, J., Zhong, C., Yu, Y. and Zhang, Q. 1996. Colchicine reduces hepatic fibrosis in mice infected with *Schistosoma japonicum*. Chin. Med. J. 109(10):795-800.

Kershenobich, D., Vargas, F., Garcia-Tsao, G., Perez Tamayo, R., Gent, M. and Rojkind, M. 1988. Colchicine in the treatment of cirrhosis of the liver. N. Engl. J. Med. 318(26):1709-1713.

Kinnman, N., Goria, O., Wendum, D., Gendron, MC., Rey, C., Poupon, R. and Housset, C. 2001. Hepatic stellate cell proliferation is an early platelet-derived growth factor-mediated cellular event in rat cholestatic liver injury. Lab. Invest. 81(12):1709-1716.

Kinnman, N., Hultcrantz, R., Barbu, V., Rey, C., Wendum, D., Poupon, R. and Housset, C. 2000. PDGF-mediated chemoattraction of hepatic stellate cells by bile duct segments in cholestatic liver injury. Lab. Invest. 80(5):697-707.

Kountouras, J., Billing, BH. and Scheuer, PJ. 1984. Prolonged bile duct obstruction: a new experimental model for cirrhosis in the rat. Br. J. Exp. Pathol. 65(3):305-311.

Lee, SJ., Kim, YG., Kang, KW., Kim, CW. and Kim, SG. 2004. Effects of colchicine on liver functions of cirrhotic rats: beneficial effects result from stellate cell inactivation and inhibition of TGF beta1 expression. Chem. Biol. Interact. 147(1): 9-21.

Marra, F., DeFranco, R., Robino, G., Novo, E., Efsen, E., Pastacaldi, S., Zamara, E., Vercelli, A., Lottini, B., Spirli, C., Strazzabosco, M., Pinzani, M. and Parola, M. 2005. Thiazolidinedione treatment inhibits bile duct proliferation and fibrosis in a rat model of chronic cholestasis. World J. Gastroenterol. 11(32):4931-4938.

Mourelle, M. and Meza, MA. 1989. Colchicine prevents D-galactosamine induced hepatitis. J. Hepatol. 8(2):165-172.

Mourelle, M., Villalon, C. and Amezcua, JL. 1988. Protective effect of colchicine on acute liver damage induced by carbon tetrachloride. J. Hepatol. 6(3):337-342.

Muriel, P. and Deheza, R. 2003. Fibrosis and glycogen stores depletion induced by prolonged biliary obstruction in the rat are ameliorated by metadoxine. Liver Int. 23(4):262-268.

Muntoni, S., Rojkind, M. and Muntoni, S. 2010. Colchicine reduces procollagen III and increases pseudocholinesterase in chronic liver disease. World J Gastroenterol.16(23):2889-2894.

Muriel, P., Quintanar, ME. and Perez-Alvarez, V. 1993. Effect of colchicine on acetaminophen-induced liver damage. Liver. 13(4):217-221.

Muriel, P., Moreno, MG., Hernandez, MC., Chavez, E. and Alcantar, LK. 2005. Resolution of liver fibrosis in chronic CCl_4 administration in the rat after discontinuation of treatment: effect of silymarin, silibinin, colchicine and trimethylcolchicinic acid. Basic. Clin. Pharmacol. Toxicol. 96(5):375-380.

Pinzani, M., Gesualdo, L., Sabbah, GM. and Abboud, HE. 1989. Effects of platelet-derived growth factor and other polypeptide mitogens on DNA synthesis and growth of cultured rat liver fat-storing cells. J. Clin. Invest. 84(6):1786-1793.

Poo, JL., Feldmann, G., Moreau, A., Gaudin, C. and Lebrec, D. 1993. Early colchicine administration reduces hepatic fibrosis and portal hypertension in rats with bile duct ligation. J. Hepatol. 19(1):90-94.

Popper, H. and Uenfriend, S. 1970. Hepatic fibrosis. Correlation of biochemical and morphologic investigations. Am. J. Med. 49:707-721.

Prado, IB., dos Santos, MH., Lopasso, FP., Iriya, K. and Laudanna, AA. 2003. Cholestasis in a murine experimental model: lesions include hepatocyte ischemic necrosis. Rev. Hosp. Clin. Fac. Med. Sao Paulo. 58(1):27-32.

Ramadori, G. and Saile, B. 2004. Portal tract fibrogenesis in the liver. Lab. Invest. 84(2): 153-159.

Reitman, S. and Frankel, S. 1957. A colorimetric method for the determination of serum glutamic oxalacetic and glutamic pyruvic transaminases. Am. J. Clin. Pathol. 28(1): 56-63.

Reyes-Gordillo, K., Segovia, J., Shibayama, M., Tsutsumi, V., Vergara, P., Moreno, MG. and Muriel, P. 2008. Curcumin prevents and reverses cirrhosis induced by bile duct obstruction or CCl_4 in rats: role of TGF-beta modulation and oxidative stress. Fundam. Clin. Pharmacol. 22(4):417-427.

Robbers, JE., Speedie, MK. and Tyler, VE. 1996. Pharmacognosy and Pharmacobiotechnology. Ch. 9. Williams and Wilkin, USA.

Rojkind, M. and Kershenobich, D. 1975. Effect of colchicine on collagen, albumin and transferrin synthesis by cirrhotic rat liver slices. Biochim. Biophys. Acta. 378(3): 415-423.

Schaffner, F. and Klion, FM. 1968. Chronic hepatitis. Annu. Rev. Med. 19:25-38.

Schermer, S. 1967. The Blood Morphology of Laboratory Animals. (3rd ed.). FA. Davis Company, Philadelphia, USA. pp. 42.

Soylu, AR., Aydogdu, N., Basaran, UN., Altaner, S., Tarcin, O., Gedik, N., Umit, H., Tezel, A., Dokmeci, G., Baloglu, H., Ture, M., Kutlu, K. and Kaymak, K. 2006. Antioxidants vitamin E and C attenuate hepatic fibrosis in biliary-obstructed rats. World J. Gastroenterol. 12(42):6835-6841.

Sweetman, SC. 2007. Martindale. The Complete Drug Reference. (35th ed.). Pharmaceutical Press, London. pp. 415-416.

van de Bovenkamp, M. 2006. Liver fibrosis *in vitro*: Liver slices as a promising alternative. Ph.D. Thesis, Department of Pharmacokinetics and Drug Delivery, University Center for Pharmacy, Groningen, Netherlands.

Warnes, TW. 1991. Colchicine in primary biliary cirrhosis. Aliment. Pharmacol. Ther. 5(4):321-329.

Weesner, FM. 1968. General Zoological Microtechniques. Williams and Wilkins. USA. pp. 185-186.

Zweig, MH. and Chignell, CF. 1973. Interaction of some colchicine analogs, vinblastine and podophyllotoxin with rat brain microtubule protein. Biochem. Pharmacol. 22(17):2141-2150.

Received: May 12, 2010; Accepted: Sept 6, 2010

SENRA Academic Publishers, Burnaby, British Columbia
Vol. 4, No. 3, pp. 1243-1248, October 2010
Online ISSN: 1920-3853; Print ISSN: 1715-9997

Canadian Journal of pure&applied sciences

INFLUENCE OF RED LIGHT ON SEED LIPASE DEPENDS ON THE LIPID CONTENT OF THE SEED

*Gincy P Thottathil[1], Elizabeth Samuel[2] and M Haridas[3]
[1]School of Biosciences, Mahatma Gandhi University, Kottayam, Kerala
[2]School of Biosciences, Mahatma Gandhi University, Kottayam, Kerala- 686560
[3]Department of Biotechnology and Microbiology, School of Lifesciences, Kannur University
Thalassery, Kannur, India- 670661

ABSTRACT

Influence of blue, green, yellow, orange, red and white lights on lipase activity of *Oryza sativa* L. (Jyothi), *Vigna unguiculata* (L.) Walp. (Kanakamani) and *Arachis hypogaea* L. (CO-3) seedlings was analysed and it showed plant-wise variations. Considering the initial 7 days of development of the seedlings, green light for *O. sativa,* yellow light for *V. unguiculata* and red light for *A. hypogaea* were more influential in inducing lipase activity. In *A. hypogaea*, lipase activity was significantly higher under red light than other wavelengths from 2nd to 5th day which is the active period of seedling establishment. In *Oryza sativa* red light induced significant variation only on certain days. In *Vigna unguiculata* red light seemed to be least effective in stimulating lipase activity except on the first day. Thus effect of red light on lipase activity is species dependent and arguably, it depends on the lipid content of the seed. Blue wavelength exposure depressed the lipase activity in all the three seedlings studied.

Keywords: Llipase, light, red light, germination.

INTRODUCTION

The regulatory processes occurring during the degradation of reserve food materials of seeds have received greatly increasing attention. Knowledge of the regulation of metabolism by environmental factors enable us to modify plant metabolism for our advantage. Light is a very important environmental stimulus for plants, which controls the growth and development. Plants respond to a broad spectrum of light, ranging from UV-B to far-red light. A large body of physiological, photo-biological and molecular genetic studies have demonstrated that plants possess distinct photoreceptors sensing UV-B, UV-A, blue, green, red and far-red lights (Fankhauser and Chory, 1997). The photo-responses observed on the morphological, structural and metabolic levels, have an equivalent counterpart on the level of enzyme activities. Photomorphogenic responses are more or less direct result of specific control of enzymes. There are many enzymes, which were reported to be controlled by light (Schopfer, 1977; Vassey, 1988; Dreier *et al*., 1995). Light controls enzymes either by regulating the genes synthesizing it (Tobin and Silverthorne, 1985; Thompson and White, 1991) or by post-translational modifications (Buchanan, 1980).

In recent years great interest has arisen in the regulatory effect of light on different enzymatic activities (Darbelley *et al*., 1997; Datta *et al.,* 1999; Barnaby *et al*., 2004). But comparatively fewer studies were done on the effect of light on lipases. Lipases are enzymes that hydrolyze triglycerides. Many seeds contain triglycerides as major food reserve for germination. Red and white light treatments were found to have promotive effect on lipase activity in *Glycine max* while far-red light and dark treatments were inhibitory (Mehta *et al*., 1975). Similar result was obtained for seeds of *Cucumis sativus* and far-red light was found to reverse the effects of red light, indicating the involvement of phytochrome in the control of lipase activity. It was also suggested that the influence of light on lipid degradation is species dependent (Davies *et al*., 1981). Promotive effects of red and white light were obtained for germinating spores of the fern, *Anemia phyllitidis* (Gemmrich, 1982). Light- regulation of lipase activity was reported in seedlings of sunflower also (Pfeiffer and Kutschera, 1997). Pulsed concentrated solar radiation (Zodape and Chauhan, 1994) and UV-B radiations (Lo *et al*., 2004) were also found to enhance lipase activity.

The classical studies on the effect of light on plants revealed the importance of red, far red and blue lights in photomorphogenic responses. So most of the studies were concentrated on these spectral regions and other regions were considered to be ineffective for a long time. Very few studies were done on the effect of other wave lengths, especially in the metabolic level. But in recent years attention was given to other regions of the spectrum and

---

*Corresponding author email: gincythottathil@yahoo.com

recent evidences show that green light also has discrete effects on plant biology, and the mechanisms that sense this light quality are now being elucidated (Folta and Maruhnich, 2007). Many of the responses induced from the green portion of the spectrum are counterintuitive, often opposing normal light effects (Ahmad *et al*., 1998; Frechilla *et al*., 2000; Talbott *et al*., 2002; Eisinger *et al*., 2003; Folta, 2004; Dhingra *et al*., 2006; Bouly *et al*., 2007). Lipids are the major storage material of many seeds and so regulation of lipid metabolism during the germination and seedling establishment needs special attention. A very recent study suggests that green, red, and red/far-red light interact with blue light and contribute to the regulation of phosphorlipase A_2 α and β gene expression in *Citrus sinensis* (Liao and Burns, 2010). The present study tries to find out the role of different spectral regions in the regulation of the lipid hydrolyzing enzyme, lipase during seed germination and seedling establishment in three different plants- *Oryza sativa* L. (Jyothi), *Vigna unguiculata* (L.) Walp. (Kanakamani) and *Arachis hypogaea* L. (CO-3).

MATERIALS AND METHODS

Plant material and growth conditions

Three types of seeds which differ in their reserve food materials were selected for study: *Oryza sativa* L. (Jyothi), *Vigna unguiculata* (L.) Walp. (Kanakamani) and *Arachis hypogaea* L. (CO-3).

The above seeds were imbibed in distilled water for 12h under darkness. They were allowed to germinate and grow in controlled chambers with 12h light/ 12h dark photoperiod at 30± 2°C. Each chamber was provided with monochromatic light from arrays of 80-90 light emitting diodes having different wavelengths; Blue (peak wavelength 470 nm), Green (peak wavelength 520 nm), Yellow (peak wavelength 590 nm), Orange (peak wavelength 610nm) and Red (peak wavelength 660nm) with intensity, 1μmol $m^{-2}s^{-1}$. Controls were grown in a similar chamber, which was exposed to light from fluorescent tubes. The intensity of light was made similar to monochromatic light by paper filters.

After imbibition, seeds were given an initial 12h of light period followed by 12h of dark period. This cycle was continued for seven days and samples were collected immediately after the dark period. Seedlings were watered every day and sample populations were taken at 24h intervals for the initial seven days. Samples were collected immediately after the imbibition to determine the enzyme activity on zeroth day.

Preparation of enzyme extracts

A known quantity of sample was homogenized with twice the volume of ice-cold acetone. The crude homogenate was filtered through Whatman No. 1 filter paper. The powdered filtrate was washed successively with acetone, acetone: ether (1:1, v/v) and ether. The powder was air-dried and 1g of the powder was extracted in 20 ml of ice-cold phosphate buffer (50mM; pH 7.0). It was centrifuged at 15,000rpm for 10min at 4°C and the supernatant was used as enzyme source.

Enzyme assay

Lipase activity was determined by estimating the liberated fatty acid (Jayaraman, 1981). Substrate for the assay was prepared by adding 2ml of olive oil to 25ml of water. It was emulsified by adding 100mg of sodium taurocholate and 2g of gum accasia.

For assay, 20ml of the substrate was taken in a beaker and 5ml of phosphate buffer was added. It was stirred slowly, maintaining the temperature at 35°C. The pH was adjusted to 7.0. and 0.5ml of the enzyme extract was added and the pH was recorded immediately. At frequent intervals the pH was noted and 0.1 N NaOH was added to bring the pH to the initial value. From the volume of consumed NaOH, the released quantity of acid was calculated at discrete time intervals. One unit of enzyme activity was defined as the amount of enzyme, which releases one milli equivalent of free fatty acid per minute per gram sample. The data were statistically compared by one-way ANOVA for each day.

RESULTS

In order to determine the effect of different wavelengths on lipase, enzyme activity was determined for the first seven consecutive days. In all the three types of seeds tested, maximum lipase activity was seemed to be on the first day and gradually decreased thereafter with slight variations. The effect of different wavelengths on lipase activity showed variations in different plants and on different days.

Lipase activity in Oryza sativa seedlings grown under different wavelengths

Significant difference in enzyme activity between seedlings grown under different wavelengths was observed on first and second days and the greatest enzyme activity was observed in seedlings grown under green light (Table 1). However, on the following days, seedlings under other wavelengths showed greater enzyme activity (Table 1). But the differences between most of the wavelengths were found to be insignificant (Table 1). Seedlings under blue light showed the least enzyme activity on most of the days (Table 1). Considering the mean enzyme activity for seven days, seedlings under green light showed the greatest enzyme activity and seedlings under red, orange and yellow were close to control (Fig.1).

Table 1. Lipase activity (meq/min/g sample) in *Oryza sativa* seedlings grown under different-wavelength-lights.

Days	Different wavelengths					
	Blue	Green	Yellow	Orange	Red	Control (White)
0	0.0323±0.0003	0.0323±0.0003	0.0323±0.0003	0.0323±0.0003	0.0323±0.0003	0.0323±0.0003
1	0.0618±0.0008	0.1215±0.0015*♣♦♥♠	0.0685±0.0005*	0.0994±0.0012*♣♠	0.0980±0.0010*♣♠	0.0718±0.0008*♣
2	0.0404±0.0004	0.0742±0.0014*♣♦♥♠	0.0626±0.0006*♥♠	0.0587±0.0027*♥	0.0546±0.0016*	0.0574±0.0010*
3	0.0455±0.0050	0.0548±0.0018*♦♠	0.0513±0.0009♦♠	0.0441±0.0011	0.0551±0.0021*♦♠	0.0441±0.0014
4	0.0305±0.0030•	0.0232±0.0012	0.0346±0.0016•	0.0317±0.0017•	0.0277±0.0027	0.0372±0.0012•♥
5	0.0382±0.0014♣♦	0.0367±0.0017♦	0.0334±0.0014♦	0.0259±0.0009	0.0350±0.0010♦	0.0351±0.0011♦
6	0.0264±0.0014	0.0262±0.0008	0.0331±0.0009*•	0.0300±0.0018	0.0404±0.0049*•♣♦	0.0462±0.0013*•♣♦
7	0.0280±0.0008	0.0316±0.0006	0.0235±0.0010	0.0228±0.0008	0.0276±0.0016	0.0292±0.0007

*enzyme activity significantly greater than that of seedlings under blue light. • enzyme activitysignificantly greater than that of seedlings under green light. ♣ enzyme activity significantly greater than that of seedlings under yellow light. ♦ enzyme activity significantly greater than that of seedlings under orange light. ♥ enzyme activity significantly greater than that of seedlings under red light. ♠ enzyme activity significantly greater than that of control. meq - milli equivalents.

Table 2. Lipase activity (meq/min/g sample) in *Vigna unguiculata* seedlings grown under different-wavelength-lights.

Days	Different wavelengths					
	Blue	Green	Yellow	Orange	Red	Control (White)
0	0.0173±0.0003	0.0173±0.0003	0.0173±0.0003	0.0173±0.0003	0.0173±0.0003	0.0173±0.0003
1	0.0208±0.0008	0.0272±0.0007*	0.0294±0.0010*	0.0321±0.0011*•♣♠	0.0405±0.0010*•♣♦♠	0.0279±0.0009*
2	0.0217±0.0007•♦♥	0.0162±0.0010♥	0.0241±0.0009*•♣♦♥	0.0150±0.0010♥	0.0101±0.0006	0.0253±0.0007*•♦♥
3	0.0199±0.0009•♦♥	0.0163±0.0007♦♥	0.0180±0.0005♦♥	0.0113±0.0009♥	0.0072±0.0010	0.0250±0.0005*•♣♦♥
4	0.0100±0.0015	0.0200±0.0008*♥♠	0.0181±0.0011*♥♠	0.0190±0.0006*♥♠	0.0107±0.0007	0.0123±0.0013
5	0.0104±0.0045	0.0085±0.0009	0.0125±0.0010	0.0098±0.0008	0.0085±0.0007	0.0094±0.0010
6	0.0124±0.0009•♥	0.0071±0.0010	0.0172±0.0007*•♦♥	0.0134±0.0009•♥	0.0065±0.0005	0.0167±0.0010*•♦♥
7	0.0173±0.0008♦♥	0.0155±0.0013♦♥	0.0234±0.0012*•♦♥♠	0.0117±0.0007♥	0.0082±0.0007	0.0175±0.0009♦♥

*enzyme activity significantly greater than that of seedlings under blue light. • enzyme activity significantly greater than that of seedlings under green light. ♣ enzyme activity significantly greater than that of seedlings under yellow light. ♦ enzyme activity significantly greater than that of seedlings under orange light. ♥ enzyme activity significantly greater than that of seedlings under red light. ♠ enzyme activity significantly greater than that of control. meq - milli equivalents.

Table 3. Lipase activity (meq/min/g sample) in *Arachis hypogaea* seedlings grown under different-wavelength-lights.

Days	Different wavelengths					
	Blue	Green	Yellow	Orange	Red	Control (White)
0	0.0103±0.0008	0.0103±0.0008	0.0103±0.0008	0.0103±0.0008	0.0103±0.0008	0.0103±0.0008
1	0.0315±0.0005	0.0315±0.0007	0.0416±0.0006*•♦♥♠	0.0342±0.0007*•	0.0333±0.0013	0.0354±0.0010*•
2	0.0181±0.0011	0.0275±0.0010*	0.0202±0.0016	0.0226±0.0063*	0.0302±0.0012*♣♠	0.0214±0.0014
3	0.0148±0.0008	0.0179±0.0009*♠	0.0187±0.0007*♠	0.0170±0.0010♠	0.0205±0.0005*•♦♠	0.0129±0.0009
4	0.0135±0.0010	0.0155±0.0007♣	0.0112±0.0012	0.0238±0.0008*•♣♠	0.0296±0.0006*•♣♦♠	0.0163±0.0013*♣
5	0.0106±0.0006	0.0104±0.0004	0.0146±0.0009*•	0.0256±0.0004*•♣♠	0.0239±0.0009*•♣♠	0.0130±0.0010*•
6	0.0212±0.0012♣♦	0.0254±0.0009*♣♦♥♠	0.0186±0.0006♦	0.0110±0.0010	0.0212±0.0007♣♦	0.0219±0.0008♣♦
7	0.0219±0.0009♣♦♥♠	0.0194±0.0014♣♦♥♠	0.0115±0.0010	0.0143±0.0008♣♥♠	0.0107±0.0007	0.0105±0.0005

*enzyme activity significantly greater than that of seedlings under blue light. • enzyme activity significantly greater than that of seedlings under green light. ♣ enzyme activity significantly greater than that of seedlings under yellow light. ♦ enzyme activity significantly greater than that of seedlings under orange light. ♥ enzyme activity significantly greater than that of seedlings under red light. ♠ enzyme activity significantly greater than that of control. meq - milli equivalents.

Lipase activity in Vigna unguiculata seedlings grown under different wavelengths

On the 1st day, the greatest lipase activity was observed in *V. unguiculata* seedlings subjected to red light treatment. But later it showed less enzyme activity than seedlings grown under other wavelengths (Table 2). Greatest level of enzyme activity was observed for seedlings grown under white light on 2nd and 3rd days, under green light on 4th day and yellow light on 5th, 6th and 7th days (Table 2). The differences in enzyme activity between seedlings under most of the wavelengths were significant up to the 4th day. But on 5th day the differences in enzyme activity on exposure to various wavelengths were insignificant. On 6th and 7th days the enzyme activity increased slightly and the difference between some of them were significant (Table 2). Considering the mean enzyme activity for seven days, seedlings under yellow light showed the greatest enzyme activity than others, but close to control. Seedlings under red light showed the least enzyme activity (Fig. 2).

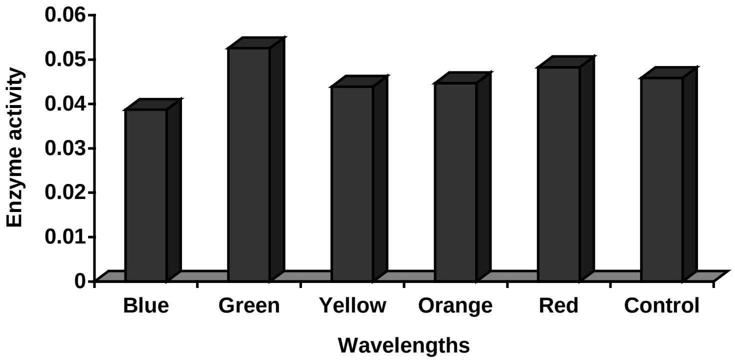

Fig. 1. Mean lipase activity for seven days of *Oryza sativa* seedlings grown under different-wavelength-lights.

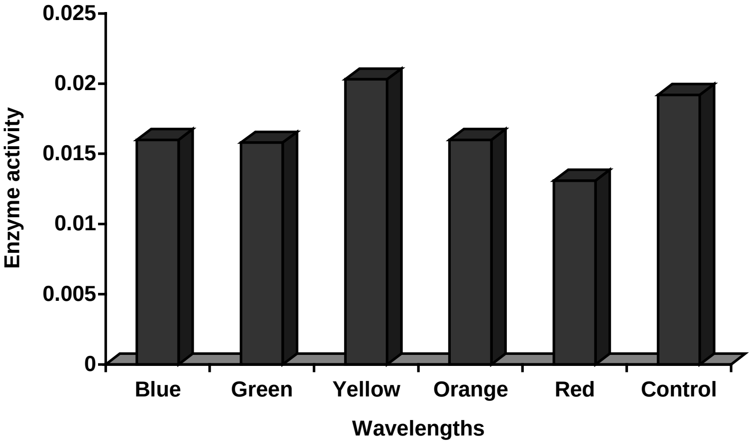

Fig. 2. Mean lipase activity for seven days of *Vigna unguiculata* seedlings grown under different-wavelength-lights.

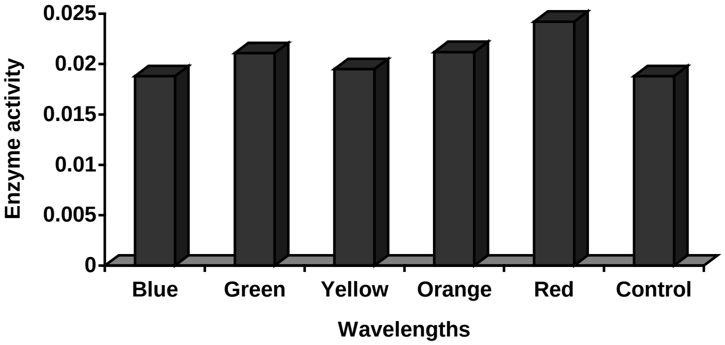

Fig. 3. Mean lipase activity for seven days of *Arachis hypogaea* seedlings grown under different-wavelength-lights.

Lipase activity in Arachis hypogaea seedlings grown under different wavelengths

On the 1st day, seedlings under yellow light showed significantly greater enzyme activity than others (Table 3). But on other days it showed less activity compared to others (Table 3). From the 2nd day onwards seedlings under red light showed significantly greater enzyme activity than most of the others (Table 3). But on 6th and 7th days it showed less activity (Table 3). Seedlings under blue light showed significantly less enzyme activity than seedlings under most of the other wavelengths up to 5th day. But on 6th and 7th days it showed significantly greater activity than some of the other wavelengths (Table 3). Seedlings under red light showed significantly greater enzyme activity than control from 2nd to 5th day. But on 1st, 6th and 7th days the differences were insignificant (Table 3). Considering the mean enzyme activity for seven days, seedlings under red light showed the greatest enzyme activity than others (Fig. 3). Thus, during the active period of seedling establishment red light enhances lipase activity.

DISCUSSION

In all experiments conducted, maximum lipase activity was observed on the first day of germination and it decreased as the growth proceeded. Of the three types of seeds tested, *A. hypogaea* has the highest lipid content, but it didn't show greater lipase activity than others as we may expect. It is in accordance with the findings of Bamann and Ullman (1957) that, there is little correlation between lipid content and lipase activity. Though some earlier studies reported that there is no correlation between light and lipase activity (Nyman, 1965; Castlefranco *et al*., 1969; Bajracharya and Schopfer, 1979) some other studies revealed that lipase activity is induced by light (Mehta *et al*., 1975; Davies *et al*., 1981; Gemmrich, 1982; Pfeiffer and Kutschera, 1997).

According to the previous reports, red and white light induce lipase activity. Some recent studies reveal the importance of other wavelengths also in lipid metabolism (Liao and Burns, 2010). Present study was an attempt to find out the influence of different wavelengths of the spectrum in the lipid mobilization during seed germination and seedling establishment in three different seeds which differ in their reserve food material. The effect of different lights on lipase activity varied on different days and on different plants. It is observed that, for *O. sativa,* green light is more influential; for *V. unguiculata,* yellow light is more influential and for *A. hypogaea,* red light is more influential in inducing lipase activity in the initial 7days of the seedlings. In the case of *A. hypogaea,* seedlings under red light showed significant increase in lipase activity than others on most of the days. Mean values of the enzyme activity for seven days showed that, in *A. hypogaea* it was higher for seedlings under red light than others and in *O. sativa*, red-light-exposed seedlings came to the second place. But in *V. unguiculata*, seedlings undergone red light exposure, showed the least in enzyme activity. However, on the first day, which may be the most active period of lipid degradation, seedlings under red light showed significantly greater enzyme activity than others. In *A. hypogaea*, a major part of the reserve food is lipid. In *O. sativa* also oil content is high, but in *V. unguiculata* it is very less. The developmental pattern is also different in the above plant groups. In *V. unguiculata* and O. *sativa* it is faster than *A. hypogaea*. Davies *et al.* (1981) suggested that the effect of red light on lipase activity is species dependent. Present study agrees with it and suggests that influence of red light on lipase activity during seed germination and seedling growth depends on the lipid content of the seed as well. It also reveals that each part of the spectrum has its own effect on lipase activity and is also species dependent. The present study reveals the depressing effect of blue wavelength on lipase activity also.

CONCLUSION

Each wavelength of the visible spectrum affects the lipase activity during seed germination and seedling establishment. Effect of red light on lipase activity depends on the lipid content of the seed. In seeds having high lipid content, the lipase activity enhances under red light. The blue wavelength has a depressing effect on lipase activity.

REFERENCES

Ahmad, M., Jarillo, JA. and Cashmore, AR. 1998. Chimeric proteins between cry1 and cry2 *Arabidopsis* blue light photoreceptors indicate overlapping functions and varying protein stability. The Plant Cell. 10:197-207.

Bajracharya, D. and Schopfer, P. 1979. Effect of light on the development of glyoxysomal functions in the cotyledons of mustard (*Sinapis alba* L.) seedlings. Planta. 145 (2):181-186.

Bamann, E. and Ullmann, E. 1957. Lipasen. In: Handbuch der Pflanzenphysiologie. Eds. Ruhland, W. Springer Verlag. pp. 109-136.

Barnaby, NG., He, F., Liu, X., Wilson, KA. and Tan-Wilson, A. 2004. Light responsive subtilisin-related protease in soybean seedling leaves. Plant Physiol. Bioche. 42 (2):125-134.

Bouly, J., Schleicher, E., Dionisio-Sese, M., Vandenbussche, F., Van Der Straeten, D., Bakrim, N., Meier, S., Batschauer, A., Galland, P., Bittl, R. and Ahmad, M. 2007. Cryptochrome blue light photoreceptors are activated through interconversion of flavin redox states. J. Biol. Chem. 282(13):9383-9391.

Buchanan, BB. 1980. Role of light in the regulation of chloroplast enzymes. Annu. Rev. Plant Physiol. 31:341-374.

Castlefranco, P., Lott, J. and Sabor, N. 1969. Respiratory changes during seed germination: Histochemical distribution of respiratory enzymes and mobilization of fat reserves in castor bean endosperm and peanut cotyledons. Plant Physiol. 44 (6):789-795.

Darbelley, N., Razafindramboa, N., Chambost, JP. and Pavia, A. 1997. Light effects on alpha-amylase activity and carbohydrate content in relation to lipid mobilization during the seedling growth of sunflower. J. Plant Res. 110 (3):347-356.

Datta, R., Selvi, MT., Seetharama, N. and Sharma, R. 1999. Stress mediated enhancement of beta-amylase activity in pearl millet and maize leaves is dependent on light. J. Plant Physiol. 154:657-664.

Davies, HV., Gaba, V., Black, M. and Chapman, JM. 1981. The control of food mobilization in seeds of *Cucumis sativus* L.: The effect of light on lipid degradation. Planta. 152(1):70-73.

Dhingra, A., Bies, DH., Lehner, KR. and Folta, KM. 2006. Green light adjusts the plastid transcriptome during early photomorphogenic development. Plant Physiol. 142 (3):1256-1266.

Dreier, W., Schnarrenberger, C. and Borner, T. 1995. Light and stress-dependent enhancement of amylolytic activities in white and green barley leaves: β-amylases are stress-induced proteins. J. Plant Physiol. 145 (3):342-348.

Eisinger, WR., Bogomolni, RA. and Taiz, L. 2003. Interactions between a blue-green reversible photoreceptor and a separate UV-B receptor in stomatal guard cells. Am. J. Bot. 90(11):1560-1566.

Fankhauser, C. and Chory, J. 1997. Light control of plant development. Annu. Rev. Cell Dev. Biol. 13:203-229.

Folta, KM. 2004. Green light stimulates early stem elongation, antagonizing light-mediated growth inhibition. Plant Physiol. 135(3):1407-1416.

Folta, KM. and Maruhnich, SA. 2007. Green light: a signal to slow down or stop. J. Exp. Bot. 58 (12):3099-3111.

Frechilla, S., Talbott, LD., Bogomolni, RA. and Zeiger, E. 2000. Reversal of blue light-stimulated stomatal opening by green light. Plant Cell Physiol. 41:171-176.

Gemmrich, AR. 1982. Effect of red light and gibberellic acid on lipid metabolism in germinating spores of the fern *Anemia phyllitidis.* Physiol. Plant. 54(1):58-62.

Jayaraman, J. 1981. Lipases. In: Laboratory manual in Biochemistry. Wiley Eastern Limited. New Delhi. p. 133-134.

Liao, H. and Burns, JK. 2010. Light controls phospholipase A2α and β gene expression in *Citrus sinensis*. J. Exp. Bot. 61(9):2469-2478.

Lo, M., Taylor, C., Wang, L., Nowack, L,. Wang, TW. and Thompson, J. 2004. Characterization of an ultraviolet B-induced lipase in *Arabidopsis.* Plant Physiol. 135(2):947-958.

Mehta, PM., Rao, BVN. and Bhat, HR. 1975. Effects of light of different spectral composition on the germination, growth and the enzymes lipase and catalase of soybean, *Glycine max* cultivar Lee. Botanique. 6(4):169-176.

Nyman, B. 1965. Localization and activity of lipase in light and dark germinated seeds of scots pine (*Pinus silvestris* L.). Physiol. Plant. 18(4):1085-1094.

Pfeiffer, I. and Kutschera, U. 1997. Effect of white light on cell expansion and lipid mobilization in sunflower cotyledons. J. Plant Physiol. 151:590-594.

Schopfer, P. 1977. Phytochrome control of enzymes. Annu. Rev. Plant Physiol. 28:223-252.

Talbott, LD, Nikolova, G., Ortiz, A., Shmayevich, I. and Zeiger, E. 2002. Green light reversal of blue-light-stimulated stomatal opening is found in a diversity of plant species. Am. J.Bot. 89(2):366-368.

Thompson, WF. and White, MJ. 1991. Physiological and molecular studies of light-regulated nuclear genes in higher plants. Annu. Rev. Plant Physiol. Plant Mol. Biol. 42:423-466.

Tobin, EM. and Silverthorne, J. 1985. Light regulation of gene expression in higher plants. Annu. Rev. Plant Physiol. 36:569-593.

Vassey, TL. 1988. Phytochrome mediated regulation of sucrose phosphate synthase activity in maize. Plant Physiol. 88(3):540-542.

Zodape, ST. and Chauhan, VD. 1994. Stimulation of lipase in cotton seed by pulsed concentrated solar radiation. Indian Journal of Plant Physiology. 37(4):289-290.

Received: July 12, 2010; Accepted: Sept 20, 2010

SENRA Academic Publishers, Burnaby, British Columbia
Vol. 4, No. 3, pp. 1249-1255, October 2010
Online ISSN: 1920-3853; Print ISSN: 1715-9997

Canadian Journal of pure&applied sciences

SCIENTIFIC EVALUATION OF AN INNOVATIVE HERBAL MEDICINE FOR RELIEF IN RESPIRATORY DISORDERS

*Neena Bedi[1], PMS Bedi[1], Hardik S Bodiwala[2], Inder Pal Singh[2] and Parikshit Bansal[2]
[1]Department of Pharmaceutical Sciences, Guru Nanak Dev University, Amritsar-143005
[2]National Institute of Pharmaceutical Education and Research (NIPER)
Sector 67, SAS Nagar-160062, India

ABSTRACT

The present paper describes scientific evaluation of a traditional herbal medicine for relief in cough and asthma. The formulation had been used by a practitioner of traditional medicine from Jalandhar (Punjab, India) over a period of time and found to be quite efficacious in providing relief in cough and asthma. The same comprises a powdered mixture of five herbs *viz*. *Acorus calamus* (rhizome), *Alpinia galanga* (rhizome), *Psoralea corylifolia* (fruit), *Piper longum* (fruit) and *Piper nigrum* (fruit) in equal proportions. This polyherbal mixture showed antibacterial activity against Gram-positive and Gram-negative bacteria as well as antifungal activity against *Aspergillus niger*. Analytical studies revealed absence of any externally added steroidal content in the formulation. To ensure adequate quality control of the formulation, HPLC fingerprints of different extracts prepared from this polyherbal mixture were generated and two major constituents, i.e. piperine and asarone were quantified by HPLC.

Keywords: herbal medicine, cough, asthma, piperine, asarone

INTRODUCTION

Herbal preparations have been a part of the Indian system of traditional medicine. There are many traditional remedies prevalent in different parts of India. However, with the passage of time, some of the time tested formulae and recipes have been lost. We came across such an herbal formulation that is being used by a practitioner of traditional medicine Mrs. Raj Katyal from Jalandhar over a period of time. The formula was given to her by her forefathers. She is at the third generation of this 100 years old formulation. Nobody in her family was interested in practicing this further. There was a fear of losing this traditional knowledge for providing relief in cough and asthma. Her quest to protect this valuable traditional knowledge led her to IPR cell of NIPER, SAS Nagar, which after a thorough search of various databases concluded that the formulation was novel and innovative. The formula, which the traditional healer had been using, offered societal benefit. However, there was no proven clinical data on its efficacy and safety. The formulation consists of a powdered mixture of five herbs *viz*. *Acorus calamus, Alpinia galanga, Psoralea corylifolia, Piper longum* and *Piper nigrum* in equal amount, which is to be taken orally with honey. These herbs are quite safe and well documented in Indian systems of medicines for their medicinal properties (Anonymous, 1986). The dose of the herbal preparation is described in table 1.

Table 1. Dosages of the herbal preparation.

S. No.	Age of Patients (years)	Herbal mixture to be taken with honey
1	>18 (Adults)	1.5 g (750 mg twice a day, morning and evening after meals)
2	12-17	0.75 g
3	5-11	0.35 g
4	3-4	0.17 g
5	< 3 years (Infants)	0.25 g

Thereafter, scientific inputs were initiated under TePP program (Department of Scientific and Industrial Research, Ministry of Science and Technology, Govt. of India) to develop this proven herbal medicine. The present paper describes standardization and scientific evaluation of this patented (1922/DEL/2005, dated: 27/07/2005) herbal formulation for providing relief in cough and asthma.

MATERIALS AND METHODS

Methodology

Evaluation for the presence of steroids

The formulation has been tested by TLC for any external steroidal contents presence.

Sample preparation for TLC: 1g each of the individual plant drugs used in the formulation i.e. *Acorus calamus* (rhizome), *Alpinia galanga* (rhizome), *Psoralea*

---

*Corresponding author email: neenagndu@yahoo.com

corylifolia (fruit), *Piper longum* (fruit), *Piper nigrum* (fruit) powders were refluxed in chloroform (50ml) for 1hr. The extract was filtered and concentrated *in vacuo*. Same methodology was adopted for the sample preparation of the herbal formulation provided by traditional healer. Each extract was diluted to a volume of 10 ml with chloroform. 10µl of the sample was applied on TLC Plate.

Thin layer chromatographic (TLC) analysis

TLC Plates: Pre coated plates of silica gel F_{254} (E. Merck) of 0.2mm thickness
Solvent system: Hexane - Ethyl acetate (8:2)
Spray reagent: Liebermann -Burchard Reagent.
Liebermann- Burchard Reagent: A solution of 5ml acetic anhydride and 5ml concentrated sulphuric acid was added carefully to 50ml of absolute ethanol while cooling in ice (Wagner and Bladt, 1996).

Evaluation of antimicrobial activity

Various microorganisms associated with respiratory tract infections were selected for the study. The antimicrobial activity of the formulation was determined by agar well-diffusion method as recommended by the National Committee for Clinical Laboratory Standards (NCCL 1992, 1997, 1998) at a concentration of 0.1mg/ml, using dimethyl sulfoxide (DMSO) as the diluent/solvent. The antibacterial activity was evaluated against Gram positive bacteria *viz. Staphylococcus aureus* MTCC 96 and Gram negative bacteria such as *Esherichia coli* MTCC 739, *Klebsiella pneumoniae* MTCC 109 and *Pseudomonas aeruginosa* MTCC 1688. Ciprofloxacin was used as standard for antibacterial activity. The antifungal activity was determined against *Aspergillus niger* MTCC 1344. Griseofulvin was used as standard antifungal drug.

HPLC fingerprinting

To ensure adequate quality control of the formulation, HPLC fingerprinting of the polyherbal formulation was done as detailed below.

Sample preparation

10g of powdered plant material was taken in a beaker, and 50ml of *n*-Hexane added in to it. Thereafter, it was sonicated at room temperature for 10minutes. The solvent was then decanted and concentrated under vacuum. The marc obtained after preparation of hexane extract was extracted sequentially with ethyl acetate and methanol under same conditions. A sample of 10mg/ml of extracts in HPLC grade Acetonitrile was prepared and filtered through 0.22µ syringe filter and injected into HPLC to obtain the fingerprints.

Chromatographic conditions

Instrument: Shimadzu SCL-10 AVP with PDA detector, Column: Kromasil (250X4.6 mm, 5µ, Phenomenex, USA) Injection volume: 10µl, Flow rate: 1 ml/min, Detection: 254nm, Solvent composition: A: Water, B: ACN.

For Hexane extract: 0-10min: 40-50% B, 10-20min: 50-70% B, 20-30min: 70-80% B, 30-40min: 80-90% B, 40-50min: 90-100% B, 50-65min: 100% B, Runtime: 65min
For Ethyl acetate extract: 0-10min: 45-55% B, 10-30min: 55-65% B, 30-40min: 65-75% B, 40-50min: 75-100% B, 50-65min: 100% B, Runtime: 65min

For Methanol extract: 0-10min: 20% B, 10-20min: 20-50% B, 20-30min: 50-70% B, 30-40min: 70-90% B, 40-50min: 90-100% B, 50-55min: 100% B, Runtime: 55min

Quantification of asarone and piperine

Quantification of the two major constituents, i.e. piperine and asarone in the formulation was performed using following methodology.

Standards

Piperine (Pip) and Asarone (Asa) were isolated and characterized as reported from *Piper nigrum* (Ikan, 1991) and *Acorus calamus* (Yingjuan *et al*., 2008).

Preparation of standard and test solutions

Standard stock solutions of Piperine (1000µg/mL) and Asarone (1000µg/mL) were prepared in Methanol. Working standard solutions were prepared by diluting appropriately the stock solutions with the same solvent. Both the calibrants were prepared over the range of 0.1-0.5µg/ml. For the preparation of test solution, 2.5g of formulation was accurately weighed into a 25mL beaker and 10mL of methanol was added in to it. It was sonicated for 20min at room temperature. After this period, the solution was filtered and dried using rotary evaporator under vacuum. A stock solution of 10 mg/mL was prepared and the test solution was prepared after adequate dilution with methanol (1mg/mL). Finally, before injecting 20µL on chromatograph, the standard and test solutions were filtered through a 0.22-µm filter.

Chromatographic conditions

The chromatographic conditions were same as of used for fingerprinting analysis. The quantitative analysis was also carried out in a gradient elution mode with 50% ACN at 0 min gradually increased to 60% at 15min, then back to 50% from 17min.

RESULTS AND DISCUSSION

Evaluation for the presence of the steroids

It is generally believed that traditional herbal practitioner use steroidal drugs like dexamethasone, prednisolone in the formulations for relief in pain and inflammation etc. Liebermann -Burchard reagent is used to detect steroids, terpenoids, lignans and saponins. Initial comparison of the chloroform extract of the individual plant drugs by TLC suggested an identical profile for the formulation with respect to its plant drugs. The spots that could be detected with Liebermann- Burchard (LB) reagent in the formulation were also observed in the individual drugs. It suggested complete absence of any externally added steroids in the formulation. Literature reports the presence of terpenoids and lignans in these plant drugs and the spots shown with LB reagent can be ascribed to individual chemical constituents of these drugs. For example, dihydrostigmasterol is present in *Piper longum*; Sesquiterpenes (acoranedione, shyobunone, alpiniol) are present in *Acorus calamus* and *Alpinia galanga.* Lignans are present in *Piper* species. All these classes of compounds give positive test with LB reagent.

Evaluation of *in vitro* anti-microbial activity

Results reveal that the herbal formulation has significant activity against Gram positive and Gram-negative microorganisms, which cause respiratory tract infections. This formulation exhibited comparable activity against *K. pneumoniae* as that of standard drug ciprofloxacin. It showed moderate activity against *P. aeruginosa.* The activity against *S. aureus* and *E.coli* is less in comparison to the standard drug. In case of antifungal screening, the formulation showed moderate activity against *A. niger.* The results are shown in table 2.

HPLC fingerprinting

The HPLC fingerprint analysis of all the three extracts *viz.* hexane; ethyl acetate and methanol of the formulation are given in figures 1, 2 and 3, respectively. From the fingerprints obtained, it is clear that the extraction process significantly influences the molecular composition of the extract. However, in the present composition the powdered herb is given as a 'whole', which ensures that no molecules are lost during extraction and the 'holistic therapeutic potential' if any is duly preserved.

Quantification of asarone and piperine

There were HPLC methods reported for piperine and asarone individually. Piperine was analyzed using a Symmetry C18 column (150X4.6mm, 5µm) and isocratic elution with 25 mM KH_2PO_4 (pH 4.5)–acetonitrile (50:50) with a flow-rate of 1 ml/min (Bajad *et al*., 2002). While, asarone was analyzed using Hypersil ODS C18 column (150X4.6mm, 5µm) and isocratic elution with acetonitrile-water (60:40) at 1mL/min flow rate (Wu and Fang, 2004). So, a method was developed using acetonitrile-water gradient at 1ml/min on Kromasil C18 Column (250×4.6, 5µm) for simultaneous determination of Asarone and Piperine. Calibration curves were obtained by plotting peak area against the concentrations of respective substances as shown in figures 4 and 5. In both cases, straight regression lines with correlation coefficients (r^2) of 0.99 were obtained. Data are summarized in table 3.

Table 3. Linearity parameters for the proposed RP-HPLC method.

Parameter	Piperine	Asarone
Concentration (µg/ml)	0.1-0.5	0.1-0.5
Regression equation	Y= 2038868*X-17818	Y= 2743932*X-16739
Correlation coefficient (r^2)	0.9982	0.9984

The precision of analysis was examined by performing the intra-day and inter-day assays by replicate injections of the sample solutions used above. The intra-assay precision was performed with the interval of 4 h in a day, while the inter-assay precision was performed over 3days. The precision result of the solution are presented in table 4, and it has been shown that the RSD values of concentration from peak area are lower than 0.11% both for the intra-assay and inter-assay precision for both calibrants.

Piperine and Asarone were identified in sample by the comparison of their retention times (t_R 10.6 and 11.3min, respectively in Figs. 6 and 7) and UV spectra with the corresponding pure compounds. The Piperine and Asarone were calculated using calibration curves results. Piperine was found to be 0.2674 ± 0.0014 µg/ml (0.4479 %w/w) and asarone was found to be 0.1901 ± 0.0029 µg/ml (0.3183 %w/w) in the formulation on dry powder basis.

Table 2. Antimicrobial activity (zones of inhibition in mm, cup diameter 6mm).

	K. pneumoniae	*S. aureus*	*P. aeruginosa*	*E. coli*	*A. niger*
Herbal Formulation (0.1mg/ml)	22	20	24	8	12
Ciprofloxacin (50µg/ml)	22	30	28	16	-
Griseofulvin (50µg/ml)	-	-	-	-	11
DMSO	-	-	-	-	-

Table 4. Precision parameters for the proposed RP-HPLC method.

	Interday precision (Conc µg/ml)	Interday precision (%RSD)	Intraday precision (Conc µg/ml)	Interday precision (%RSD)
Piperine	0.2680 ± 0.0011	0.04	0.2668 ± 0.0016	0.08
Asarone	0.1895 ± 0.0033	0.11	0.1906 ± 0.0015	0.07

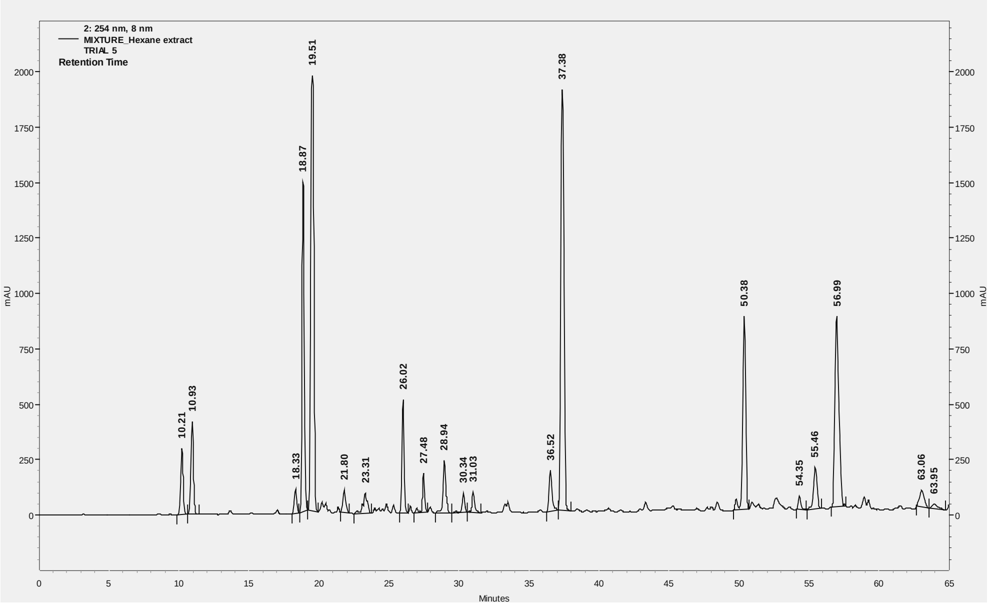

Fig. 1. HPLC fingerprint of hexane extract of the polyherbal mixture.

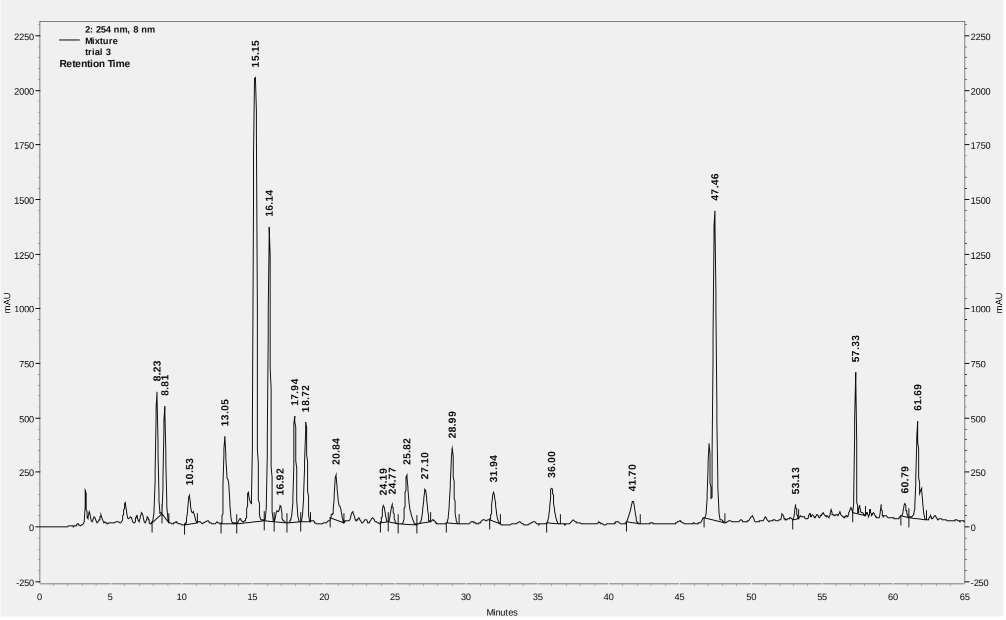

Fig. 2. HPLC fingerprint of ethyl acetate extract of the polyherbal mixture.

Significance of asarone estimation

The beta form of pure asarone, which is present in *Acorus calamus* oil, has been associated with toxicity and there are concerns in the western scientific world regarding possible carcinogenic effect of pure asarone. However, the powdered root as well as rhizome of *Acorus calamus* has been used in India for thousands of years without any reports of toxicity or cancer. The pharmacological profile

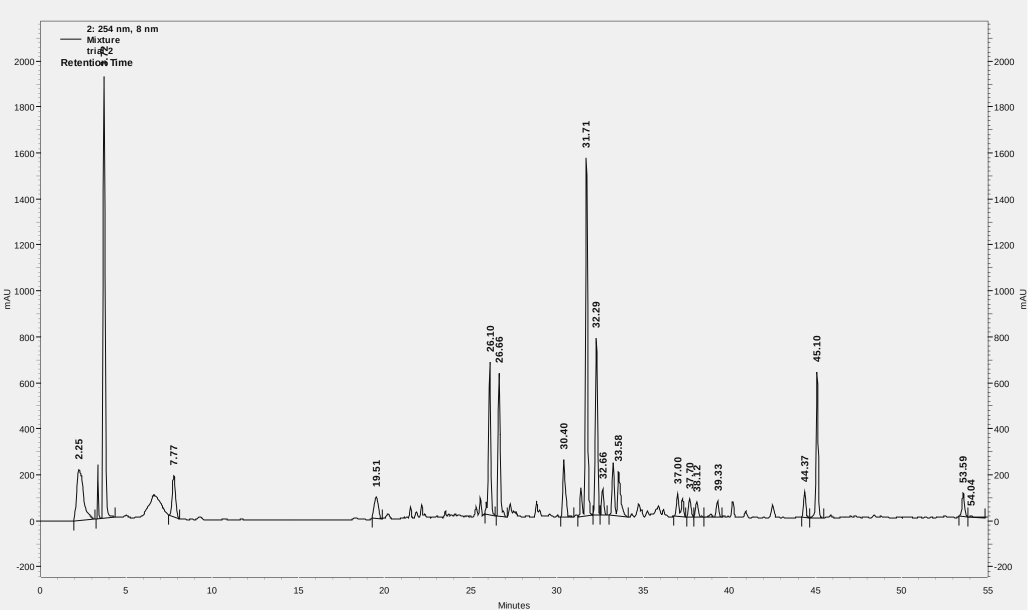

Fig. 3. HPLC fingerprint of methanol extract of the polyherbal mixture.

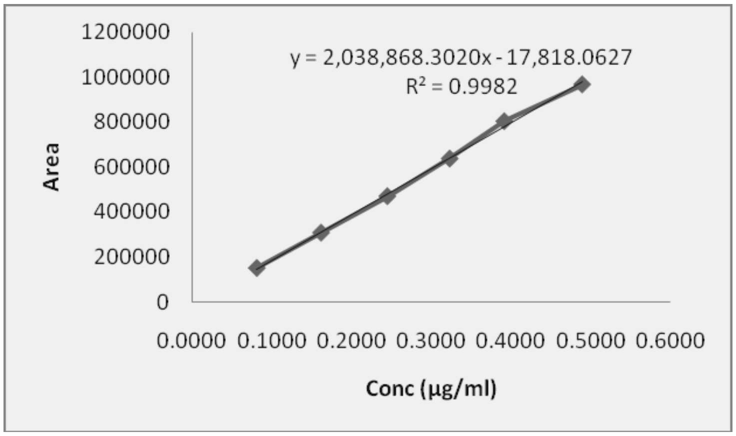

Fig. 4. Calibration curve of Piperine.

of *Acorus calamus* has been reviewed in detail (Yende *et al.*, 2008).

The 'Indian Materia Medica' also lists several useful properties of *Acorus calamus* root and rhizome. The powdered oral dose of *Acorus calamus* indicated for dyspepsia (impairment of digestive function) ranges from 144mg to 433mg (20-60 grains in a mixture of seven ingredients in equal proportion). For respiratory disorders, small powdered doses of 10 grains (650mg) repeated every two or three hours till relief has been obtained are indicated. The present formulation recommends a dose of only 750mg of the mixture, which amounts to 150mg of *Acorus calamus* in powdered form- well within the safe limit. Even if the formulation is taken twice or thrice a day, the maximum intake of *Acorus calamus* amounts to only 300mg and 450mg respectively- again well within the range already documented.

Significance of piperine estimation

Piperine is the alkaloid responsible for the pungency of black pepper and long pepper, along with chavicine (an isomer of piperine). It has also been used in some forms of traditional medicines and as an insecticide. Piperine has also been found to inhibit human CYP3A4 and P-glycoprotein, enzymes important for the metabolism and transport of xenobiotics and metabolites (Bhardwaj *et al.*, 2002). In animal studies, piperine also inhibited other enzymes important in drug metabolism (Atal *et al.*, 1985) (Reen *et al.*, 1993).

By inhibiting drug metabolism, piperine may increase the bioavailability of various compounds. Notably, piperine may enhance bioavailability of curcumin by 2000% in humans (Shoba *et al.*, 1998). Due to its effects on drug metabolism, piperine should be taken cautiously (if at all) by individuals taking some other medications.

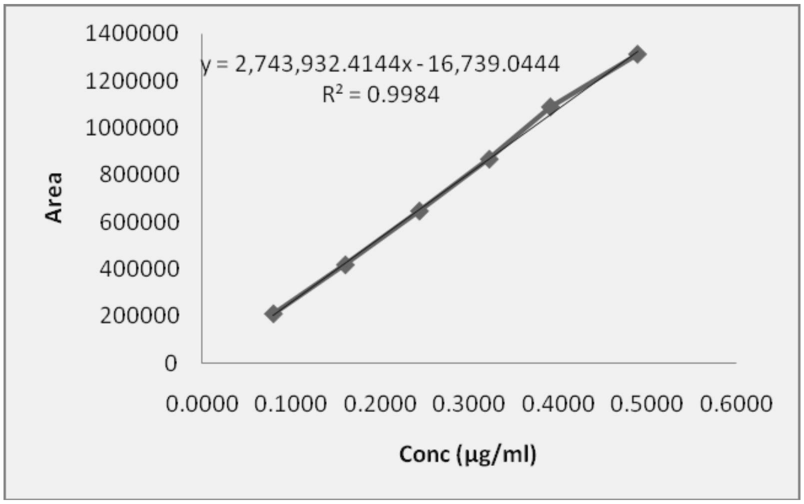

Fig. 5. Calibration curve of Asarone.

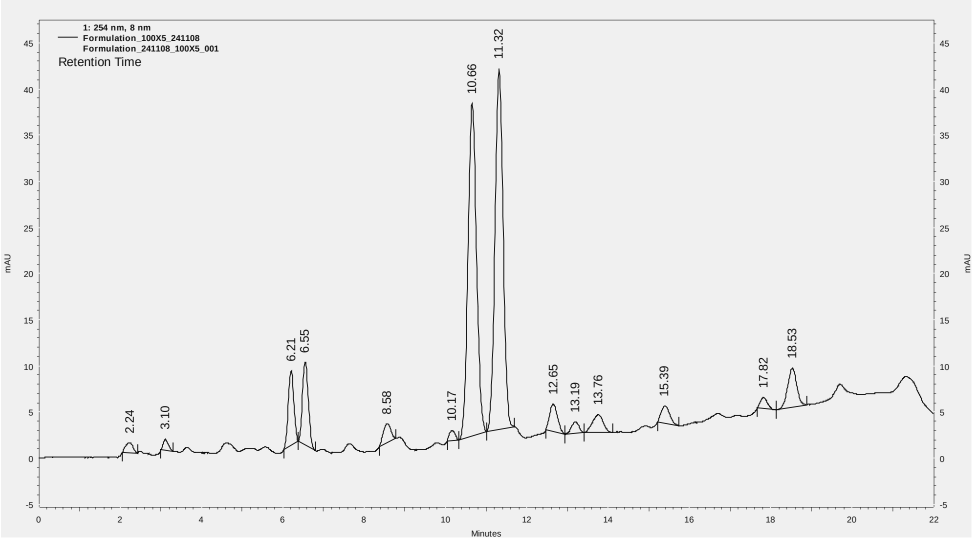

Fig. 6. HPLC Chromatogram of methanol extract for quantification.

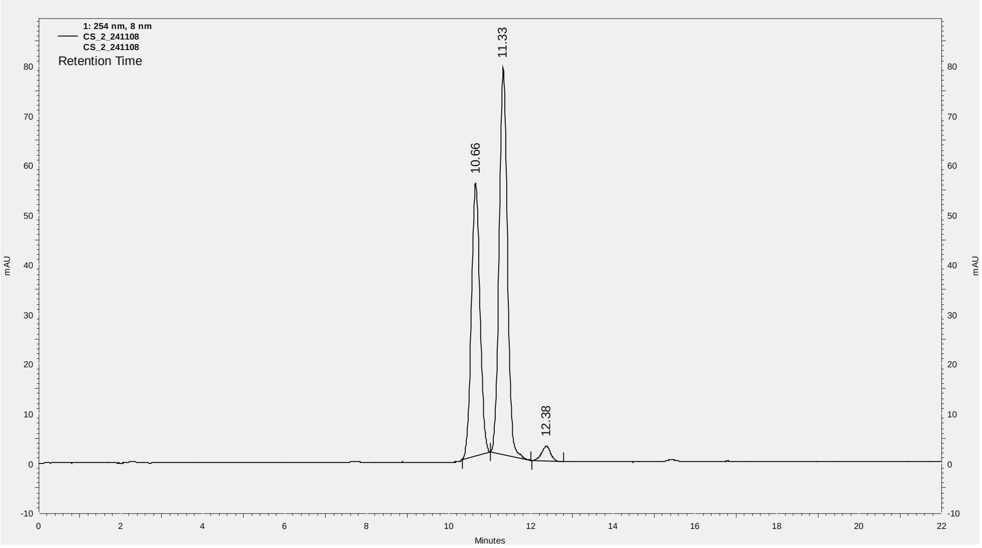

Fig. 7. HPLC Chromatogram of Piperine and Asarone.

CONCLUSIONS

Based on the detailed scientific evaluation of the herbal formulation, it is clear that the one of the major reason for its good therapeutic efficacy is the highly potent anti-microbial activity of the formulation, which can be attributed to synergistic effect of the ingredients. The formulation holds promise as a safe, low-cost medicine for the treatment of respiratory disorders. A point worthy of mention is the use of the herbs in 'whole powdered form' and not as extracts, which might prevent loss of bioactive components that would occur during extraction.

ACKNOWLEDGEMENTS

Financial support provided under the TePP program (Project No. DSIR/TEPP/1176/6) of Department of Scientific and Industrial Research, Ministry of Science and Technology, Govt. of India is greatly acknowledged.

REFERENCES

Anonymous. 1986. The useful Plants of India. Publication and Information Directorate, Council of Scientific and Industrial Research, New Delhi. India.

Atal, CK., Dubey, RK. and Singh, J. 1985. Biochemical basis of enhanced drug bioavailability by piperine: evidence that piperine is a potent inhibitor of drug metabolism. The Journal of Pharmacology and Experimental Therapeutics. 232 (1):258-262.

Bajad, S., Johri, RK., Singh, K., Singh, J. and Bedi, KL. 2002. Simple high-performance liquid chromatography method for the simultaneous determination of ketoconazole and piperine in rat plasma and hepatocyte culture. Journal of Chromatography A. 949:43-47.

Bhardwaj, RK., Glaeser, H., Becquemont, L., Klotz, U., Gupta, SK. and Fromm, MF. 2002. Piperine, a major constituent of black pepper, inhibits human P-glycoprotein and CYP3A4. The Journal of Pharmacology and Experimental Therapeutics. 302 (2):645-650.

Ikan, R. 1991. Natural Products: a laboratory guide. (2nd ed.). Academic Press, London. 233-238.

National Committee for Clinical Laboratory Standards. 1992. Methods for Determining Bactericidal Activity of Antimicrobial agents: Tentative Guideline, Villanova (PA), NCCLS; (Publication no NCCLS M 26-T).

National Committee for Clinical Laboratory Standards. 1997. Methods for Antimicrobial Susceptibility Testing Anaerobic Bacteria, Approved Standard (4th ed.), Villanova (PA), NCCLS; (Publication no NCCLS M 11-A4).

National Committee for Clinical Laboratory Standards. 1998. Performance standards for Antimicrobial Susceptibility Testing. Eighth Information Supplement, Villanova (PA), NCCLS; (Publication no NCCLS M 100-58).

Reen, RK., Jamwal, DS., Taneja, SC., Koul, JL., Dubey, RK., Wiebel, FJ. and Singh, J. 1993. Impairment of UDP-glucose dehydrogenase and glucuronidation activities in liver and small intestine of rat and guinea pig in vitro by piperine. Biochemical Pharmacology. 46 (2): 229-238.

Shoba, G., Joy, D., Joseph, T., Majeed, M., Rajendran, R. and Srinivas, PS. 1998. Influence of piperine on the pharmacokinetics of curcumin in animals and human volunteers. Planta Medica. 64 (4):353-356.

Wagner, H. and Bladt, S. 1996. Plant Drug Analysis- a thin layer chromatography atlas. Springer-Verlag, Berlin, New York. pp. 362.

Wu, HB. and Fang, YQ. 2004. Pharmacokinetics of β-asarone in rats. Acta Pharmaceutica Sinica. 39(10):836-838.

Yende, SR., Harle, UN., Rajgure, DT., Tuse, TA. and Vyawahare, NS. 2008. Pharmacological profile of *Acorus calamus:* An overview. Pharmacognosy Reviews. 2(4): 22-26.

Yingjuan, Y., Wanlun, C., Changju, Y., Dong, X. and Yanzhang, H., 2008. Isolation and Characterization of insecticidal activity of (*Z*)-asarone from *Acorus calamus* L. Insect Science. 15:229-236.

Received: March 16, 2010; Revised: Sept 6, 2010;

Accepted: Sept 20, 2010

SENRA Academic Publishers, Burnaby, British Columbia
Vol. 4, No. 3, pp. 1257-1265, October 2010
Online ISSN: 1920-3853; Print ISSN: 1715-9997

Canadian Journal of pure&applied sciences

IMPACT OF HABITAT DESTRUCTION ON THE POPULATION OF AMPHIBIANS WITH REFERENCE TO CURRENT STATUS OF FROGS AND TOADS IN KARACHI AND THATTA, SINDH

M Zaheer Khan, *Nazia Mahmood, Syed Ali Ghalib, Babar Hussain,
Saima Siddiqui, Shahnaz Perween and Darakhshan Abbas
Department of Zoology (Wildlife & Fisheries), Faculty of Science
University of Karachi, Karachi-75270

ABSTRACT

The present study is based on the impact of habitat destruction on the population of amphibians with reference to status of frogs and toads in Karachi and Thatta districts of Sindh. During the years 2004-2006, four species of frogs, *Euphlyctis cyanophlyctis cyanophlyctis* (Common Skittering Frog), *Hoplobatrachus tigerinus* (Tiger Frog), *Tomopterna breviceps* (Indian Burrowing Frog) and *Limnonectes limnocharis* (Indian Cricket Frog), and two toads species, *Bufo stomaticus* (Marbled Toad) and *Bufo melanostictus* (Common Asian Toad) were recorded from the area. In Thatta district, four species of frogs and two species of toads were recorded, *Euphlyctis cyanophlyctis cyanophlyctis* was rated as abundant, *Bufo stomaticus* as common, *Bufo melanostictus* as less common, while *Hoplobatrachus tigerinus*, *Tomopterna breviceps* and *Limnonectes limnocharis* were rated as rare. Three species of frogs and two species of toads were recorded in Karachi district. *Euphlyctis cyanophlyctis cyanophlyctis* was found to be abundant, *Bufo stomaticus* as common, *Bufo melanostictus* as less common, while *Hoplobatrachus tigerinus* and *Tomopterna breviceps* were rated as rare. On the basis of present study, it is concluded that due to habitat alteration, destruction of habitat, indiscriminate use of pesticides, chemical fertilizers and increase in human population, three species viz. *Hoplobatrachus tigerinus*, *Tomopterna breviceps* and *Limnonectes limnocharis* have declined and may be recorded as threatened species in Thatta district, while two species *Hoplobatrachus tigerinus* and *Tomopterna breviceps* were found to be rare in Karachi district.

Keywords: Sindh, habitat destruction, population status, frogs and toads.

INTRODUCTION

Since the 1980s herpetologists have been researching, and documenting the overall decline in the health and abundance of amphibian populations (Rabb, 1999). Global declines in amphibian populations have been attributed to a number of anthropogenic activities, including habitat destruction, habitat alteration, and introduction of exotic species, exposure to environmental contaminants, climate change, increased acid precipitation and increased UV flux associated with ozone depletion. Many studies have illustrated that declines in amphibian population health have also taken place in relatively pristine habitats such as national parks and reserves, where specific environmental stressors are not readily apparent (DAPTF, 2001). Recently SSC Red List shows that 1,895 of the planet's 6,285 amphibians are in danger of extinction, making them the most threatened group of species known to date. Of these, 39 are already Extinct or Extinct in the Wild, 484 are Critically Endangered, 754 are Endangered and 657 are Vulnerable (IUCN, 2010). Several species of amphibians provide benefit to human beings. Frogs have been used as food. Many countries in Europe and USA import large quantities of frog legs, mostly from Asia. They also provide food for fish, birds, and mammals. Frog legs are considered to be delicacies (Martin, 2000).

Amphibians are collected for pets, food, medicines, bait, and for use in teaching. Some of the edible species include the Sardinian Discoglossid *(Discoglossus surdus)*, the Tiger Frog (*Hoplobactracus tigrina)* of Asia, and the Southeast Asian species *Limnonectes limnocharis* and *Rana hudsti*.

The impact of the frog leg trade in several countries, such as the USA, Pakistan, India and Bangladesh has been also a cause of amphibian declines (Abdulali, 1985; Pandian and Marian, 1986; Khan, 1990; Jacques, 1999). Amphibians have very porous skin, it is considered that they may be more susceptible to chemicals in the environment than many other animals. The amphibian's tadpoles living in the water and the adults being exposed to the air, it is considered that polluted chemicals in either environment may affect them.

Work has been done on bioecology, taxonomy and effect of pesticides on amphibians by Hora and Chopra (1923), Dubois and Khan (1979), Bogart (1992), Hall and Henry (1992), Barry and Shaffer (1994), Iffat (1994), Pechman

---

*Corresponding author email: nazo_nazoku@hotmail.com

and Wilbur (1994), Fisher and Shaffer (1996), Berrill *et al*. (1997, 1998), Didiuk (1997), Dupuis (1997), Fox *et al*. (1997), Green (1997), Khan (1987, 1997, 1999, 2000, 2001, 2003), Ovaska (1997), Waldick (1997), Conant and Collins (1998), Lannoo (1998), Marantelli and Parkes (1998), Bridges (2000), Khan and Khan (2000), Khan and Law (2005), Khan and Yasmeen (2008) and Yasmeen *et al*. (2009).

No detailed work has been reported on population and status of frogs and toads in Karachi and Thatta districts of Sindh province. The main object of present study was to investigate the impact of habitat destruction on the population of amphibians with reference to status of frogs and toads in Karachi and Thatta.

MATERIALS AND METHODS

Study areas

On the basis of preliminary surveys and baseline study, areas such as Ghullamullah Canal, Sakhro Branch, Tallah, Wadi Khar Dhund, Jafri Lake, LBOD, Mahboobshah Lake, Dargah Shaikh Sakhi Ahmed and Daro Branch in Thatta district, Lyari River, Hub River, Ibrahim Hyderi, Hub Dam and Malir River in Karachi district were selected as study areas (see Table 1, 2, Figs.1, 2).

Several reliable methods and surveys techniques were employed for the observation and census of frogs and toads. The observations were usually made from a raised position in order to get a clear view of the habitat. During each visit to the study areas, the population of each species of frogs and toads was recorded and relevant data collected.

COUNTING METHODS

A. DIRECT COUNTING

1. Field Surveys

Field surveys of one week duration in each district were undertaken on quarterly basis each year during the period 2004-2006 in two selected districts of Sindh Province. Nine sites in Thatta District and five sites in Karachi District were surveyed.

Table. 1. Study Areas of Thatta District.

S. No.	Sub Dist. of Thatta District	Study Areas	Co-ordinates	Habitat Type
1	Thatta	Ghullamullah Canal	24 36 20.8 N 67 49 14.8 E	Fresh Water Canal
2	Mirpur Sakhro	Sakhro Branch	24 36 2.1 N 67 49 13.9 E	Fresh Water Canal
3	Ghora Bari	Tallah	24 37 10.1 N 68 21 17.3 E	Slightly Brackish Water Lake
4	Mirpur Bathoro	Wadi Khar Dhund	24 41 44.8 N 68 7 9.1 E	Slightly Brackish Water Lake
5	Shah Bunder	Jafri Lake	24 06 24.12 N 67 54 68.15 E	Brackish Water Lake
6	Jati	Wetlands in the Left Bank Outfall Drain Area	24 18 41.8 N 68 46 51.0 E	Slightly Brackish / Fresh Water Lake
7	Sujawal	Mahboobshah Lake	24 36 51.8 N 68 15 20 E	Fresh Water Lake
8	Kharo Chan	Dargah Shaikh Sakhi Ahmed	24 38 23.9 N 68 21 36.6 E	Brackish Water Canal Near Dargah
9	Keti Bunder	Daro Branch	24 31 25.4 N 68 1 50.2 E	Brackish Water Canal

Table. 2. Study Areas of Karachi District

S. No	Districts of Karachi	Study Areas	Co-ordinates	Habitat Type
1	East	Lyari River	24 56 43.6 N 67 07 17.5 E	Fresh Water River
2	West	Hub River	24 55 02.12 N 66 43 14.5 E	Fresh Water River
3	South	Ibrahim Hyderi	24 48 23.5 N 67 10 39.2 E	Fresh Water Nala near Ibrahim Hyderi
4	Central	Hub Dam	25 14 51.8 N 67 07 24.0 E	Fresh Water Storage Reservior
5	Malir	Malir River	24 48 14.9 N 67 05 36.2 E	Fresh Water River

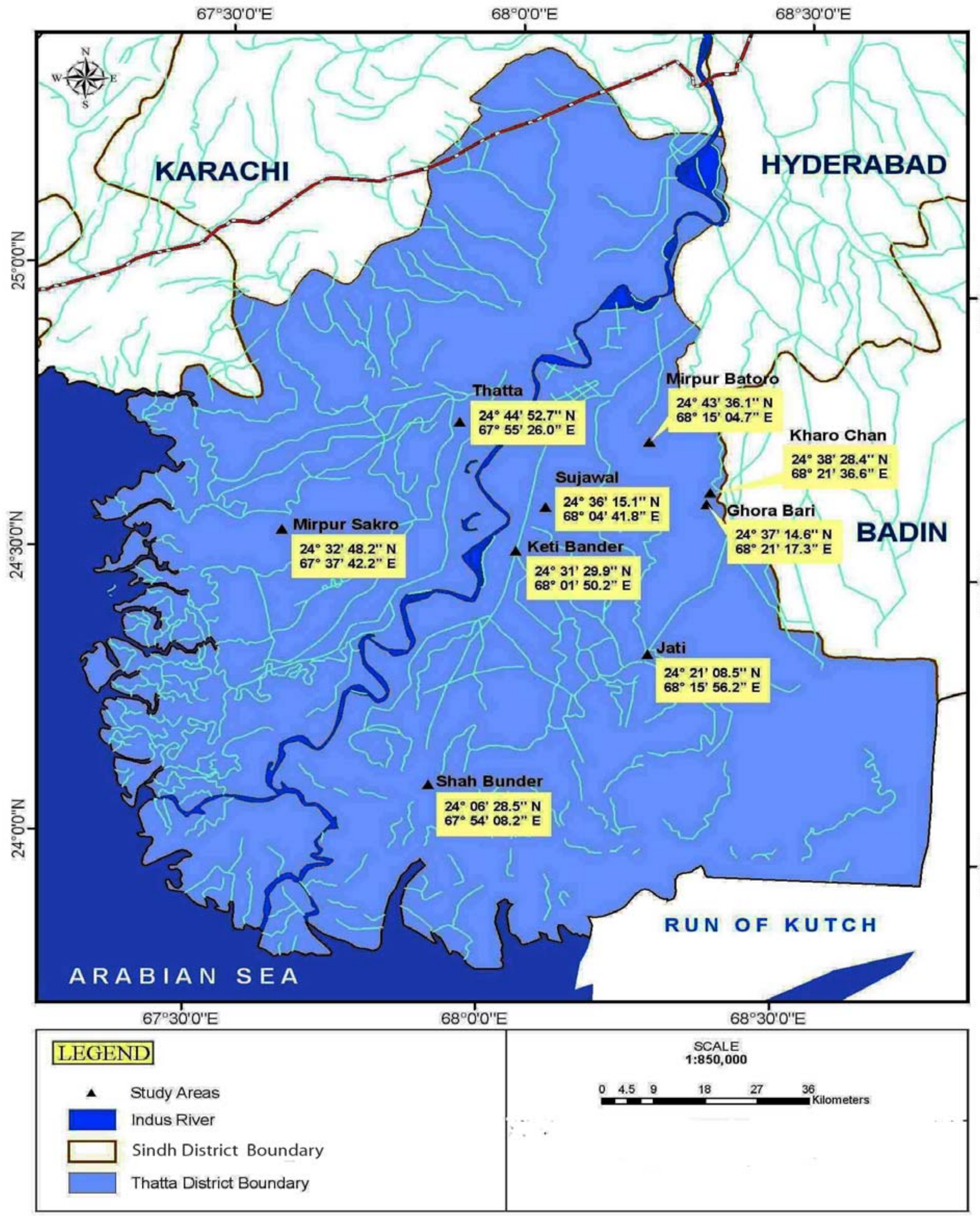

Fig. 1. Map showing Study Areas in Thatta District.

Mostly frogs were observed or netted during the day but some frogs were observed at night, while toads were observed at night. At dusk and during night, however, they prowl on the surface and were easily observed. During really warm weather periods many amphibians are most active at night.

2. Incidental Sightings

Incidental sighting is also helpful to determine the presence and population status of the species. In this way, number of species, date, time, location and habitat type were recorded.

3. Basking Behavior

This method of sitting or locating the species is the most suitable but it can be applied mostly in winter season. In winters the temperature of the water of river becomes very low. Due to cooler weather and cold water, these cold blooded amphibians avoid living in water and so they come outside the lake to enjoying sunshine to keep them warm.

B. INDIRECT COUNTING METHODS

Information from Different Sources

Information has been collected by contacting field staff of Sindh Wildlife Department, local fishermen, field staff of Irrigation Department and other members of local communities.

ESTIMATION OF POPULATION

Strip Census

This method enables to estimate animal populations by counting animals along a pre-determined line of set length. The strip census method entails walking on a pre-determined line, counting the animals observed along line and recording the distance at which they are seen (Ahmed, 1988).

RESULTS AND DISCUSSION

THATTA DISTRICT

In the present study, four species of frogs, *Euphlyctis cyanophlyctis cyanophlyctis*, *Hoplobatrachus tigerinus*, *Tomopterna breviceps* and *Limnonectes limnocharis*, and two species of toads, *Bufo stomaticus* and *Bufo melanostictus* were recorded from Thatta district (see Table 3). *Euphlyctis cyanophlyctis cyanophlyctis* was rated as abundant, *Bufo stomaticus* as common, *Bufo melanostictus* as less common, while *Hoplobatrachus tigerinus*, *Tomopterna breviceps* and *Limnonectes limnocharis* were rated as rare.

In 2004, *Euphlyctis cyanophlyctis cyanophlyctis* was recorded as 35%, *Hoplobatrachus tigerinus* as 5%, *Tomopterna breviceps* as 4%, *Limnonectes limnocharis* as 2%, *Bufo stomaticus* as 29%, and *Bufo melanostictus* as 26% (see Table 5). In the year of 2005, *Euphlyctis cyanophlyctis cyanophlyctis* was recorded as 34%, *Hoplobatrachus tigerinus* as 4%, *Tomopterna breviceps* as 4%, *Limnonectes limnocharis* as 2%, *Bufo stomaticus* as 29%, and *Bufo melanostictus* as 27% (see Table 6). In the year of 2006, *Euphlyctis cyanophlyctis cyanophlyctis* was recorded as 36%, *Hoplobatrachus tigerinus* as 4%, *Tomopterna breviceps* as 3%, *Limnonectes limnocharis* as 1%, *Bufo stomaticus* as 30% while, *Bufo melanostictus* recorded as 26% (see Table 7).

KARACHI DISTRICT

Euphlyctis cyanophlyctis cyanophlyctis was rated as abundant, *Bufo stomaticus* as common, *Bufo melanostictus* as less common, while *Hoplobatrachus tigerinus* and *Tomopterna breviceps* as rare (see Table 4).

According to data, in 2004, *Euphlyctis cyanophlyctis cyanophlyctis* was recorded as 36%, *Hoplobatrachus tigerinus* as 1%, *Tomopterna breviceps* as 0.1%, *Bufo stomaticus* as 33%, and *Bufo melanostictus* as 30% (see Table 8). In the year of 2005, *Euphlyctis cyanophlyctis cyanophlyctis* was recorded as 35%, *Hoplobatrachus tigerinus* as 1%, *Tomopterna breviceps* as 0%, *Bufo stomaticus* as 33%, and *Bufo melanostictus* as 31% (see Table 9). In the year of 2006, *Euphlyctis cyanophlyctis cyanophlyctis* was recorded as 38%, *Hoplobatrachus tigerinus* as 1%, *Tomopterna breviceps* as 0%, *Bufo stomaticus* as 32%, and *Bufo melanostictus* as 29% (see Table 10).

In Thatta district, frogs and toads belonging to two families, five genera, and six species were recorded. During the study, *Euphlyctis cyanophlyctis cyanophlyctis* was recorded as having highest population percentage (35% in 2004, 34% in 2005 and 36% in 2006) among frog species in Thatta district. *Hoplobatrachus tigerinus* as 5% in 2004, 4% in 2005 and 2006. *Tomopterna breviceps* was recorded as 4% in 2004 and 2005, and 3% in 2006. *Limnonectes limnocharis* recorded as 2% in 2004, 2% in 2005 and 1% in 2006. While *Bufo stomaticus* was recorded as 29% in 2004 and 2005, 30% in 2006. *Bufo melanostictus* recorded as 26% in 2004, 27% in 2005 and 26% in 2006.

In Karachi district, four genera, and three species of frogs and two species of toads were recorded, among frog species *Euphlyctis cyanophlyctis cyanophlyctis* was recorded as having highest population percentage (36% in 2004, 35% in 2006 and 38% in 2006). *Hoplobatrachus tigerinus* recorded as 1% in 2004, 2005 and 2006. *Tomopterna breviceps* recorded as 0.1% in 2004, 0% in 2005 and 2006. While *Bufo stomaticus* was recorded as 33% in 2004, 2005 and 32% in 2006. *Bufo melanostictus* was recorded as 30% in 2004, 31% in 2005 and 29% in 2006.

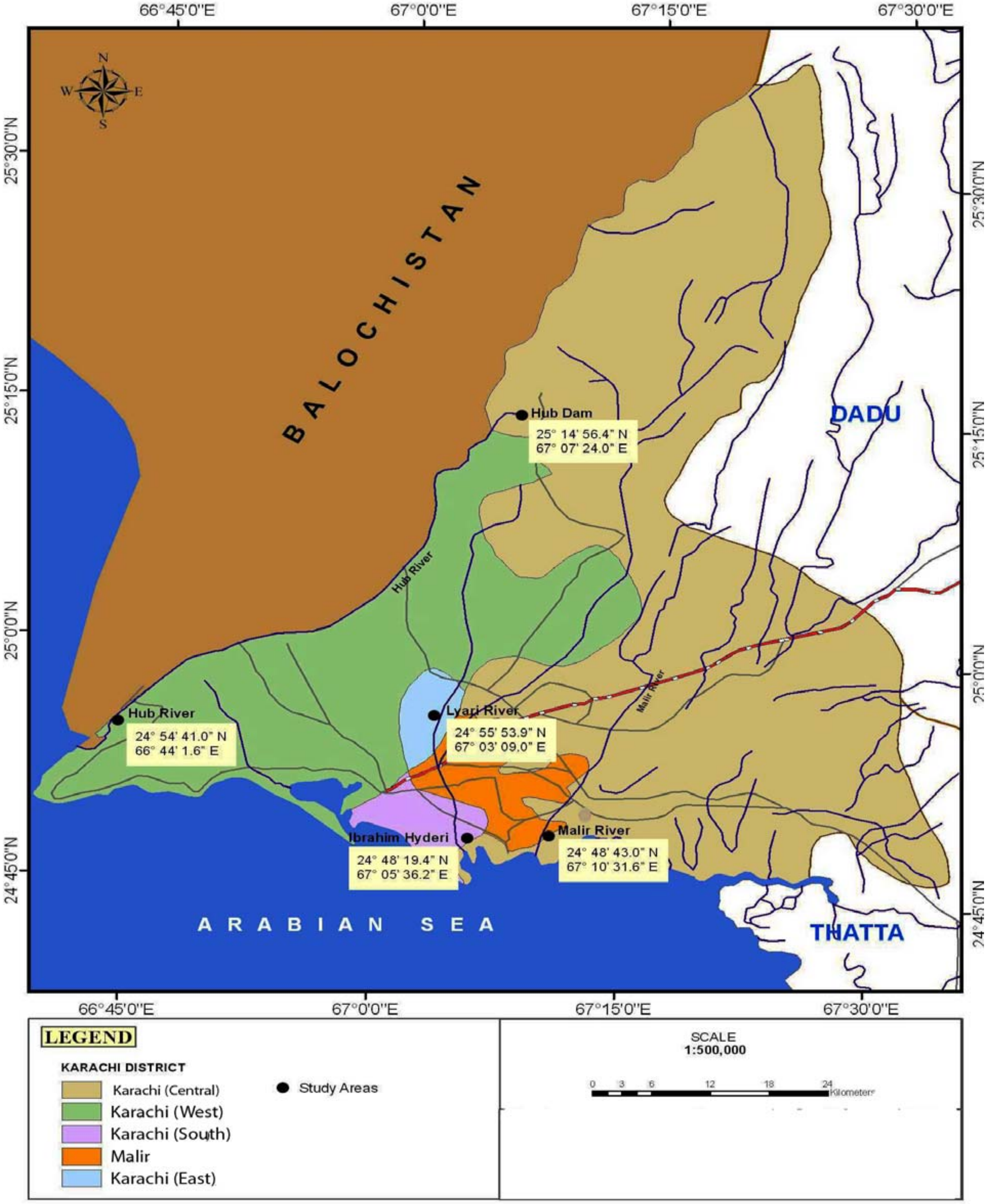

Fig. 2. Map showing Study Areas in Karachi District.

Table 3. List of Frogs and Toads recorded from Thatta District.

Family	Genus	Species	Common name
Bufonidae	*Bufo*	*Bufo melanostictus*	Common Asian Toad
		Bufo stomaticus	Marbled Toad
Ranidae	*Euphlyctis*	*Euphlyctis cyanophlictis cyanophlictis*	Common Skittering Frog
	Holobatrachus	*Holobatrachus tigerinus*	Tiger Frog
	Limnonectes	*Limnonectes limnocharis*	Indian Cricket Frog
	Tomopterna	*Tomopterna breviceps*	Indian Burrowing Frog

Table 4. List of Frogs and Toads recorded from Karachi District.

Family	Genus	Species	Common name
Bufonidae	*Bufo*	*Bufo melanostictus*	Common Asian Toad
		Bufo stomaticus	Marbled Toad
Ranidae	*Euphlyctis*	*Euphlyctis cyanophlictis cyanophlictis*	Common Skittering Frog
	Holobatrachus	*Holobatrachus tigerinus*	Tiger Frog
	Tomopterna	*Tomopterna breviceps*	Indian Burrowing Frog

Table 5. Population Distribution of Frogs and Toads in Thatta District -2004.

S N	Location	Observed Species							
1.		*Euphlyctis cynophlyctis cynophlyctis*	*Hoplobatrachus tigerinus*	*Tomopterna brevicep*	*Limnonectes limnocharis*	*Bufo stomaticus*	*Bufo melanostictus*	Total	%
2.	Thatta	210	26	23	19	198	183	659	22
3.	Mirpur Sakhro	67	8	4	5	64	57	205	7
4.	Ghora Bari	126	14	8	7	108	96	359	12
5.	Mirpur Bathoro	51	8	7	0	58	54	178	6
6.	Shah Bunder	97	14	13	0	90	78	292	10
7.	Jati	176	21	19	0	105	82	403	13
8.	Sujawal	189	24	21	11	122	117	484	16
9.	Kharo Chan	57	9	8	0	52	41	167	5
10.	Keti Bunder	106	14	12	9	96	74	311	10
	Total	1079	138	115	51	893	782	3058	
	%	35	5	4	2	29	26		

Due to habitat destruction, eutrophication, use of pesticides, chemical fertilizers, over grazing of aquatic vegetation and paucity of water, the populations of *Hoplobatrachus tigerinus, Tomopterna breviceps* and *Limnonectes limnocharis* have decreased. These species were recorded as rare in Thatta district while *Hoplobatrachus tigerinus* and *Tomopterna breviceps* were recorded as rare in Karachi district.

Based on present study results, *Euphlyctis cyanophlyctis cyanophlyctis* was the most common frog species in Karachi and Thatta districts, while *Bufo stomaticus* was the commonest toad, which was widely distributed in Karachi and Thatta districts. The population of *Euphlyctis cyanophlyctis cyanophlyctis, Bufo stomaticus* and *Bufo melanostictus* were higher than the other species of frogs and toads. So in spite of destruction of habitat and development of areas, there was no effect on their population, may be due to high tolerance against climate changes etc.

Due to habitat destruction and construction, *Hoplobatrachus tigerinus* was recorded as rare in Karachi district while, *Hoplobatrachus tigerinus*, *Tomopterna breviceps* and *Limnonectes limnocharis* were recorded as rare in Thatta District. The population status of *Tomopterna breviceps* was critical during three years of study in Karachi district. *Tomopterna breviceps* was recorded only once in 2004 in Karachi district

In Pakistan, frogs are extensively used for demonstration in schools, colleges and universities and experimentation in laboratories. Capture for biological research appears to have affected the local populations of frogs and toads.

Increased traffic on roads has contributed largely in the reduction of local population of common toads, *Bufo stomaticus.* Large number of amphibians, mainly toads, are crushed or mutilated by the passing traffic at night, thus affecting natural local populations (Khan, 1990).

Table 6. Population Distribution of Frogs and Toads in Thatta District -2005.

SN	Location	Observed Species							
		Euphlyctis cynophlyctis cynophlyctis	*Hoplobatrachus tigerinus*	*Tomopterna brevicep*	*Limnonectes limnocharis*	*Bufo stomaticus*	*Bufo melanostictus*	Total	%
1.	Thatta	184	23	19	16	147	136	525	16
2.	MirpurSakhro	101	11	9	6	92	86	305	9
3.	Ghora Bari	126	19	16	10	121	110	402	13
4.	Mirpur Bathoro	92	10	9	0	85	75	271	8
5.	Shah Bunder	105	12	11	0	90	84	302	9
6.	Jati	145	19	15	0	127	121	427	13
7.	Sujawal	156	21	17	15	132	130	471	15
8.	Kharo Chan	61	10	10	0	55	62	198	6
9.	Keti Bunder	112	15	15	9	95	82	328	10
	Total	1082	140	121	56	944	886	3229	
	%	34	4	4	2	29	27		

Table 7. Population Distribution of Frogs and Toads in Thatta District -2006.

SN	Location	Observed Species							
		Euphlyctis cynophlyctis cynophlyctis	*Hoplobatrachus tigerinus*	*Tomopterna brevicep*	*Limnonectes limnocharis*	*Bufo stomaticus*	*Bufo melanostictus*	Total	%
1.	Thatta	219	27	21	19	182	162	630	18
2.	Mirpur Sakhro	63	9	5	4	79	67	227	7
3.	Ghora Bari	138	17	9	6	118	106	394	12
4.	Mirpur Bathoro	61	8	7	0	81	72	229	7
5.	Shah Bunder	122	14	13	0	97	82	328	10
6.	Jati	185	19	16	0	125	110	455	13
7.	Sujawal	203	24	19	9	169	143	567	17
8.	Kharo Chan	59	9	7	0	67	51	193	6
9.	Keti Bunder	163	12	10	7	110	87	389	11
	Total	1213	139	107	45	1028	880	3412	
	%	36	4	3	1	30	26		

Table 8. Population Distribution of Frogs and Toads in Karachi District- 2004.

SN	Location	Observed Species						
		Euphlyctis cyanophlyctis cyanophlyctis	*Hoplobatrachus tigerinus*	*Tomopterna brevicep*	*Bufo stomaticus*	*Bufo melanostictus*	Total	%
1.	East	64	0	0	48	42	154	15
2.	West	82	3	0	79	75	239	23
3.	South	58	0	0	49	43	150	15
4.	Central	57	2	0	51	46	156	15
5.	Malir	112	8	1	107	98	326	32
	Total	373	13	1	334	304	1025	
	%	36	1	0.1	33	30		

On the basis of present study, it is concluded that due to habitat alteration, destruction of habitat, indiscriminate use of pesticides, utilization in experiments and increase in human population are major factors influcing on the populations of *Hoplobatrachus tigerinus*, *Tomopterna breviceps* and *Limnonectes limnocharis* populations.

Prior to the present study, no scientific data was available about the population, distribution and status of frogs and toads of Karachi and Thatta districts, and this is first scientific study to provide a baseline data. Hopefully, this study will serve as a springboard for further research, conservation, education and future management.

Table 9. Population Distribution of Frogs and Toads in Karachi District- 2005.

SN	Location	Observed Species						
		Euphlyctis cyanophlyctis cyanophlyctis	*Hoplobatrachus tigerinus*	*Tomopterna brevicep*	*Bufo stomaticus*	*Bufo melanostictus*	Total	%
1.	East	60	1	0	51	45	157	16
2.	West	79	1	0	80	75	235	24
3.	South	62	0	0	52	47	161	16
4.	Central	42	1	0	45	42	130	13
5.	Malir	103	10	0	97	99	309	31
	Total	346	13	0	325	308	992	
	%	35	1	0	33	31		

Table 10. Population Distribution of Frogs and Toads in Karachi District- 2006.

SN	Location	Observed Species						
		Euphlyctis cyanophlyctis cyanophlyctis	*Hoplobatrachus tigerinus*	*Tomopterna brevicep*	*Bufo stomaticus*	*Bufo melanostictus*	Total	%
1.	East	53	1	0	41	38	133	14
2.	West	90	2	0	78	68	238	25
3.	South	48	0	0	41	42	131	14
4.	Central	57	0	0	50	45	152	16
5.	Malir	122	6	0	97	89	314	32
	Total	370	9	0	307	282	968	
	%	38	1	0	32	29		

REFERENCES

Abdulali, H. 1985. On the export of frog legs from India. J. Bombay Nat. Hist. Soc. 2: 347-375.

Ahmed, MF. 1988. Wildlife estimation techniques. Records Zool. Sur. of Pak. 9:115-123.

Barry, SJ. and Shaffer, HB. 1994. The status of the California Tiger Salamander (*Ambystoma Californiense*) at lagunita a 50 years update. Journal of Herpetology. 28(2):159– 164.

Berrill, M., Bertram, S. and Pauli, B. 1997. Effects of pesticides on amphibian embryo and tadpoles. Herpetological Conservation. 1:233-245.

Berrill, M., Coulson. D., McGillivary, L. and Pauli, B. 1998. Toxicity of endosulfan to aquatic stages of anuran amphibians. Environ. Toxicol. Chem. 17:1738-1744.

Bogart, JP. 1992. Monitoring genetic diversity. Proceeding of a workshop on declines in Canadian amphibian populations. Designing a national monitoring strategy. Canadian Wildlife Service. 50-52.

Bridges, CM. 2000. Long-term effects of pesticide exposure at various life stages of Southern Leopard Frog (*Rana Sphenocephala*). Archives of Environmental Contamination and Toxicology. 39:91-96.

Conant, R. and Collins JT. 1998. Reptiles and amphibians of North America. (4th ed.). Houghton Mifflin Company. New York, USA.

DAPTF. 2001. Declining Amphibians Populations Task Force.

Didiuk, A. 1997. Status of amphibians in Saskatchewan. In: Amphibians in decline. Canadian studies of a global problem. Ed. Green, DM. Canadian studies of a global problem. SSAR, St. Louis, MO. 110-116.

Dubois, A. and Khan, MS. 1979. A new species of frog (Genus *Rana, Subgenus Paa*) from Northern Pakistan. J. Herpetol. 13:403-410.

Dupuis, LA. 1997. Effects of logging on terrestrial amphibians of costal British Colombia. In: Amphibians in decline. D. M. Ed. Green, DM. Canadian Studies of a global problem. SSAR, ST. Lovis. 185-190.

Fisher, RN. and Shaffer, HB. 1996. The decline of amphibians in California's Great Central Valley. Conserv. Biol. 10:1387 -1397.

Fox, CK., Fox, WM., Reaser, JK., Launer, AE. and Fee, C. 1997. California Tiger Salamanders: Threats in an urban landscape. Presented at the Society for Conservation Biology meetings June, Victoria, BC, Canada.

Green, DM. (Ed.). 1997). Amphibians is decline. Canadian studies of a global problem. Herpetol. Conserv. 1, SSAR, St. Lovis, MO. Xiv:338.

Hall, RT. and Henry, PFP. 1992. Assessing effects of pesticides on amphibians and reptiles. Herpetol. Jour. 2:65 -71.

Hora, SL. and Chopra, B. 1923. Reptilia and batrachia of Salt Range, Punjab. Rec. Ind. Mus. 25:369-376.

Iffat, F. 1994. Notes on the Collection of Amphibians in the Zoological Survey Department. Rec. Zool. Surv. Pakistan 12: 120-124.

IUCN. 2010. SSC Red List. www.iucnredlist.org.

Jacques, M. 1999. Bengali frog legs export and uses of pesticides. TED case studies N.http:/www.american.edu/projects/mandala/TED/bangfrog.htm 9(1):508.

Khan, MS. 1987. Checklist, distribution and zoogeographical affinities of herpetofauna of Balochistan. Proc. Pakistan Zool. Congr. 7:105-112.

Khan, MS. 1990. The impact of human activity on the status and distribution of amphibians in Pakistan. Hamadryad. 15:21-24.

Khan, MS. 1997. A new subspecies of Common Skittering Frog (*Euphylyctis cyanophylctis*) (Schneider, 1799) from Balochistan, Pakistan. Pakistan J. Zool. 29(2):107-112.

Khan, MS. 1999. Herpetology of habitat types of Pakistan. Pakistan J. Print J. 14:17-20.

Khan, MS. 2000. Sar Zameen-a-Pakistan kay maindak aur Khazinday (frogs and lizards of Pakistan). Urdu Science Board, 299 Upper Mall, Lahore, Pakistan.

Khan, MS. 2001. Notes on Cranial Ridged Toads of Pakistan and description of a new subspecies (Amphibia: Bufonidae). Pakistan J. Zool. 33(4):293-298.

Khan, MS. 2003. Morphology of riparian tadpoles: *Euphlyctis cyanophlyctis* (Schneider, 1799) Bulletin of the Chicago Herpetological Society: 38(5):95-98.

Khan, MS. and Khan, AQ. 2000. Species richness of terrestrial vertebrates of Pakistan. Pak. J. Zool. 32(3):193-199.

Khan, MZ. and Law, FCP. 2005. Adverse effects of pesticides and related chemicals on enzyme and hormone systems of fish, amphibians and reptiles. Proc. Pakistan Acad. Sci. 42(4):315-323**.**

Khan, MZ. and Yasmeen, G. 2008. Effect of sandaphos and β-cypermethrin exposure on Cholinesterase and Alkaline phosphatase activity in liver, kidney and brain of *Euphlyctis cyanophlyctis*. Canadian Journal of Pure and Applied Sciences. 2(3):511-519.

Lannoo, MJ. 1998. Amphibian conservation and wetland management in the upper midwest a catch 22 for the cricket frog. In: Status and conservation of Midwestern Amphibians. Ed. Lanoo MJ. Iowa City Lowa, University of Iowa Press. 330 -339.

Marantelli, G. and Parkes, H. 1998. Chytridiomycosis causes amphibian mortality associated with population declines in the rainforests of Australia and Central America. National Academy Science. 95: 9031-9036.

Martin, RE. 2000. Other aquatic life of economic significance: Frogs and frog legs. In: Marine and freshwater products handbook. Eds. Martin, EP., Flick, GJJ. and Davis, LM. Lancaster, Technomic. Pub. Con. Inc. 279-287.

Ovaska, K. 1997. Vulnerability of amphibians in Canada to global warming and increased solar ultraviolet radiation. 206-225.

Pandian, TJ. and Marian, MP. 1986. Production and utilization of frog: an ecological view. Proc. Indian Acad. Sci. 95(3):289-301.

Pechmann. JHK. and Wilbur, HM. 1994. Putting declining amphibian populations in perspective: Natural fluctuations and human impacts. Herpetologica. 50:65-84.

Rabb, GB. 1999. The amphibians decline phenomenon. Chicago Zoological Society, Brookfield. II.

Waldick, R. 1997. Effects of forestry practice on amphibians populations in Eastern North America. In: Amphibians in decline. Ed. Green, DM. Canadian studies of a global problem. SSAR, ST. Louis, MO. 191- 205.

Yasmeen, G., Khan, MZ. and Akbar, A. 2009. A Study of the induced effect of β-Cypermethrin on the skin of *Euphlyctis cyanophlyctis*. Canadian Journal of Pure and Applied Sciences. 3(3):937-941.

Received: March 16, 2010; Revised: Sept 27, 2010;
Accepted: Sept 30, 2010

SENRA Academic Publishers, Burnaby, British Columbia
Vol. 4, No. 3, pp. 1267-1274, October 2010
Online ISSN: 1920-3853; Print ISSN: 1715-9997

Canadian Journal of pure&applied sciences

APPLICATION OF ABLATIVE LASER DEPTH-PROFILING (ICP-MS) TO PROBE DIAGENETIC INFORMATION LINKED TO SECONDARY MINERAL DEPOSITION IN CARBONATE RESERVOIR ROCK – PART 2

B Ghosh[1], *AE Pillay[2], SS Kundu[1], B Senthilmurugan[1] and S Stephen[2]
[1]Department of Petroleum Engineering, [2] Department of Chemistry
The Petroleum Institute, PO Box 2533, Abu Dhabi, UAE

ABSTRACT

Laser depth-profiling is a valuable tool for unraveling the complexities of subterranean diagenetic processes and post-depositional change associated with carbonate reservoirs. Core fragments were subjected to high-performance ICP-MS laser irradiation (213nm) at several ablation points to depths of 50µm at 10µm intervals. The method is convenient and adequately competent to study diagenetic phenomena of carbonates. It is capable of estimating the dimensions of pore spaces and grain-size distribution in carbonate reservoir rock and shedding light on sedimentary dolomitic-limestone trends within the matrix. Spectral evidence of secondary deposition and co-habitation of strontium and iron due to secondary fluid inclusions was observed at matrix grain boundaries. The application was successful in exploring the internal microstructure of carbonate cores and providing clues linked to certain aspects of pore sizes. The study is of relevance to geologists, reservoir engineers and petro-physicists and can be useful in geostatistical modeling and simulation.

Keywords: Diagenesis, laser ablation, ICP-MS, mineral-deposition, carbonate-rock.

INTRODUCTION

Carbonate oil fields can be generally classified into sedimentary limestone [calcium carbonate/calcite, $CaCO_3$] and dolomite [calcium-magnesium carbonate, $CaMg(CO_3)_2$] reservoirs. Limestone that is partially replaced by dolomite is referred to as dolomitic limestone or magnesian limestone. Carbonate sediments are mostly biological in origin and their features (grain size and sorting) depend largely on the population of the subsisting organism. Intense primeval chemical reactivity of carbonates led to early diagenesis, dissolution and cementation under the influence of meteoric water, pressure and temperature which jointly resulted in complexities in pore type and structure (Pedersen, 1993; Stewart *et al*., 2000; Wilkinson and Haszeldine, 1998). Unraveling and interpreting such complexities is remarkably challenging and forms the basis of understanding fluid flow through porous media (Pedersen and Bjorlykke, 1994; Mclimans, 1987; Haszeldine *et al*., 2000). The pore fluid itself comprises multiple chemical components which intermittently precipitate and re-dissolve under certain conditions of temperature and pressure. The analysis of embedded elements linked to minerals and salts in host rock matrices gives useful information on the diagenetic characteristics of oil-bearing reservoir rocks and also provides significant details on the conditions of mineral growth. Some chemical compounds such as strontium and iron bearing salts enter the calcite matrix through secondary fluid inclusions. Therefore, a detailed knowledge of fluid inclusion chemistry would be helpful to develop sustainable petrophysical models for inveterate rock deposits (Pedersen and Bjorlykke, 1994; Haszeldine *et al*., 2000). Often inclusions are filled with aqueous fluids and brine laden with low-solubility minerals and salts (containing metals such as Mg, Sr, Fe, Ba) that deposit as secondary sediments under favorable physical and chemical conditions deep within the rock itself (Pedersen, 1993). Of significance is that the diagenesis process in carbonate systems tend to occur mainly in two major realms: shallow water and normal marine diagenetic environments (Stewart *et al*., 2000; Wilkinson and Haszeldine, 1998). Generally, meteoric water is strongly acidic and understaurated with $CaCO_3$, and thus has the capacity to dissolve carbonates and cause precipitation elsewhere. This sediment-water reaction also leads to precipitation of metal impregnated salts which provide important clues to diagenetic phenomena linked to meteoric water environments (Touret, 2001).

Depth profiling of reservoir cores by laser ablation ICP-MS (Inductively Coupled Plasma-Mass Spectrometry) is fast emerging as a useful contemporary tool for extracting valuable information on diagenetic phenomena and internal elemental profiles (Sunderlin, 2009). The application uses a micro-beam to ablate samples in a special sample chamber. The fine ablated material is

---

*Corresponding author email: apillay@pi.ac.ae

rapidly transported to hot plasma by a carrier gas (argon). The extremely high temperature of the plasma (about 10,000K) separates the sample into individual atoms, which are ionized ($M \rightarrow M^+ + e-$) and detected by the mass spectrometer. The technique is highly sensitive and can attain a limit of detection in the parts per trillion range (10^{-6} mg/kg) for most elements. Due to its superior sensitivity, LA-ICP-MS has gained popularity in mineralogical and ore analysis and has been reported to be faster and more accurate than most other techniques. The aim of our work, therefore, was to explore the potential of ablative laser technology to rapidly track specific elemental profiles (magnesium, iron and strontium) within carbonate core sections and examine diagenetic phenomena and post-depositional trends linked to these elements.

MATERIALS AND METHODS

Instrumentation / Sample handling

Samples were investigated with a Perkin Elmer SCIEX DRC-e ICP-MS fitted with a New Wave UP-213 laser ablation system. Core fragments (Fig. 1) were subjected to 213-nm laser irradiation at random points on each sample. The level of the beam energy was 30%, with a fluence of approximately 3 J/cm^2 and beam diameter of 100µm. The laser was programmed to ablate a depth of 10µm at each point and repeatedly scanned the surface, recording measurements after each ablation to a total depth of 50µm. The study was largely semi-quantitative in the absence of standardization, and for comparative purposes all measurements were conducted under identical experimental conditions. Prior to each run the instrument underwent appropriate calibration (certification) and correction for background (Jarvis *et al.*, 1992; Robinson *et al.*, 2005). Depth-profiling spectra were recorded for each measurement. It is necessary to underscore that in the absence of matching-matrix standards our method was based on evaluating relative intensities (counts/sec) for purposes of comparison. Further details of sampling and instrumentation are reported elsewhere (Pillay *et al.*, 2010).

RESULTS AND DISCUSSION

Diagenesis and reservoir rock

Diagenesis of sedimentary rock is a series of post-depositional processes involving marked physical and chemical transformation of sedimentary rock over a period of time (Pedersen, 1993; Wilkinson and Haszeldine, 1998). Compacted sediments formed from primeval precipitation (deposition) from subterranean streams and salty water can undergo post-depositional change (or diagenesis) resulting in the blockage of pores and pore throats. Figure 2 represents a cross-section of a typical sedimentary rock fragment showing the fundamental components and features within the structure (Petr, 2009). Such rock must be both permeable and porous to permit passage of the fluids. It comprises outlying cementitious areas (where chemicals form), sedimentary clays, compacted fossils and pore spaces usually filled with brine (fluid inclusions). Diagenesis linked to reservoir rock is of significance because it tends to decrease the porosity of the rock and reduces the volume of hydrocarbons that it can hold (Mclimans, 1987; Wilkinson and Haszeldine, 1998). A good example is the precipitation of magnesite ($MgCO_3$) from underground brine and subsurface fluid that blocks the pores, thus restricting the flow of petroleum through the rock. A diagenetic change like this also leads to entrapment of magnesium inside the calcite lattice through fluid incursions. In addition, certain compounds originating from Paleolithic fossils could be incorporated as part of the calcite deposition, creating agglomerates that gradually fill the porous regions (Saigal *et al.*, 1992). Petrologists study the permeability of source rock and are concerned with physical and chemical changes in the rock environment that produce irregular dissolution and deposition processes that limit permeability. Laser depth profiling of subsurface cores provides valuable evidence of diagenetic changes of this nature, which could be ultimately linked to petroleum production.

Pore spaces, grain boundaries and secondary deposition

Depth profiling is capable of estimating the dimensions of ensconced pore spaces and providing an insight into secondary deposition processes. Typical depth-profiling plots of several core fragments depicting significant features of the study appear in figures 3 to 6 Each figure represents Mg, Sr and Fe spectra superimposed on a Ca spectrum (to identify their position on the matrix structure) taken from a common ablation point on the same core-section. The blue spectra in each figure represent the Ca substrate ($CaCO_3$) and the red spectra correspond to Mg, Sr and Fe intensities (originating from relevant deposits). The penetration of the laser 50 µm from the irradiated surface into the core produced fluctuating elemental intensities that are clearly visible in figures 3 to 6. The recorded spectra portray strong, medium and weak peaks of the metals of interest interspersed by significant breaks or gaps in between the lines corresponding roughly to depths of 5µm in most cases. Prominent Ca lines suggest the impact of the laser into the heart of a calcite grain, whereas diminished Ca lines could reflect grain boundaries (Haszeldine *et al.*, 2000). These features are clearly seen in figures 3A to 6A where the general trend depicts a pattern of strong and intermediate Ca lines at a depth of 5µm from the irradiated surface or at the surface itself. Subsequent Ca peaks appear at recurring depths of about 3-10µm representing calcite grains followed by spectral voids of roughly 5µm reflecting inter-granular pore spaces (primary porosity – Fig. 2) (Chaika, 2000). These spectral voids corresponding to diminished Ca intensities seem to be fairly uniform indicating homogeneous pore size distribution (especially prominent in Figs. 4A and 5A). Spectral voids < 5μm could be ascribed to minor intra-granular pore spaces (secondary porosity – Fig. 2). The intrinsic variation of the spectral features is expected and is due to irregularity of grain size generally encountered in limestone rock. It could also be due to the possibility of the laser beam passing through the edge of some of the grains (see Fig. 2). Superimposition of Mg spectra on Ca spectra (Figs. 3A to 6A) delineate concomitant occurrence of Mg and Ca distinctly suggesting the presence of Mg within the calcite grain. This phenomenon further suggests that during the diagenetic process sedimentary dolomitic limestones possibly originated during magnesian calcite dissolution, followed by calcite and dolomite precipitation reactions (Wilkinson and Haszeldine, 1998). Alternatively, these dolomitic limestones could have resulted from the dissolution and subsequent deposition of calcium carbonate precursors in the presence of magnesium ions. Peaks representing Mg at the origin of the relevant spectra (corresponding to 0-5μm depth in figures 3A to 6A) were identified as part of the Ca grain boundary; while other Mg peaks appearing in the spaces where Ca was almost absent were ascribed to entrapment in the calcite lattice (Saigal, 1992). These

Fig. 1. Fragments of core plugs used in investigation.

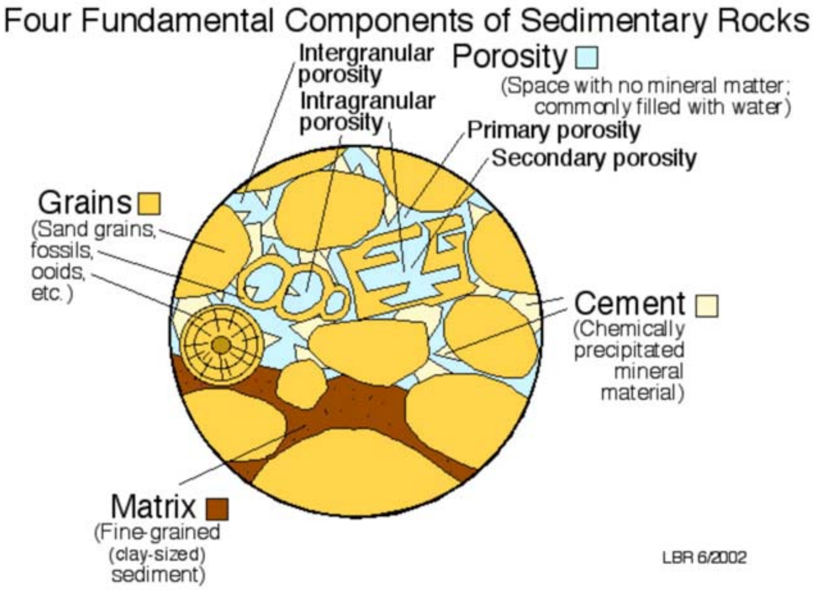

Fig. 2. The fundamental micro-features of a rock fragment.

deposits could be attributed to potential secondary deposition processes in the presence of fluid inclusions and incursions.

Fluid inclusions and co-deposition

One form of diagenetic change arises when the calcite matrix is overlaid with Sr and Fe deposits originating from fossils and fluid inclusions rich in aquifer brine containing these elements. In subterranean environments it is well known that certain physical and chemical conditions exist within reservoir rock that lead to precipitation of metal salts with low solubilities (such as $SrSO_4$ and $Fe(OH)_3$), and formation of post-depositional layers on the primeval calcite matrix (Wilkinson and Haszeldine, 1998). More than one metal salt can co-precipitate this way and a study of our experimental data revealed evidence of co-deposition. Typical depth-profiling spectra of Sr and Fe, (Figs. 3B, 4B, 6B & 3C, 4C, 6C) clearly show that Sr deposits tend to be more prolific in the pore area where Ca is virtually absent. It is reasonable to assume that this phenomenon is related to post-depositional growths from fluid inclusions rich in Sr

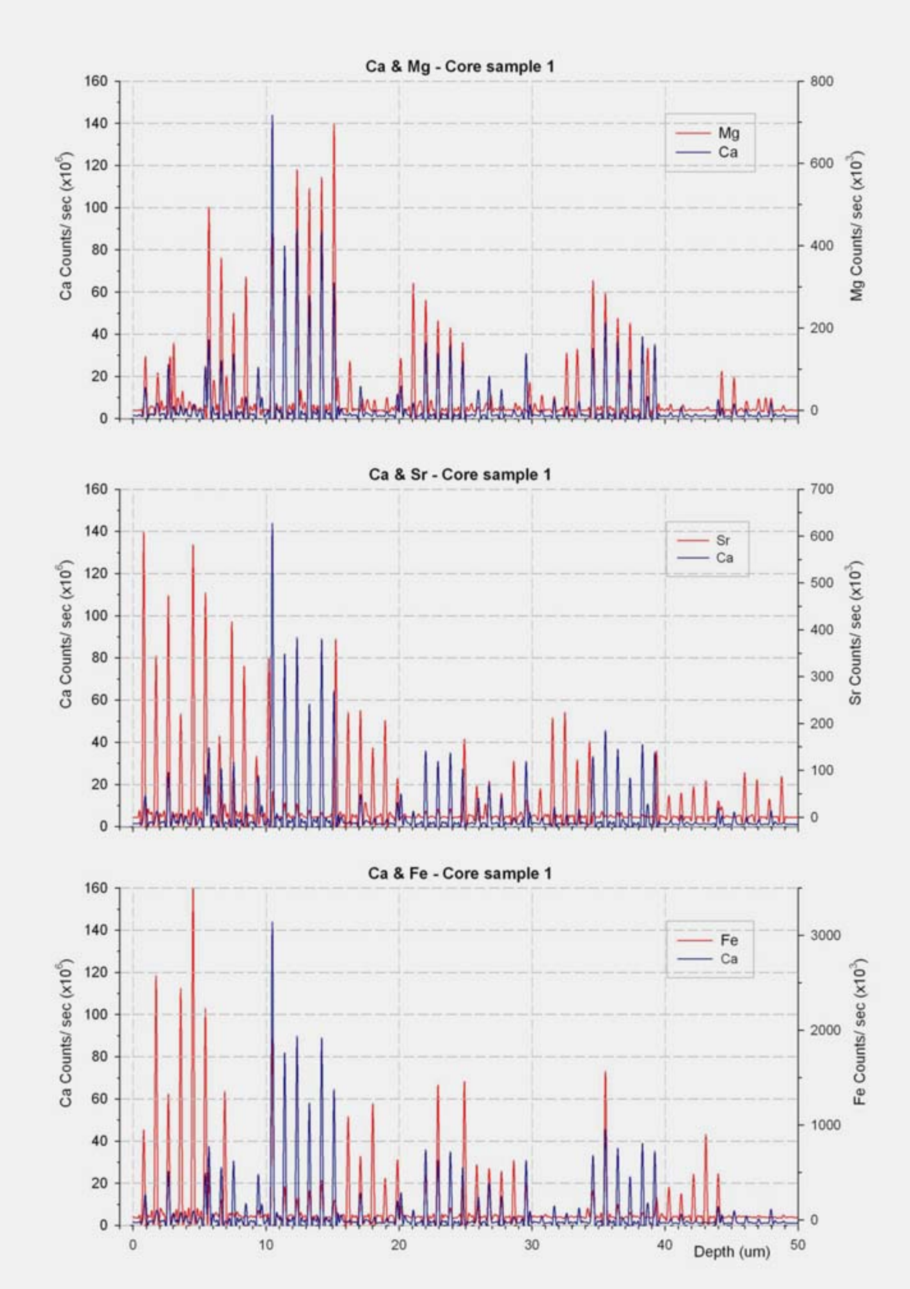

Fig. 3. LA-ICP-MS depth-profiling of Mg, Sr and Fe superimposed on Ca (core-fragment #1).

and Fe because their presence is pronounced at the grain boundaries bordering pore spaces (Bjorlykke, 1993; Kvenvolden and Roedder, 1971). However, at points where the pore fluid made inroads into the matrix itself ingrained deposits of Sr and Fe appear. This particular feature is strongly corroborated in figures 5B and 5C where Sr and Fe peaks are barely separable from Ca peaks, indicating potential co-habitation in the calcite matrix. A point to note is that the experimental data indirectly revealed that for diagenetic change and post-depositional formation of this nature to have transpired favorable conditions must have existed deep within the rock structure (Stewart, 2000).

Impact of our findings

The diagenetic features of reservoir rock are a record of its geological (and paleontological) histories and are inextricably linked to reservoir quality (Stewart, 2000). The diagenetic history of source rock usually determines the formation and migration of petroleum and availability of pore space during oil emplacement (Saigal, 1992). Of significance is that the diagenesis pattern can vary from one limestone to another both laterally and vertically within the same structure and depends largely on pore-fluid chemistry, subterranean temperature/pressure, pore flow rates, mineral and biogenic composition (Pedersen, 1993). During such processes the major events that form

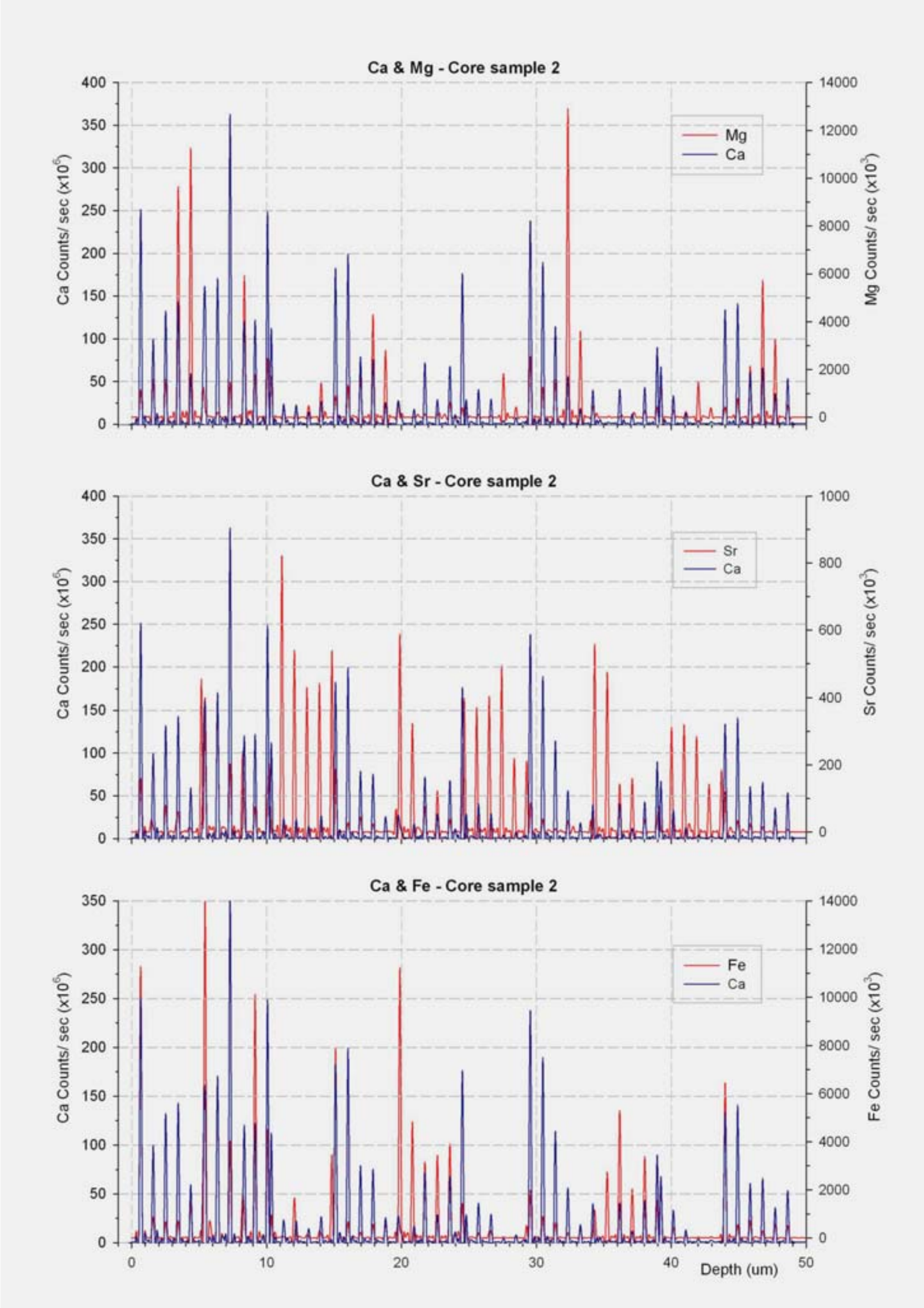

Fig. 4. LA-ICP-MS depth-profiling of Mg, Sr and Fe superimposed on Ca (core-fragment #2).

the rock are cementation of loose sediment to solid rock, dissolution of minerals leading to formation of pores and re-crystallization of various rock components (Fig. 2). In figures 3A and 6A, for example, the phenomenon of cementation was clearly visible in the first 5 µm where the intensities of Mg outweighed the Ca intensities suggesting cementation of loosely bound Mg deposits on the edge of the calcite matrix abutting pore spaces (Wilkinson and Haszeldine, 1998). On the other hand the precipitous trend of Sr peaks (Figs. 3B, 4B and 6B) in the 'pore spaces' reflecting sharp fluctuations in intensities tend to suggest intermittent dissolution and re-crystallization processes. Similar trends were observed for Fe (Figs. 3C, 4C, 6C). Furthermore, figure 5 (A, B, C) is a good example of ingrained deposits, where Mg, Sr and Fe peaks occur concomitantly with Ca in the core sample between 10-40µm, delineating the porous nature of the matrix that permits fluid infiltration and crystal growth. Such growths and deposits could contribute to reduction of porosity and permeability of an oil reservoir (Chaika, 2000).

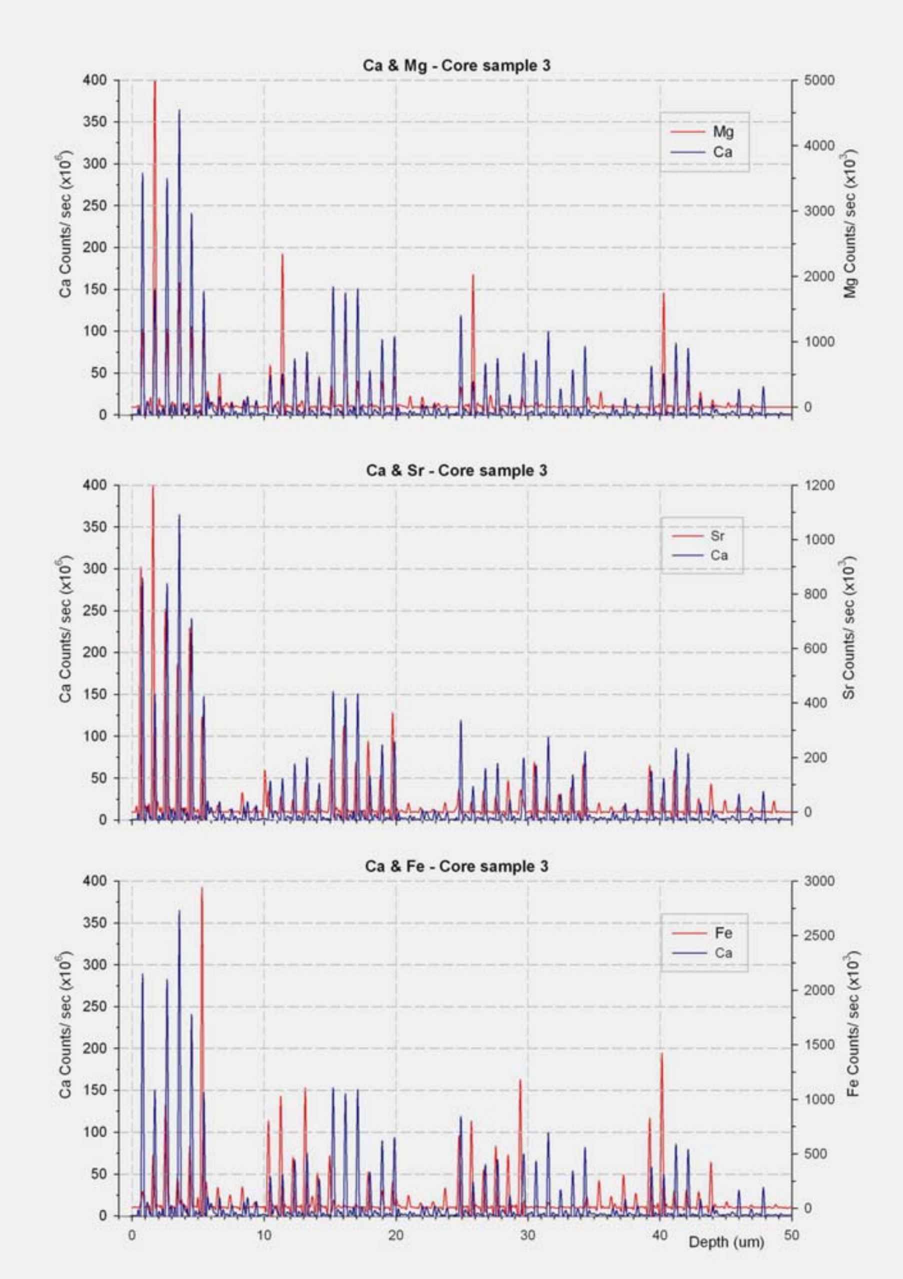

Fig. 5. LA-ICP-MS depth-profiling of Mg, Sr and Fe superimposed on Ca (core-fragment #3).

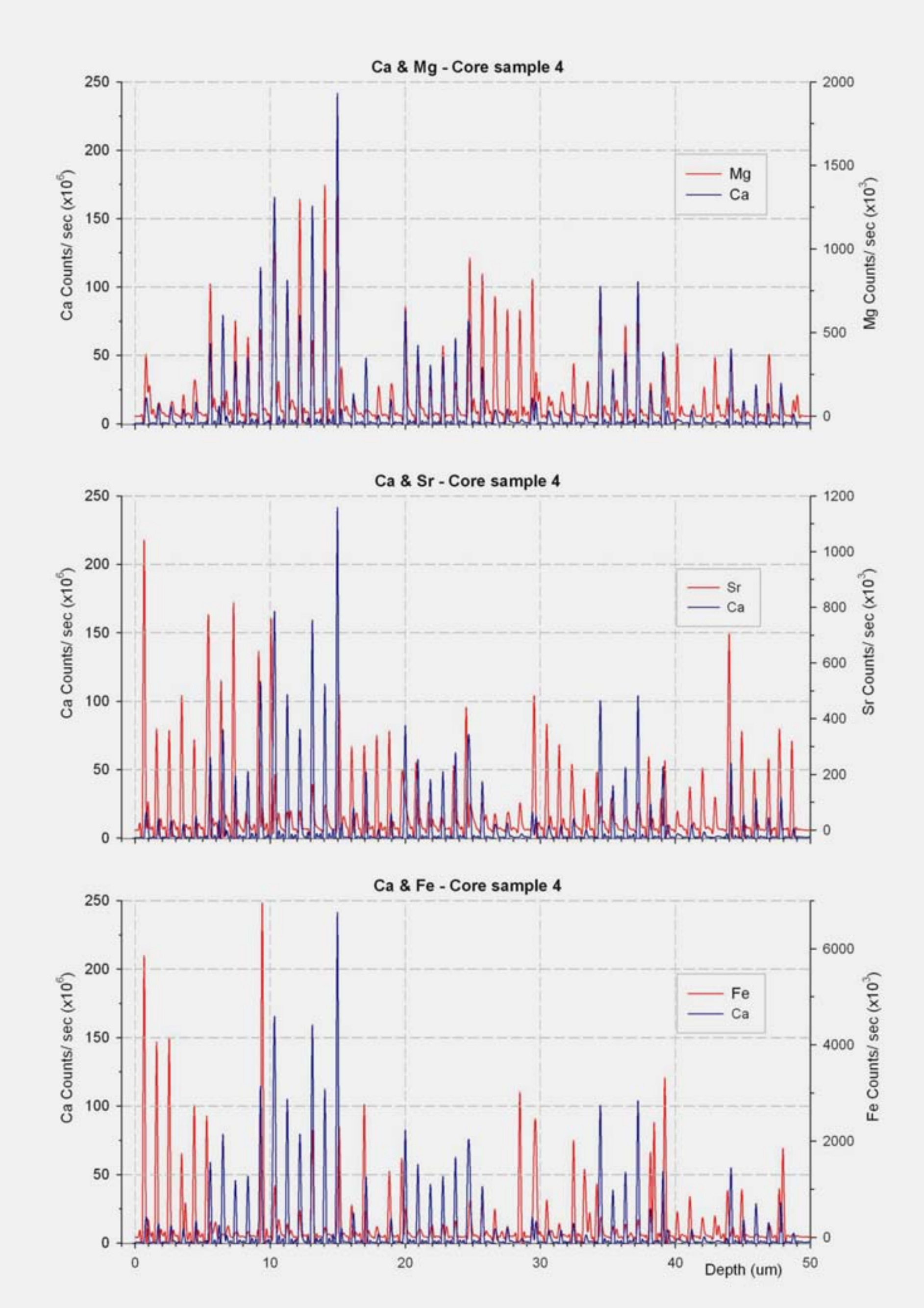

Fig. 6. LA-ICP-MS depth-profiling of Mg, Sr and Fe superimposed on Ca (core-fragment #4).

CONCLUSIONS

The laser technique has the unique capability of creating 'micro-channels' through the matrix of reservoir rock and unearthing hidden information of geological importance. Such information is difficult to extract from other contemporary methods such as SEM and XRD and highlights the pre-eminent nature of depth profiling. Our research has provided an insight into diagenetic processes in carbonate reservoir cores and a suitable extension of this study would be to apply the data in modeling and simulation studies associated with geosciences and petrophysics.

ACKNOWLEDGEMENTS

The authors would like to thank the Petroleum Institute for financial assistance. The authors would also like to thank Mr. M. Bhattacharya, Senior Geologist, KOC for his suggestions.

REFERENCES

Bjørlykke, K. 1993. Fluid flow in sedimentary basin. Sedimentary Geology. 86:137-158.

Chaika, C. and Dvorkin, J. 2000. Porosity reduction during diagenesis of diatomaceous rocks. AAPG Bulletin. 84:1173-1184.

Haszeldine, RS., Macaulay, CI., Marchand, A., Wilkinson, M., Graham, CM., Cavanagh, A., Fallick, AE. and Couples, GD. 2000. Sandstone cementation and fluids in hydrocarbon basins. Journal of Geochemical exploration. 69:195-200.

Jarvis, KE., Gray, AL. and Houk, RS.1992. Handbook of ICP-MS, Blackie Publishers, London, UK.

Kvenvolden, KA. and Roedder, E. 1971. Fluid inclusions in quartz crystals from southwest Africa. Geochim. Cosmochimica Acta. 35:1209-1229.

Mclimans, RK.1987. The application of fluid inclusions to migration of oil and diagenesis in petroleum reservoirs. Applied Geochemistry. 2:585-603.

Pedersen, K.1993. The deep subterranean biosphere. Earth Sci. Reviews. 34:243-260.

Pedersen, P. and Bjørlykke, K. 1994. Fluid flow in sedimentary Basins: model of pore water flow in a vertical fracture. Basin Research. 6:1-16.

Pillay, AE., Ghosh, B., Senthilmurugan, B., Stephen, S. and Abd-Elhameed A. 2010. Ablative laser depth profiling (ICP-MS) of reservoir cores to evaluate homogeneity of strontium and barium distributions linked to scale deposition. Canadian Journal of Pure and Applied Sciences. 4:1081-1085.

Qi, L., Hu, J. and Gregoire, DC. 2000. Determination of trace elements in granites by inductively coupled plasma mass-spectrometry. Talanta. 51:507-513.

Petr.http://infohost.nmt.edu/~petro/faculty/Adam%20H.%20571/PETR%20571-Week3notes.pdf. Accessed: 2009

Robinson, JW., Skelly-Frame, EM. and Frame, GM. 2005. Undergraduate Instrumental Analysis, Marcel Dekker, New York, USA.

Saigal, GC., Bjørlykke, K. and Larter, S. 1992. The Effects of oil Emplacements on Diagenetic Processes-Examples from the Fulmar Reservoir sandstones, Central North Sea. AAPG Bulletin. 76:1024-103.

Stewart, RNT., Haszeldine, RS., Fallick, AE., Wilkinson, M. and Macaulay, CI. 2000. Regional distribution of diagenetic carbonate cement in Paleocene deepwater sandstones: North Sea. Clay Minerals. 35:119-133.

Sunderlin, K. http://keckgeology.org/files/pdf/symvol/15th/ohio/sunderlin.pdf. Accessed 2009.

Touret, JLR. 2001. Fluids in metamorphic rocks. Lithos. 55:1-25.

Wilkinson, M. and Haszeldine, RS. 1998. Discussion: Diagenesis: a short (2 million year) story- Miocene sandstones of Central Sumatra, Indonesia. Journal of Sedimentary Research. A68:231-234.

Received: June 10, 2010; August 26, 2010

SENRA Academic Publishers, Burnaby, British Columbia
Vol. 4, No. 3, pp. 1275-1281, October 2010
Online ISSN: 1920-3853; Print ISSN: 1715-9997

Canadian Journal of pure&applied sciences

RIVER DISCHARGE PREDICTION USING ARTIFICAL NEURAL NETWORK

*Archana Chowdhary[1] and R K Shrivastava[2]
[1]Civil Engg Deptt IES IPS Academy Indore
[2]SGSITS, Indore, India

ABSTRACT

The research described in this article investigates the utility of Artificial Neural Networks (ANNs) for predicting the daily river discharge. The work explores the capabilities of ANNs and compares the performance of Feed Forward Neural Network (FFNNS) and Radial Basis Function (RBF) network. Perceived strengths of ANNS are the capability for representing complex, non linear relationships as well as being able to model interaction effects. The application of the ANN approach is to a portion of Seonath River in Chhattisgarh and forecasting was conducted using daily records. ANN technique shows an enhancement of prediction capabilities & reduces the over fitting problem of neural networks. The results show that the ANN technique can be used to extract information from the data & to describe the non-linearity of river discharge.

Keywords: Artificial neural network, radial basis function, regression analysis.

INTRODUCTION

Many of the activities associated with the planning and operation of the components of a water resource system require forecast of future events. For the hydrologic components, there is a need for both short term and long term forecasts of streamflow events, discharge in order to optimize the system or to plan for future expansion or reduction. Many of these systems are large in spatial extent and have a hydrometric data collection network that is very sparse. These conditions can result in considerable uncertainty in the hydrologic information that is available.

Furthermore, the inherently non-linear relationships between input and output variables complicate attempts to forecast streamflow events. There is thus a need for improvement in forecasting techniques. Many of the techniques currently used in modelling hydrological time-series and generating synthetic streamflow assume linear relationships amongst the variables. The two main group of techniques include physically based conceptual models time-series models. Techniques in the first group are specifically designed to mathematically simulate the sub-processes and physical mechanisms that govern the hydrological cycle. These models usually incorporate simplified forms of physical laws and are generally non-linear, time-invariant, and deterministic, with parameters that are representative of watershed characteristics (Hsu *et al.*,1995) but ignore the spatially distributed, time-varying, and stochastic properties of the rainfall runoff (R-R) process. Kitanidis and Bras (1980[a,b]) state that conceptual watershed model is reliable in forecasting the most important features of the hydrograph. However, the implementation and calibration of such a model can typically present various difficulties (Duan *et al.*, 1992), requiring sophisticated mathematical tools (Duan *et al.*, 1992, 1994; Sorooshian *et al.*,1993), significant amount of calibration data (Yapo *et al.*, 1996) and some degree of expertise and experience with the models (Hsu *et al.*,1995).The problem with the conceptual models is that empirical regularities or periodicities are not always evident and can often be masked by noise.

Currently, environmental prediction and modelling includes a variety of approaches, such as rainfall-runoff modelling or statistical techniques, which entail exogenous input together with a number of assumptions. Conventional numerical modelling addresses the physical problem by solving a highly- coupled, non- linear, partial differential equation set which demands huge computing cost and time. However, physical processes affecting flooding occurrence can be highly complex and uncertain, and can be difficult to capture in some form of deterministic or statistical model.

In time-series analysis, stochastic or time-series model are fitted to one or more of the time-series describing the system for purpose which include forecasting, generating synthetic sequences for use in simulation studies, and investigating and modelling the underlying characteristics of the system under study. Most of the time-series modelling procedures fall within the framework of multivariate autoregressive moving average (ARMA) models (Raman and Sunil Kumar, 1995). Traditionally, the class of ARMA models has been the statistical method

---

*Corresponding author email: archanakeertichowdhary@yahoo.co.in

most widely used for modelling water resource time-series (Maier and Dandy, 1996). In streamflow forecasting, time-series models are used to describe the stochastic structure of the time sequence of streamflows and precipitation values measured over time. Time-series models are more practical then conceptual models because one is not required to understand the internal structure of the physical processes that are taking place in the system being modeled. The limitation of univariate time-series methods in streamflow forecasting is that the only information they incorporate is that which is present in past flows. Many of the available techniques are deficient in that they do not attempt to represent non-linear dynamics inherent in the transformation of rainfall to runoff.

Therefore a relatively new, improved and efficient soft computing technique such as Artificial Neural Networks (ANNs) is used in this study to overcome the above-mentioned problems. The distinguishing feature of the ANN based hydrological model is the use of the capability of ANNs to approximate virtually any continuous function up to an arbitrary degree of accuracy which is not otherwise true of other conventional hydrological techniques (Hornik *et al*., 1989). Very often, in hydrology, the problems are not clearly understood or are too ill-defined for a meaningful analysis using physically based methods. Even when such models are available, they have to rely on nonlinear rainfall- runoff modelling assumptions that make ANNs seem more attractive. It provides one alternative to hydrological time-series modelling.

This study has the following objectives:

1. To analyze historical flow data for the River Seonath and to test its suitability for streamflow/flood forecasting.
2. To develop an improved and efficient streamflow/flood forecasting model using feed forward neural networks (FFNNs) and radial basis function neural networks (RBFNNs).

A number of flood/ streamflow forecasting studies have been undertaken throughout the world, using various techniques. Among these techniques, conventional auto-regressive integrated moving average (ARIMA) models and ANNs have been extensively applied. The following paragraphs describe major flood/streamflow forecasting studies using these techniques. Bhattacharya and Solomatine (2000) have used an ANN to model the stage-discharge relationship at the Swarupgunj gauging station on the Bhagirathi River in India. They concluded that the percentage error of the ANN output for all ranges of data sets was less compared to that of conventional models like auto-regressive integrated moving average (ARIMA) techniques. Birkundavyi *et al*. (2002) have used feed forward multi-layer perceptron neural networks as predictors for daily streamflow forecasting up to 7 days of lead- time at a Mistassibi River station in Canada. Furthermore they noticed that the reliability value does not depend upon the ANN structure and the input data. Burian *et al*. (2001) have trained artificial neural networks to perform disaggregation of rainfall data from three gauging stations in Alabama, USA. The study concluded that using 20 or 50 hidden neurons would produce accurate results as compared to ANNs with 4 hidden neurons. Coulibaly *et al*. (2001) applied temporal neural networks to predict multivariate time-series, specifically for hydropower reservoir inflow at the Chute-du-Diable watershed, in Canada. It was found that the Elman recurrent neural network (RNN) was more efficient than any of the other models for short term reservoir inflow forecasting. Elshorbagy *et al*. (2001) explored the applicability of chaos theory to find the segments of missing data of streamflows. They concluded that ANN models were superior to linear regression (LR) models. Their results showed that the process of nonlinear noise reduction did not help to improve the accuracy of estimating the missing data. Hsu *et al*. (2002) applied a hybrid ANN model named a self-organizing linear output (SOLO) network with 6 input variables for daily streamflow prediction. They concluded that SOLO could provide not only a quick and effective solution, but also an analysis tool to the modelling system. Islam and Kothari (2000) have used ANNs coupled with remote sensing of hydrological processes and its data at spatial and temporal levels. Self-organization feature maps (SOFMs) provide a lower dimensional representation that preserves the topological structure of the original and higher dimensional data. Liong *et al*. (2000) applied an ANN with feed forward architecture having back propagation algorithms as a flow prediction tool, which yielded a very high degree of water level prediction accuracy at Dhaka Bangladesh up to 7 days leads time. Maier and Dandy (1997) stated that auto-regressive-moving average (ARMA) models have been used conventionally for stochastic modelling of time series data of water resources. Maier and Dandy (1999) also studied that it is important to follow a systematic approach in the development of ANN models, taking into account factors such as data pre-processing, the determination of appropriate model inputs and a selection of appropriate topology, parameter estimation and model validation. Mani and Desai (2005) developed a relationship between stage and discharge using artificial neural networks. This model was applied to three gauging stations, which are located on the downstream side of Godavari River, India. The results showed that the ANN models were able to generalize the relationship between input and output variables. The Levenberg-Marquardt algorithm, which is a standard second-order non-linear least squares technique, based on the back-propagation process was used to increase the speed of training (Masters, 1993).

Thandaveswara and Sajikumar (2000) used adaptive resonance theory (ART) and multi-layer perceptron for pattern clustering to identify the hydrological homogeneity of Indian River basin. Thirumalaih and Deo (2000) developed a neural network model for specific sites in a river basin where adequate meteorological information was not available. The sufficiency of the impending monsoon rainfall was adequately judged by an appropriately trained network, which helped in hydrological forecasting. Tokar and Johnson (1999) stated that the auto-regressive integrated moving average (ARIMA) model does not attempt to represent the non-linearity inherent in the hydrologic processes, and may not always perform well. Tokar and Markus (2000) applied artificial neural networks to rainfall-runoff modelling of the Fraser River, Colorado, USA along with conceptual models. To compare the model results, they used statistical indices such as coefficient of determination between predicted and observed discharge and the ratio between the root mean square error and standard deviation of observed discharge. The results revealed that ANNs could accurately model nonlinear relationships between hydrologic inputs (i.e., rainfall, snowmelt equivalent, temperature) and the output–streamflow.

Study Area

The Seonath River originates near village Panabaras in the Rajnandgaon district. The basin (Fig. 1) is located between latitude 20^0 16’ N to 22^0 41’ N and longitude 80^0 25’ E to 82^0 35’ E. The basin area of river up to confluence with the Mahanadi River is 30,860 Sq Km. The river traverses a length of 380 Km. The main tributary of Seonath river are Tandula, Kharun, Arpa, Hamp, Agar and Maniyari rivers. The mean annual rainfall in the basin varies from 1005mm to 1255mm.

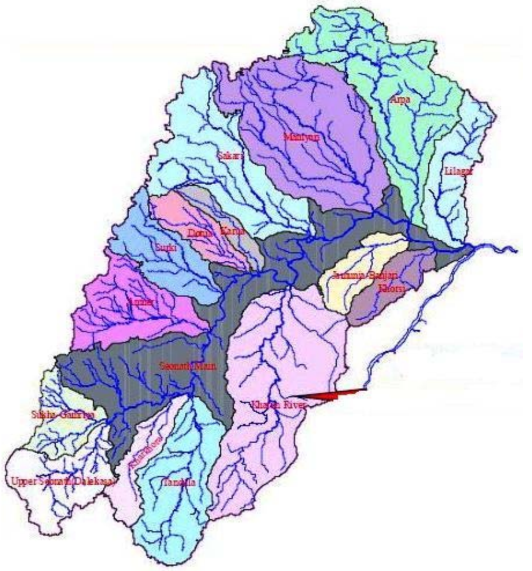

Fig. 1. Location map of Seonath basin.

Artificial Neural Network

A neural network is a computational method inspired by studies of the brain and nervous systems in biological organisms (Haykin, 1999). Typically neural networks consist of a layered processing units and weighted interconnections. Neural networks operate on the principle of learning from a training set. The typical architecture of ANNs is shown in figure 2. The most commonly used training algorithm for feed forward networks is the back propagation algorithm by Rumelhart *et al.* (1986). Earlier studies are limited primarily to feed forward neural networks with logistic activation function, as these are mostly used for the prediction and forecasting of water resource variables. Radial basis function neural network (RBFNN) can be considered as a three-layer network in which the hidden layer performs a fixed nonlinear transformation with no adjustable parameters. The primary difference between the RBF network and back-propagation is in the nature of the nonlinearities associated with the hidden nodes. The nonlinearity in back –propagation algorithm (BP) is implemented by a fixed function such as a sigmoid, whereas in radial basis function (RBF) method applies its nonlinearities on the data in the training set. ANNs offer real merit over traditional modelling, including the ability to handle large amounts of noisy data from dynamic nonlinear systems, especially when the underlying physical relationships are not fully understood (Pan and Wang, 2004).

Selection of input and output variable(s)

For any type of forecasting or estimation problem, it is very important to determine appropriate input variables which will help us for mapping the non-linear relationship between the input and output variables. The goal of an ANN is to generalize a relationship of the form.

$$Y^m = f(X^n) \qquad (1)$$

where X^n is an n-dimensional input vector consisting of variables x_1, $x_2 \ldots x_i \ldots\ldots x_n$; and Y^m an m-dimensional output vector consisting of resulting variables of interest $y_1 \ldots\ldots\ldots y_i \ldots\ldots\ldots y_m$. In hydrology, the values of x_i can be causal variables such as rainfall, temperature, previous flows, spatial locations, evaporation, basin area, slope, elevation, meteorological data, and so on. The values of y_i can be hydrological responses such as runoff, streamflow and others. For this present study, the value of X and Y are river stage and discharge respectively. An optimal dataset should be representative of the probable occurrence of an input vector that should facilitate the mapping of the underlying nonlinear process.

Data collection and preprocessing

There is no hard and fast rule for determining the number of input-output data combinations that will be required. An optimal data set should be representative of the probable occurrence of an input vector and should facilitate mapping of the underlying nonlinear process.

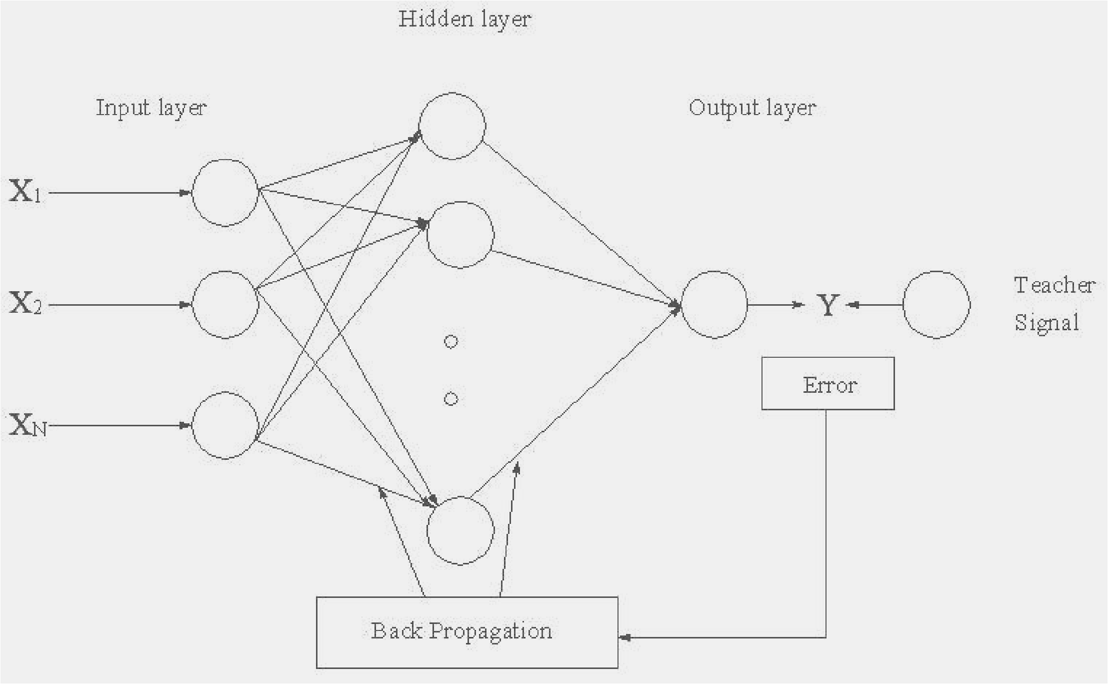

Fig. 2. Typical ANN architecture with three neuron layer.

Inclusion of less important patterns will reduce the network learning speed but an insufficient data set could lead to poor learning. This makes it useful to analyze and pre-process the data before it is used for the artificial neural network application. The following equations are used for scaling the input and output data set.

$$\text{Data}_{\text{scaled}} = \frac{H}{1.24H_{\max}} + 0.1 \qquad (2)$$

$$\text{Data}_{\text{scaled}} = \frac{Q}{1.24Q_{\max}} + 0.1 \qquad (3)$$

Where Q and H are the discharge and the stage at any time t and $Q_{\max}$ and $H_{\max}$ are the maximum discharge and maximum stage within the period of the ANN simulation. The values of $Q_{\max}$ and $H_{\max}$ used here are 9106cumecs and 249.70m.

RESULTS AND DISCUSSION

The applicability and potential of two different types of ANN in daily streamflow forecasting is explored in this study. Table 1 (a) and (b) gives the preliminary statistical analysis of the daily discharge and the stage. The choice of the neural network architecture, the training algorithm and the definition of error are usually determined based on past experience and preference of the users, rather than the physical aspects of the problem. Note that the ANN simulated (FFNN) daily discharge values are plotted continuously irrespective of missing years up to 726 days (i.e., 2 water years) in figure 4 during testing, 3053 (i.e., 8 water years) in figure 3 during training respectively. In India, the water year generally starts on the first day of June and ends on the last day of May in every year. The applicability and potential of two different types of ANN in daily streamflow forecasting is explored in this study. Performance of the model outputs is compared in terms of correlation coefficient (CC), normalized mean-squared-error (NMSE).

In this case study, daily discharge during the monsoon period was predicted using the daily stage and the previous time-step discharge as inputs. Ten water years of daily discharge from June to May (1996-2006) were used for developing the models. Since neural networks are capable to do well only with interpolation not with extrapolation. Because of that two different training and testing sets were used. In the first case, eight water years of data were used for training and two water years of data were used for testing the models. Therefore, the training and testing of the daily discharge prediction models were performed using a total of 3053 and 726 data sets. The daily discharge model was developed with only one hidden layer. Initially the experimentation was performed by changing the number of hidden layer neurons from 5 to 20. Beyond that of 20 hidden layer neurons, the performance of RBFNN model didn’t improve significantly. That’s why we used the number of neurons in the hidden layer was kept at a constant of 20. By

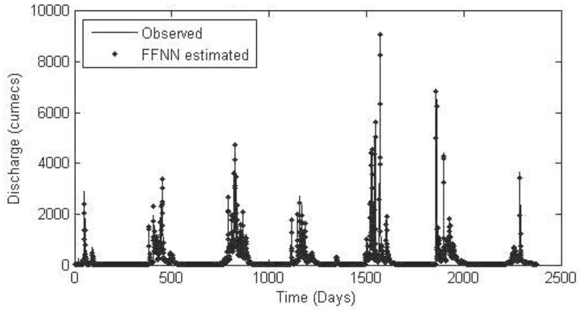

Fig. 3. Comparison of the observed & the FFNN estimated daily discharge during training period.

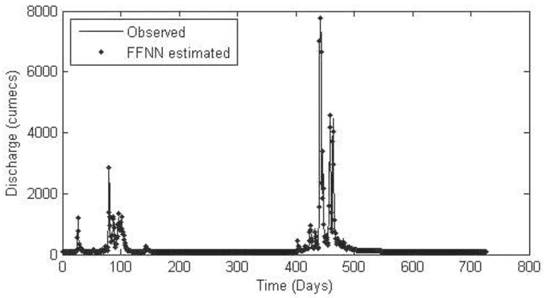

Fig. 4. Comparison of the observed & the FFNN estimated daily discharge during testing period.

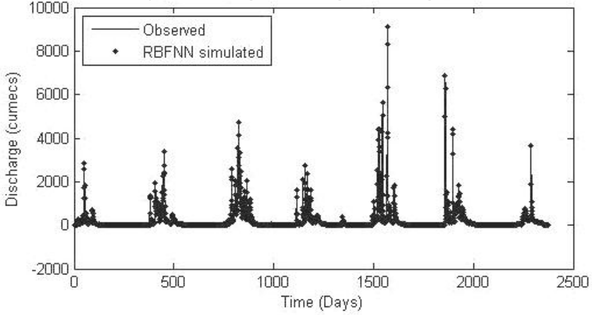

Fig. 5. Comparison of the observed & the RBFNN simulated daily discharge during training period.

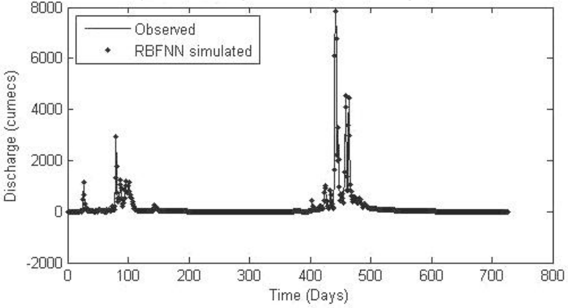

Fig. 6. Comparison of the observed & the RBFNN simulated daily discharge during testing period.

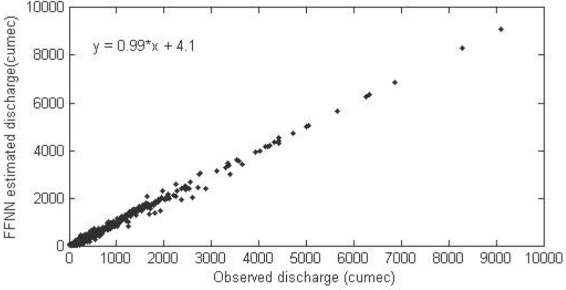

Fig. 7. Scatter plot between observed & the FFNN estimated daily discharge during training period.

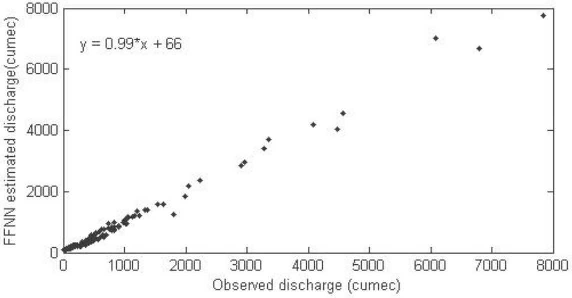

Fig. 8. Scatter plot between observed & the FFNN estimated daily discharge during testing period.

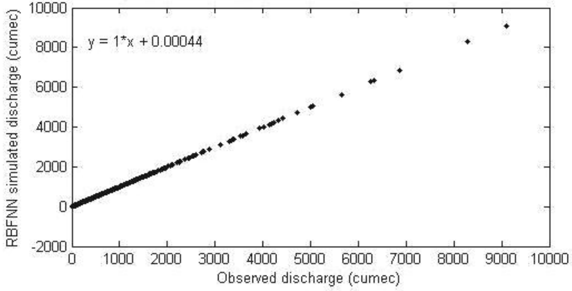

Fig. 9. Scatter plot between observed & the RBFNN simulated daily discharge during training period.

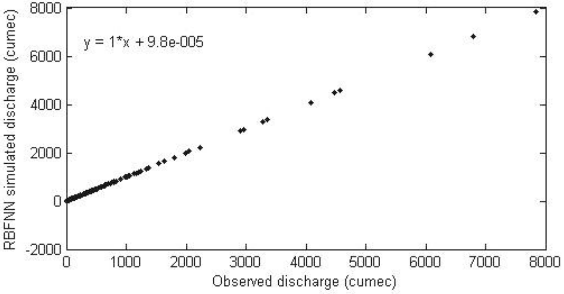

Fig.10. Scatter plot between observed & the RBFNN simulated daily discharge during testing period.

changing the values of spread in RBFNN from 0.05 to 1.00 simulation runs were performed to predict the daily discharge and thereafter the best RBFNN model was selected. The RBFNN simulated daily discharge values are plotted continuously irrespective of missing years up to 726 days (i.e., 2 water years) in figure 6 during testing, 3053 (i.e., 8 water years) in figure 5 during training respectively The daily hydrographs and the linear agreement between the observed and the ANN simulated using FFNN and RBFNN streamflows are depicted in figures 7 & 8 and figures 9 & 10 respectively.

Table1a. SEONATH DISCHARGE.

Year	Mean	Standard Deviation	Skewness	Kurtosis	Covariance	Max	Min
2000-2001	78.4117	268.67	7.262	64.08	72180	2870	0
2001-2002	194.866	430.73	3.711	19.8	185000	3372.63	0.1
2002-2003	93.64	280.144	5.2	39.1362	78400	2914.8	0.04
2003-2004	332.78	657.168	3.209	15.5597	413870	4724.8	0.84
2004-2005	160.1	365.6419	3.8343	19.5274	133690	2722.6	0.65
2005-2006	372.163	1049.9	4.9512	31.6813	1102300	9105.7	0.83
2006-2007	248.0292	830.633	6.0083	43.9904	689950	7848.8	0.76
2007-2008	247.9557	701.9785	6.2978	49.6811	492770	6867.07	2.02
2008-dec2008	185.1562	338.1807	6.8233	64.971	114370	3625.7	2.55

Table1b. SEONATH STAGE.

Year	Mean	Standard Deviation	Skewness	Kurtosis	Covariance	Max	Min
2000-2001	236.07	0.895	3.65	22.31	0.8023	242.86	235
2001-2002	236.55	1.347	2.18	8.14	1.8612	244.35	236.57
2002-2003	237.13	0.933	2.89	11.84	0.871	242.78	236.54
2003-2004	237.93	1.675	2.04	7.53	2.8071	246.63	236.77
2004-2005	237.47	1.416	2.23	8.22	1.3136	242.95	236.55
2005-2006	237.82	2.022	3.04	13.66	4.0909	249.7	236.56
2006-2007	237.54	1.638	3.86	20.46	2.6856	248.25	236.65
2007-2008	237.69	1.523	3.25	17.91	2.3209	248.05	236.67
2008-dec2008	237.56	0.871	3.64	24.69	0.7597	244.3	236.66

CONCLUSIONS

Feed forward neural networks trained with back-propagation usually start with a large network and proceeds by removing weights to which sensitivity of the error is minimal. The optimal architectures of ANN for the present investigation are 5-30-1 for feed forward neural networks and 5-20-1 for radial basis function neural networks with different range of spread values. This is similar to the idea of calibration that is an integral part of most of the time series modelling in the field of hydrology. The results show that the radial basis function neural networks are found to produce an accurate forecast of daily streamflow when compared to feed forward neural networks to the particular gauge/discharge station. The prediction accuracy of the ANN based model is highly dependent on many issues associated with network structure identification and network parameters such as interconnected weights, learning rate, momentum coefficient, and the number of epochs needed for optimization. This study aims to improve the model performance by explicitly incorporating hydrological a priori knowledge, reducing the network sensitivity to input errors and changing the training objective function. The results of this case study, demonstrated in the Seonath nandghat G/D station at Seonath River Basin under experimentation, were encouraging. To improve the performance of the ANN models, the incorporation of other climatic variables such as rainfall and temperature into the input data set and use of recurrent and modular neural networks, may be a good focus for the future direction of research work.

REFERENCES

Bhattacharya, B. and Solomatine, DP. 2000. Application of artificial neural networks in stage discharge relationship, Proc. of 4th International conference on Hydro informatics, lowa City, USA.

Birikundavyi, S., Labib, R., Trung, HT. and J. Rousselle, J. 2002. Performance of neural network in daily streamflow forecasting. J. Hydrologic Engg., ASCE. 7 (5):392-398.

Burian, JS., Durrans, SR., Nix, SJ. and Pitt, RE. 2001. Training artificial neural networks to perform rainfall disaggregation. J. Hydrologic Engg., ASCE. 6(1):43-51.

Coulibaly, P., Anctil, F. and Bobee, B. 2001. Multivariate reservoir inflow forecasting using temporal neural networks. J. Hydrologic Engg., ASCE. 6(5): 367-376.

Duan, Q., Sorooshian, S. and Gupta, VK. 1992. Effective and efficient global optimization for conceptual rainfall runoff models. Water Resources Research. 28 (4):1015-1031.

Duan, Q., Sorooshian, S. and Gupta, VK. 1994. Optimal use of SCE-UA global optimization method for calibrating watershed models, Journal of Hydrology. 158:265-284.

Elshorbagy, A., Panu, US. and Simonovic, SP. 2001. Analysis of cross-correlated chaotic streamflows. J. Hydrological Sciences. 46 (5):781-793.

Haykin, S. 1999. Neural networks- A comprehensive foundation. (2nd ed.) Prentice-Hall of India Private Limited, New Delhi. India.

Hornik, K., Stinchcombe, M. and White, H. 1989. Multilayer feed forward networks are universal approximators. Neural Networks. 2(5):359-366.

Hsu, K., Gupta, HV. and Sorooshian, S. 1995. Artificial neural network modeling of the rainfall runoff process. Water Resources Research. 31:2517-2530.

Hsu, K., Gupta, HV., Sorooshian, XGS. and Imam, B. 2002. SOLO- an artificial neural network suitable for hydrological modeling and analysis. Water Resources Research. 38(12):1302-1310.

Islam, S. and Kothari, R. 2000. Artificial neural networks in remote sensing of hydrologic processes. J. Hydrologic Engg., ASCE. 5(2):138-144.

Kitanidis,PK. and Bras, RL. 1980[a]. Adaptive filtering through detection of isolated transient errors in rainfall-runoff models. Water Resources Research. 16 (4):740-748.

Kitanidis, PK. and Bras RL. 1980[b]. Real time forecasting with a conceptual hydrological model,1,Analysis of uncertainity. Water Resources Research. 16 (6):1025-1033.

Liong, SY., Lim, WH. and Paudyal, GN. 2000. River stage forecasting in Bangladesh Neural networks approach. J. Computing in Civil Engg., ASCE. 14 (1):1-8.

Maier, HR. and G.C Dandy, GC. 1996. The use of artificial neural networks for the prediction of water quality parameters. Water Resources Research. 32:1013-1022.

Maier, HR. and Dandy, GC. 1997. Determining inputs for neural network models of multivariate time series. Microcomputers in Civil Engg. 12:353-368.

Maier, HR. and Dandy, GC. 1999. Neural network based modeling of environmental variables: A systematic approach. Mathematical and Computer Modeling. 33(6-7):669-682.

Mani, A. and Desai, VR. 2005. Artificial neural networks (ANNs) –A state-of-the-art computing technique in stage-discharge relationship, Second Indian International Conference on Artificial Intelligence (IICAI-2005), Dec. 20-22, 2005 Pune, India.

Masters, T. 1993. Practical neural Network Recipes in C++. Academic Press. San Diego, Calif, USA. 173-199.

Pan, TY. and Wang, RH. 2004. State space neural network for short-term rainfall runoff forecasting. J. Hydrol. 297:34-50.

Raman, H. and Sunilkumar, N. 1995. Multivariate modeling of water resources time series using artificial neural networks. J. Hydrol. Sci. 40:145-163.

Rumelhart, DE**.,** Hinton, GE. and Williams, RJ. 1986. Learning Internal Representations by Error Propagation. In: Parallel Distributed Processing Explorations in the Microstructure of Cognition **(**vol**.** 1). Eds. Rumelhart, DE.**,** McClelland, JL. MIT Press, Bradfords Books, Cambridge**,** MA. 318-362**.**

Sorooshian, S., Duan, Q. and Gupta, VK. 1993. Calibration of rainfall-runoff models: Application of global optimization to the Sacramento soil moisture accounting model. Water Resources Research. 29(4):1185-1194.

Thandaveswara, BS. and Sajikumar, N. 2000. Classification of river basins using artificial neural network. J. Hydrologic Engg., ASCE. 5(3):290-298.

Thirumalaiah, K. and Deo, MC. 2000. Hydrological-forecasting using neural networks, J. Hydrologic Engg., ASCE. 5(2):180-189.

Tokar, AS. and Johnson, PA. 1999. Rainfall-runoff modeling using artificial neural networks. J. Hydrologic Engg., ASCE. 4(3):232-239.

Tokar, AS. and Markus, M. 2000. Precipitation-runoff modeling using artificial neural networks and conceptual models. J. Hydrologic Engg. ASCE. 5(2):156-161.

Yapo, P., Gupta, VK. and Sorooshian, S. 1996. Calibration of conceptual rainfall–runoff models: Sensitivity to calibration data. Journal of Hydrology. 181:23-48.

Received: May 1, 2010; Revised: Sept 6, 2010; Accepted: Sept 27, 2010

SENRA Academic Publishers, Burnaby, British Columbia
Vol. 4, No. 3, pp. 1283-1287, October 2010
Online ISSN: 1920-3853; Print ISSN: 1715-9997

Canadian Journal of pure&applied sciences

EFFECT OF COPPER ADDITION ON THE MECHANICAL BEHAVIOR, MICROSTRUCTURE, AND MICROHARDNESS OF Zn-21% Al CAST ALLOY

*S M A. Al-Qawabah[1], Ubeidulla F. Al-Qawabeha[1] and A A. Mahasneh[2]
[1]Mechanical Engineering Department, Faculty of Engineering
[2]Department of Applied Physics, Faculty of Science
Tafila Technical University, PO. Box: 179, Tafila 66110, Jordan

ABSTRACT

In this study the literature related to Zinc-Aluminium cast alloy was reviewed and discussed. Few works have been published on the effect of Copper addition on the mechanical behaviour, hardness, and microstructure of the obtained alloys. The effect of 4% Cu addition to Zn-21Al on the mechanical behaviour and microhardness was investigated. It was found that the addition of 4% Cu resulted in 18.3% enhancement in microhardness where the mechanical characteristics were reduced (softening) by 14.5% at 0.2 strain. It has been found that after upsetting test, the microhardness was enhanced by 53.3 % and 42.7 % for Zn-21Al and Zn-21Al-4%Cu respectively.

Keywords: Zinc, aluminium, copper, mechanical properties, microhardness, microstructure.

INTRODUCTION

Zn-based alloys have a number of advantages over traditional bearing materials (Murphy and savaskan, 1984; savaskan and Murphy, 1987; Lee *et al*., 1987). These advantages can be summarized as high resistance to wear, excellent castability, and low cost (savaskan *et al*., 2002; Prasad *et al*., 1996; Prasad *et al*., 2001; Savaskan and Aydiner, 2004; Purcek *et al*., 2002). Among the monotectoid-based alloys, the best mechanical properties and wear performance were obtained with the Zn–40Al–2Cu alloy (Savaskan *et al*., 2004; Savaskan *et al*., 2003). Zinc-based alloys have been found to be promising energy and cost effective substitute to conventional bearing bronzes under heavy load and slow-to-medium speed applications (Grevais *et al*., 1980; Apelian *et al*., 1981).

The basic emphasis of the present work is to investigate the copper addition at a rate of 4% on the mechanical characteristics of some Zinc-aluminium alloys, namely, ZA-21Al, in addition, the effect of upsetting process on both alloys are presented and discussed.

MATERIALS AND METHODS

Materials

Zinc, commercially pure aluminum, and pure copper were used in the preparation of the two Alloys; Zn-21%Al and Zn-21%Al-4%Cu. In this work Zn-21%Al will be reviewed as ZA21.

Zinc and Aluminum

Zinc is a bluish, lustrous, diamagnetic metal with HCP structure of density 7.14 g cm^{-3} and melting point of 419.5 °C. Zinc powder of 99.9 % purity was used to prepare the two casted Alloys. The commercially pure aluminum of 99.98 % was used.

Casting Alloy (ZA-21) and ZA-21- 4%Cu

The chemical analysis of the prepared alloys ZA-21 and ZA-21-4%Cu are shown in table 1 and table 2 respectively. The density of ZA-21 is 6.23 gm. cm^{-3} and the melting point ranges between (380-386) °C.

Copper

Pure copper is used extensively as cable, wire, and pure powder. The density of copper is 9.95 gm.cm^{-3} and the melting point is 1080°C. Copper has many important advantages; its corrosion resistance, easily fabricated, high electrical and thermal conductivity. Copper of 99.99% purity was used.

Equipment

The following set of machines and equipment were used throughout the experimental work:

1. An electric resistance furnace (Carbolite) with 0-1100°C.
2. XRF Model 1800- shemadzu, Japan
3. Digital microhardness tester (model HWDM-3).
4. Universal Testing Machine with 100KN capacity (Quasar 100).
5. Microscope type NIKON 108.
7. CNC lathe machine (Boxford).
9. Casting mould

---

*Corresponding author email: safwan_q@yahoo.com

Table 1. Chemical analyses of ZA21 alloy wt.

Element	Al	Mg	Fe	Pb	Cd	Sn	Zn
%, Wt	20.3-21.3	0.03-.08	0.1	0.005	0.004	0.003	Bal

Table 2. Chemical analyses of ZA-21-4% Cu alloy wt.

Element	Al	Cu	Mg	Fe	Pb	Cd	Sn	Zn
%, Wt	20.3-21.3	4	0.03-.08	0.1	0.005	0.004	0.003	Bal

Experimental Procedure

Preparation of test specimens

The ZA-21%Al alloy (in weight) was prepared by melting 99.99% Zn and 99.99% Al, where ZA-21%Al-4%Cu alloy was prepared as the first alloy just adding the predetermined amount of copper powder into molten ZA-21%Al at 550 °C under flux (aluminum florid and calcium florid). A graphite crucible and graphite rod were used in stirring the molten metal. The temperature was kept constant for five minutes and the alloy was stirred for five minutes before pouring it into brass mould. A number of cylinder specimens of 11mm diameter and 65 mm length mm from each ZA-21%Al and ZA-21%Al-4%Cu alloy were prepared for upsetting and microhardness tests. In addition, several specimens of 10 mm diameter and 10 mm height (h/D = 1) were prepared for investigating the mechanical behavior on compression test.

Compression Test

The prepared cylindrical specimens were subjected to compression test using Quasar 100 Universal Testing Machine with 100 KN capacity at $1*10^{-3}$/s strain rate. The load-deflection curve was obtained for each type of the prepared alloy from which the true stress-true strain curve was determined. Three tests were carried out on each ZA-Cu alloys where the average was calculated. The compressed work piece is shown in figure1.

Fig. 1. Compression test specimen.

Microhardness and Microstructure Tests

Microhardness test was carried out using HWDM-3 microhardness tester at 500 gm force on each ZA-Cu alloys. Finally, metallurgical examination was carried out on ZA-21 and ZA-21-4%Cu alloys to determine the effect of copper addition on its microstructures,50 % natal and 50% ethanol solution was used in etching process.

RESULTS AND DISCUSSION

In this section, the effect of copper addition on the microstructure, microhardness, and mechanical characteristics of ZA alloys will be presented and discussed.

Effect of copper addition on the microstructure of ZA21 cast alloy

Figure 2 shows the optical micrographs of ZA21 and ZA21-4 % Cu before upsetting (as casted). It is clearly shown that the microstructure consists of primary aluminium-rich **α** zinc-rich **η** and copper-rich **ε** phases. It is worth to mention that these results are consistent with those of El-Tayeb *et al.* (2006). Their results indicated that the microstructure of the ternary Zn–40Al–2Cu alloy consists of aluminium-rich **α** zinc-rich **η** and copper-rich **ε** phases.

Other studies pointed out that the microstructure of the binary monotectoid alloy (Zn-40Al) consists of aluminum-rich **α** dendrites and zinc-rich **η** phase in the interdendritic regions. Addition of copper produced copper-rich ε phase particles, but had no effect on the dendritic structure of the alloys. It was observed that the **ε** phase was formed in the interdendritic region of the alloys containing more than 2% Cu. This type of microstructure seems to be ideal for bearing materials which usually have two phases, one of which is hard and the other one is soft (Savaskan, 1980). In zinc-aluminum-copper alloys, the aluminum-rich **α** phase having a face-centered cubic (FCC) crystal structure that exhibits excellent ductility (Purecek *et al*., 2002; Pandey and Prasad, 1997; Prasad *et al*., 1997). The zinc-rich **η** phase having a hexagonal-close-packed (HCP) crystal structure with a large (c/a) ratio.

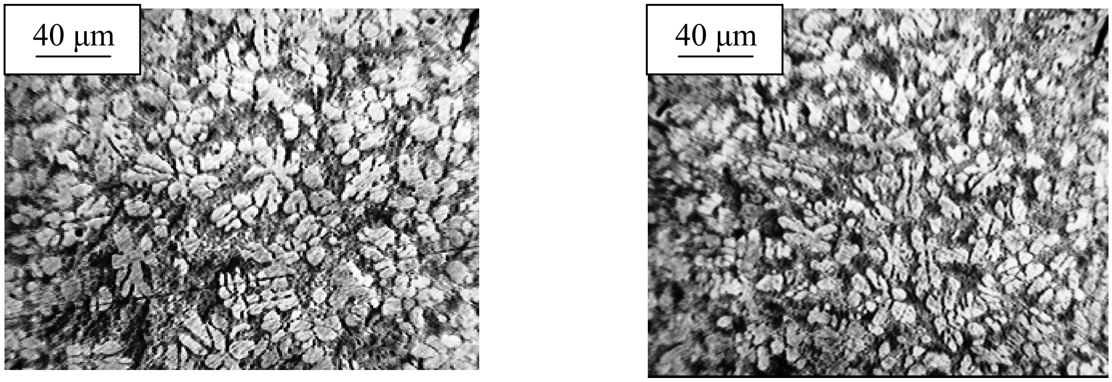

a) Za21

b) Za21-4% Cu

Fig. 2. Photomicroscan of a) ZA21 and b) ZA21-4%Cu at 250x.

Effect of copper addition on the microhardness of ZA21 cast alloy

It is obviously shown in figure 3 that the addition of 4% copper resulted in 18.3% enhancement in microhardness . The results are consistent with those of Joong *et al.* (2007). They observed that the hardness of the alloys increased continuously with increasing copper content up to 5%. Microhardness of the aluminium-rich **α** phase was also affected by the copper content in a manner similar to that of the tensile strength. It was found that the wear loss of the alloys decreased with increasing copper content and reached a minimum at 2% Cu for a sliding distance of 700 km. However, the coefficient of friction and temperature due to frictional heating were found to be generally less for the copper containing alloys than the one without the element. Furthermore, they explained the effect of copper on the wear behaviour of the alloys in terms of their microstructure, hardness, tensile strength, percentage elongation, and microhardness of the phase.

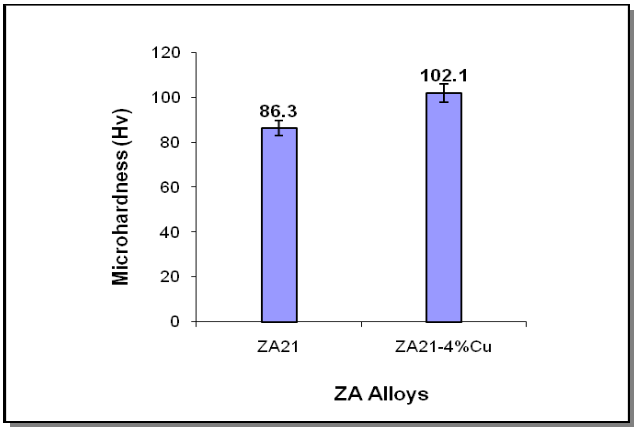

Fig. 3. Microhardness of ZA alloys (as casted).

Effect of copper addition the microstructure of ZA21 after upsetting

It can be seen from figure 4 that the interdendritic areas are decreased where the dendritic areas were increased.

Effect of Upsetting on the microhardness of ZA21 and ZA21- 4%Cu cast alloys

As illustrated by figure 5, there is an enhancement in microhardness after the upsetting test. A 53.3% enhancement in microhardness of ZA21 alloy and 42.7% enhancement in ZA21- 4%Cu were achieved.

Effect of copper addition on the mechanical characteristics of ZA21 cast alloy

As shown in figure 6, the mechanical properties after 4% Cu addition were deteriorated, however the structure become softer, the maximum reduction is about 14.5% at 0.2 strain. This result is consistent with that of El-Tayeb *et al.* (2006) where their result indicated that the tensile strength increased with increasing copper content up to 2%, but above this level the strength decreased as the copper content increased further.

Upon the work of structural softness due to morphological change of (**α+η**) phases from fine lamellar structure to coarse equiaxed grains (Joong *et al*., 2007). According to hall-pitch equation, the strength of microstructure with lamellar or equiaxed grains morphology is inversely proportional to the grain size or interlamellar spacing.

On the other hand, the softness is related to two opposite defects; solid solution hardening of α phase and weakling effect through cracking tendency to ε phase, where the later is more effective at copper counted beyond 3% addition (Yasin and Savaskan, 2009).

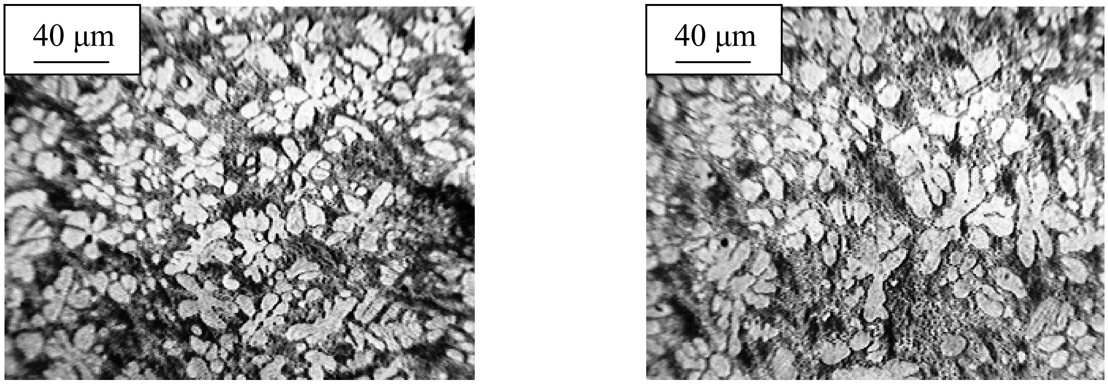

a) Za21

b) Za21-4% Cu

Fig. 4. Photomicroscan of a) ZA21 and b) ZA21-4%Cu after upsetting process at 250x.

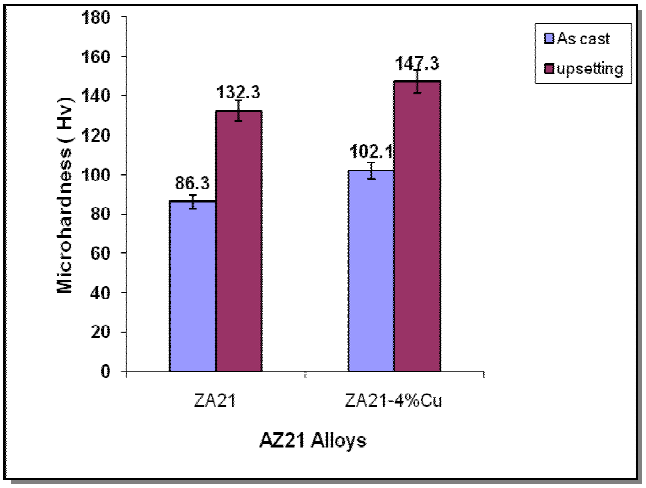

Fig. 5. Microhardness of ZA alloys before and after upsetting.

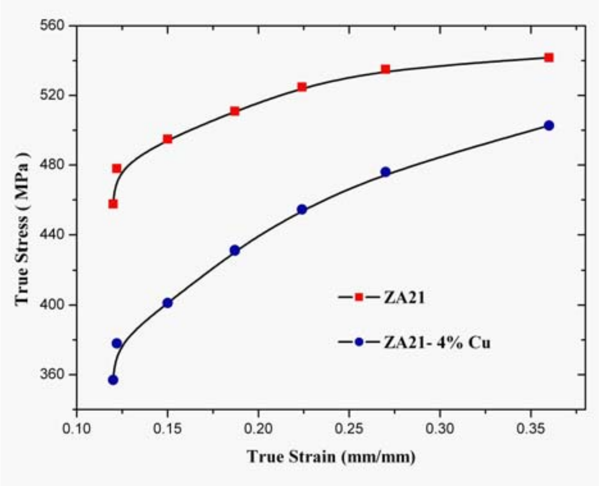

Fig. 6. True stress- true strain for ZA21 and ZA21- 4% copper.

CONCLUSION

The mechanical strength and the microhardness of ZA21 and ZA21-4%Cu have been investigated. The mechanical strength was decreased at 4% copper addition, and the structure become softer. On the other hand, the microhardness increased at 4% copper addition and this could be attributed to the new intermetalic compounds Al_2Cu which has been produced. Furthermore, after the addition of 4%Cu to ZA21 cast alloy, the structure of the produced alloy become softer, so this will reduce the press capacity during the forming processes. This study has thrown many questions in need. The machinability, the corrosion resistance, and wear resistance of these new alloys can be investigated. Further investigation into mechanical strength and microhardness for different alloys with different additives is strongly recommended.

ACKNOWLEDGEMENT

This work has been supported by Tafila Technical University which is acknowledged. The efforts of the technical staff at mechanical engineering laboratories and workshops are highly appreciated.

REFERNCES

Apelian, D., Paliwal, M. and Herrschaft, DC. 1981. Casting with Zinc Alloys. Journal of Metals. 33(11):12-19.

El-Tayeb, NSM, Low, KO. and Brevern, PV. 2006. Influence of roller burnishing contact width and burnishing orientation on surface quality and tribological behavior of Aluminum 6061. Journal of material processing technology. 186:272-278.

Grevais, E. and Levert, H.1980. The development of a family of zinc-base foundry alloys. M. Bess, Trans. AFS. 68:183-194.

Joong-Hwan Jur. Ki-Duk Seong, Jeong-Min Kim, Ki-Tae Kim. and Woon-Jae Jung. 2007. Strain-induced macrostructural evaluation and work softening behaviour of Zn-15%Al alloy. Alloys and compound.435:311-314.

Lee, PP., Savaskan, T. and Laufer, E. 1987. Wear resistance and microstructure of Zn–Al–Si and Zn–Al–Cu alloys.Wear. 117:79-89.

Murphy, S. and Savaskan, T. 1984. Comparative wear behaviour of Zn–Al based alloys in an automotive engine application. Wear. 98:151-161.

Pandey, JP. and Prasad, BK.1997. Dry sliding wear behaviour of a zinc based alloy against different counterface materials. Z Metallkd. 88:739-43.

Prasad, BK, Pathwardhan, AK. and Yegnesvaran, AH. 2001. Wear characteristics of a zinc- based alloy compared with a conventional bearing bronze under mixed lubrication conditions: Effects of material and test parameters.Can. Metall. Q. 40 (2):193.

Prasad, BK, Pathwardhan, AK. and Yegnesvaran, AH. 1996. Characterization of the wear response of a modified zinc-based alloy vis-a` -vis a conventional zinc-based alloy and a bearing bronze at a high sliding speed Metall. Mater.Trans. A 27A 3513.

Prasad, BK, Patwardhan, AK. and Yegneswaran, AH. 1997. Microstructural modifications through compositi.onal alteration and their influence on the mechanical and sliding wear properties of zinc-based alloys. Scripta Materialia. 37(3):323-328.

Prasad, BK, Patwardhan, AK. and Yegneswaran, AH. 1997. Influence of aluminium content on the physical, mechanical and sliding wear properties of zinc-based alloys. Z Metallkd.88:333-338.

Pu¨rc¸ek G., Savaskan, T., Ku¨c¸u¨ko¨merogˇlu, T. and Murphy, S. 2002. Dry sliding friction and wear properties of zinc-based alloys. Wear.252:894-901.

Savaskan, T. 1980.The structure and properties of zinc-aluminum based bearing alloys. Ph.D. thesis, University of Aston, Birmingham, UK.

Savaskan, T. and Aydıner, A. 2004. Effects of silicon content on the mechanical and tribological properties monotectoid-based zinc–aluminium–silicon alloys. Wear. 257:377-388.

Savaskan, T., Hekimoˇglu, AP. and P¨urc¸ek, G. 2004. Effect of copper content on the mechanical and sliding wear properties of monotectoid-based zinc–alumi- nium–copper alloys. Tribol. Int. 37:45-50.

Savaskan, T. and Murphy, S. 1987. Mechanical properties and lubricated wear of Zn–25Al- based alloys. Wear. 116:211-224.

Savaskan, T., Pu¨rc¸ek G. and Murphy, S. 2002. Sliding wear of cast zinc-based alloy bearings under static and dynamic loading conditions. Wear.252:693-703.

Savas¸kan, T., Turhal, MS. and Murphy, S. 2003. Relationships between cooling rate, copper content and mechanical properties of monotectoid based Zn–Al–Cu alloys. Mater. Sci. Technol. 19:67-74.

Yasin, A. and Savaskan,T. 2009. Mechanical and tribological properties of Al-40Zn-Cu alloys. Tribology international 42:176-182.

Received: May 31, 2010; Accepted: Sept 11, 2010

SENRA Academic Publishers, Burnaby, British Columbia
Vol. 4, No. 3, pp. 1289-1292, October 2010
Online ISSN: 1920-3853; Print ISSN: 1715-9997

Canadian Journal of pure&applied sciences

SIGNATURE OF ATMOSPHERIC DYNAMICS ON SURFACE OZONE VARIABILITY IN NIGERIA

Akinyemi M L and T V Omotosho
Department of Physics, Covenant University, Ota, Ogun State Nigeria

ABSTRACT

An examination of analysis revealed that surface ozone concentration over Nigeria varied with direction of the local trade winds, namely the Harmatan, and the Gulf of Guinea maritime trade winds. In DJF and MAM the period of the dry dusty Harmatan seasons, surface ozone concentration in the southern Nigeria exceeded that of the north by 21DU and 24DU respectively. Whereas in the JJA and SON, the rainfall season, reversal was the case, the surface ozone concentration in the northern Nigeria exceeded that of the south by 20DU and 15DU respectively. Maximum temporal variation gradient of 20DU was also observed in MAM season while the minimum of 11DU occurred in JJA which is the peak of the raining season.

Keywords: Surface ozone concentration, spatial gradient, temporal gradient.

INTRODUCTION

Air transportation is the major atmospheric constituents recognised as one of the key factors influencing the variability of total surface ozone concentration and distribution Tarasova *et al.* (2003), though photochemical processes is also a major contributor, it has been shown that the contributions of photochemical process and atmospheric dynamic process differs for different seasons except in strong localized convective currents when vertical atmospheric velocities are relevant. But majorly the horizontal wind flow dominates the atmospheric motion which makes its effect more pronounced on total ozone distribution. The most important of the horizontal flow in ozone variation and distribution is the horizontal frictionless flow (HFF) Tyson (1997). HFF is assumed to be the wind flow that is well above the boundary layer and much higher than all the uneven terrain within the lower troposphere.

If we let the components of the horizontal pressure P be expressed in forces in the natural coordinates as b_z *and* b_n

$$b_z = -\alpha \frac{dP}{dS} = -\alpha \frac{dP}{N} \sin\gamma \tag{1}$$

$$b_n = -\alpha \frac{dP}{dn} = -\alpha \frac{dP}{dN} \cos\gamma \tag{2}$$

Where n is the coordinate in the direction of the horizontal pressure gradient.

γ = the cross-isobar wind direction assumed positive towards lower pressure and negative toward higher pressure. Assuming rough approximation by taking the wind along the isobars, HFF can results in three kind of a geostrophic wind component depending on horizontal variation of pressure gradients namely;

(a) Diffluent isobar patterns (straight or curved)
(b) Parallel isobars patterns (straight or curved)
(c) Confluent isobar pattern (straight or curved)

These three major HFF trends were observed in this study. A strong correlation had been observed between the seasonal HFF of air masses, a key component of atmospheric dynamics and seasonality of total ozone distribution (Fusco and Salby, 1999; Kawa *et al*., 2005). Sharp increases in total ozone concentration during winter had been observed for a long time. According to them total ozone during a particular season reflects its net change during the preceding season. This makes it important to study seasonal peculiarity of total ozone distribution in a more detailed manner over Nigeria.

MATERIALS AND METHODS

Methodology and Data analysis

In order to make the influence of atmospheric signal on total surface Ozone distribution over Nigeria distinct and easy to identify, the Map of Nigeria which could be contained in a rectangular box of latitudes 4^o-14^oN and longitudes 2^o-15^o S, was subdivided into eight zones namely; North-North (NN), North-East (NE), North-West (NW), North-Central (NC), South-South (SS), South-East (SE), South-West (SW) and Middle-Belt (MB). Samples of the diagrams showing the locations of the maximum and minimum ozone are shown in figure 1(a-f) for the day and night pattern. The data used in this study were retrieved from AIRS satellite 2002 to 2009.

---

*Corresponding author email: marvel.akinyemi@gmail.com

RESULTS AND DISCUSSION

Intra-Seasonal Atmospheric Dynamic Signature in Total Ozone Distribution

The study of analysis revealed that surface ozone concentration over Nigeria varied with the local trade winds. Distinct trend and pattern observed from both day and night data (AIRS satellite 2002- 2009) revealed the strong influence of atmospheric dynamic on the surface ozone concentration over Nigeria. Ozone transportation was observed to follow various isobars patterns (Tables 1 and 2), direct singular flow occurred in DJF 2003-2005 (daytime), with flow direction from NN to SE, resulting in minimum concentration in the NN and maximum in the SE, wide spread flow occurred in DJF 2007-2009 (night) with flow direction from NW/NE to SW/SS; diffluent isobar pattern occurred DJF 2006-2009 (daytime) NN to SW/SE and confluent isobar pattern DJF 2006 (Night) only, NW/NE to SS.

On general observations, minimum ozone concentration was recorded in the northern Nigeria during DJF and MAM seasons, while maximum concentration was recorded in the southern part of the country (Tables 1 and 2). In these seasons, average surface ozone concentration in the south exceeded those of the north by 21DU and 24DU respectively. Relating this to wind flow transport, trace gases such as smoke flow in the direction of the wind pattern downstream. The wind flow pattern during the season DJF is from north to south. DJF is the peak of the dry season over the country, when the dry Harmattan wind blowing across the Sahara desert bring along with it the dust from the desert as it proceeds toward the Gulf of Guinea of the Atlantic Ocean. It can therefore be suggested that the same atmospheric dynamics responsible for the hazy and dusty Harmattan season

Table 1. Day-time Seasonal and Spatial Variability of Ozone Maxima and Minima.

Year	Pattern	Seasonal Location of Maximum and Minimum Ozone Values (DU)			
		DJF	MAM	JJA	SON
y03	Max	SE (279)	NE (301)	NW (310)	NE-MB (288)
	Min	NN (261)	NW (279)	SS (281)	SS (274)
y04	Max	SE (281)	SS (297)	NW (315)	NE (284)
	Min	NN (253)	NN (270)	SS (301)	SS (269)
y05	Max	SE (286)	SE (294)	NW (295)	SW-MB (299)
	Min	NN (272)	NN (269)	SS (273)	SS (284)
y06	Max	SW-SE (278)	SE-SS (303)	NW (318)	NE (287)
	Min	NN (259)	NW (278)	SE (299)	SS (272)
y07	Max	SW-SS (276)	SE-SW (299)	NW (300)	SW (292)
	Min	NN (259)	NW (278)	SS (272)	SS (282)
y08	Max	SE-SS (282)	SS (309)	NC (311)	NW (293)
	Min	NN (253)	NW (282)	SS (299)	SS (270)
y09	Max	SW-SE (288)	SE (298)	NW (302)	SW (298)
	Min	NN (265)	NW (278)	SS (288)	SS (286)

Table 2. Night-time Seasonal and Spatial Variability of Ozone Maxima and Minima.

Year	Pattern	Seasonal Location of Maximum and Minimum Ozone Values (DU)			
		DJF	MAM	JJA	SON
y03	Max	SS (265)	MB (275)	NW (297)	NW-NE (275)
	Min	NE (243)	NW (263)	SE (268)	SE (266)
y04	Max	SW-SS (267)	SS (283)	NW (303)	NW-NE (272)
	Min	NW-NE (236)	NW (258)	SE (287)	SE (255)
y05	Max	SW-SS (273)	NE-NW (274)	NW (285)	NE (282)
	Min	NE (253)	SSE (257)	SE (260)	SE (265)
y06	Max	SS (264)	NE (281)	NW (307)	NW-NE (275)
	Min	NW-NE (239)	NC (265)	SE (289)	SE (256)
y07	Max	SW-SS (262)	SS (282)	NW (290)	NE (279)
	Min	NW-NE (238)	NE (265)	SE (262)	SS (264)
y08	Max	SW-SS (272)	SS (290)	SW (300)	NW (281)
	Min	NW-NE (239)	NC (268)	SE (287)	SS (255)
y09	Max	SW-SS (276)	SS-MB (279)	NW (295)	SW (282)
	Min	NW-NE (247)	NC (261)	SE (273)	MB (274)

carries along with it some ozone rich air from the northern part of Nigeria southward. This could be responsible for the consistent observation of minimum ozone concentration in the north and maximum in the southern part of the country in this period. This trend was observed in the seven years studies for the two seasons DJF and MAM. This confirmed distinctly the signatures of the atmospheric flow pattern on the ozone distribution in DJF and MAM in Nigeria (Fig.1a-f).

The next two seasons JJA and SON revealed clear reversal in the trend of ozone distribution over the country. In the two seasons, surface Ozone concentration in the north exceeded the south by 20DU and 15DU respectively. This observation is also in accordance with the prevailing atmospheric phenomenon over the country. The period coincided with the Tropical rainfall season. Rainfall over West Africa is controlled by advection of moisture from the Gulf of Guinea. Through atmospheric dynamics, the moisture rich air flow northward inland and brings the Inter-Tropical Convergence Zone (ITCZ) and the associated rainfall maxima to the farthest north which is the Sahel region (Cook,1999; Diedhiou *et al.*, 1999; Sultan and Janicot, 2000). During these seasons JJA and SON maximum ozone concentration was consistently observed in the north except on two occasions when it migrated to the SW (Table 2).

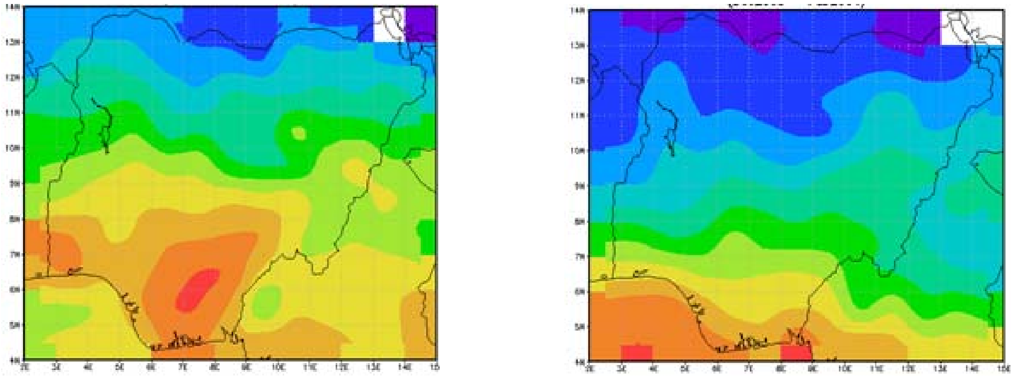

(a) DJF 2003/2004 Day-time (b) DJF 2003/2004 Night-time

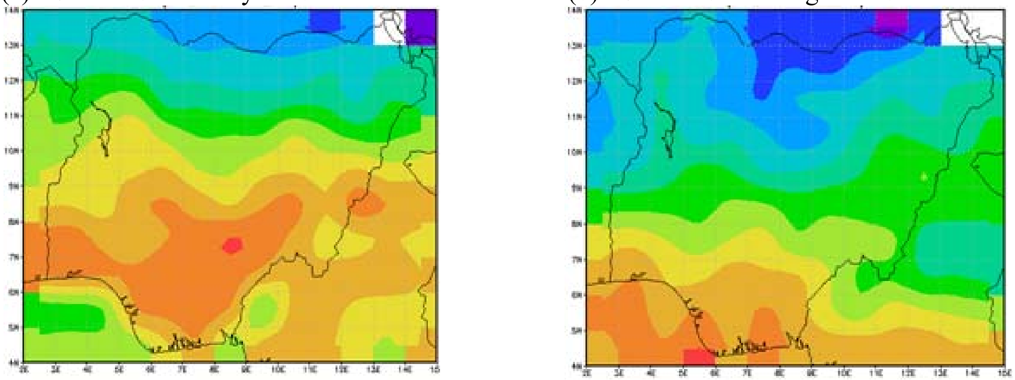

(c) DJF 2005/2006 Day-time (d) DJF 2005/2006 Night-time

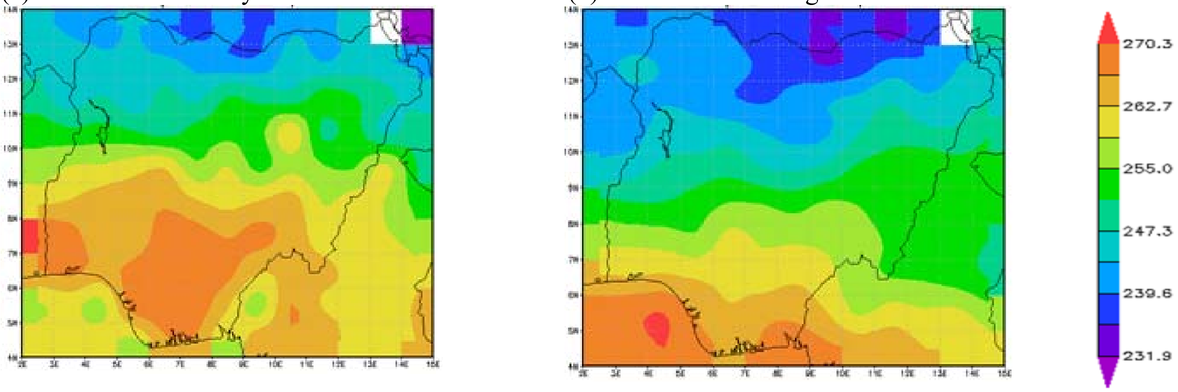

(e) DJF 2008/2009 Day-time (f) DJF 2008/2009 Night-time

Fig. 1. Temporal and spatial variability of ozone concentration in Nigeria in DJF season showing the day and night pattern

Spatial and Temporal Variability of Ozone maxima and minima in Nigeria

The transition in surface ozone pattern as dictated by the day and night atmospheric dynamics was also observed in the study. The major factor influencing variability in day and night is the change in temperature and solar activity. Maximum temporal variation gradient of 20DU was observed in MAM season while the minimum of 11DU occurred in JJA which is the peak of the raining season. DJF and SON both had temporal variation gradient of 13DU

In the day time ozone advection and transportation was observed to follow either the parallel straight isobar patterns or the diffluent isobar pattern. Example of the parallel isobar pattern flow was DJF (day) 2003, 2005, and DJF (night) 2007-2009, while DJF (day) 2006 to 2009 recorded diffluent isobar pattern flow (Table 1). In the diffluent isobar pattern the minimum ozone concentration was observed in the North-North (NN) while there was a spread out of the maximum from SW across to the SE. Night time maximum surface ozone concentration in the DJF season were observed to move farther south above the Gulf of Guinea, while the minimum covered much wider expanse as expected due to nil solar radiation.

In the seven years studied, the confluent isobar pattern flow was observed only in 2006 DJF (night) when minimum ozone concentration spread was observed from NW to NE but maximum was localized to SS, this revealed the convergence of atmospheric dynamics toward SS.

The exact locations of ozone maxima and minima over Nigeria in the day time were observed to differ slightly from those of the nights. DJF day time ozone minima for the seven years were centred in NN, while night minima for the same season DJF, were observed at either NW or NE for the seven years. Similarly for the JJA, the day time minimum was centred in the SS majorly whereas the night time minimum was in SE (Table2). The following average temporal variations between day and night surface ozone values were observed; DJF and SON recorded 13DU, while maximum of 20DU was in MAM, and minimum of 11DU in JJA. The JJA minimum temporal variation in surface ozone concentration coincided with the period of minimum temperature gradient observed in the peak rainfall season.

CONCLUSION

Result from the analysis showed the effect of the Harmattan wind in DJF and MAM blowing from north to south, and that of the Gulf of Guinea Maritime coastal wind blowing inland from south to north in JJA and SON on the distribution of surface ozone concentration in Nigeria. These two trade winds which are the main drivers of the dry and wet seasons in Nigeria have been associated with the spatial and temporal variability of surface ozone concentration in Nigeria from this study.

This study revealed a correlation of 1.0 between the prevalent atmospheric flow pattern across the country and spatial distribution of maximum and minimum ozone concentration per season in DJF (day and night) and in JJA (day and night) when all the minimum concentration was northward and maximum southward for DJF, while the reverse was the case in JJA when all the minimum concentration was located in the south and maximum in the north, with the exception of 2008 JJA (night) only. This confirmed the signature of atmospheric dynamics on spatial and temporal variation of ozone concentration over Nigeria.

REFERENCES

Cook, KH. 1999. Generation of the African Easterly Jet and Its Role in Determining West Africa Precipitation. Journal of Climate, American Meteorological Society. 12:1165-1184.

Diedhiou, A., Janicot, S., Viltard, A., Felice, PDe. and Laurent, H. 1999. Easterly Waves Regime and Associated Convection over West Africa and Tropical Atlantic: Results from the NCEP/NCAR and ECMWF reanalyses. Climate Dynamics. 15):795-822

Fusco, AC. And Salby, ML.1999. Interannual Variations of Total Ozone and Their Relationship to Variation of Planetary Wave Activity, Journal of Climate, American Meteorological Society. 12:1619-1629.

Kawa, SR., Newman, PA., Storlarski, RS. and Bevilacqua, RM. 2005. Fall Vortex ozone as a predictor of spring time total ozone at high norther latitudes. Atmospheric Chemistry and Physics Discussion. 5:155-178.

Sultan, B. and Janicot, S. 2000. Abrupt Shift of the ITCZ over West Africa and Intra-Seasonal variability. Geophysical Research Letert. 27(20):3352-3356.

Tarasova, OA., Elansky, NF., Kuznetsov, GI., Kuznetsova, IN. and Senik, IA. 2003. Impact of air Transport on Seasonal Variations and Trends of Surface Ozone at Kislovodsk High Moutain Station. Journal of Atmospheric Chemistry. 45(3):245-259.

Tyson, PD. 1997. Atmospheric Transport of Aerosols and Trace Gases over Southern Africa, Pro. Phys. Geog. 21(1):79-101.

Received: May 28, 2010; Accepted: Sept 6, 2010

SENRA Academic Publishers, Burnaby, British Columbia
Vol. 4, No. 3, pp. 1293-1302, October 2010
Online ISSN: 1920-3853; Print ISSN: 1715-9997

Canadian Journal of pure&applied sciences

IMPACT OF HEAVY METALS IN MYCORRHIZOSPHERE: STRATEGY FOR PHYTOREMEDIATION

Anamika S and *MH Fulekar
Department of Life Sciences, University of Mumbai, Santacruz (E), Mumbai- 400 098, India

ABSTRACT

The pot culture technique has been employed for development of mycorrhizal soil in the green house. Mycorrhizal soil is a symbiotic association of bacteria, fungi and Actinomycetes which provides the effective rhizosphere for the growth of plants. The enrichment of microbial enzymes and plants exudates in mycorrhizosphere influences phytoremediation. The heavy metals (cadmium, lead and zinc) toxicity at varying concentrations, viz. 5, 10, 20, 50, 75 and 100ppm has been assessed for seed germination and growth of *Medicago sativa* plants both in mycorrhizal soil and non mycorrhizal soil. Mycorrhizosphere has found to provide suitable conditions for seed germination and growth of plants at concentrations ranging from 5-50ppm. The germination rate was found comparatively lower in NMS at the metal concentrations 5-50ppm. The seed germination *M. sativa* in cadmium amended mycorrhizal soil was found 87, 80, 70 and 55% at concentration of 5, 10, 20 and 50ppm, respectively; while for lead amended mycorrhizal soil, the percentage of seed germination was observed 80, 75, 70, and 60% at 5, 10, 20 and 50ppm, respectively. The seed germination percentage was 95, 90, 91 and 89% when zinc was amended with the concentration of 5, 10, 20 and 50ppm, respectively in mycorrhizal soil. Similarly the root/ shoot growth of *M. sativa* for each of this metal was propound in mycorrhizal soil. The higher metal concentrations i.e. 75 and 100ppm were found inhibitory for the seed germination and root/shoot growth. The enzymes studied; in particular acid & alkaline phosphatase and dehydrogenase in mycorrhizal soil have propounded the growth of plants in the mycorrhizosphere. The present research study has proved the effect of mycorrhizal soil for phytoremediation of heavy metals at concentrations ranging from 5-50 ppm using *M. sativa* as a potential candidate.

Keywords: *Mycorrhizosphere,* heavy metals, *Phytoremediation, Medicago sativa.*

INTRODUCTION

Mycorrhiza is a mutualistic symbiotic association of plant and fungi (Krik, 2001) which provide the effective rhizosphere by the action of microbial enzymes and plant enzymes along with the root zones of the plants. These symbioses are characterized by bi-directional movement of nutrients and largely based on the transfer of carbon (C) from plants to fungus, and mineral nutrients mainly phosphorus [P] and /or nitrogen [N] from fungus to host plants. In mycorrhizosphere, the assemblage of bacteria, fungi and Actinomycetes supply the effective rhizosphere for the growth and development of plants. Mycorrhizal association stimulates branching of the root and increases the absorption surface of the root, which influences uptake of heavy metals by plants (Daniell *et al*., 1999; Miller and Jastrow, 2000; Smith and Read, 1997). Sieverding (1991) has reported that the uptake of trace elements, such as zinc, copper, boron and molybdenum is thought to be enhanced by mycorrhizae. They play an important role in remediation of heavy metal contaminated soil (de Val *et al*., 1999) and mycorrhizal fungi provide a direct link between soil and plants (Carvalho *et al*., 2006). In addition to accelerating the nutritional state of their host plant, heavy metals can also be transported to plants via fungal hyphae.

Heavy metals traces in soil and water originate from the natural (weathering processes of the Earth's crust) and anthropogenic sources, like agriculture, mining, smelting, electroplating and other industrial activities (Fargasova, 1994; Theofanis *et al*., 2001; Xie *et al.*, 2006; Verma *et al*., 2007). Such contaminations result in high concentrations of heavy metals in environment, which clearly demonstrate pollution by these metals and contribute one of the most significant factors of degradation of the biosphere. The high concentrations of heavy metals in the environment may be deleterious for biotic lives. Therefore, effective cleanup needs their immobilization to reduce or remove toxicity. The use of phytoremediation can be a cost-effective, environmentally sound, sustainable, *in situ* technology (Salt *et al*., 1998; Prasad, 2003; Zhou and Song, 2004; Erakhrumen, 2007) to remove or stabilize toxic chemicals. It is also a way of concentrating and harvesting valuable metals that are thinly dispersed in the ground, and offers an attractive option for the remediation of contaminated sites. This method suggests significant potential for certain application and permit a much larger site to be restored would generally be possible using more traditional remediation technologies (Fulekar, 2005). The aim of the research is to develop mycorrhizal soil for assessing the

---

*Corresponding author email: mhfulekar@yahoo.com toxicity of heavy metals for phytoremediation to decontaminate the environment.

Medicago sativa has been reported as a potential plant for phytoremediation of heavy metals and grow well in contaminated soils (Baligar *et al*., 1993; Peralta-Videa *et al*., 2004). The presence of heavy metals in the contaminated environment upto the tolerable limit to the plants is of major concern for effective phytoremediation. Mycorrhizosphere influences phytoremediation, therefore the present research study investigated the impact of heavy metals at various concentrations ranging from 5-100 ppm on *M. sativa* as a potential plant in mycorrhizal soil and non mycorrhizal soil. The seed germination and growth of the plants in heavy metal contaminated mycorrhizal soil show the efficiency of plants for phytoremediation. The growth of the plants at the particular concentrations of metals (Cd, Pb and Zn) has been assessed by measuring the percentage of seed germination and morphological characteristics viz. root and shoot growth of the plants. This study will give scope for the phytoremediation of heavy metals using green plants- *M. sativa* in mycorrhizosphere.

MATERIALS AND MEHTODS

Soil sampling and characterization

Alluvial soil used for the experiment was collected from a depth of about 0-15cm along the banks of Surya River, Palghar (located 100km away from Mumbai). The soil was screened through 2mm stainless steel sieve, and stored in a plastic bag at room temperature (27-30^{o}C) until use. The physico-chemical characteristics of the soil were measured by standard methods (Table 1). The content of heavy metals (Cd, Pb and Zn) in soil was estimated by atomic absorption spectrophotometer (APHA, 1998).

Development of Mycorrhizal inoculum

Soil based mycorrhizal inoculum was developed by Pot culture technique at laboratory scale with the help of starter inoculums and using sorghum as a host plant. A starter culture of mycorrhizal fungi (VAM) was procured from Division of Microbiology, IARI, New Delhi. The mixture of 3:1, soil-sand was taken in a pot (5kg capacity with perforated base for proper aeration and drainage of water) and the starter culture of mycorrhizal was mixed thoroughly. Fifty sterilized sorghum seeds were sown in each pot to a depth of 0.5cm. The experiment was carried out in three replicates including control, i.e. without mycorrhizal starter for a period of two and half months. The pots were placed in greenhouse at 27-28^{0}C and watered daily to maintain moisture. After incubation (two and half months), pots were not watered and left for 15 days for rhizo-degradation. The dried roots were chopped and mixed with the same soil and used for the phytoremediation of heavy metals. The physico-chemical parameters and microbial characterization of soil were done during development of mycorrhizal soil at the intervals of 15 days. The mycorrhizal soil was also characterized for its root colonization by trypan blue method of Phillips and Hayman (1970) and spores counts were done by extracting spores by the Wet-sieving and decanting method (Gerdrman and Nichalson, 1963). Bacterial, fungal and Actinomycetes colony forming units (CFUs) were calculated using the standard dilution plate technique of fresh soil suspension on selective media. Bacteria were determined on tryptic soy agar (Martin, 1975). Fungi were estimated on rose bengal agar (Martin, 1950) and Actinomycetes colonies were counted on Kenknight and Munaier's medium. In graphics the total number of microorganisms (bacterial, fungal or Actinomycetes) was expressed as logarithms per g dry soil [log of CFU per gram of dry soil].

Table 1. Physico-chemical characterization of Alluvial soil and mycorrhizal soil*.

Parameters	Methods used	Alluvial Soil	Developed mycorrhizal soil
pH	APHA 1998	7.2	7.3
Electrical conductivity (mMohs)	APHA 1998	0.2	0.34
Moisture (%)	APHA 1998	35	42.2
Water holding capacity (%)	APHA 1998	65	67
Organic carbon (gm/kg)	Walkley-Black method (Jackson, 1973)	72	259
Nitrogen (gm/kg)	APHA 1998	5.8	8.4
Phosphorus (gm/kg)	APHA 1998	0.72	0.81
Sodium (mg/kg)	APHA 1998	23	32
Potassium (mg/kg)	APHA 1998	21	22
Heavy metal (ppm)			NA
Zn	APHA 1998	10.5	
Cd	APHA 1998	BDL	
Pb	APHA 1998	BDL	

*All the values are mean of three replicates. APHA= American Public Health Association; BDL= Below Detection Limit.

Enzyme assays

Acid and alkaline phosphatase [ACP & ALP] activities

Rhizospheric enzyme activities, in particular acid and alkaline phosphatase (Tabatabai and Bremner, 1969; Eivazi and Tabatabai, 1977) were analyzed using colorimetric methods. The enzyme activities were expressed on a dry-weight basis.

Dehydrogenase [DHA] activities

Determination of soil dehydrogenase activity in soils is based on the use of soluble tetrazolium salts [2, 3, 5-triphenyltetrazolium chloride (TTC)], as artificial electron acceptors, which are reduced to red-coloured formazans, extracted and then determined calorimetrically (Casida *et al.*, 1964). The concentration of formazan was calculated from a standard curve. Dehydrogenase activity is expressed as mg formazan formed / 10g of soil per 24h.

Mycorrhizal influence on seed germination and plant growth

The plant species *Medicago sativa* selected for the study of heavy metals toxicity on seed germination and root/ shoot growth in MS and NMS at a varying concentration of heavy metals, so as to decide the concentration of heavy metals which could be taken for the phytoremediation.

The growth medium in the pots consisted soil: sand at the ratio of 3:1 and 20% of mycorrhizal inoculum (developed in laboratory by Pot culture technique) treated as Mycorrhizal soil (MS) used for the toxicity experiment. The dried and sieved soil is treated as Non Mycorrhizal Soil (NMS). Soil was amended with heavy metals: Cd as $Cd(NO_3)_2 \cdot 4H_2O$; Pb as $Pb(NO_3)_2$ and Zn as $ZnSO_4$. The varying concentrations applied for each heavy metal was; 0, 5, 10, 20, 50, 75 and 100 ppm. *Medicago sativa*, var Lucerene CoI seeds were obtained from Ratanshi Agro-Hortitech (Byculla, Mumbai). The healthy seeds of *M. sativa* were surface-sterilized with 0.1% mercuric chloride for 5min, thoroughly rinsed 5-6 times with distilled water to avoid fungal contamination. Ten sterilized seeds of *M. sativa* were sown in 400g all-purpose plastic pots filled with 300g of previously analyzed soil and 20% of mycorrhizal inoculum amended with respective heavy metals (Cd, Pb and Zn) at selected concentrations, viz. 0, 5, 10, 20, 50 75 and 100ppm separately. The pots were randomly placed in a green house at an average diurnal temperature of 25-27^{o}C for 15 days. The moisture was maintained by watering the plants during the experiment.

Determination of seed germination and root/shoot length

Germination rate was determined by counting the numbers of seeds for 7 days, at 24hour intervals. Alfalfa seeds were considered to have germinated when the radical visibly protruded from the seed coat by at least 2mm.

The percentage of seed germination was computed by following formula:

$$\text{Seed germination \%} = \frac{\text{No. of germinated seedlings}}{\text{Total no. of seeds}} \times 100$$

The experiment was carried out for 15 days for studying the effect of heavy metals on plant's growth. A sample of 3 plants from each pot was randomly selected to evaluate the length of the plants. The length of roots and shoots of all plants was measured by Vernier calipers, separately of each concentration of heavy metals and noted for MS and NMS. The length of the roots was measured from the main root apex to the crown of the plant and the shoot's length was measured from the crown of the plant to the main shoot apex.

Statistical analysis

All the experiments were conducted with three replicates and data were analyzed for mean and standard deviation (X± S.D.) using standard statistical methods (Mahajan, 1997).

RESULTS AND DISCUSSION

Phytoremediation is a recent, low cost-effective technology for remediation of heavy metals from the contaminated environment. Mycorrhizal soil provides the suitable environment wherein bacteria, fungi and Actinomycetes associates along with the root zone and plant exudates make the effective rhizosphere. In mycorrhizosphere both microbial enzymes and plant enzymes have propound effect on phytoremediation. Therefore the present research study has been carried out to assess the impact of heavy metals (cadmium, lead and zinc) on seed germination of *Medicago sativa* at varying concentrations, viz. 0, 5, 10, 20, 50, 75 and 100 ppm both in mycorrhizal and non mycorrhizal soil.

Mycorrhizal soil has been developed under controlled conditions using sorghum as a host plant for a period of two and half months. The physico-chemical and mycorrhizal characteristics were assessed during the development process at the interval of 15 days. Physico-chemical properties of alluvial and developed mycorrhizal soil are listed in table 1, which showed pH- 7.3; EC- 0.34; OC- 259; Na- 32; K-22; N-8.4; P-0.81, in developed mycorrhizal soil. pH of the soil is almost neutral and within the recommended value for proper growth and efficient uptake of nutrients and compounds from soil. The organic carbon content was observed to be low i.e. 72gm/kg in collected alluvial soil which increased upto 259g/kg in developed mycorrhizal soil (Fig. 1). However, nitrogen content of the soil was noticed to fall between

5.8 -8.4gm/ kg and phosphorus content in the soil was found varied from 0.72- 0.81gm/kg (Fig. 2). The increase in C/N (12.41 to 30.83) and N/P (8.06 to 10.73) results increase in mycorrhizal colonization. Increase in organic carbon and nitrogen contents found to contribute to the better growth and health of the plants. Sodium and potassium content was found to be constant (Fig. 3). The mycorrhizal soil is containing high nutrients which contribute proper growth and development of the plants.

Mycorrhizal characterization was done by evaluating VAM colonization and spore counts during the development process at the interval of 15 days. The microbial diversity assessed was found to be comprised of bacteria such as *Alcaligens, Bacillus, Pseudomonas, Sarciana, Serratia, Streptococcus;* Fungi -*Asergillus flavus, A. fumigatus, A. niger, Penicillium, Rhizopus, Mucor* and Actinomycetes- *Micromonospora, Nocardia.* The mycorrhizosphere was found rich in microbial assemblages and comprising of total viable counts of bacteria- $7.8x10^{6}$, fungi- $4.6x10^{5}$ and Actinomycetes- $4.4x10^{5}$ per gm of air-dried soil (Fig. 4). The results indicate that spore count and root colonization were enhanced with increasing period of development process (Fig. 5a and 5b). The spore counts were increased from 10 – 576 spores / 100gm mycorrhizal soil from day 0-75, whereas in control soil it was found 10-25 spores/ 100gm from day 0-75. The mycorrhizal root colonization was 0% in MS and CS during the initial stage (0 day] and increased upto 78% on 75 days in MS, while in CS root

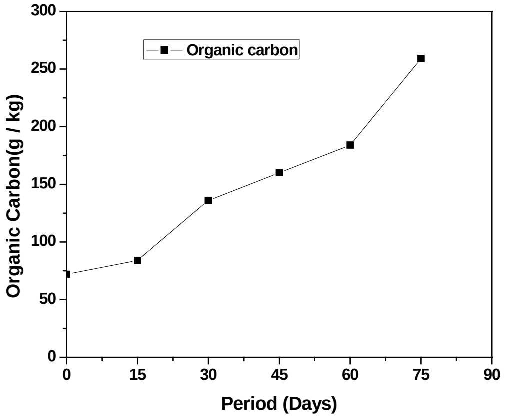

Fig. 1. Organic Carbon contents of the soil during the development of mycorrhizal soil. Organic Carbon was quantified from the soil samples taken at diffenent time intervals of 75 days of process. All the values are mean of three replicates.

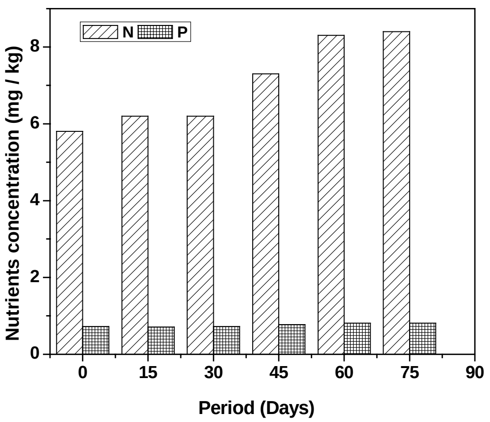

Fig. 2. Nitrogen [N] and phosphorus [P] contents of the soil during the development of mycorrhizal soil. The soil sample was analysed for N and P at the different time intervals of 75 days of process. All the values are mean of three replicates.

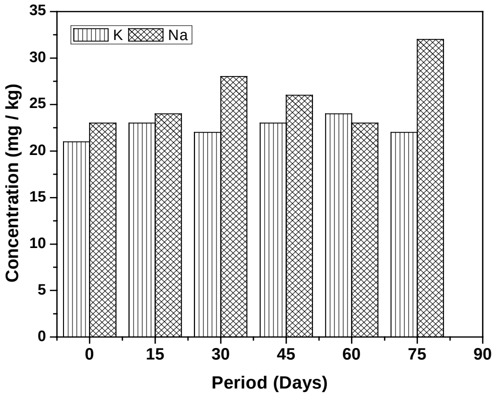

Fig. 3. Potassium [K] and sodium [Na] contents of the soil during the development of mycorrhizal soil. K and Na contents was quantified from the soil samples taken at diffenent time intervals of 75 days of process. All the values are mean of three replicates.

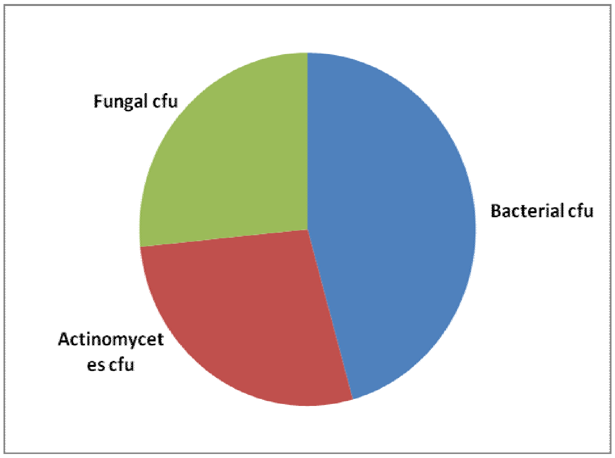

Fig. 4. Bacterial, fungal and Actinomycetes cfu present in the developed mycorrhizal soil. Log cfu/gm of soil. All the values are mean of three replicates.

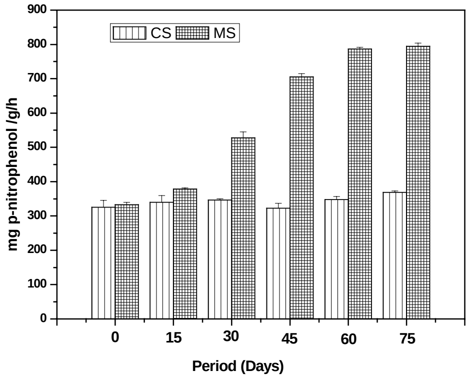

Fig. 6a. Acid phosphatase activity during Mycorrhizal development. CS- Control Soil; MS- Mycorrhizal Soil. All the values are mean of three replicates.

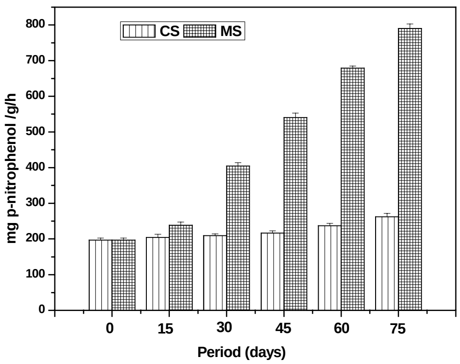

Fig. 6b. Alkaline phosphatase activity during Mycorrhizal development. CS- Control Soil; MS- Mycorrhizal Soil. All the values are mean of three replicates.

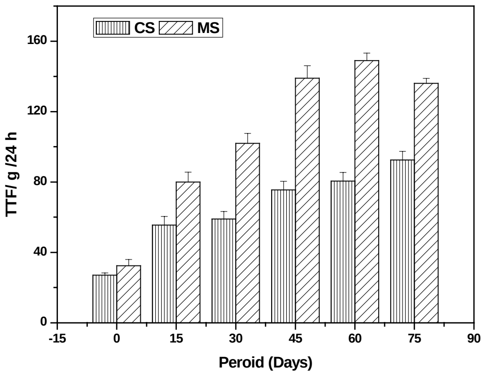

Fig. 7. Dehydrogenase activity during Mycorrhizal development. CS- Control Soil; MS- Mycorrhizal Soil. All the values are mean of three replicates.

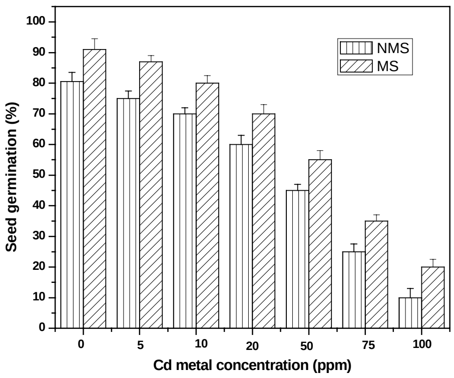

Fig. 8. Seed germination (%) of *Medicago sativa* plants in NMS and MS amended with various concentrations of cadmium metal. All the values are mean of three replicates.

colonization was reported only 6% on 75th days. The final spore count in developed mycorrhizal soil was found to be 546 spores/100gm of soil with 78% of root colonization. High levels of AM colonization observed with low nutrient diffusion rate, such as P, decreasing plant availability. Our results were in accordance and showed AM colonization was higher, when P mineralization was lower and microbial immobilization was higher.

In rhizosphere the enzyme activities released which make the suitable environment for the microbes to grow and multiply in numbers along with the root zone (Dick and Tabatai, 1992; Eivazi and Tabatabai, 1997; Dick *et al*., 2000). The enzyme activities assessed include acid and alkaline phosphatases and dehydrogenase. The results obtained indicate that the soil phosphatases (ACP and ALP) activity significantly increased in all soil samples during development of mycorrhizal soil and were higher in developed mycorrhizal soil comparatively with the control soil (Fig. 6a, 6b). Acid phosphatase activity increased 2.38 times on 75 days while alkaline phosphatase increased 4 times on 75 days. This increase, however, was proportionally higher for the first few days for acid phosphatase activity while in later stages there was increase in alkaline phosphatase activity after successful mycorrhizal colonization. The study reveals that alkaline phosphatase is generally higher when the soil is rich in organic matters. The high levels of organic matter (Fig. 3) in the soil represent sources of energy used by microorganisms that is the reason for microbial biomass and enzyme activities may increase with increasing period of experiment as there is increase in

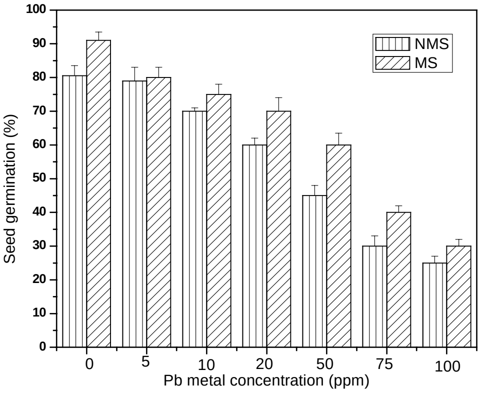

Fig. 9. Seed germination (%) of *Medicago sativa* plants in NMS and MS amended with various concentrations of lead metal. All the values are mean of three replicates.

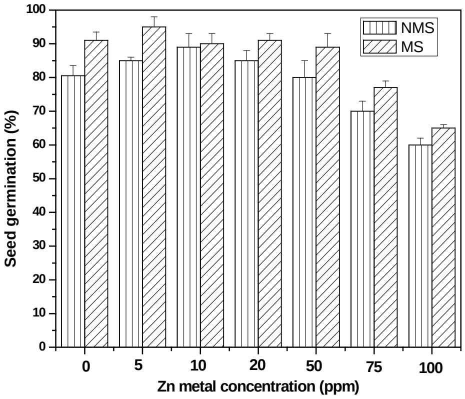

Fig. 10. Seed germination (%) of *Medicago sativa* plants in NMS and MS amended with various concentrations of zinc metal. All the values are mean of three replicates.

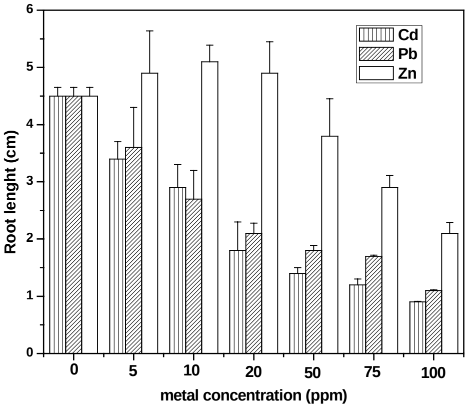

Fig. 11a. Root length of *M. sativa* grown in heavy metals (Cd, Pb and Zn) contaminated non mycorrhizal Soil (NMS). All the values are mean of three replicates.

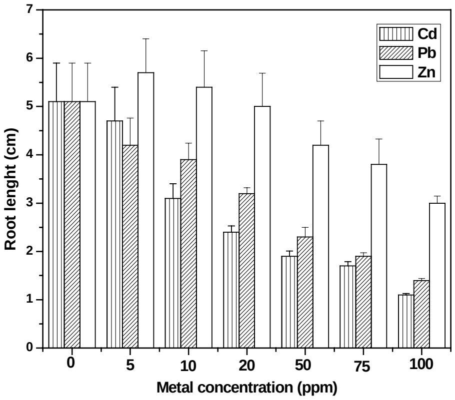

Fig. 11b. Root length of *M. sativa* grown in heavy metals (Cd, Pb and Zn) contaminated mycorrhizal Soil (MS). All the values are mean of three replicates.

organic matter contents. The acid phosphatase increases significantly in the soil with inorganic P. Dehydrogenase enzymes play a significant role in the biological oxidation of soil organic matter by transferring protons and electrons from substrates to acceptors. The data showed that DHA significantly increased during the development of mycorrhizal soil at different time intervals (Fig. 7). DHA activity has increased 4.18 times on 75 days. DHA can associate with changes in the microbial biomass due to long-term soil amendment (Goyal *et al.*, 1993). Mycorrhizosphere soil's bacterial, fungal and Actinomycetes viable plate counts were assessed to relate DHA as indicator of soil microbial activity. The importance of soil microorganisms in these studies has been evaluated in terms of the content of nutrients in the microbial biomass. The increase in enzyme activities and nutrients in particular has been found to have suitable and favourable conditions for the plant growth (Rodrı´guez and Fraga, 1999; Oliveira *et al*., 2009). Mycorrhizosphere provide a direct link between soil and roots, and are renowned for their ability to increase plant mineral nutrients, notably P (Leyval *et al*., 1997; Gaur and Adholeya, 2004; Bush, 2008) and enhance phytoremediation.

In the laboratory setup, the toxicity of heavy metals at varying concentrations 0, 5, 10, 20, 50, 75 and 100ppm were assessed for seed germination and plant growth of *M. sativa* in mycorrhizal soil and non mycorrhizal soil separately. The percentage of seed germination and root/

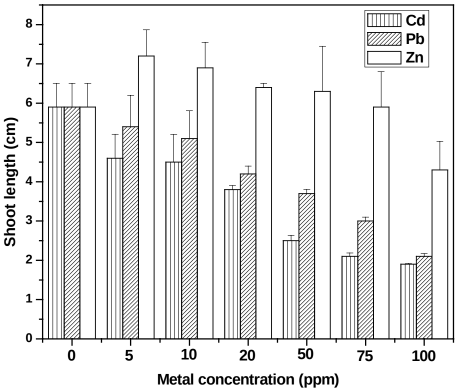

Fig. 12a. Shoot length of *M. sativa* grown in heavy metals (Cd, Pb and Zn) contaminated non mycorrhizal Soil (NMS). All the values are mean of three replicates.

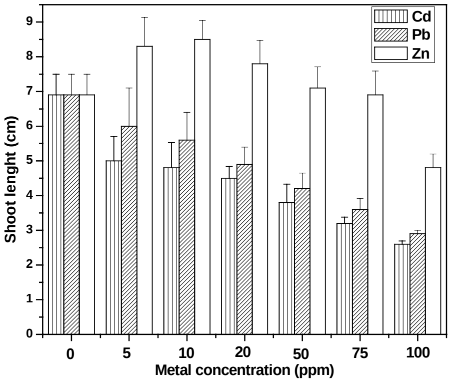

Fig. 12b. Shoot length of *M. sativa* grown in heavy metals (Cd, Pb and Zn) contaminated mycorrhizal Soil (MS). All the values are mean of three replicates.

shoot growth of plants was assessed for each heavy metal. The results showed that the seeds were found grown from a concentration of 0- 100 ppm in MS as well as NMS (Figs. 8-10) of each metal (Cd, Pb and Zn). The percentage of seed germination decreased with increasing concentrations of heavy metals. In NMS the percentage of seed germination for Cd decreased from 75-1% (5-100ppm), Pb was found 79- 25% (5-100ppm), and Zn was 85-60% (5-100 ppm). Besides, in MS the seed germination for Cd was found 87-20%, Pb was 80-30% and Zn was 95-65% from lowers to higher concentrations. Mycorrhizal soil has enhanced the seed germination by 5-20% more than non mycorrhizal soil. The results indicated that *M* .sativa tolerated Cd at 20ppm, however, levels at 50- 100ppm impacted plant growth as measured by plant root/ shoot length. The research findings show that the higher concentrations of the metal i.e. 50, 75 and 100ppm in respect of Cd, Pb and Zn are inhibitory to the growth of the plants in NMS. However in MS the growth was enhanced upto 50ppm in case Cd, Pb and Zn. MS which serve as a biofertilizers and provide condition favourable for seed germination and growth of the plants. Mycorrhizal fungi are an essential component of soil ecosystem. Mycorrhizae are ubiquitous symbiotic associations between plants and soil (Smith and Read, 1997) and their extra radical mycelium form bridges between plant roots and soil, and mediate the transfer of various elements into plants. It has been demonstrated that mycorrhizas could protect plants grown in metal-contaminated soils by enhancing metal retention in root and reducing metal partitioning to shoots (Leyval *et al.*, 2002). There is direct evidence for the strong binding capacity of fungal mycelium to heavy metals, such as Zn and Cd (Chen *et al.*, 2001; Joner *et al.*, 2000). The findings of the present research proved that the nutrients taken up by the mycorrhizal fungi can lead to improved plant growth and reproduction. As a result, the plants grown in MS are often more competitive and better able to tolerate in heavy metals contaminated environment than the NMS.

The effect of heavy metals viz. Cd, Pb and Zn on the growth of root in non mycorrhizal and mycorrhizal soil is illustrated in figure 11a & 11b, respectively. Figure 12a and 12b report the data relative to the effect of metals (Cd, Pb and Zn) on shoot growth of *M. sativa* in non mycorrhizal soil and mycorrhizal soil. Mycorrhizal soil has promoted the roots/ shoots growth of *M. sativa* as compared to non mycorrhizal soil. The increase in metal concentrations in the germination medium leads to the reduction in roots/ shoots growth of the plants. The root length of *M. sativa* in mycorrhizal soil was found 38% -Cd, 54% -Pb and 65% -Zn more from the non mycorrhizal soil. Mycorrhizal soil has enhanced the shoot growth upto 23% (Cd), 26% (Pb) and 50% (Zn) more than non mycorrhizal soil. The increase in metal concentrations in the germination medium leads to the reduction in roots/ shoots growth of the plants. Research findings show that the growth of roots and shoots of *M. sativa* was found in order of Cd < Pb < Zn. Zn being the micro nutrient was found growth higher than the Cd and Pb. Cd was found phytotoxic for the growth as compared to Pb and Zn. Pb accumulates in the root and reduces the length of root and growth of plant. Whereas, Cd exposure to be toxic to roots and shoots proportionately. Cd is more phytotoxic to plant- *M. sativa.* The result of present research proved that seed germination and plant's growth were much better in MS compared to NMS. Mycorrhizae have enhanced the metal tolerance efficiency of alfalfa plants by providing high nutrients. Galli *et al.* (1994) suggested that mycorrhizae can play a crucial role in protecting plant roots from heavy metals.

Though Zn is an essential trace element for plants, it is highly toxic at elevated concentrations. Researchers have reported that the range of beneficial concentration of Zn is often very narrow for most plant species (Küpper *et al*., 2000; Clemens, 2006). On the other hand, Pb and Cd are widely known to be non-essential elements for plants, and both cause adverse effects on the plant's biochemical mechanisms, resulting in various symptoms of Phytotoxicity, such as chlorosis, reduction of biomass, inhibition of root elongation and finally death (Milone *et al*., 2003). Peralta *et al*. (2001) found that 20 and 40ppm of Cu, Cd and Ni inhibited ability of seeds of *Medicago sativa* to germinate and grow in the contaminated solid medium, whereas Zn did not reduce the seed germination. Compared to the control, at and above 10ppm Cr (VI) concentration, significant inhibitory effect on seedling growth of tested rice cultivars were detected by Xiong (1998). The experiment conducted by Peralta-Videa *et al*. (2004) showed that the tolerance of alfalfa plants to Cd, Cu and Zn was positively correlated to the age of the plants. They also reported that after four days germination, Cr, Cd, Ni, except Zn, had lethal effects on the alfalfa seedlings. The experiments of Gardea-Torresdey *et al*. (1999) have shown the ability of *M. sativa* to bind several metal ions under multi-contaminant conditions.

The seed germination trails have relevance in selection of plants and metal's concentrations in for their prospective use in phytoremediation. The research study shows that the plants of *M. sativa* were growing in mycorrhizal soil amended with heavy metals with a range of 5-50ppm. However the higher concentrations i.e. 75 and 100ppm were found to be toxic for plant growth and survival. The present research has proved the effectiveness of mycorrhizosphere for resistance of heavy metals which can be efficiently used for remediation of heavy metals using the recent advanced technique – phytoremediation.

CONCLUSION

The present research study deals with the development of mycorrhizal soil and the significance of enzymes released by plants and microbes in rhizosphere to tolerate the toxicants and bioaccumulate/ uptake of heavy metals. Heavy metals concentrations ranging from 5, 10, 20 and 50ppm were found tolerance by the seed of *Medicago sativa.* The heavy metals above these concentrations (17 and 100ppm) were found inhibitory for the growth of the plants. The study has proved the significance of mycorrhizal soil as compared to non mycorrhizal soil for phytoremediation of heavy metals upto a concentration of 50 ppm, which could be used for the remediation of heavy metals to clean up the environment.

ACKNOWLEDGEMENT

Authors are grateful to Board of Research in Nuclear Sciences (BRNS), Department of Atomic Energy (DAE) Government of India for sponsoring the research project and rendering financial assistance to Ms. Anamika Singh.

REFERENCES

APHA, AWWA. and WPCF. 1998. Standard Methods for the Examination of Water and Waste water. American Public Health Association/American Waterworks Association/ Water Environmental Federation, Washington DC.

Baligar, VC., Campbell, TA. and RJ. Wright. 1993. Differential responses of alfalfa clones to aluminum-toxic acid soil, J. Plant Nutrition. (16):219-233.

Bush, JK. 2008. The potential role of mycorrhizae in the growth and establishment of Juniperus seedlings. Eds. Van Auken, OW. Western North American Juniperus Communities. Springer, New York, pp. 111-130.

Carvalho, SM., Cacador, I. and Martins-Loucao, MA. 2006. Arbuscular mycorrhizal fungi enhance root cadmium and copper accumulation in the roots of the salt marsh plant Aster tripolium L. Plant Soil. 285:161-169.

Casida, L., Johnson J. and Klein, D. 1964. Soil dehydrogenase activity. Soil Sci. 98:371-376.

Chen, BD., Christie, P. and Li, XL. 2001. A modified glass bead compartment cultivation system for studies on nutrient uptake by arbuscular mycorrhizal. Chemosphere. 42:185-192.

Clemens, S. 2006. Toxic metal accumulation, responses to exposure and mechanisms of tolerance in plants. Biochemie. 88:1707-1719.

Daniell, TJ., Hodge, A., Young JPW. and Fitter, A. 1999. How many fungi does it take to change a plant community? Trends Plant Science. 4:81-82.

del Val, C. 1999. Diversity of arbuscular mycorrhizal fungus population in heavy metal contaminated soil. Appl. Environ. Microbiol. 65:718-723.

Dick, WA. and Tabatai, MA. 1992. Potential uses of soil enzymes. In: Soil Microbial Ecology: Applications in Agricultural and Environmental Management. Ed. Metting, FB Jr. Marcel Dekker, New York. pp. 95-127.

Dick, WA., Cheng L. and Wang, P. 2000. Soil acid and alkaline phosphatase activity as pH adjustment indicators. Soil Biol. Biochem. 32:1915-1919.

Eivazi, F. and Tabatabai, MA. 1977. Phosphatases in soils. Soil Biology Biochemistry. 9:167-172.

Erakhrumen, AA. 2007. Phytoremediation: an environmentally sound technology for pollution prevention, control and remediation in developing countries. Educational Research and Review. 2(7):151-156.

Fargasova, A. 1994. Effect of Pb, Cd, Hg, As, and Cr on germination and root growth of Sinapis alba seeds, Bull. Environ. Contam. Toxicol. 52:452-456.

Fulekar, MH. 2005. Environmental Biotechnology, Oxford & IBH Publishing Co. Pvt. Ltd.

Galli, U., Schuepp, H. and Brunold, C. 1994. Heavy-metal binding by mycorrhizal fungi. Physiol. Plantarum 92:364-368.

Gardea-Torresdey, JL., Tiemann, KJ., Gamez, G. and Dokken, K. 1999. Effects of chemical competition for multi-metal binding by *Medicago sativa (*alfalfa) Journal of Hazardous Materials. 69:41-51.

Gaur, A. and Adholeya, A. 2004. Prospects of arbuscular mycorrhizal fungi in phytoremediation of heavy metal contaminated soils. Current Science. 86:528-534.

Gerdemann, JW. and Nicholson, TH. 1963. Spores of mycorrhizal endogone species extracted from soil by wet sieving and decanting. Transactions of the British Myological Society. 46:235-244.

Goyal, S., Mishra, MM., Dhankar, SS., Kappor, KK. and Batra, R. 1993. Microbial biomass turnover and enzyme activities following the application of farmyard manure to field soils with and without previous long-term applications. Biol. Fert. Soils 15:60-64.

Joner. EJ., Briones, R. and Leyval, C. 2000. Metal-binding capacity of arbuscular mycorrhizal mycelium. Plant Soil. 226:227-234.

Korade, DL. and Fulekar, MH. 2009. Effect of organic contaminants on seed germination of *Lolium multiflorum* in soil. Biology and Medicine. 1 (1):28-34.

Kirk, PM., Cannon, PF., David, JC. and Stalpers, J. 2001. Ainsworth and Bisby's Dictionary of the Fungi (9th ed.), CAB International, Wallingford, UK.

Küpper, H., Lombi, E., Zhao Fj. and McGrath, SP. 2000. Cellular compartmentation of cadmium and zinc in relation to other elements in the hyperaccumulator *Arabidopsis halleri*. Planta. 212:75-84.

Leyval, C., Turnau, K. and Haselwandter, K., 1997. Effect of heavy metal pollution on mycorrhizal colonization and function: physiological, ecological and applied aspects. Mycorrhiza. 7:139-153.

Leyval, C., Joner, EJ., del Val, C. and Haselwandter, K. 2002. Potential of arbuscular mycorrhizal fungi for bioremediation. In: Mycorrhizal Technology in Agriculture. Eds. Gianinazzi, S., Schuepp, H., Barea, JM., Haselwandter, K. and Birkhauser, Verlag, Basel Switzerland. pp 175-186.

Mahajan, BK. 1997. Methods in Biostatistics for medical students and research workers (6th ed.), Jaypee Brothers, New Delhi:.

Martin, JP. 1950. Use of acid. Soil Sci. 69:215-232.

Martin, JK., 1975. Comparison of agar media for counts of viable soil bacteria. Soil Biol. Biochem. 7:401-402.

Miller, RM. and Jastrow, JD. 2000. Mycorrhizal fungi influence soil structure. In: Arbuscular Mycorrhizae: Physiology and Function. Eds. Kapulnik, Y. and Douds, DD. , Kluwer Academic Publishers, Dordrecht, pp 3-18

Milone, MT., Sgherri C., Clijsters, H. and Navari-Izzo, F. 2003. Antioxidative responses of wheat treated with realistic concentration of cadmium. Envron. Exp. Bot. 50:265-276.

Oliveira, CA., Alves, VMC., Marriel, IE., Gomes, EA., Scotti, MR., Carneiro, NP., Guimara, CT., Schaffert, RE. and Sa´, NMH. 2009. Phosphate solubilizing microorganisms isolated from rhizosphere of maize cultivated in an oxisol of the Brazilian Cerrado Biome. Soil Biology & Biochemistry. 41:1782-1787.

Prasad, MNV. 2003. Phytoremediation of metal-polluted ecosystems: hope for commercialization. Russian Journal of Plant Physiology. 50:764-780

Peralta, JR., Gardea-Torresdey, JL., Tiemann, K.J., Gomez, E., Arteaga, S., Rascons, E. and Parsons, JG. 2001. Uptake and effects of five heavy metals on seed germination and growth in Alfalfa (*Medicago sativa L.*). Bulletin of Environmental Contamination and toxicology, 727-734.

Peralta-Videa, JR., de la Rosa, G., Gonzalez, JH. and Gardea-Torresdey, JL. 2004. Effects of the growth stage on the heavy metal tolerance of alfalfa plants. Advances in Environmental Research. 8:679-685.

Phillips, JM. and Hayman, DS. 1970. Improved procedure for clearing roots and staining parasitic and vesicular arbuscular mycorrhizal fungus for rapid assessment of infection. Transactions of the British Myological Society. 55:158-161.

Rodrı´guez, H. and Fraga, R. 1999. Phosphate solubilizing bacteria and their role in plant growth promotion. Biotechnology Advances. 17:319-339.

Salt, DE., Smith, RD. and Raskin, I. 1998. Phytoremediation, Annual Review of Plant Physiology 49:643-668.

Sieverding, E. 1991. Vesicular-Arbuscular Mycorrhiza Management. Technical Cooperation-Federal Republic of German. Eschborn.

Smith, SE. and Read, DJ. 1997. Mycorrhizal Symbiosis. Academic Press,San Diego, USA.

Tabatabai, MA. and Bremner, JM. 1969. Use of *p*-nitrophenyl phosphate for assay of soil phosphatase activity. Soil Biology Biochemistry. 1:01-307.

Theofanis, ZU., Astrid, S., Lidia, G. and Calmano, WG. 2001. Contaminants in sediments: remobilization and demobilization, Sci. Total Environment. 266:195-202.

Xie , RK., Seip, HM., Wibetoe, G., Nori, S. and McLeod, CM. 2006. Heavy coal combustion as the dominant source of particulate pollution in Taiyuan, China, corroborated by high concentrations of arsenic and selenium in PM_{10}. Science of total Environment. 370:409-415.

Xiong, Z.T. 1998. Lead uptake and effects on seed germination and plant growth in a Pb hyperaccumulator Brassica pekinensis Rupr. Bull. Environ. Contam. Toxicol., (6):258-291.

Zhou, QX. and Song, YF. 2004. Principles and Methods of Contaminated Soil Remediation. Science Press, Beijing, China.

Received: Feb 4, 2010; Accepted: Sept 3, 2010

SENRA Academic Publishers, Burnaby, British Columbia
Vol. 4, No. 3, pp. 1303-1309, October 2010
Online ISSN: 1920-3853; Print ISSN: 1715-9997

Canadian Journal of pure&applied sciences

CHARACTERIZATION OF ZnO NANOPOWDERS SYNTHESIZED BY THE DIRECT PRECIPITATION METHOD

*HK Farag[1], Z M Hanafi[1], M Dawy[2] and EM Abd El Aziz[1]
[1]Inorganic Chemistry Department, National Research Centre, Dokki, Cairo
[2]Physical Chemistry Department, National Research Centre, Dokki, Cairo, Egypt.

ABSTRACT

The present paper deals with the synthesis of zinc oxide nanoparticles via a direct precipitation method using zinc acetate dihydrate as a precursor. The synthesized ZnO powder was characterized by means of XRD, UV-Visible and IR spectroscopy, SEM-EDX and TG-DTA. The XRD results reveal that the synthesized ZnO has the wurtzite phase structure with a crystallite size of about 50nm. The ZnO particles are spherical in shape and only zinc and oxygen were detected by EDX analysis signifying the high purity of the synthesized ZnO. The UV-Vis. spectrum of the ZnO powder indicates a band gap of about 3.2 eV, showing a slight red shift compared to the band gap of the bulk ZnO (3.37 eV). The prepared ZnO powder exhibits a specific surface area of 16.5 m^2 g^{-1}, determined by Brunauer-Emmett-Teller (BET) equation.

Keywords: Zinc oxide, direct precipitation, characterization, band gap.

INTRODUCTION

In recent times, wide bandgap semiconductor oxides such as ZnO, TiO_2 or SnO_2 have attracted extensive attention due to their wide range of technological applications including gas sensing, photocatalysis, piezoelectricity and optoelectronics (Carotta *et al*., 2005). Among semiconductor oxides ZnO has found much interest. Its high gas sensitivity and chemical stability make ZnO a potential candidate for gas sensing (Martins *et al*., 2004 and Carotta *et al*., 2009). The wide band gap of ZnO (3.37 eV) as well as its high exciton binding energy (60 meV) promote its application as light emitting or laser diodes (Alivov *et al*., 2003). ZnO nanorodes have been characterized for the application as hydrogen gas sensors (Wang *et al*., 2005). Jiaquiang *et al*. (2005) have reported the gas sensing properties of ZnO nanorodes. ZnO powders have successfully been employed as electrode materials for dye-sensitized solar cells (DSSCs) as an alternative to TiO_2 (Redmond *et al*., 1994). Furthermore, nanocrystalline ZnO is generally used in cosmatics because of its ability to protect from ultraviolet rays and its capability to kill and restrain bacterium (Deng *et al*., 2001).

There are several methods for synthesis of ZnO via solution based processes such as, e.g., sol-gel (Gao *et al*., 2007; Rani *et al*., 2008), hydrothermal (Xu *et al*., 2004), direct precipitation (Sigoli *et al*., 1997, Music *et al*., 2002 ; Bitenc *et al*., 2008) and electrochemical routes (Nyffenegger *et al*., 1998). Direct precipitation from aqueous solutions of zinc salts, such as $ZnCl_2$, $ZnSO_4$, $ZnNO_3$, in presence of ammonium carbonate or urea is a widely used method for synthesis of nanostructured ZnO. This method involves the precipitation of zinc hydroxyl carbonate (basic zinc carbonate) precursors which transform to ZnO via thermal decomposition at temperatures above 300°C.

In the present paper we have employed the direct precipitation method to synthesize nanocrystalline ZnO by using zinc acetate dihydrate as a precursor. Different microscopic and spectroscopic techniques were used to characterize the synthesized ZnO powder, such as scanning electron microscopy with energy dispersive X-ray (SEM-EDX), X-ray diffraction (XRD), infrared (IR), ultraviolet-visible (UV-vis.), thermogravimetric (TG) and differential thermal analysis TG-DTA. The surface area of the ZnO powder was determined by BET (Brunauer-Emmett-Teller) measurements.

MATERIALS AND METHODS

EXPERIMENTAL

Zinc acetate dihydrate (Aldrich, 99.99 %) and anhydrous ammonium carbonate (Alfa 99.99%) were used without further purification as the starting materials for the synthesis of ZnO. Distilled water was used to prepare the precursor solutions. Sodium hydroxide (Sigma-Aldrich 98%) was used to adjust the pH.

The phase compositions of the prepared powder were analyzed by X-ray diffraction (XRD) using a Siemens D-5000 diffractometer with CoK_α radiation. The morphology and composition of the obtained ZnO powder were investigated by means of a high resolution field emission scanning electron microscope (Carl Zeiss DSM

---

*Corresponding author email: msherif888@yahoo.com

982 Gemini) and energy dispersive X-ray analyzer. UV/Vis absorption spectrum was recorded on a Hewlett-Packard 8452A diode array spectrophotometer. The IR spectrum was recorded using a Bruker-Vector 22 spectrometer. The KBr pellet technique with about 1 wt. % of sample was used for sample preparation.

Thermal gravimetric (TG) and differential thermal analysis (DTA) were carried out by a NETZSCH STA 409 PC thermal analyzer at a heating rate of 10 °C /min. starting from room temperature up to 700°C in air. Nitrogen sorption results were obtained using a Quantachrome Autosorb-1 automated gas sorption analyser. Prior to sorption measurements, the sample was degassed for 6 hours at 150^{o}C under pressure of 100 µTorr. The surface area was calculated by the BET (Brunauer-Emmett-Teller) equation.

RESULTS AND DISCUSSION

Synthesis of ZnO nanoparticles

The nanocrystalline ZnO powder was prepared using $Zn(CH_3COO)_2.2H_2O$ and anhydrous $(NH_4)_2CO_3$ as starting materials by a direct precipitation method. Appropriate amounts of both $Zn(CH_3COO)_2.2H_2O$ and $(NH_4)_2CO_3$ were separately dissolved in 100mL distilled water to prepare 0.5M and 1M solutions, respectively. Then the two solutions were carefully mixed under continuous stirring and then heated at 60^{o}C for 3 hours to complete the reaction. A white precipitate of basic zinc carbonate was the reaction product. The resulting precipitate was filtered and washed several times with distilled water. Afterwards, the obtained precipitate was calcined at 450^{o}C for 3 hours. The calcination was carried out in order to thermally decompose the formed basic zinc carbonate to ZnO.

Characterization of the synthesized ZnO

XRD and SEM-EDX

The XRD pattern of the synthesized ZnO powder is shown in figure 1. It is clearly seen that ZnO is highly crystalline and all diffraction peaks are well indexed to the diffraction pattern of wurtzite phase of ZnO (JCPDS 36-1451). The inset of figure 1 shows the broadening of the main diffraction peaks, (100), (002) and (101). As seen the recorded peaks are broad indicating the small crystallite size of the synthesized ZnO. The average crystallite size of ZnO was estimated according to Scherrer's equation (Scherrer 1918):

$$d = 0.9\lambda / \beta_{1/2} \cos \theta \qquad (1)$$

where, d is the crystallite size, λ the X-ray wavelength (1.7889 Å for CoKα), $\beta_{1/2}$ the full-width half maximum

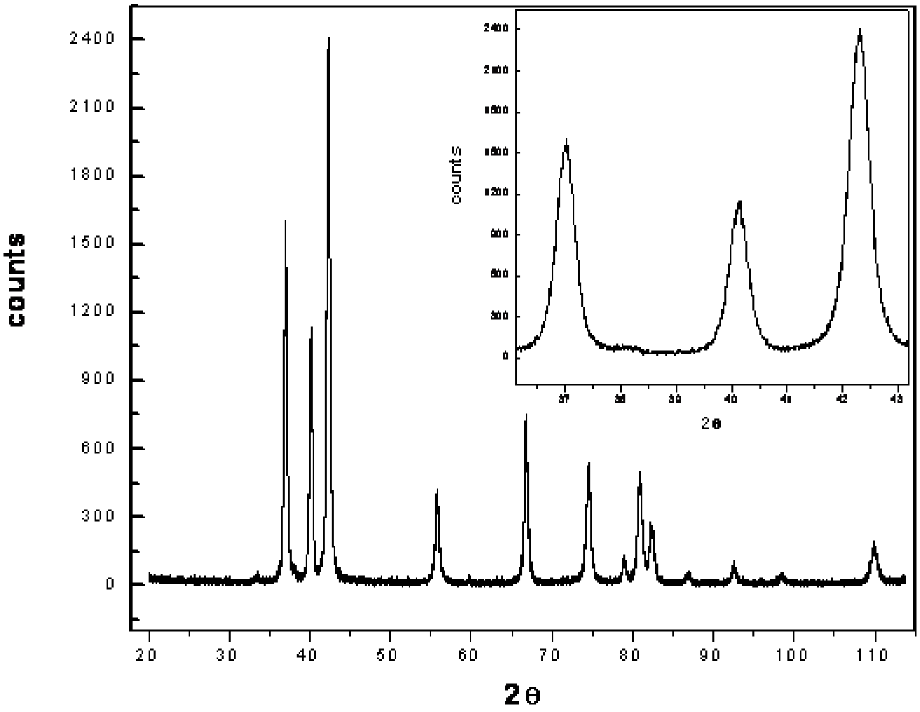

Fig. 1. XRD patterns of the synthesized ZnO powder.

(FWHM) and θ is the diffraction angle. The average size of ZnO crystallites was found to be 45nm.

The prepared ZnO powder was characterized by means of high resolution field–emission scanning electron microscopy (SEM) and energy dispersive X-ray (EDX) to explore surface morphology and composition, respectively. The SEM micrograph of figure 2 shows the morphology of a synthesized ZnO sample. As can be seen, the prepared ZnO contains very fine particles with an average size of about 50nm (Fig. 2a) which is in agreement with the XRD results. The EDX analysis was randomly performed on three different areas across the investigated sample to determine the zinc to oxygen ratio. As manifested in the EDX profile of figure 2b, only zinc and oxygen are detected indicating the high purity of the synthesized ZnO. Quantitatively the oxygen to zinc weight ratio was found to be approximately 1 to 4, respectively, indicating the stoichiometric formation of ZnO.

Nitrogen adsorption-desorption measurements were also carried out in order to determine the specific surface area of the synthesized ZnO. The prepared ZnO powder exhibits a specific surface area of 16.5 m^2 g^{-1}, determined by Brunauer-Emmett-Teller (BET) equation. Generally, the nanocrystalline materials should exhibit a high surface area. However, the relatively low surface area of the synthesized nanocrystalline ZnO might be attributable to agglomeration of clusters of nanoparticles.

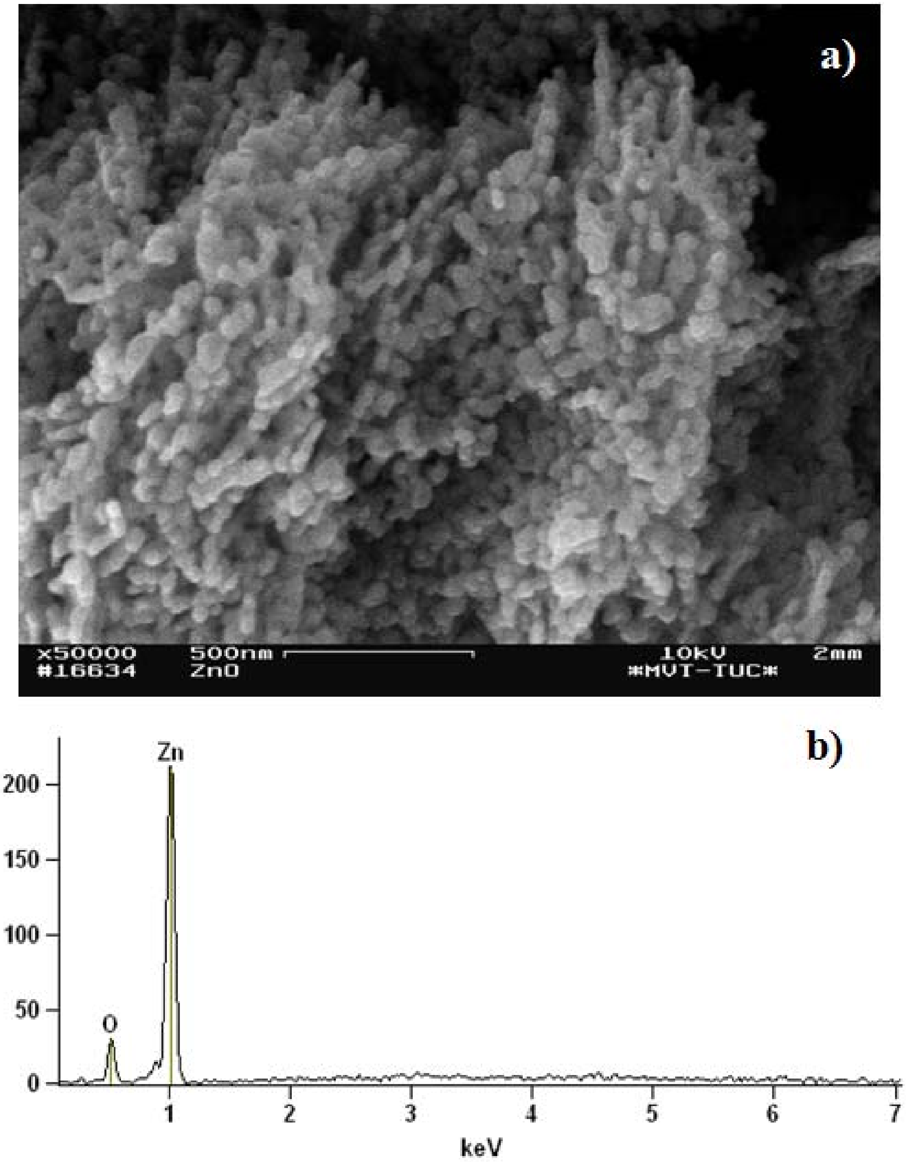

Fig. 2 SEM-EDX analysis of the prepared ZnO.

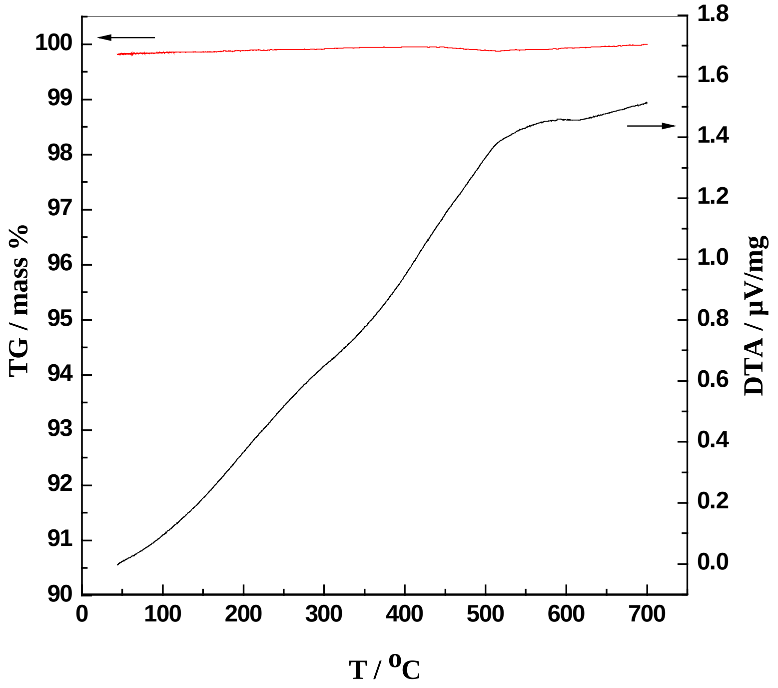

Fig. 3. DTA-TG curves of the prepared ZnO.

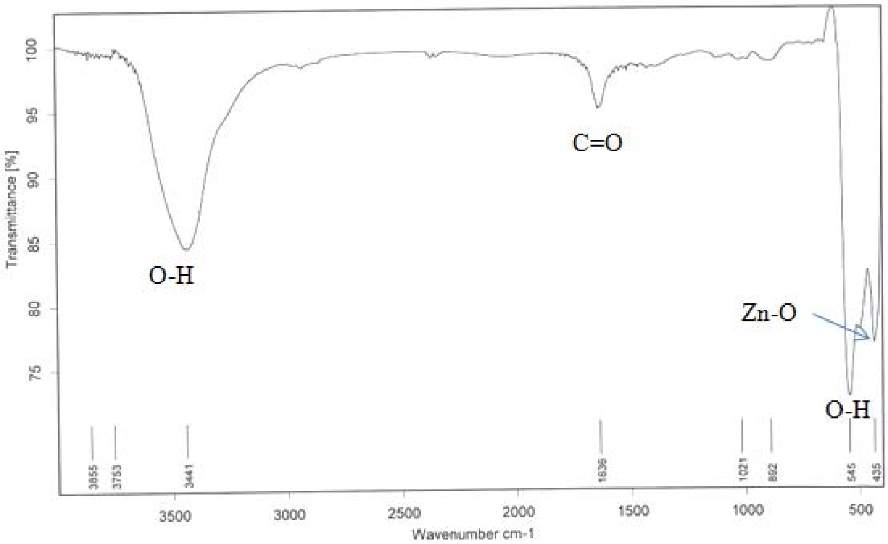

Fig. 4. IR spectrum of the prepared ZnO.

DTA-TG

The differential thermal analysis – thermogravimetric (DTA-TG) curves of the prepared ZnO are displayed in figure 3. It is clearly seen that the TG curve does not show any significant weight loss in the studied temperature range. This is not surprising as the sample was calcined at 450^{o}C for 3hours. Therefore, the physically adsorbed water was totally evaporated. Furthermore, calcination has led to complete thermal transformation into ZnO. The DTA curve does not exhibit defined endothermic/exothermic peaks, however, an exothermic rise in the DTA curve is recorded from the

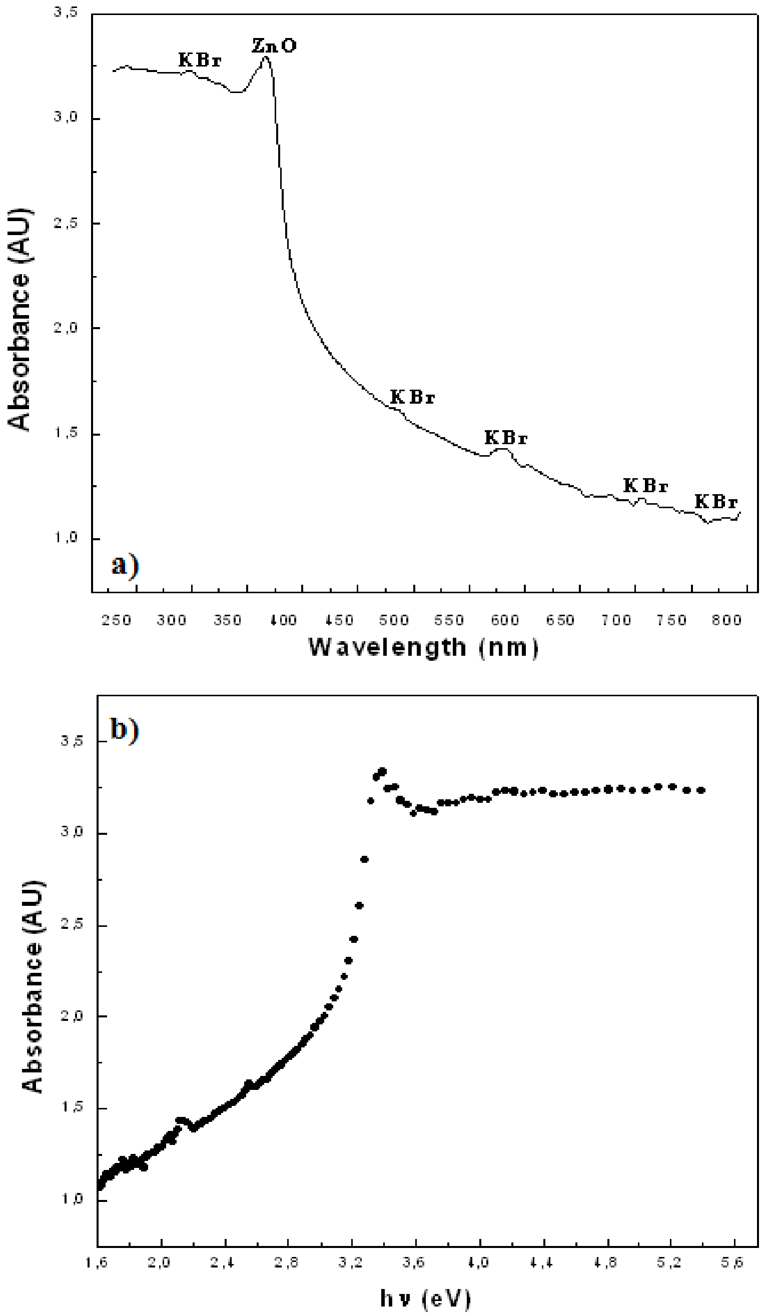

Fig. 5. UV-Visible spectrum of the prepared ZnO, a) absorbance vs. wavelength and b) absorbance vs. energy of the incident photon.

beginning up to 550 °C. This could be ascribed to the crystallization of the wurzite phase.

FT-IR Spectroscopy

The IR spectrum of the prepared ZnO powder is shown in figure 4. A significant absorption peak is observed at 3441 cm^{-1} as a result of O-H stretching vibrations. The peak observed at 1636 cm^{-1} is due to C=O stretching of carboxylate anions adsorbed on the surface of ZnO particles. The detection of such a peak indicates the difficulty of complete removing of the adsorbed carboxylate anions (from the zinc acetate precursor) even after extensive washing of the synthesized ZnO powder. The peak observed at 545 cm^{-1} is assigned to O-H bending vibrations. Finally, the recorded peak at 435 cm^{-1} is ascribed to Zn-O stretching vibrations. The obtained IR results are consistent with literature data; see (Maensiri *et al*., 2006).

UV-Visible Spectroscopy

The band gap energy (E_g) is an important property of semiconductors as it determines their applications in electronics in general. In crystalline materials the (E_g) value is directly obtained from the absorption in the UV-visible region. The peak position of the absorption band of semiconductors can be well defined from the UV spectrum and hence, the band gap energy can be obtained. The UV-vis. absorption spectrum of the as-obtained ZnO powder is shown in figure 5a. Besides the standard weak peaks of KBr, the spectrum shows a significant absorption peak at 384 nm which is typical for ZnO (Shen, 2006). Figure 5b displays the absorption spectrum as a function of energy of the incident photon. The band gap energy (E_g) of the prepared ZnO powder was determined using the following equation:

$$\alpha (h\nu) = A (h\nu - E_g)^{m/2} \qquad (2)$$

where, α is the absorption coefficient, h is the Planck's constant, ν is the frequency of the incident photon and m = 1 represents a direct transition between valance and conduction bands. From the UV-vis. spectrum (Fig. 5b) the (E_g) was obtained by extrapolating a straight line from the absorption spectrum to the zero absorbance; $E_g = h\nu$ when α is zero. The results indicate a band gap of about 3.2 eV, showing a slight red shift compared to 3.37 eV for the bulk ZnO. This might be attributed to the agglomeration of ZnO particles.

CONCLUSIONS

In the present paper we have employed the direct precipitation method to synthesize nanocrystalline ZnO by using zinc acetate dihydrate as a precursor. Different microscopic and spectroscopic techniques were used to characterize the synthesized ZnO powder, SEM-EDX, XRD, IR, UV-vis., TG-DTA. The XRD results indicate that the synthesized ZnO has the wurtzite (hexagonal) structure with a crystallite size of about 45nm. The UV-vis. spectrum of the ZnO powder reveals a band gap of about 3.2 eV, showing a slight red shift. The prepared ZnO powder exhibits a specific surface area of 16.5 $m^2 g^{-1}$, determined by Brunauer-Emmett-Teller (BET) equation.

REFERENCES

Alivov, Ya.I., Kanilina, EV, Cherenkov, AE, Look, DC, Ataev, BM., Omaev, AK., Chukichev, MV. and Bagnall, DM. 2003. Fabrication and characterization of n-ZnO/p-AlGaN heterojunction light-emitting diodes on 6H-SiC substrates. Appl. Phys. Lett. 83: 4719-4721.

Bitenc, M., Marinsek, M. and Orel, ZC. 2008. Preparation and characterization of zinc hydroxide carbonate and porous zinc oxide particles. J. Eur. Ceram. Soc. 28**:**2915-2921.

Carotta, MC., Cervi, A., di Natale, V., Gheradi, S., Giberti, A., Guidi, V., Puzzovio, D., Vendemiati, B., Martinelli, G., Sacerdoti, M., Calestani, D., Zappettini, A., Zha, M. and Zanotti, L. 2009. ZnO gas sensors: A comparison between nanoparticles and nanotetrapods-based thick films. Sens. Actuators B. 137:164-169.

Carotta, MC., Guidi, AV., Malagù, C., Vendemiati, B. and Martinelli, G. 2005. Gas sensors based on semiconductor oxides: Basic aspects onto materials and working principles. Mater. Res. Soc. Symp. Proc. 828:173-184.

Deng, HM., Ding, J., Shi, Y., Liu XY. and Wang, J. 2001. Ultrafine zinc oxide powders prepared by precipitation/mechanical milling. J. Mater. Sci. 36:3273-3276.

Gao, YP., Sisk,CN. and Hope-Weeks, LJ. 2007. A sol-gel route to synthesis monolithic zinc oxide aerogels. Chem. Mater. 19:6007-6011.

Jiaquiang, X. Yuping, C., Yadong, L. and Jianian, S. 2005. Gas sensing properties of ZnO nanorodes prepared by hydrothermal method. J. Mater. Sci. 40:2919-2921.

Maensiri, S., Laokul, P. and Promarak, V. 2006. Synthesis and optical properties of nanocrystalline ZnO powders by a simple method using zinc acetate dihydrate and poly(vinyl pyrrolidone). J. Cryst. Growth 289:102-106.

Martins, R., Fortunato, E., Nunes, P., Ferreira, I., Marques, A., Bender, M., Katsarakis, N., Cimalla, V. and Kiriakidis, G. 2004. Zinc oxide as an ozone sensor. J. Appl. Phys. 96:1398-1408.

Music, S., Dragcevic, D., Maljkovic, M. and Popovic, S. 2002. Influence of chemical synthesis on the crystallization and properties of zinc oxide. Mater. Chem. Phys. 77**:**521-530.

Nyffenegger, RM., Craft, B., Shaaban, M., Gorer, S., Erley, G. and Penner, RM. 1998. A hybrid electrochemical/chemical synthesis of zinc oxide nanoparticles and optically intrinsic thin films. Chem. Mater.10:1120-1129.

Rani, S., Suri, P., Shishodia, PK. and Mehra, RM. 2008. Solar Energy Mater. & Solar Cells. Synthesis of nanocrystalline ZnO powder via sol-gel route for dye-sensitized solar cells. 92:1639-1645.

Redmond, G., Fitzmaurice, D. and Graetzel, M. 1994. Visible-light sensitization by cis-bis(thiocyanato)bis(2,2-bipyridyl-4,4-dicarboxylato)ruthenium(II) of a transparent nanocystalline ZnO film prepared by sol-gel techniques. Chem. Mater. 6:686-691.

Scherrer, P. 1918. The Scherrer Formula for X-Ray Particle Size Determination. Göttinger Nachrichten. 2:98-100.

Shen, L., Bao, N., Yanagisawa, K., Domen, K., Gupta, A. and Grimes, CA. 2006. Direct synthesis of ZnO nanoparticles by a solution-free mechanochemical reaction. Nanotechnology. 17:5117-5123.

Sigoli, FA., Davolos, MR. and Jafelicci Jr., M. 1997. Morphological evolution of zinc oxide originating from zinc hydroxide carbonate. J. Alloys Comp. 262-263:292-295.

Wang, HT., Kang, BS., Ren, F., Tien, LC., Sadik, PW., Norton, DP., Pearton, SJ. and Lin, J. 2005. Hydrogen-selective sensing at room temperature with ZnO nanorods. App. Phys. Lett. 86:243503.

Xu, HY., Wang, H., Zhang, YC., He, WL., Zhu, MK., Wang, B. and Yan, H. 2004. Hydrothermal synthesis of zinc oxide powders with controllable morphology. Ceram. Inter. 30:93-97.

Received: July 9, 2010; Accepted: Aug 26, 2010

SENRA Academic Publishers, Burnaby, British Columbia
Vol. 4, No. 3, pp. 1311-1314, 2010
Online ISSN: 1920-3853; Print ISSN: 1715-9997

Canadian Journal of pure&applied sciences

LIGHT D WAVE MESON SPECTRUM IN A NON-RELATIVISTIC QUARK MODEL WITH INSTANTON INDUCED INTERACTION

Antony Prakash Monteiro and *KB Vijaya Kumar
Department of Physics, Mangalore University, Mangalagangothri, Mangalore, 574199, India

ABSTRACT

The mass spectrum of the D wave mesons has been investigated in the frame work of non-relativistic quark model (NRQM). The Hamiltonian used in the investigation has kinetic energy, confinement potential, one-gluon-exchange potential (OGEP) and instanton induced quark-antiquark interaction (III). The calculated D wave meson masses are in agreement with the experimental D wave meson masses. The respective role of III and OGEP in the D wave meson spectrum is discussed.

Keywords: Quark Model, one-gluon-exchange potential, instanton induced interaction, D wave meson spectra.

PACS Nos. 14.40.-n; 14. 40. Aq; 14. 40. Ev; 12.39.-x; 12.39. Jh

INTRODUCTION

The non-relativistic quark models (NRQM) are a class of phenomenological models developed to explain the hadron interactions. They give the most complete description of hadron properties and are the most successful phenomenological models of hadron structure (Chliapnikov, 2000). The Hamiltonian of these quark models usually contains three main ingredients: the kinetic energy, the confinement potential and a hyperfine interaction term, which has often been taken as an effective one-gluon-exchange potential (OGEP) (De Rujula *et al*., 1975). Other type of hyperfine interaction is Instanton-Induced Interaction (III) deduced by a non-relativistic reduction of the 't Hooft interaction (Hooft, 1976).

In the constituent quark model, conventional mesons are bound states of a spin ½ quark and spin ½ antiquark bound by a phenomenological potential. Essentially, in all phenomenological QCD based quark models, the Hamiltonian for the quark system consists of the kinetic energy, the two–body confinement potential and OGEP. The short distance behaviour is dominated by one gluon exchange and the behaviour at large distance is accounted by the confinement potential. The confinement potential must come ultimately from a non-perturbative treatment of QCD, whereas the residual interaction OGEP is based on perturbation theory. It is well known that the colour magnetic interaction term in OGEP is responsible to reproduce many of the hadron properties. By adjusting the strength of OGEP (α_s), colour magnetic interaction can reproduce the hyperfine splittings (Bhaduri *et al*., 1981) as well as the short range repulsion of the two-nucleon systems in the relative S-wave (Khadkikar and Vijaya Kumar, 1991). However, the strength of OGEP determined in this empirical way is much greater than 1, which makes it hard to treat it as the perturbative effect. There exists another QCD based candidate for such a residual, effective interaction obtained by 't Hooft from instanton effects (Blask *et al*., 1990; Semay *et al*., 1997, 1999). The main achievement of III in hadron spectroscopy is the resolution of the $U_A(1)$ problem, which leads to a good prediction of the masses of η and η' mesons.

Previously, we had employed the NRQM (Bhavyshri *et al*., 2005, 2008) and the relativistic harmonic model (RHM)(Khadkikar *et al*., 1983) along with III to investigate the ground state masses of S and P wave mesons. In RHM Hamiltonian (Vijaya Kumar, 2004) we had used, a Lorentz scalar plus vector confinement potential along with two body OGEP and III potential. The results obtained for the S and P wave mesons in both NRQM and RHM showed that the inclusion of III diminishes the relative importance of OGEP and also the contribution of III is essential in explaining the mass difference between η and η' mesons and to reproduce S and P wave meson masses. The aim of our earlier investigations was also to test whether quark gluon coupling constant (α_s) can be treated as perturbative effect and to understand the role played by the III in meson spectra. Having met with good success (Bhavyshri *et al*., 2007, 2008), in this work we have extended the NRQM to study the D wave meson spectra. The full Hamiltonian used in the investigation has, in addition to the kinetic energy, two bodies OGEP and III. The III also has antisymmetric spin-orbit term proportional to $\vec{L}\cdot\vec{\Delta}$ where $\vec{\Delta}$ is defined in terms of the Pauli matrices

---

*Corresponding author email: kbvijayakumar@yahoo.com as $\frac{1}{2}\left(\vec{\sigma}_1-\vec{\sigma}_2\right)$. We have examined the role of antisymmetric spin-orbit term of III which couples ${}^1L_{J=L}$ and ${}^3L_{J=L}$ in the K-meson sector.

The Model

In NRQM (Bhavyshri *et al*., 2005) the full Hamiltonian is,

$$H = K + V_{OGEP}(\vec{r}_{ij}) + V_{CONF}(\vec{r}_{ij}) + V_{III}(\vec{r}_{ij}) \qquad (1)$$

where

$$K = \sum_{i=1}^{2}\left(M_i + \frac{P_i^2}{2M_i}\right) - K_{CM} \qquad (2)$$

where M_i and P_i are the mass and momentum of the ith quark. The K is the sum of the kinetic energies including the rest mass minus the kinetic energy of the center of mass motion (CM) of the total system. The potential energy part consists of confinement term V_{CONF}, the residual interaction V_{OGEP} and instanton induced interaction V_{III}.

The confinement term is taken to be linear.

$$V_{CONF}(\vec{r}_{ij}) = -a_c \mathrm{r}_{ij}\left(\boldsymbol{\lambda}_i.\boldsymbol{\lambda}_j\right) \qquad (3)$$

where a_c is the confinement strength. The term r_{ij} here and elsewhere in the paper stands for the relative distance between the two quarks Here, $\boldsymbol{\lambda}_i$ and $\boldsymbol{\lambda}_j$ are the generators of the color SU(3) group for the i^{th} and j^{th} quark,

The following central part of two-body potential due to OGEP is usually employed (De Rujula *et al*., 1975),

$$V_{OGEP}^{cent}(\vec{r}_{ij}) = \frac{\alpha_s}{4}\boldsymbol{\lambda}_i.\boldsymbol{\lambda}_j\left[\frac{1}{r_{ij}} - \frac{\pi}{M_iM_j}\left(1+\frac{2}{3}\boldsymbol{\sigma}_i.\boldsymbol{\sigma}_j\right)\delta(\vec{r}_{ij})\right] \qquad (4)$$

where the first term represents the residual Coulomb energy and the second term the chromo-magnetic interaction leading to the hyperfine splitting. The $\boldsymbol{\sigma}_i$ is the Pauli spin operator and α_s the quark-gluon coupling parameter.

The non-central part of OGEP has two terms, the spin-orbit interaction $V_{OGEP}^{SO}(\vec{r}_{ij})$ and the tensor term $V_{OGEP}^{TEN}(\vec{r}_{ij})$. The spin-orbit interaction of OGEP is given by

$$V_{OGEP}^{SO}(\vec{r}_{ij}) = -\frac{\alpha_s}{4}\boldsymbol{\lambda}_i.\boldsymbol{\lambda}_j\left[\frac{3}{8M_iM_j}\frac{1}{r_{ij}^{\;3}}\left(\vec{r}_{ij}\times\vec{P}_{ij}\right)\cdot\left(\boldsymbol{\sigma}_i+\boldsymbol{\sigma}_j\right)\right] \qquad (5)$$

where the relative angular momentum is defined as usual in terms of relative position $\vec{r}_{ij}$ and the relative momentum $\vec{P}_{ij}$.

The tensor part of the OGEP is,

$$V_{OGEP}^{TEN}(\vec{r}_{ij}) = -\frac{\alpha_s}{4}\boldsymbol{\lambda}_i.\boldsymbol{\lambda}_j\left[\frac{1}{4M_iM_j}\frac{1}{r_{ij}^3}\right]\hat{S}_{ij} \qquad (6)$$

where,

$$S_{ij} = [3(\vec{\sigma}_i.\hat{r})(\vec{\sigma}_j.\hat{r}) - \vec{\sigma}_i.\vec{\sigma}_j].$$

The tensor potential is a scalar which is obtained by contracting two second rank tensors.

The non-central part of III has contributions from both spin- orbit and tensor terms. The spin-orbit contribution comes from relativistic corrections to the central potential of III. It is given by (Semay *et al*., 1999),

$$V_{III}^{SO}(\vec{r}_{ij}) = V_{LS}(\vec{r}_{ij})\vec{L}\cdot\vec{S} + V_{L\Delta}(\vec{r}_{ij})\vec{L}\cdot\vec{\Delta} \qquad (9)$$

The first term in Eqn. (9) is the traditional symmetric spin-orbit term proportional to the operator $\vec{L}\cdot\vec{S}$. The other term is the anti-symmetric spin-orbit term proportional to $\vec{L}\cdot\vec{\Delta}$ where $\vec{\Delta} = \frac{1}{2}\left(\vec{\sigma}_1-\vec{\sigma}_2\right)$. The radial functions of Eqn. (9) are expressed as (Semay *et al*., 1999),

$$V_{LS}(\vec{r}_{ij}) = \left(\frac{1}{M_i^2}+\frac{1}{M_j^2}\right)\sum_{k=1}^{2}\kappa_k\frac{\exp(-\mathrm{r}_{ij}^2/\eta_k^2)}{(\eta_k\sqrt{\pi})^3} + \left(\frac{1}{M_iM_j}\right)\sum_{k=3}^{4}\kappa_k\frac{\exp(-\mathrm{r}_{ij}^2/\eta_{k-2}^2)}{(\eta_{k-2}\sqrt{\pi})^3} \qquad (10)$$

and

$$V_{L\Delta}(\vec{r}_{\mathrm{ij}}) = \left(\frac{1}{M_i^2}-\frac{1}{M_j^2}\right)\sum_{k=5}^{6}\kappa_k\frac{\exp(-\mathrm{r}_{\mathrm{ij}}^2/\eta_{k-4}^2)}{(\eta_{k-4}\sqrt{\pi})^3} \qquad (11)$$

The term $V_{LS}(\vec{r})$ is responsible for the splitting of the ${}^3L_J$ states with $J = L-1$, L, L+1. With such a term L is still good quantum numbers but S is not. The term $V_{L\Delta}(\vec{r})$ couples states ${}^1L_{J=L}$ and ${}^3L_{J=L}$. Due to the mass dependence in Eqn. (11), it is clear that this term is inoperative when the quarks are identical. In practice the antisymmetric spin orbit term is important only in the K-sector. The κ_i and η_i are free parameters in the theory (Semay *et al*., 1999; Bhavyshri *et al*., 2008). The M_i corresponds to the mass of the strange quark (s) and M_j corresponds to mass of (u/d) quark. This term accounts for the splitting between 1^1D_2 and 1^3D_2 states in the K sector.

The tensor interaction of III is,

$$V_{III}^{TEN}(\vec{r}_{ij}) = \frac{\hat{S}_{ij}}{M_i M_j}\sum_{k=7}^{8}\kappa_k \frac{\exp(-r_{ij}^2/\eta_{k-4}^2)}{(\eta_{k-4}\sqrt{\pi})^3} \qquad (12)$$

With the tensor interaction, L is no longer a good quantum number since this term couples the states $^3L_{J=L+1}$ and $^3(L+2)_{J=L+1}$. It is to be noted that III and OGEP have the same spin dependence except for $V_{L\Delta}(\vec{r})$ term.

RESULTS AND DISCUSSIONS

In our calculation we have expressed the product of quark-antiquark oscillator wave functions in terms of oscillator wave functions corresponding to the relative and centre-of-mass coordinates (CM).

We are able to calculate the light D wave meson masses with all η's and κ·s held fixed and by varying only the κ_7 and κ_8 parameters. The parameters used in our model are listed in tables 1 and 2. The oscillator quantum number for the CM wave functions is restricted to $N_{cm}=0$. The Hilbert space of relative wave functions is truncated at radial quantum number $n_{max} = 4$. The Hamiltonian matrix is constructed for each meson separately in the basis states of $\left|N_{CM}=0, L_{CM}=0;\ ^{2S+1}L_J\right\rangle$ and is diagonalised.

Table 1. Values of parameters for D wave parameters.

b	0.62 fm
$M_{u,d}$	380 MeV
M_s	560 MeV
a_c	10 MeV fm^{-1}
α_s	0.2
η_1	0.2 fm
η_2	0.29 fm
η_3	1.4 fm
η_4	1.3 fm
κ_1	1.8
κ_2	1.7
κ_3	1.9
κ_4	2.1
κ_5	-22.0
κ_6	-24.5

The masses of the singlet and triplet D wave mesons after diagonalisation in harmonic oscillator basis with $n_{max}= 4$ are listed in tables 3 and 4, respectively. The results show that III along with OGEP interaction is necessary to obtain the meson mass spectra. If OGEP is taken as the only source of hyperfine interaction, the value of α_s necessary to reproduce the hadrons spectrum is generally much larger than one; this leads to a large spin-orbit interaction, which destroys the overall fit to the spectrum (Bhayshri *et al.*, 2005). The important role played by III in obtaining the masses of these mesons can be understood by examining table 5. In table 5, we have listed the calculated masses of triplet D wave mesons without the inclusion of III potential. The role of III is crucial in explaining the mass differences of D wave K mesons. It is interesting to note that the calculated masses without III contribution of triplet D wave mesons involving only u/d quarks are higher than the experimental masses. The inclusion of III lowers the masses of D mesons in u/d sector. In case of other triplet D wave mesons III has attractive contribution.

Table 2. Values of κ_7 and κ_8 parameters.

Meson	κ_7	κ_8
$\omega(1650)$	32.0	46.0
K*(1680)	32.0	46.0
$K_2(1820)$	38.0	46.0
$\omega_3(1670)$	-13.5	-16.0
K*(1780)	1.5	3.2
$\phi_3(1850)$	29.2	35.0

We have also investigated two singlet light D wave mesons and six triplet light D wave mesons namely $\pi_2(1670)$ (1^1D_2) , $K_2(1770)$ (1^1D_2), ω(1650) (1^3D_1), K*(1680) (1^3D_1), $K_2(1820)$ (1^3D_2), $\omega_3(1670)$ (1^3D_3), K*(1780) (1^3D_3), $\phi_3(1850)$ (1^3D_3) (Amsler et.al., 2008). In case of singlet mesons, both colour electric (CE) and colour magnetic (CM) parts of OGEP are attractive. However, the dominant contribution to the masses comes from the kinetic energy and linear confinement potential. In case of triplet D wave mesons the contribution of III potential is very significant. We have noted that in case of 1^3D_1 mesons along with the tensor contribution of III, the spin orbit contribution of III is also significant and attractive. The contribution of tensor term of III in case of 1^3D_2 is repulsive. It is to be noted that the anti-symmetric spin orbit potential of the III contributes substantially to the mass difference between the 1^1D_2 and 1^3D_2 mesons in the K meson sector. The mass difference between K*(1680) and $K_2(1820)$ (Burakovsky *et al.*, 1997) mesons is due to the large difference in tensor part of III potential which in case of the former is attractive and in the latter case is repulsive. In case of $\omega_3(1670)$ and K*(1780) mesons III contribution is repulsive, whereas in case of $\phi_3(1850)$ it is attractive. From tables 3 and 4, we conclude that the calculated meson masses are in good agreement with the experimental masses.

Table 3. Masses of the singlet mesons (in MeV).

$N^{2S+1}L_J$	Meson	Experimental Mass	Calculated Mass
1^1D_2	π_2 (1670)	1670±20	1696.6
	K_2 (1770)	1773±8	1727.4

Table 4. Masses of the triplet mesons (in MeV).

$N^{2S+1}L_J$	Meson	Experimental Mass	Calculated mass
1^3D_1	ω(1650)	1649 ± 24	1649.8
	K*(1680)	1717 ± 27	1720.2
1^3D_2	K_2(1820)	1816 ±13	1817.2
1^3D_3	ω_3 (1670)	1667 ± 4	1667.1
	K*(1780)	1776 ± 7	1778.9
	ϕ_3 (1850)	1854 ± 7	1855.3

Table 5. Masses of triplet mesons (in MeV) without III.

Meson	Experimental Mass	Calculated Mass
ω(1650)	1649 ± 24	1679.9
K*(1680)	1717 ± 27	1716.1
K_2(1820)	1816 ±13	1730.1
ω_3 (1670)	1667 ± 4	1737.4
K*(1780)	1776 ± 7	1755.9
ϕ_3 (1850)	1854 ± 7	1777.7

CONCLUSIONS

We have investigated the effect of the III on the masses of the D wave mesons in the frame work of NRQM. We have shown that the computation of the mesonic masses using only OGEP is inadequate. The contribution of the III is found to be significant. To obtain the masses of D wave mesons, 5x5 Hamiltonian matrix was constructed and was diagonalised. The contribution from the tensor and spin-orbit part of the III is found to be significant in case of triplet D wave mesons. To obtain the physical masses of the mesons in the K sector it is necessary to include the anti-symmetric part of III. There is a good agreement between the calculated and experimental masses of D wave mesons with the inclusion of III.

ACKNOWLEDGEMENTS

One of the authors (APM) is grateful to the DST, India, for granting the JRF. The other author (KBV) acknowledges the DST for funding the project (Sanction No. SR/S2/HEP-14/2006).

REFERENCES

Amsler, C., DeGrand, T. and Krusche, B. 2008. Quark model. Physics Letters B, 667(1-5):172-191.

Bhaduri, RK., Cohler, L. E. and Nogami, Y. 1981. A Unified Potential for Mesons and Baryons. Nuovo Cimento A. 65:376-390.

Bhavyashri, Antony Prakash, Yong-Liang Ma. and Vijaya Kumar, KB. 2008. P wave meson spectrum in a relativistic model with Instanton Induced Interaction.[arXiv:hep-ph/0811.4308v2].

Bhavyashri, Vijaya Kumar, KB., Hanumaiah, B., Sarangi, S. and Shan-Gui Zhou. 2005. Meson spectrum in a non relativistic model with instanton – induced interaction. Journal of Physics G: Nuclear and Particle Physics. 31:981-986.

Blask, WH., Bohn, U., Huber, MG., Metsch, B. Ch. and Petry, HR. 1990. Hadron spectroscopy with insatanton induced quark forces. Z. Phys. A. 337:327-335.

Burakovsky, L. and Goldman, T. 1997. On D-wave meson spectroscopy and the K*(1410) - K*(1680) problem. Nuclear Physics A. 625:220-230.

Chliapnikov, PV. 2000. S-and P- wave meson spectroscopy in the nonrelativistic quark model Physics Letters B. 496:129-136.

De Rujula, A., Georgi, H. and Glashow, SL. 1975. Hadron masses in a gauge theory. Physical Review D. 12:147-162.

Khadkikar, SB. and Gupta, SK. 1983. Magnetic moments of light baryons in harmonic Model. Physics Letters B. 124:523-526.

Khadkikar, SB. and Vijaya Kumar, KB. 1991. N-N scattering with exchange of confined gluons. Physics Letters B. 254:320-324.

Semay, C. and Silvestre- Brac, B. 1997. Potential models and meson spectra. Nuclear Physics A. 618:455-482.

Semay, C. and Silvestre-Brac, B. 1999. Determination of quark- antiquark potentials and meson spectra. Nuclear Physics A. 647:72-96.

Hooft, TG. 1976. Computation of the quantum effects due to a four dimensional pseudoparticle. Physical Review D. 14:3432-3450.

Vijaya Kumar, KB., Hanumaiah, B. and Pepin, S. 2004. Meson spectrum in a relativistic harmonic model with instanton- induced interaction. The European Physical Journal A.19: 247-250.

Received: Oct 22, 2009; Accepted: May 26, 2010

SENRA Academic Publishers, Burnaby, British Columbia
Vol. 4, No. 3, pp. 1315-1321, October 2010
Online ISSN: 1920-3853; Print ISSN: 1715-9997

Canadian Journal of pure&applied sciences

TEMPERATURE OPTIMIZATION FOR BIOETHANOL PRODUCTION FROM CORN COBS

*Clarence S Yah, Sunny E Iyuke, Emmanuel I Unuabonah¸ Odelia Pillay, Chetty Vishant and Samuel M Tessa
School of Chemical and Metallurgical Engineering, Faculty of Engineering and the Built Environment
University of the Witwatersrand, Wits 2050 Johannesburg, South Africa

ABSTRACT

Dilute sulphuric acid and enzymatic hydrolysis methods were used for sugar extraction. Xylose and glucose sugars were obtained from corn cobs. Acid hydrolysis of corn cobs gave higher amount of sugars than enzymatic hydrolysis. The results showed that optimal temperature for sugar fermentation was approximately 25°C by two yeast strains (*S. cerevisiae* and *P. Stipitis).* At 20°C and 40°C, less bioethanol was produced. Bioethanol produced at 25°C was 11.99mg/ml, while at 40°C and 20°C were 2.50mg/ml and 6.40 mg/ml respectively. Data obtained revealed that while xylose level decreased from 27.87 mg/ml to 3.92mg/ml during the first 50h of fermentation and complete metabolism of glucose was observed during this time. Xylose and bioethanol levels remained constant after 50 h. Therefore, by varying the temperature of the fermentation process the effective utilization of corn cobs sugars for bioethanol production can be achieved.

Keywords: Bioethanol, corn cobs, optimization, fermentation, hydrolysis.

INTRODUCTION

In an attempt to maximize waste product into useful material, this article seeks to determine the optimal temperature for large scale bioethanol production from corn cobs. Corn cob, a waste product of corn contains large amount of sugars that can be further utilized to produce various compounds (Cao *et al*., 1986; Adesanya and Raheem, 2009). The bioconversion of lignocellulosics to biofuel from cheap non-edible materials such as corn cob for renewal energy is imperative. Thus, by varying temperature conditions during the fermentation process, maximum productivity of biofuel on an industrial scale can be optimized.

In the brewing industry, production of biofuel is carried out by the fermentation of starchy materials, in which case, sugars are converted into bioethanol with carbon dioxide and water (Hongguang, 2006) as by-products. For waste plant materials to be valuable, it must be converted to fuel as a sustainable substitute to fossil fuel. Therefore, there is a need for renewable energy resources from non-edible agricultural sources such as corn cob to replace fossil forms. This is because gas emissions from plant feedstock fuel are less than those emitted by fossil forms and thus beneficial to the environment and global warming (Demirbas, 2005; Hongguang, 2006). Bioethanol produced from corn uses only a small part of the plant material, whereby only the starch from the kernel is transformed into bioethanol (Cao *et al*., 1986). Several research studies have been carried out on the production of bioethanol from corn cobs through simultaneous saccharification and fermentation of lignocellulosic agricultural wastes by Kluyveromyces marxianus 6556 (Zhang *et al*., 2009), using *Aspergillus niger* and *Saccharomyces cerevisae* in simultaneous saccharification and fermentation (Zakpaa *et al*., 2009) and from Lignocellulosic Biomass (Kumar *et al*., 2009).

Corn however, is a main staple food in South Africa with an annual production of 8.04 million tons (Adesanya and Raheem, 2009). The cobs produced from corn are mainly used as manure for agricultural production. According to the report of Latif and Rajoka (2001), modern biotechnology allows the use of such lignocellulosic substrates as corn cobs in the production of chemicals and fuels, utilizing microorganisms. It has been shown that when corn is used for bioethanol production at higher temperatures, yeast cells die resulting in a decrease in alcohol yield when the pulp is concentrated, while optimal temperature for maximum productivity occurs at 32˚C (Araque *et al*., 2008). It is therefore, necessary to select the optimum temperature at which yeast strains can ferment the sugars from lignocellulosic material.

The simultaneous saccharification and fermentation (SSF) process has been identified as economically viable for the conversion of these substrates to fermentation products

---

Corresponding author email: sunny.iyuke@wits.ac.za

(Cao *et al*., 1986). Conversion of glucose and xylose to ethanol by co-yeast strains has been successfully obtained by Taniguchi *et al*. (1997) using a respiratory deficient mutant of *Saccharomyces cerevisiae* and *Pitchia stipitis. Pichia stipitis* strains ferment xylose at a high capacity of 57g/l than any other yeast, provided the pH is maintained at between 4.5 and 6 and temperature of 25-26°C (Jeffries *et al*., 2007). According to Jeffries *et al*. (2007), maximum yield of ethanol is obtained when a mixture of *S. cerevisiae* and *P. stipitis* are introduced into a medium containing both glucose and xylose. The amount of bioethanol produced therefore, depends on the optimal temperature which, invariably influence sugar utilization by yeast cells (Mwesigye and Barford, 1996). Presently, there is no report on the combined use of *P. stipitis* yeast to *S. cerevisiae* in the production of bioethanol from corn cobs. This study, therefore, seeks to optimize temperature for bioethanol production using corn cobs using two yeast strains.

MATERIALS AND METHODS

The chemicals and reagents used in the study were of analytical grade. The sugar extraction process from the corn cobs was according to Cao *et al*. (1986). The sugar analyses were determined using the HPLC (Agilent Technologies, Waldbronn, Germany). Two strains of yeast: *S. cerevisiae* and *P. stipitis* were used for the fermentation experiment and were obtained from the School of Molecular Biology, University of the Witwatersrand.

Ammonia steeping: Twenty grams of milled corn cobs of particle size of 2mm was mixed with 100ml 2.9 M NH_4OH solution in a 250ml Erlenmeyer flask. The mixture was then incubated in a shaker for 24h at 30^0C. The content was then filtered using a 2µm filter paper into 250ml Erlenmeyer flask. It was further rinsed twice using distilled water. The corn cobs were then dried at 30^0C in an oven overnight.

Dilute acid hydrolysis: The dried corn cobs were then delignified by treating with 0.3 M HCl solution at 121^0C for 1h. The amount of HCl added to dry biomass weight is in the ratio of 1:10 w/v. 0.5 M NaOH was then used to neutralize the acidic hemicellulose hydrolyzate. The Pre-treated cellulosic residue was then washed with distilled water to remove residual acid.

Enzymatic hydrolysis: In a 250ml flask, 50ml of water and 300µl of cellulose was added to the cellulosic residue to convert cellulose to fermentable sugars at 50^0C for 48 h (Sun and Cheng, 2002).

Yeast Culture: Each yeast strain was grown in cooled 25ml broth yeast potato dextrose (YPD) medium prepared by adding 1 g of yeast extract, 2g of peptone powder and 2g of glucose powder to 25ml of distilled water and autoclaved at121^0C for 15minutes. The cultured medium was then placed in an incubator shaker at 220rpm for 18h.

Bioethanol fermentation: Twenty five ml each of hemicellulose hydrolyzate and cellulose hydrolyzate were mixed, inoculated in 500µl each of yeast medium and covered with cheese cloth to allow for proper gaseous exchange. The samples were then put into incubator shakers at different temperatures and shaken for 180rpm. The sugar concentrations were then analysed with HPLC according to the method described by Duke and Henson (2008). In order to remove the yeast cells from the fermentation products, the cultured broth were sterilely filtered. The temperature was varied from 15^0C to 40^0C. The fermentation process was carried out according to Cao *et al*. (1986).

RESULTS

In order to investigate the optimum temperature the acid and enzymatic hydrolysis were used to determine the amount of sugars produced. There was a significant difference ($p< 0.001$) of the sugars obtained from acid and enzymatic hydrolysis. The results showed that the acid hydrolysis produced 1.6mg/ml and 30.23mg/ml of glucose and xylose respectively while the enzymatic hydrolysis 0.12mg/ml and 5.7mg/ml of glucose and xylose respectively. This indicates that enzymatic hydrolysis produces fewer sugars than acid hydrolysis (Fig.1). The fermentation process was repeated for the temperatures 20°C, 25°C, 30°C and 40°C. During the fermentation process, the levels of glucose, xylose and bioethanol were measured after every 5h.

The result in figure 2 shows the concentration of glucose during the fermentation period. It was found that the level of sugar utilization by the yeast strains was faster at 25^0C than at 20^0C, 30^0C and 40^0C. It took 25h for the glucose to be completely metabolized at 25^0Cwhile 50h at 20^0C and 30^0C respectively. It also took 63h for the glucose to be metabolized by the yeast strains at 40^0C (Fig. 2).The glucose concentrations for the temperatures 20°C, 25°C, 30°C and 40°C all dropped from 0.74mg/ml to 0mg/ml at time 25h (25°C), 50h (20 and 30°C) and 63h(40°C) (Fig. 2).

The results of xylose fermentation at varying temperatures are shown in figure 3. The results indicated that at 25°C, the yeast strains utilize the xylose faster than at any other temperature. The utilization was poor at 20°C, 30°C and 40°C (Fig. 3). The xylose concentrations for the temperatures 20°C, 25°C, 30°C and 40°C all dropped from 29.77 mg/ml to 11.99 mg/ml (20°C), 3.92mg/ml (25°C), 5.80mg/ml (30°C) and 15.01mg/ml (40°C) respectively at time 50h (Fig. 3).

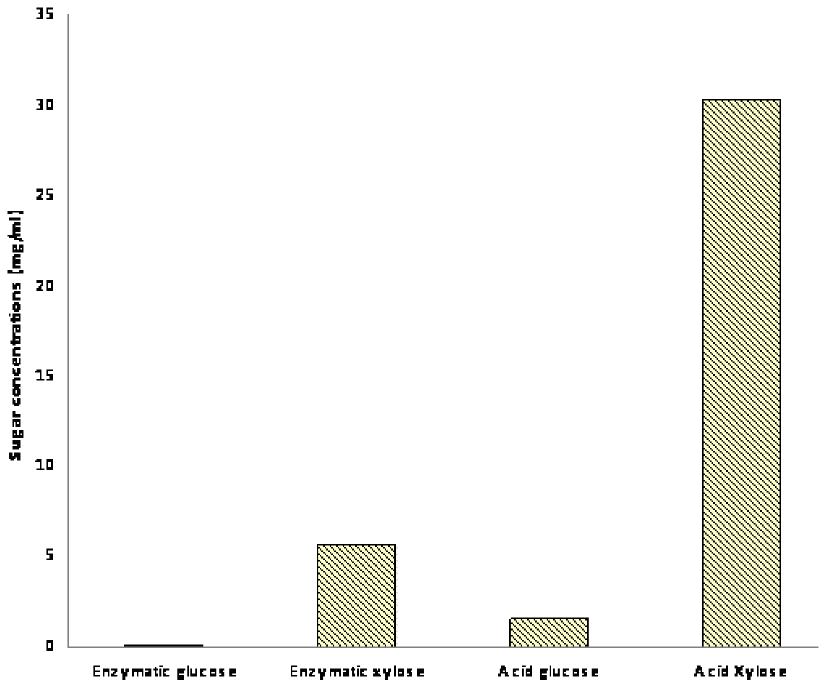

Fig. 1. The concentration of sugars produced from corn cobs using both acid and enzymatic hydrolysis.

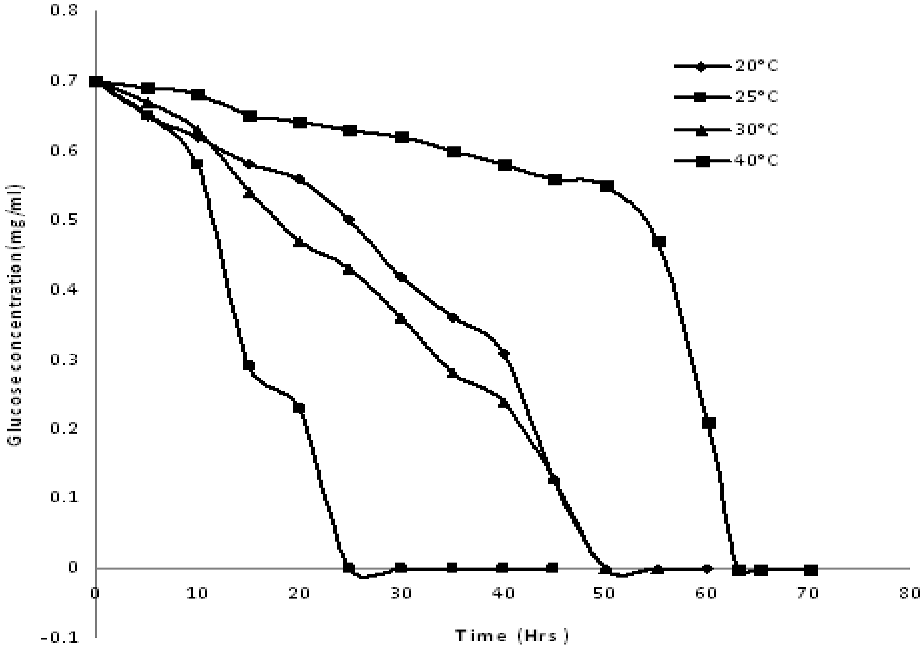

Fig. 2. The amount of Glucose fermentation from corn cob by *S. cerevisiae* and *P. Stipitis.*

The result of the bioethanol concentration at the various temperatures is shown in figure 4. The two yeast cells were able to ferment the sugars at optimum temperature (Fig. 4).

The highest concentration of bioethanol produced from both sugars was 11.99mg/ml at 25°C. The lowest concentration of bioethanol produced was 2.47 mg/ml at a temperature of 40°C. At temperatures of 20°C and 30°C, the concentrations of bioethanol were found to be 6.40mg/ml and 11.08mg/ml respectively (Fig. 4).

Figure 5 shows the production of bioethanol at 25^{0}C. The results showed that the concentrations of the sugars decreased while the concentration of bioethanol increased with respect to time. According to Jeffries *et al*. (2007) by using *S. cerevisiae* only, the glucose gets converted quickly (after about 12.5h), while the xylose takes approximately 48h to be converted to bioethanol and other products. Therefore, the addition of *P. stipitis* yeast to *S. cerevisiae* enhanced the conversion rate of the sugars into bioethanol.

Figure 5 shows that the concentrations of glucose and xylose decrease as the concentration of bioethanol

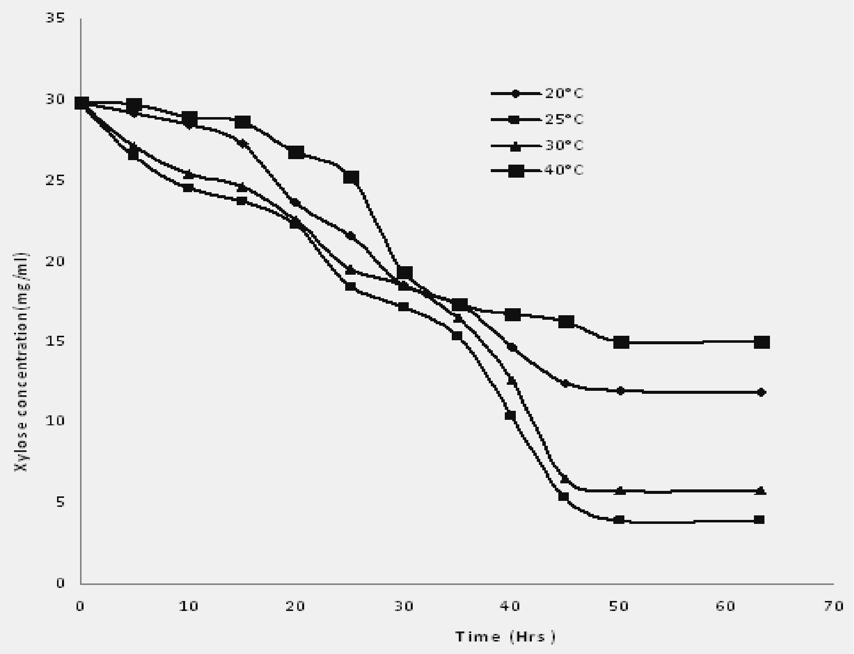

Fig. 3. The amount of Xylose fermentation from corn cob by *S. cerevisiae* and *P. Stipitis.*

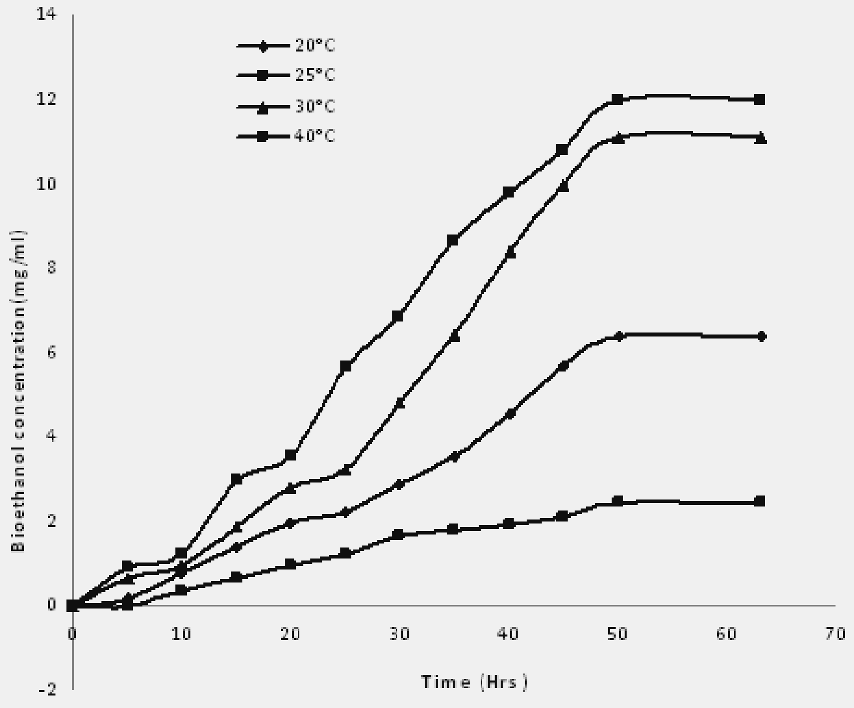

Fig. 4. The amount of bioethanol produced from glucose and xylose sugars.

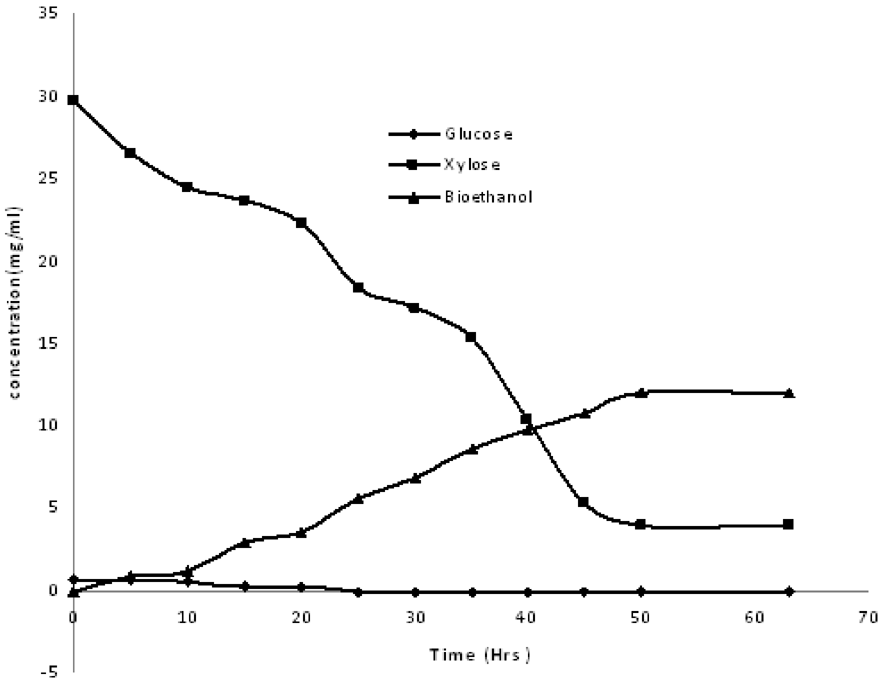

Fig. 5. Temperature optimization of bioethanol production from glucose and xylose sugars at 25°C.

increased to a constant concentration of 11.99 mg/ml at 25°C. All of the glucose was used up. However, the final concentration of xylose was found to be 3.92mg/ml after 50h.

DISCUSSION

The high concentration of xylose present after acid hydrolysis (Fig.1) could be due to the fact that very little lignin was removed during ammonia steeping. Similar observation has been made by Cao *et al.* (1986) and Kumar *et al.* (2009) where they found very high amounts of xylose produced during acid hydrolysis from hemicellulosic material. The analytical studies reveal glucose level of 1.62mg/ml during acid hydrolysis and enzymatic level of 0.12mg/ml. The concentration of the sugar hydrolysates after acid hydrolysis was similar to previous reports by Latif and Rajoka (2001). The xylose fraction during acid hydrolysis was 30.23mg/ml as compared to 5.70 mg/ml of enzymatic hydrolysis. This also follows similar findings by Deng *et al.* (2007) that cellulosic biomass can be easily be hydrolyzed with dilute acid to produce monomeric sugars. The high xylose production was due to the ammonia steeping process which stimulated the cellulosic materials to swell, therefore promoting the efficiency of the acid hydrolysis process. This finding confirm earlier reports by Cao *et al.* (1996) that after the ammonia steeping process the corn cob hemicellulosic fraction can easily be hydrolyzed by dilute acid as well as separated from the cellulosic fraction.

According to Figure 2, the concentrations of glucose decreased with respect to time for all temperatures (Cao *et al.*, 1986). It can also be seen that at 25°C and 30°C, the glucose was used up faster than at 20°C and 40°C. It can be seen that at 25°C, the glucose concentration reached 0mg/ml after 25h and the concentration at 30°C reached 0mg/ml after 50h. The reason for this is because *S. cerevisiae* and *P. stipitis* are known to convert sugars into bioethanol at temperature range of 25°C and 30°C (VanVleet and Jeffries, 2009).

Figure 3 shows the concentration of xylose which also decreased with respect to time for all temperatures correlating with those reported by Cao *et al.* (1986). The xylose was converted faster at 25°C than at 30°C. At this temperature the xylose concentration was found to be approximately 3.92mg/ml after 50h. This could be due to the fact that *P. stipitis* converts xylose into bioethanol at an optimum temperature of 25°C (Jeffries, 2007). Theoretically, 100g of glucose should produce approximately 50.4g of bioethanol and 48.8g of carbon dioxide. However, in practice, the microorganisms use most of the glucose for growth and the actual yield is less than 100% (Araque *et al.*, 2008). From literature it has been shown that the operating temperatures are less than desired because yeast cells performance can be inhibited by other inherent components within in the fermentation process (Vollhals, 1994; Sinha *et al.*, 2006; Deng *et al.*, 2007).

In figure 4, the concentration of the bioethanol was found to increase with respect to time for all temperatures which also correlates to literature (Cao *et al*, 1986; Demirbas, 2005). The highest amount of bioethanol was produced at 25°C and was found to be 11.99 mg/ml approximately 50 h of metabolism. The second highest concentration of bioethanol was found at 30°C to be approximately 11.08mg/ml after 50h. At 40°C, there was a poor conversion of sugars and therefore the bioethanol produced after 50 h was approximately 2.47mg/ml. Araque *et al*. (2008) during fermentation at high temperatures, observed that some adaptable resistance factors from the yeast cells can be generated that can give rise to the difference in ethanol yield. Similar effects were reported previously by Abdel-Fattah *et al*. (2000). From figure 4, the initial rapid decrease of sugar was due to a rapid multiplication of yeast cells and the rapid conversion of the sugars to alcohol via the glucose metabolism (Gibson *et al*., 2008). Generally there was a positive correlation between the sugars reduction of the fermenting medium and a concomitant increase in the ethanol production (Fig. 5). Figure 5 shows the optimum temperature of bioethanol production from glucose and xylose at 25°C where the highest amount of ethanol was produced. Generally, during fermentation, monomeric sugars are metabolized faster than di-, tri- and polymeric sugars. There was a significant difference ($p<0.001$) in ethanol production when the fermentation process approached 50h after that the concentrations of xylose and bioethanol remain constant. This is due to the yeast cells dying and hence after this point no fermentation was really successful.

CONCLUSION

Varying the temperature of the fermentation of corn cobs sugars has an impact on bioethanol production. It was observed that the concentration of sugars (glucose and xylose) after enzymatic hydrolysis was less than that of the acid hydrolysis. The results showed that the combination of ammonia steeping followed by dilute acid hydrolysis gave high amount of sugars. The glucose and xylose concentrations were found to decrease with respect to time whilst that of the bioethanol was found to increase with respect to time. The optimum temperature for bioethanol production *S. cerevisiae* and *P. stipitis* strains was found at 25°C. It was also observed that after 50 h, the xylose and bioethanol concentrations remained constant while glucose was completely metabolized. This was as a result of yeast cells death and hence zeros conversion of sugars to bioethanol.

ACKNOWLEDGEMENTS

The authors acknowledge the financial support from the National Research Fund (NRF) and SA-chair Program, APV Invensys, equipment donation from Falcon Engineering (Pty) Ltd, South Africa, raw material supply from SABMiller of Alrode, South Africa, and moral and technical support from John Cluett of IBD Africa Section and Anton Erasmus of SABMiller, South Africa.

REFERENCES

Abdel-Fattah, W., Fadil, M. and Banet, I. 2000. Isolation of thermotolerant ethanologenic yeast and use of selected strains in industrial scale fermentation in an Egyptian distillery. Biotechnol Bioeng. 68:531-2.

Adesanya, DA. and Raheem, AA. 2009. Development of corn cob ash blended cement. Const. Build. Mater. 23:347-352.

Araque, E., Parra, C., Rodriguez, M., Freer, J. and Baeza, J. 2008. Selection of thermotolerant yeast strains *Saccharomyces cerevisiae* for bioethanol production. Enzyme Microb.Technol. 43:120-123.

Cao, NJ., Krishnan, MS., Du JX., Gong, CS., Ho, NWY., Chen, ZD. and Tsao, G. T. 1986. Ethanol production from corn cob pretreated by the ammonia steeping process using genetically engineered yeast, Biotechnol. lett. l18:1013-1018.

Demirbas, A. 2005. Bioethanol from cellulosic materials: A Renewable Motor Fuel from Biomass. Energy Sources. 27:327-337.

Deng, L., Wang, Y., Zhang, Y. and Runyu, MA. 2007. The enhancement of ammonia pretreatment on the fermentation of rice straw hydrolysate to xylitol. J. Food Biochem. 31:195-205.

Duke, SH. and Henson, CA. 2008. A Comparison of Barley Malt Quality Measurements and Malt Sugar Concentrations. J. Am. Soc. Brew. Chem. 66(3): 151-161.

Gibson, BR., Boulton, CA. and Box, WG., Graham, NS., Lawrence, SJ., Linforth, RST. and Smart, KA. 2008. Carbohydrate utilization and the lager yeast transcriptome during brewery fermentation. Yeast. 25:549-562.

Hongguang, W. 2006. Biomass energy development welcoming bright prospects. Helmholtz Gemeinschaft. en.ce.cn/Insight/200703/02/t20070302_10560407.shtml

Jeffries, TW., Grigoriev, IV., Grimwood, J., Laplaza, JM., Aerts, A., Salamov, A., Schmutz, J., Lindquist, E., Dehal, P., Shapiro, H., Jin, Y., Passoth, V. and Richardson, PM. 2007. Genome sequence of the lignocellulose – bioconverting and xylose – fermenting yeast *Pichia stipitis.* Nat. Biotechol. 25**:**319-326.

Kumar, S., Singh, SP., Mishra, IM. and Adhikari, DK. 2009. Recent Advances in Production of Bioethanol from Lignocellulosic Biomass. Chem. Eng. Technol. 32(4):517-526.

Latif, F. and Rajoka, BI. 2001. Production of ethanol and xylitol from corn cobs by yeasts. Bioresour. Technol. 77:57-63.

Mwesigye, P. and Barford, J. 1996. Batch Growth and Transport Kinetics of Utilization of Mixtures of Sucrose and Maltose by *Saccharomyces cerevisiae.* J. Ferment. Bioeng. 2:101-108.

Sun, Y. and Cheng, J. 2002. Hydrolysis of lignocellulosic materials for ethanol production: a review. Bioresour. Technol. 83:1-11.

Sinha, B., Srakar, PK., Ron, SN. and Bandyopadhyay. 2006. Yeast separation by ceramic membrane and flux recovery after chemical cleaning. Indian Chemical. Engr. 48(1):49-53.

Taniguchi, M., Tohma, T. and Fujii, M. 1997. Ethanol production from a mixture of glucose and xylose by co-culture of Pitchia stipitis and a respiratory-de®cient mutant of *Saccharomyces cerevisiae*. J. Ferment. Bioeng. 83:364-370.

Van Vleet, JH. and Jeffries, TW. 2009. Yeast metabolic engineering for hemicellulosic ethanol Production. Curr. Opin. Biotechnol. 20:300-306.

Vollhals, B. 1994. Energy Saving in the Brewhouse. MBAA Tech. Quart. 31:1-4.

Zakpaa, HD., Mak-Mensah, EE. and Johnson, FS. 2009. Production of bio-ethanol from corncobs using *Aspergillus niger* and *Saccharomyces cerevisae* in simultaneous saccharification and fermentation. Afri. J. Biotechnol. 8 (13): 3018-3022.

Zhang, M., Shukla, P., Ayyachamy, M., Permaul, K. and Singh, S. 2009. Improved bioethanol production through simultaneous saccharification and fermentation of lignocellulosic agricultural wastes by Kluyveromyces marxianus 6556. World J Microbiol Biotechnol. DOI 10.1007/s11274-009-0267-0

Received: May 21, 2010; Accepted: Sept 6, 2010

SENRA Academic Publishers, Burnaby, British Columbia
Vol. 4, No. 3, pp. 1323-1332, October 2010
Online ISSN: 1920-3853; Print ISSN: 1715-9997

MELITTIN – INDUCED CHANGES IN LIPID BILAYERS: A MOLECULAR ACOUSTIC STUDY

Linus N. Okoro
Department of Petroleum Chemistry and Engineering
American University of Nigeria, Yola, Nigeria

ABSTRACT

The effect of melittin at mole fractions of up to 3.75mol%, on the dynamic and mechanical properties of 1,2-dipalmitoyl-*sn*-glycero-3-phosphatidylcholine (DPPC) was investigated using ultrasound velocimetry and densitometry. The isothermal compressibility and volume fluctuations of DPPC – melittin bilayer membrane in their different transition phases were determined. At the melting temperature, T_m, a general increase in velocity number $[u]$ as compared to the pure lipid was noticed. However, at 3.75 mol%, melittin displays the broadest peak and lowest value of $[u]$ compared to the other melittin concentrations, which could be linked to the lytic property of melittin at high peptide concentrations. The melittin concentration effects on the partial specific volume, ν^o and the adiabatic compressibility coefficient of the lipid, β_S^{lipid} of the DPPC bilayer reveals a slight shift of the main transition to lower temperature and a continuous decrease in ν^o with concentration increase above the T_m (except between 1 and 1.25%), as well as a decrease in β_S^{lipid} with decrease in melittin concentration. Again, the isothermal compressibility peak at the main transition drops drastically upon addition of melittin at concentrations as low as 1 mol% and then increases with increase in melittin concentration. At all melittin concentrations, β_T^{lipid} is greater than β_S^{lipid} in the gel-fluid region by ~ 20%. The maximum value of the relative volume fluctuations of 12 % is reached for DPPC at the main transition, and is strongly dampened upon addition of melittin. Only a slight decrease in the calculated relative volume fluctuations with melittin concentration is observed between concentrations 0 and 1.0 mol%.

Keywords: DPPC, Melittin, phospholipid ultrasound velocimetry, densitometry.

INTRODUCTION

Melittin, the principal toxic component in the venom of the European honeybee, *Apis mellifera*, is a cationic hemolytic peptide (Sessa *et al.*, 1969; Habermann, 1972; Tosteson *et al.* 1985). It constitutes 50% of the dry weight of the bee venom. The active peptide melittin is released from its precursor, promelittin, during its biosynthesis in honey bee and later gets formylated (Habermann, 1972). It is composed of 26 amino acids (NH2-G-I-G-A-V-L-K-V-L-T-T-G-L-P-A-L-I-S-W-I-K-R-K-R-Q-Q-CONH2) in which the amino-terminal region (residues 1–20) is predominantly hydrophobic whereas the carboxy-terminal region (residues 21–26) is hydrophilic due to the presence of a stretch of positively charged amino acids. Melittin amphiphilic property makes it water soluble and yet it spontaneously associates with both natural and artificial membranes (Dempsey, 1990). The crystal structures of melittin have been resolved by X-ray crystallography (Terwilliger *et al.*, 1982). In an aqueous solution of high peptide concentration, high pH value, or high ionic strength, tetrameric melittin of high symmetry is formed readily (Dempsey, 1990). The hydrophobic surface of each amphipathic *α*-helical monomer is essentially completely removed from solvent exposure upon tetramerization.

Melittin has been a source of inspiration for the development of novel antiviral and antibacterial agents that act at the membrane level to cause leakage in their lethal mechanism (Baghian *et al.*, 1997). Melittin causes bilayer micellization and membrane fusion and has also been observed to form voltage-dependent ion channels across planar lipid bilayers (Bechinger, 1997; Monette and Lafleur, 1996). The characteristic action of melittin is its hemolytic activity (Habermann, 1972; DeGrado *et al.*, 1982; Rudenko, 1995; Raghuraman and Chattopadhyay, 2005). It is commonly believed that multimeric pore formation is the mode of action of many naturally produced peptides such as antimicrobial peptides and toxins (Allende *et al.*, 2005; Rapaport *et al.*, 1996; Rex, 1996). Few studies have been attempted to monitor the structure and function of such pores and their results show that melittin forms pores that have a rather wide distribution of sizes. For example, the sizes of the melittin pores that are characterized by the inner pore diameter have been reported to be in the range of 10–60 A°, 13–24 A° and 25–30 A° (Rex, 1996; Matsuzaki *et al.*, 1997) from vesicle leakage experiments. The diameter of these pores is expected to increase when the peptide concentration is increased.

Under certain conditions, melittin molecules insert into the lipid bilayer and form multiple aggregated forms that

---

*Corresponding author email: Linus.okoro@aun.edu.ng

are controlled by temperature, pH, ionic strength, lipid composition and the lipid-to-peptide ratio. Lipid composition and phase separation appears to play a critical role in melittin-induced pore formation. The action of melittin on membrane proteins has been studied and apart from its ability to disrupt lipid bilayers, melittin affects the dynamics of membrane proteins. For instance, it has been shown that lytic concentrations of melittin dramatically reduce the rotational mobility of band 3 protein in human erythrocyte membranes (Clague and Cherry, 1988; Hui *et al*., 1990).

Melittin oligomers appear to be involved in membrane permeabilization, which supralinearly depends on the peptide concentration in both voltage-gated ion channel experiments (Pawlak *et al*., 1991). The orientation of melittin in a phospholipid bilayer has been explored (including molecular dynamics simulation studies) and was found to be sensitive to the experimental conditions (Bachar and Becker, 2000; Bradshaw *et al*., 1994; Lin and Baumgaertner, 2000). The aggregation state of melittin in membranes is an important issue since this property is presumed to be associated with the function of melittin. This can be appreciated by the fact that melittin forms voltage-gated channels (Tosteson, 1981) which may require self association of melittin monomers to form pores in membranes. It is not known whether pore-forming melittin aggregates pre-exist in the membrane in the absence of an applied membrane potential.

Light scattering and ^{31}P-NMR have been used to monitor the effects of melittin on phosphatidylcholine (PC) bilayers of variable acyl chain length (from C16:0 to C20:0). From the experiment it was observed that melittin interacts with all lipids provided the interaction is initiated in the lipid fluid phase (Faucon *et al*., 1995). Unger *et al.* (2001) has studied the effect of cyclization of melittin analogues on the structure, function, and model membrane interactions. It was found that cyclization altered the binding of melittin analogues to phospholipid membranes and had increased the antibacterial activity but decreased the hemolytic activity. The interaction of melittin and phospholipids has been extensively studied partly because it has a secondary amphiphilic property (Terwilliger *et al*., 1982; Ladokhin and White, 1999) as well as a model for this class of peptides. Interestingly, the role of melittin–lipid interactions has also been shown to be responsible, along with more specific binding of melittin with membrane proteins, for the inhibition of the Ca^{2+}-ATPase (Baker *et al*., 1995) and protein kinase C (Raynor *et al*., 1991). The dependence of melittin aggregation on temperature (Iwadate *et al*., 1998) and its thermodynamics, as determined by circular dichroism spectroscopy, has been reported (Wilcox and Eisenberg, 1992).

The interaction of melittin with membranes in general, and with cholesterol-containing membranes in particular has been explored, with possible relevance to its interaction with the erythrocyte membrane (Raghuraman and Chattopadhyay, 2004). In an experiment to investigate the lipid-binding behavior of three peptides: melittin, magainin II, and cecropin P1, Lad et al. observed that melittin binding to lipids was 50% greater for either magainin or cecropin (Lad *et al*., 2007).

The lytic activity of melittin has been reported to strongly depend on the membrane composition. Whereas zwitterionic lipids are more affected by the melittin lytic activity (Monette and Lafleur, 1995), membranes with longer hydrocarbon chains are less affected (Bradrick *et al*., 1995). Although cell lysis by melittin has been extensively studied, the molecular mechanism of its hemolytic activity is still not well understood. In particular, the role of specific lipids on melittin-induced hemolysis is not yet clear. Detailed mechanical properties and thermodynamic information on melittin in membranes is important due to the widespread occurrence of the motif in host-defense peptides and membrane proteins. DPPC, one of the best studied phospholipids is a zwitterionic phospholipid with a medium tail consisting of 16 carbons and has a length appropriate for the study of melittin action on lipids.

In the present study, a more detailed dynamic and mechanical picture of melittin-DPPC bilayers around the phase transition temperature as revealed by ultrasound velocimetry and densitometry is obtained, and to gain more insight into the molecular mechanism of the lytic and fusion activity of melittin on DPPC membranes.

MATERIALS AND METHODS

Liposome Preparation

1,2-Dipalmitoyl-3-*sn*-phosphatidylcholine (DPPC) was purchased from Avanti Polar Lipids (Alabaster, AL, USA), while Melittin (≥97% purity) as a lyophilized solid was obtained from Calbiochem (Germany). Both were used without further purification. Multilamellar vesicles (MLV) of DPPC and melittin with designated mole ratios were mixed in chloroform-methanol mixture (3:1 v/v) and dried as a thin film under a stream of nitrogen and then freeze-dried in a freeze-dryer (Christ, Osterode, Germany) under high vacuum overnight. The lipid films were hydrated in a Tris buffer (10 mM Tris-HCl, 100 mM NaCl, pH 7.4), followed by vortexing at ~60°C (above the main phase transition temperature, T_m, of DPPC (~41.5°C (Cevc and Marsh, 1987; Okoro and Winter, 2008) and five freeze-thaw cycles, resulting in homogeneous multilamellar vesicles (MLVs). Large unilamellar vesicles (LUVs) of uniform shape and size used in the ultrasound velocity and the density measurements were prepared from the MLVs by extrusion (MacDonald *et al*., 1991) using a Mini-Extruder (Avanti Polar Lipids Inc., USA), and passing them through 100nm Nuclepore® Polycarbonate Track-Etch™ Membranes (Whatman GmbH, Dassel, Germany) at ~60°C. The final DPPC concentration used in the ultrasound velocity and the density measurements for melittin was 5mg/mL.

Ultrasound velocity and density measurements

The ultrasound velocity *u* of the vesicles was determined simultaneously using a differential ultrasonic resonator device ResoScan (TF Instruments, Heidelberg, Germany, operating in a frequency range of 7.2 – 8.5 MHz. (Eggers and Kustin, 1969; Eggers and Funk, 1973; Stuehr and Yeager, 1965).

Ultrasonic measurements are extremely sensitive to temperature changes. Reproducibility and accuracy is therefore crucially dependent on TFI's Ultra-high Precision Peltier-Thermostat that reaches temperature constancy better than 1 mK (0,001°C), and features a fast heating, cooling and equilibration time between 5 and 85°C.

The sound velocity of the lipid dispersion was determined relative to that in the buffer solution at the same temperature in terms of the velocity number, [*u*], defined as (Stuehr and Yeager, 1965).

$$[u] = (u - u_0)/u_0 c \tag{1}$$

Where u and u_o denote the sound velocity in the solution and in the solvent, respectively, and c is the solute concentration in mol/L.

The densities, ρ and ρ_0, of the lipid solution and the solvent, respectively were measured by a high-precision density meter DMA 5000 (Anton Paar, Graz, Austria) based on the mechanical oscillator principle (Kratky *et al.*, 1973), corrected for viscosity-induced errors.

The partial molar volume, V^0, of the lipid is evaluated from the density data by the given relation:

$$V^{\mathrm{o}} = \left(\frac{\partial V}{\partial n}\right) \cong \frac{M}{\rho_0} - \frac{\rho - \rho_0}{\rho_0 c} \tag{2}$$

Where V is the volume, n the number of solute molecules in moles, and M is the molar mass of the solute. The very right term is valid only for diluted lipid suspensions as used in this study.

The adiabatic compressibility coefficient, $\beta_S = -1/V\ (\partial V/\partial p)_S$ (V, p and S are the volume, the pressure and entropy, respectively), the speed of sound propagation, u, in the medium, and the density, ρ are related by the expression:

$$\beta_S = 1/\,u^2\,\rho \tag{3}$$

In molecular acoustics, due to the additivity of all components of the system, the partial molar adiabatic compressibility, K_S^{o}, is generally used, which is given by;

$$K_S^{\mathrm{o}} = \left(\frac{\partial K_S}{\partial n}\right) = \left(\frac{\partial V^{\mathrm{o}}}{\partial p}\right)_S \cong \beta_{S,0}\left(2\left(V^{\mathrm{o}} - [u]\right) - \frac{M}{\rho_0}\right), \tag{4}$$

where $K_S = \beta_S V$ is the adiabatic compressibility and $\beta_{S,0}$ is the adiabatic compressibility coefficient of the solvent. By dividing the partial molar quantities V^{o} and K_S^{o} by the molar mass of the solute we obtain the partial specific values, i.e., the partial specific volume, v^{o}, and the partial specific adiabatic compressibility, k_S^{o}. Accordingly, the concentration, c, in Eq. 1 becomes c/M, which is then expressed in mg/mL.

The sound velocity was determined with a relative error better than 10^{-3} %, corresponding to a precision higher than 5×10^{-5} mL/g in [u]. The density values were measured with relative error smaller than 10^{-3} %, so the accuracy in v^{o} is better than 10^{-4} mL/g. Therefore, considering the relative errors of [u] and v^{o}, the certainty in k_S^{o} taken from Eq. 4 is within 10^{-12} mL/gPa. In both methods, the corresponding values were measured at discrete temperatures (read with an accuracy of 10^{-3} °C), resulting in an average temperature scan rate of ~12 °C/h.

The adiabatic compressibility of the lipids, β_S^{lipid}, is defined as

$$\beta_S^{\mathrm{lipid}} = -\frac{1}{v^{\mathrm{o}}}\left(\frac{\partial v^{\mathrm{o}}}{\partial p}\right)_S \tag{5}$$

which is related to the partial specific adiabatic compressibility, k_S^{o}, by

$$k_S^{\mathrm{o}} = v^{\mathrm{o}}\beta_S^{\mathrm{lipid}} \tag{6}$$

β_S^{lipid} can thus be directly obtained from combined ultrasound velocity and density measurements.

Lipid bilayer thermotropic main phase transitions are considered to be of weak first-order, i.e., they show typical features of first-order phase transitions, such as abrupt changes in specific volume or a peak in the enthalpy and entropy, but also significant fluctuations in volume and lamellar *d*-spacing, which are typical for a second-order phase transition. The isothermal compressibility, K_T, is directly proportional to the volume fluctuations of the system (Wilson, 1957; Hill, 1960). In a system exhibiting a first-order transition, K_T diverges at the phase transition temperature, whereas it exhibits a power-law behavior ($K_T \propto |T\text{-}T_c|^{-\gamma}$), with a particular critical exponent ($\gamma = 1.24$ for 3D systems) in the critical-point region of a second-order phase transition (Stanley, 1971; Winter *et al.*, 1999). By the ultrasound velocity and the density measurements, however, only the adiabatic compressibility, K_S, can be determined (see Eqn. 3 and 4). The isothermal compressibility can be calculated from (Hill, 1960)

$$K_T = K_S \frac{C_p}{C_V} \tag{7}$$

where C_p and C_V are the heat capacities at constant pressure and volume, respectively, which, using Maxwell relations, can also be expressed as

$$K_T = K_S + \frac{T}{C_p}\left(\frac{\partial V}{\partial T}\right)_p^2 = K_S + \frac{TE^2}{C_p} \tag{8}$$

with the thermal expansion $E = (\partial V/\partial T)_p$. Hence, the isothermal compressibility can be obtained from the adiabatic one when the thermal expansion and the heat capacity data are available. Differentiating Eqn. 8 yields the exact differential of K_T, $\mathrm{d}K_T$, which is given as:

$$\mathrm{d}K_T = \mathrm{d}K_S + \frac{E^2}{C_p}\mathrm{d}T + 2\frac{TE}{C_p}\mathrm{d}E - \frac{TE^2}{C_p^2}\mathrm{d}C_p \tag{9}$$

For convenience, Eqn. 8 is adapted through Eqn. 9 by thermodynamic treatment to a form where the corresponding partial specific quantities are taken (Chalikian, 2003):

$$k_T^{\mathrm{o}} = k_S^{\mathrm{o}} + \frac{T\alpha_0^2}{\rho_0 c_{p,0}}\left(2\frac{e^{\mathrm{o}}}{\alpha_0} - \frac{C_p^{\mathrm{o}}}{\rho_0 c_{p,0}}\right) \tag{10}$$

k_T^{o} is the partial specific isothermal compressibility, α_0 ($\alpha = E/V$) and $c_{p,0}$ are the thermal expansion coefficient and the specific heat capacity of the solvent, respectively; e^{o} and C_p^{o} are the partial specific expansivity and the partial specific heat capacity of the lipid, respectively; the latter is given by (Privalov, 1980)

$$C_p^{\mathrm{o}} = \frac{\Delta C_p}{m} + \frac{v^{\mathrm{o}}}{v_0^{\mathrm{o}}} c_{p,0} \tag{11}$$

where m is the mass of the solute.

The corresponding isothermal compressibility of the lipid, $\beta_T^{\mathrm{lipid}} = k_T^{\mathrm{o}}/v^{\mathrm{o}}$ (note that β_T^{lipid} differs from the partial specific isothermal compressibility coefficient, β_T^{o}, which is defined as $\beta_T^{\mathrm{o}} = 1/M\ (\partial\beta_T/\partial n) = \beta_T\ v^{\mathrm{o}}/V$), can be obtained from Eqn. 10 and is given as:

$$\beta_T^{\mathrm{lipid}} = \beta_S^{\mathrm{lipid}} + \frac{T\alpha_0^2}{v^{\mathrm{o}}\rho_0 c_{p,0}}\left(2\frac{e^{\mathrm{o}}}{\alpha_0} - \frac{C_p^{\mathrm{o}}}{\rho_0 c_{p,0}}\right) \tag{12}$$

For simplification, we denote in Eqn. 12 the second and third term as β_e^{lipid}, and β_C^{lipid}, respectively:

$$\beta_T^{\mathrm{lipid}} = \beta_S^{\mathrm{lipid}} + \beta_e^{\mathrm{lipid}} - \beta_C^{\mathrm{lipid}} \tag{13}$$

Hence, the isothermal compressibility coefficient, β_T^{lipid}, is given as a sum of the adiabatic compressibility, β_S^{lipid}, an expansion term, β_e^{lipid}, and a heat capacity term, β_C^{lipid}. Interestingly, as can be seen from Eqs. 10 and 12, the heat capacity term has a compensating effect, balancing that of the thermal expansion on the adiabatic compressibility.

The thermodynamic parameters C_p, K_T and E are directly related to corresponding fluctuation parameters (Cooper, 1984): i) the square average of the enthalpy fluctuations, its variance, $\langle \Delta H^2 \rangle$, is determined by the heat capacity, C_p, of the system, ii) the square average of the volume fluctuations $\langle \Delta V^2 \rangle$ as given by the respective isothermal compressibility, K_T, and iii) the covariance between H and V, $\langle \Delta H\ \Delta V \rangle$, is related to the thermal expansion, E:

$$\left\langle \Delta H^2 \right\rangle = RT^2 C_p \tag{14a}$$

$$\left\langle \Delta V^2 \right\rangle = RTK_T \tag{14b}$$

$$\left\langle \Delta H\ \Delta V \right\rangle = RT^2 E = RT^2 V\alpha \tag{14c}$$

As seen from Eqn. 14c, the thermal expansion couples contributions from the heat capacity and the isothermal compressibility.

RESULTS AND DISCUSSION

Sound velocimetry and densitometry are sensitive tools to study the mechanics and thermodynamics of biomolecules and biocolloids. When the two methods are used simultaneously to study the phase transition peculiarities of lipid bilayer, they enable one to determine the degree of phase transition cooperativity. This advantage is most useful in the study protein / peptide-lipid interactions, since the determination of mechanical parameters is crucial for an evaluation of the size of distorted membrane structure around proteins or peptides (Hianik and Passechnik, 1995). Ultrasound and densitometry techniques were used to measure the velocity number, [*u*], and the partial specific volume, v^{o}, of the DPPC-melittin mixtures. From equation 4, the partial specific adiabatic compressibility, k_S^{o}, of the lipid dispersion was determined.

Figure 1a shows the temperature dependence of velocity number [*u*] for the DPPC – melittin mixtures. Decrease of [*u*] with rise in temperature is observed, leading to the typical anomalous dip (Mitaku *et al.*, 1978; Kharakoz *et al.*, 1993; Schrader *et al.*, 2002; Krivanek *et al.*, 2008) in the vicinity of T_{m} for pure lipids. The lowest value of [*u*] at T_{m} is ~-0.15mL/g for pure DPPC, which is consistent with Mitaku and co-workers data (Mitaku *et al.*, 1978). It should be noted, however, that the size and the width of the dip in [*u*] depends on the sample preparation Mitaku *et al*. (1978), which is related to the different degree of cooperativity of the main phase transition, on the lipid concentration (Kharakoz *et al*., 1993), and on the ultrasound frequency applied for the measurement itself (Mitaku and Data, 1982), which is related to the heat exchange within the period of the sound wave (Osdol *et al*., 1989; Heimburg and Marsh, 1996). The dip in the ultrasonic number profiles will be more pronounced at lower frequencies, because C_p assumes higher values, leading to an increase of the adiabatic compressibility at lower frequencies. The frequency dependence of the ultrasonic absorption coefficient of DPPC suspensions has been measured. The excess absorption data has been described by a relaxation term with a discrete relaxation time, displaying some evidence of critical slowing down near the phase transition (Heimburg and Marsh, 1996).

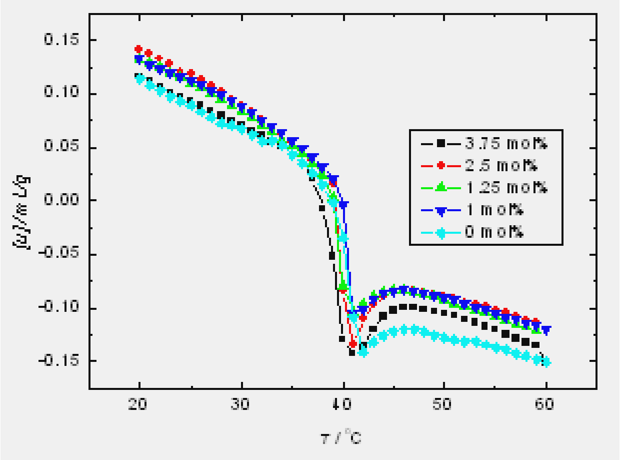

Fig. 1a. The temperature dependence of the ultrasound velocity number, [*u*], for DPPC – melittin mixtures.

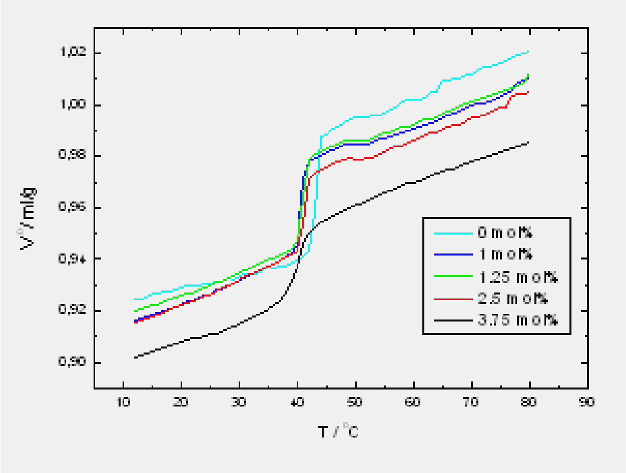

Fig. 1b. The temperature dependence of the partial specific volume, *v*o, for DPPC – melittin mixtures.

Upon addition of melittin to DPPC, and at T_m, there is a general increase in [*u*] as compared to the pure lipid. However, the sample with 3.75% melittin is observed to have the lowest value of [*u*] compared to the lower melittin concentrations studied. It also exhibits the broadest peak. The dip continues to increase with a decrease in melittin concentration, with the highest value being at 1.25% and 1% melittin. This is in contrast to the earlier studied systems lipid-gramicidin D and lipid-sterol systems (Krivanek *et al*., 2008) and might be linked to the lytic property of melittin at higher concentrations, in particular in the lipid phase transition region.

Further observation is that pure DPPC has the least [*u*] both in the gel phase and in the fluid phase region. The ultrasonic velocity profiles provide information about isothermal and adiabatic compressibilities and reveal the deep linkage between the different thermodynamic response functions.

In addition, for the DPPC-melittin mixture, both below the pre-transition and above the main transition, the sound velocity number is approximately the same for the concentrations 1, 1.25 and 2.5% melittin. Generally, addition of melittin to DPPC bilayers causes a slight shift of the melting phase transition to lower temperatures. The ultrasonic velocity profiles provide information about isothermal and adiabatic compressibilities and reveal the deep linkage between the different thermodynamic response functions.

The temperature dependence of the partial specific volume, ν^o, as measured by the densitometer, is shown in figure 1b, and an increase of ν^o with temperature is observed throughout the whole melting transition regime. A step-like change at the transition temperature T_m is observed for pure DPPC and for DPPC – melittin concentrations up to 2.5 mol%. As already stated above, the changes in [*u*] and ν^o with increase in melittin concentration are clearly observed in the T_m region, indicating increased volume fluctuations in this temperature region. The partial specific volume ν^o is smaller both below and above T_m for the DPPC – melittin mixtures. A substantial decrease is observed for ν^o upon addition of melittin up to 3.75 mol%, which could be attributed to the lytic property of melittin at high melittin concentrations. A more detailed behaviour of ν^o in the gel phase (25°C) and in the fluid phase (55°C) is illustrated in figure 2.

Figure 3a displays the temperature dependent partial specific adiabatic compressibility, k_S^o, of the transitions of both pure DPPC and the DPPC – melittin mixtures, as determined from Equation 4. The k_S^o for pure DPPC has the highest value, increasing from 2.35mL/gPa at 20°C and abruptly reaching 5.25 mL/gPa (55°C) at T_m, as expected. A slight drop occurs right after T_m, and k_S^o finally continues to increase with increasing temperature to reach the highest level of 5.4mL/gPa at 60°C. Generally, a slight shift to lower temperatures for k_S^o in the melting transition region is observed, just as observed in [u](T). Significant broadening of the transition peak is observed at the 3.75 % concentration. The temperature dependence of β_S^{lipid} for the DPPC – melittin mixtures is displayed in Fig.3b and exhibits similar shape as $k_S^{\mathrm{o}}(T)$ (Eqn.6).

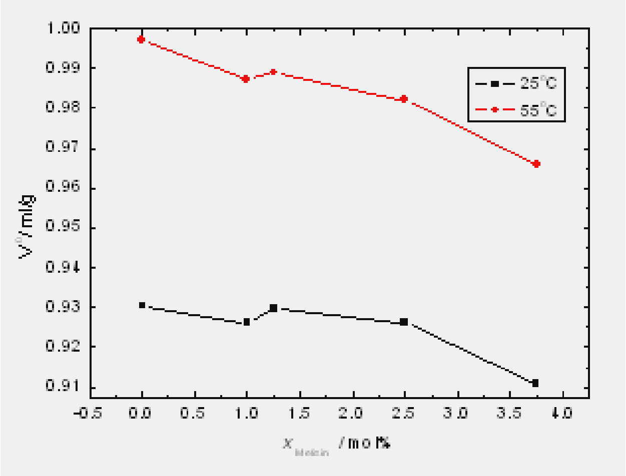

Fig. 2. The partial specific volume of DPPC-melittin mixtures as a function of melittin concentration at 25 and 55 °C.

At 20 and 60 °C, the β_S^{lipid} vales are 3.0 x 10^{-10} Pa^{-1} and 5.4 x 10^{-10} Pa^{-1}, respectively. The value for β_S^{lipid} of 3.4×10^{-10} Pa^{-1} at 30 °C is in good agreement with $\beta_S^{\mathrm{lipid}} = 3.5\times10^{-10}$ Pa^{-1} obtained by Mitaku and coworkers (Mitaku *et al*., 1978). Just as for k_S^{o}, the anomalous increase of β_S^{lipid} around T_{m} is still significant at all melittin concentrations. The data for the adiabatic compressibility coefficient of the DPPC-melittin mixtures as a function of melittin concentration at 25 and 55 °C is summarized in figure 4. The plot reveals a gradual decrease in β_S^{lipid} with melittin concentration in both the gel (25°C) and the fluid phase (55°C) up to 2.5 mol% melittin. An increase in β_S^{lipid} upon addition of 3.75mol% is observed, implying a disordering effect (which could be attributed to melittin pore formation) at these higher melittin concentrations.

Isothermal Compressibility and Volume fluctuations of DPPC – melittin mixtures

Figure 5 displays the temperature dependence of the isothermal compressibility coefficient of DPPC-melittin mixtures at different melittin concentrations. It was observed that the isothermal compressibility peak at the main transition drops drastically (~ 75%) upon addition of melittin at concentrations as low as 1 mol%. This decrease in β_T^{lipid} corresponds to a similar observed strong decrease (80%) of the thermal expansion coefficient in a differential scanning calorimetry (unpublished), again indicating the close relationship between the corresponding fluctuations ($\langle\Delta V^2\rangle$ *vs*. $\langle\Delta H\Delta V\rangle$) (Krivanek *et al*., 2008; Okoro and Winter, 2008). Furthermore, there was an increase in β_T^{lipid} with increase in melittin concentrations at the transition temperature (disordering effect at higher melittin concentrations). At all melittin concentrations, β_T^{lipid} is greater than β_S^{lipid} by ~ 20% in the whole temperature range covered.

Assuming that the partial specific volume, *v*o, is largely determined by the lipid term (see Eqn. 2), i.e. *v*o reflects the "real" volume of the lipid molecule, which allows us to modify Eq. 18 and to convey the relative volume fluctuations given as

$$\sqrt{\frac{\langle\Delta V^2\rangle}{V^2}} = \sqrt{\frac{RT\beta_T^{\mathrm{lipid}}}{Mv^o}} \tag{15}$$

The calculated temperature dependent relative volume

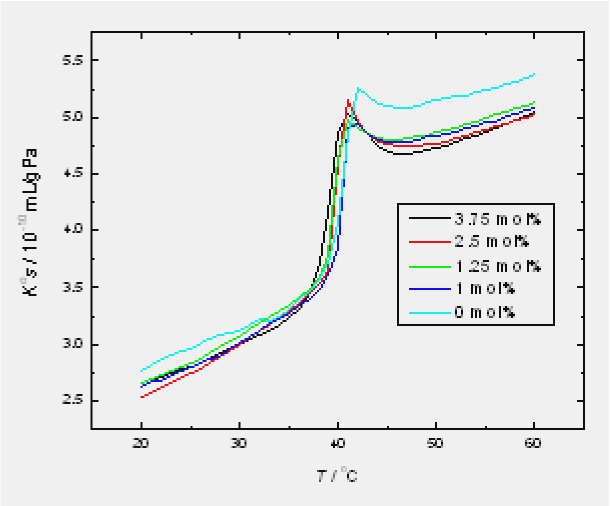

Fig. 3a. The temperature dependence of the partial specific adiabatic compressibility, k_S^{o}, of DPPC-melittin mixtures.

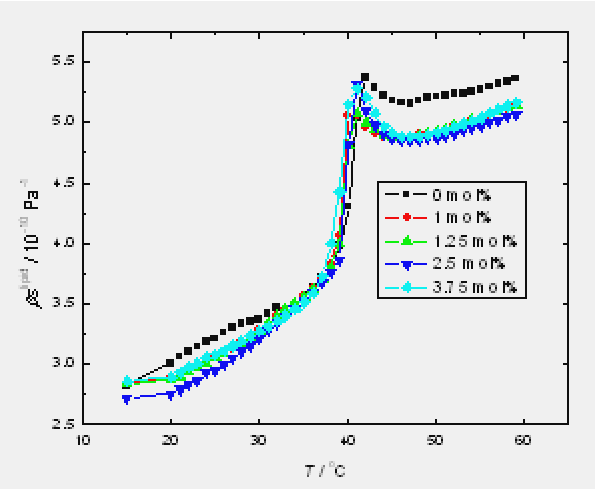

Fig. 3b. The temperature dependence of the adiabatic compressibility coefficient, β_S^{lipid}, of DPPC - melittin fractions.

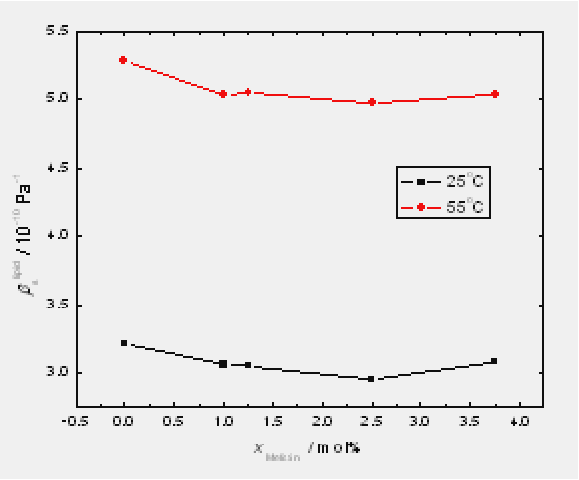

Fig. 4. The adiabatic compressibility coefficient of lipid data of DPPC-melittin mixtures as a function of melittin concentration at 25 and 55°C, respectively.

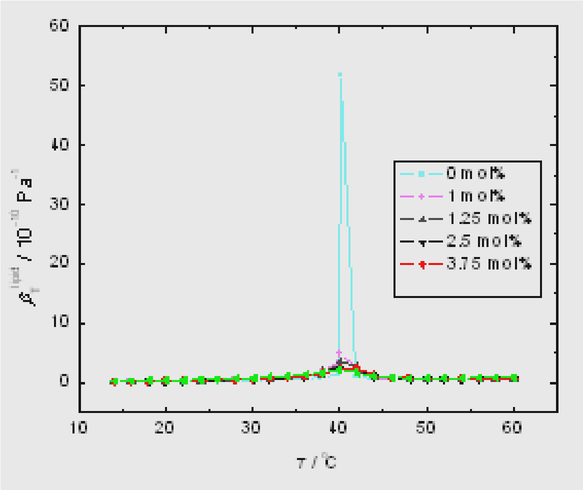

Fig. 5. The temperature dependence of the isothermal compressibility coefficient of the DPPC – melittin mixtures, $\beta_T{}^{lipid}$.

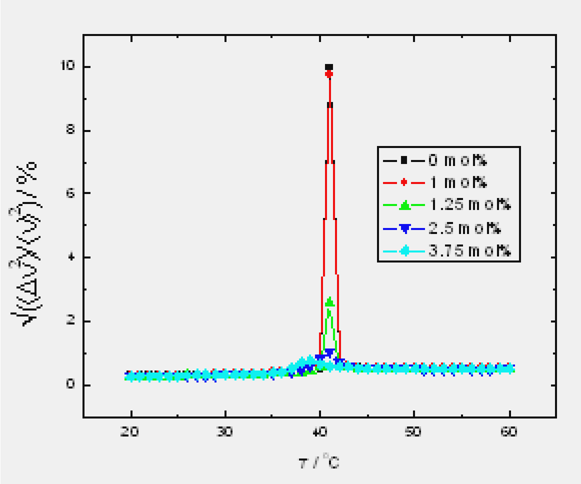

Fig. 6. The calculated relative volume fluctuations for DPPC-melittin mixtures at different melittin molar fractions x_m.

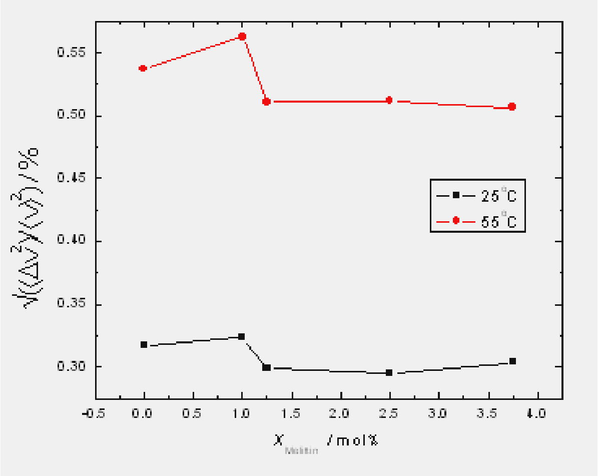

Fig. 7. The temperature dependence of the calculated relative volume fluctuations at 25 and 55°C for DPPC-melittin mixtures at different melittin mole fractions X_m.

fluctuations for DPPC-melittin mixtures are displayed in figure 6. Only a slight decrease in the calculated relative volume fluctuations with melittin concentration was observed between concentrations 0% and 1.0mol%. Above the main transition temperature, basically no change is observed in the temperature dependence of the calculated relative volume fluctuations (at 55°C) for DPPC-melittin concentrations of between 1.25 and 3.75mol% (Fig. 7).

CONLUSION

In summary, the study has provided further insights into the disruptive effects of melittin on membrane bilayers. In this work, molecular acoustics (ultrasound velocity and densitometry) and calorimetry were used to determine isothermal compressibility and volume fluctuations of DPPC – melittin bilayer membranes in their different phases. The study revealed a considerable influence of melittin on the thermodynamic, mechanical, and compressibility properties of DPPC bilayers. It is observed that fluctuations are maximal at the melting point, and that the compressibility is proportional to the local fluctuations in the volume. Oliynyk *et al.* (2007) have demonstrated that melittin incorporation to membranes lead to pore formation and the structure of the melittin pores depends on the thermodynamic state of the membrane. From their AFM images they concluded that at 1mol% melittin, transmembrane pores are induced in the gel phase of DPPC bilayers. Generally, the peptides in model and biological membranes can strongly affect the local state of the system, and the effect of peptide may also depend on the overall state of the membrane. Peptides like alamethicin tend to increase the permeability of biological membranes by not only forming water pores, but also by shifting the surrounding bilayer to more disordered states which are more permeable for small molecules. Hence, the state of the membrane can be a regulating factor of the action of antibiotic peptides like melittin, influencing their capability to form transmembrane pores. At T_m, a general increase in [u] as compared to the pure lipid is observed. However, the 3.75 % melittin induces the broadest peak and lowest value of [u] compared to other melittin concentrations which could be due to changes of hydration of the membrane as a result of the binding process. The dip continued to increase with decrease in melittin concentration, with the highest value being at 1.25 and 1% melitiin. The melittin concentration effects on ν^o and β_S^{lipid} of the bilayer reveals a slight shift of the main transition to lower temperature and a continuous decrease in ν^o (within the range of concentrations studied) above the T_m with concentration (except between 1 and 1.25%), as well as a decrease in β_S^{lipid} with decrease in melittin concentration. Furthermore, the isothermal compressibility peak at the main transition drops drastically upon addition of melittin at concentrations as low as 1 mol% and then increases with increase in melittin concentration. In addition, it was found that at all melittin concentrations β_T^{lipid} is greater than β_S^{lipid} in the gel-fluid region by ~ 20%. The maximum value of the relative volume fluctuations of 12% is reached for DPPC at the main transition, and is strongly dampened upon addition of melittin. Only a slight decrease in the calculated relative volume fluctuations with melittin concentration is observed between concentrations 0 and 1.0 mol%.

ACKNOWLEDGEMENT

Grateful to Prof. Dr. R. Winter, Department of Physical Chemistry, Dortmund University of Technology, Germany, in whose laboratory this work was carried out. Krivanek useful discussion is appreciated. Financial support from the Deutsche Forschungsgemeinschaft (DFG), and the regional country Northrhine Westfalia is gratefully acknowledged.

REFERENCES

Allende, D., Simon, SA. and McIntosh, TJ. 2005. Melittin-induced bilayer leakage depends on lipid material properties: evidence for toroidal pores. Biophys. J. 88:1828-1837.

Bachar, M. and Becker, O. 2000. Protein-induced membrane disorder: A molecular dynamics study of melittin in a dipalmitoylphosphatidylcholine Bilayer. Biophys. J. 78:1359-1375.

Baghian, A., Jaynes, J., Enright, F. and Kousoulas, K. 1997. An amphipatic ∝-helical synthetic peptide analogue of melittin inhibits herpes simplex virus-1 (HSV-1)-induced cell fusion and virus spread. Peptides. 18:177-183.

Baker, KJ., East, JM. and Lee, AG. 1995. Mechanism of inhibition of the Ca2+-ATPase by melittin. Biochemistry. 34:3596-3604.

Bechinger, B. 1997. Structure and functions of channel-forming peptides: Magainins, cecropins, melittin and alamethicin. J. Membr.Biol. 156:197-211.

Bradrick, TD., Philippetis, A. and Georghiou, S. 1995. Stopped-flow fluorometric study of the interaction of melittin with phospholipid bilayers: Importance of the physical state of the bilayer and the acyl chain length. Biophys. J. 69:1999-2010.

Bradshaw, JP., Dempsey, CE. and Watts, A. 1994. A combined x-ray and neutron diffraction study of selectively deuterated melittin in phospholipid bilayers: Effect of pH. *Mol*. Membr. Biol. 11:79-86.

Cevc, G. and Marsh, D. 1987. Phospholipid Bilayers. John Wiley and Sons, New York, USA.

Chalikian, TV. 2003. Volumetric Properties of Proteins. Annu. Rev. Biophys. Biomol. Struct. 32:207-235.

Clague, MJ. and Cherry, RJ. 1988. Comparison of p25 presequence peptide and melittin. Red blood cell haemolysis and band 3 aggregation. Biochem J. 252:791-794.

Cooper, A. 1984. Protein fluctuations and the thermodynamic uncertainty principle. Prog. Biophys. Molec. Biol. 44:181-214.

DeGrado, WF., Musso, GF., Lieber, M., Kaiser, ET. and Kezdy, FJ. 1982. Kinetics and mechanism of hemolysis induced by melittin and by a synthetic melittin analogue. Biophys J. 37:329-338.

Dempsey, CE. 1990. The actions of melittin on membranes. Biochim. Biophys. Acta. 1031:143-161.

Eggers, F. and Kustin, K. 1969. Ultrasonic methods. Methods Enzymol. 16:55-80.

Eggers, F. and Funk, T. 1973. Ultrasonic measurements with millilitre liquid sample in the 0.5 – 100 MHz range. Rev. Sci. Instr. 44:969-978.

Faucon, J-F., Bonmatin, J-M., Dufourcq, J. and Dufourc, E. 1995. Acyl chain length dependence in the stability of melittin-phosphatidylcholine complexes. A light scattering and 31P-NMR study. Biochim. Biophys. Acta. 1234:235-243.

Habermann, E. 1972. Bee and wasp venoms. Science. 177:314-322.

Heimburg, T. and Marsh, D. 1996. Thermodynamics of the interaction of proteins with lipid membranes. In: Biological Membranes: A Molecular Perspective from Computation and Experiment. Eds. Merz, KM. and Roux, B. Birkhauser, Boston. 405-462.

Hianik, T. and Passechnik, VI. 1995. Bilayer Lipid Membranes: Structure and Mechanical Properties, Kluwer Academic, Dordrecht/ Boston/London.

Hill, TL. 1960. An Introduction to Statistical Thermodynamics. Dover, New York, USA.

Hui, SW., Stewart, CM. and Cherry, RJ. 1990. Electron microscopic observation of the aggregation of membrane proteins in human erythrocyte by melittin. Biochim Biophys. Acta. 1023:335-340.

Iwadate, M., Asakura, T. and Williamson, MP. 1998. The structure of the melittin tetramer at different temperatures. An NOE-based calculation with chemical shift refinement. Eur J. Biochem. 257:479-487.

Kharakoz, DP., Colotto, A., Loher, K. and Laggner, P. 1993. Fluid-gel interphase line tension and density fluctuations in dipalmitoylphosphatidylcholine multilamellar vesicles: an ultrasonic study. J. Phys. Chem. 97:9844-9851.

Kratky, O., Leopold, H. and Stabinger, H. 1973. The determination of partial specific volume of protein by the mechanical oscillator technique. Methods Enzymol. 27:98-110.

Krivanek, R., Rybar, P., Prenner, EJ. and McElhaney, RE. 2001. Interaction of the antimicrobial peptide gramicidin S with dimyristoyl-phoshatidyl choline bilayer membranes: A densitometry and sound velocimetry study Biochim. Biophys Acta. 1510:452-463.

Krivanek, R., Okoro, L. and Winter, R. 2008. Effect of cholesterol and ergosterol on the compressibility and volume fluctuations of phospholipid-sterol bilayers in the critical point region – A molecular acoustic and calorimetric study. Biophys. J. 94:3538-3548.

Lad, M., Birembaut, F., Clifton, L., Frazier, R., Webster, J. and Green, R. 2007. Antimicrobial Peptide-Lipid Binding Interactions and Binding Selectivity. Biophys. J. 92:3575-3586.

Ladokhin, A. and White, S. 1999. Folding of amphiphilic $\propto$-helices on membranes: Energetics of helix formation by melittin. J. Mol. Biol. 285:1363-1369.

Lin, J-H. and Baumgaertner, A. 2000. Stability of a Melittin Pore in a Lipid Bilayer: A Molecular Dynamics Study. Biophys. J. 78:1714-1724.

MacDonald, RC., MacDonald, RI., Menco, BP., Takeshita, K., Subbarao, NK. and Hu, LR. 1991. Small-volume extrusion apparatus for preparation of large unilamellar vesicles. Biochim. Biophys. Acta. 1061:297-303.

Matsuzaki, K., Yoneyama, S. and Miyajima, K. 1997. Pore formation and translocation of melittin. Biophys. J. 73:831-838.

Mitaku, S., Ikegami, A. and Sakanishi, A. 1978. Ultrasonic studies of lipid bilayer phase transition in synthetic phosphatidylcholine liposomes. Biophys. Chem. 8:295-304.

Mitaku, S. and Data, T. 1982. Anomalies of nanosecond ultrasonic relaxation in the lipid bilayer transition. Biophys. Biochim. Acta. 688:411-421.

Monette, M. and Lafleur, M. 1996. Influence of lipid chain unsaturation on melittin-induced micellization. Biophys. J. 70:2195-2202.

Okoro, L. and Winter, R. 2008. Pressure Perturbation Calorimetric Studies on Phospholipid-Sterol Mixtures. Z. Naturforsch. 63b:769-778.

Oliynyk, V., Kaatze, U. and Heimburg, T. 2007. Defect formation of lytic peptides in lipid membranes and their influence on the thermodynamic properties of the pore environment. Biochim. Biophys. Acta. 1768:236-245.

Osdol, VW., Biltonen, RL. and Johnson, ML. 1989. Measuring the kinetics of membrane phase transition. J. Bioenerg. Biophys. Methods. 20:1-46.

Pawlak, M., Stankowski, S. and Schwarz, G. 1991. Melittin induced voltage-dependent conductance in DOPC lipid bilayers. Biochim. Biophys. Acta. 1062:94-102.

Privalov, PL. 1980. Scanning microcalorimeters for studying macromolecules. Pure Appl. Chem. 52:479-497.

Raghuraman, H. and Chattopadhyay, A. 2004. Interaction of melittin with membrane cholesterol: A fluorescence approach. Biophys. J. 87:2419-2432.

Raghuraman, H. and Chattopadhyay, A. 2005. Cholesterol inhibits the lytic activity of melittin in erythrocytes. Chem Phys Lipids. 134:183-189.

Rapaport, D., Peled, R., Nir, S. and Shai, Y. 1996. Reversible surface aggregation in pore formation by pardaxin. Biophys J. 70:2502-2512.

Raynor, RL., Zheng, B. and Kuo, JF. 1991. Membrane interactions of amphiphilic polypeptides mastoparan, melittin, polymyxin B, and cardiotoxin. Differential inhibition of protein kinase C, Ca2+/calmodulindependent protein kinase II and synaptosomal membrane Na,K-ATPase, and Na+ pump and differentiation of HL60 cells. J. Biol. Chem. 266:2753-2758.

Rex, S. 1996. Pore formation induced by the peptide melittin in different lipid vesicle membranes. Biophys. Chem. 58:75-85.

Rudenko, SV. and Patelaros, SV. 1995. Cation-sensitive pore formation in dehydrated erythrocytes. Biochim Biophys Acta. 1235:1-9.

Sessa, G., Freer, JH., Colacicco, G. and Weissmann, G. 1969. Interaction of a lytic polypeptide, melittin, with lipid membrane systems. J. Biol. Chem. 244:3575-3582.

Schrader, W., Ebel, H., Grabitz, P., Hanke, E., Heimburg, T., Hoeckel, M., Kahle, M., Wente, F. and Kaatze, U. 2002. Compressibility of Lipid mixtures studied by calorimetry and ultrasonic velocity measurements. J. Phys. Chem. 106:6581-6586.

Stanley, HE. 1971. Introduction to Phase Transitions and Critical Phenomena. Oxford University Press, New York.

Stuehr, J. and Yeager, E. 1965. The Propagation of Sound in Electrolytic Solutions. In: Physical Acoustics. Ed. Mason, WP. (Vol. 2A). Academic Press, New York.

Terwilliger, T., Weissman, L. and Eisenberg, D. 1982. The structure of melittin in the form I crystals and its implication for melittin's lytic and surface activities, Biophys. J. 37:353-361.

Tosteson, MT. and Tosteson, TC. 1981. The sting. Melittin forms channels in lipid bilayers. Biophys J. 36:109-116.

Unger, T., Oren, Z. and Shai, Y. 2001. The effect of cyclization of magainin 2 and melittin analogues on the structure, function, and model membrane interactions: Implication to their mode of action. Biochemistry. 40:6388-6397.

Wilcox, W. and Eisenberg, D. 1992. Thermodynamics of melittin tetramerization determined by circular dichroism and implications for protein folding. Protein Sci. 1:641-653.

Wilson, AH. 1957. Thermodynamics and statistical mechanics. Cambridge University Press, Cambridge.

Winter, R., Gabke, A., Czeslik, C. and Pfeifer, P. 1999. Power-law fluctuations in phase-separated lipid membranes. Phys. Rev. E. 60:7354-7359.

Received: June 6, 2010; Revised and Accepted: Sept 30, 2010